Van der Waals Layered Materials: Surface Morphology, Interlayer Interaction, and Electronic Structure

Po-Chun Yeh
葉柏均

Submitted in partial fulfillment of the

requirements for the degree of

Doctor of Philosophy

in the Graduate School of Arts and Sciences

COLUMBIA UNIVERSITY

2015

Po-Chun Yeh
葉柏均

ABSTRACT

Van der Waals Layered Materials - Surface Morphology, Interlayer Interaction, and Electronic Structure

Po-Chun Yeh
葉柏均

Over the past decades, new materials have formed the backbone in shaping the landscape of technology. From the Si-based transistors in our smart devices to the carbon fibers that have redefined air-transportation, the pursuit for a stronger, lighter, and cost-effective material has never ceased, as well as the attempt to fully understand their physics and material properties. Moore's law just turned 50th this year. Moore's law seems harder and harder to hold as the industry has reached a point where the dimensions of those Si-based transistors are getting too small and thin to proceed quickly and without incurring substantial additional cost. Also, the transistor dimensions have been getting closer and closer to the physical limitation of the Si. Today, the most advanced node is merely "7 nm" – less than 15 layers of Si, silicon oxides, or other metal oxides. At this point, every layers of atoms counts. The search for new ultrathin materials as the "new silicon" has begun.

In this regard, graphene, which is a single sheet of carbon atoms arranged in a hexagonal honeycomb lattice, has led to a huge interest in the science and technology communities due to its exotic physics that arises from low-dimensional confinement. This interest soon extended to two-dimensional (2D) electronic materials systems, especially

semiconducting van der Waals layered-materials such as MoS_2 that, unlike graphene, has a direct bandgap material in its monolayer form. There are also many other promising candidates such as transition metal dichalcogenides (TMDCs), black phosphorene, and perovskites on this rapid growing "2D materials" family tree. From condensed matter physics' point of view, studying the electronic behavior of these 2D systems can provide insight into a variety of phenomena, including epitaxial growth, interfacial charge transfer, energy-momentum relation, and carrier mobility, that leads to advanced device fabrication and engineering. In this dissertation, I examine (1) the surface structure, including the growth, the crystal quality, and thin film surface corrugation of a monolayer sample and a few layers of MoS_2 and WSe_2, and (2) their electronic structure. The characteristics of these electronic systems depend intimately on the morphology of the surfaces they inhabit, and their interactions with the substrate or within layers. These physical properties will be addressed in each chapter.

This thesis has dedicated to the characterization of mono- and a few layers of MoS_2 and WSe_2 that uses surface-sensitive probes such as low-energy electron microscopy and diffraction (LEEM and LEED). Prior to our studies, the characterization of monolayer MoS_2 and WSe_2 has been generally limited to optical and transport probes. Furthermore, the heavy use of thick silicon oxide layer as the supporting substrate has been important in order to allow optical microscopic characterization of the 2D material. Hence, to the best of our knowledge, this has prohibited studies of this material on other surfaces, and it has precluded the discovery of potentially rich interface interactions that may exist between MoS_2 and its supporting substrate. Thus, in our study, we use a so-called SPELEEM system (Spectroscopic Photo-Emission and Low Energy Electron Microscopy) to address these

imaging modalities: (1) real-space microscopy, which would allow locating of monolayer MoS_2 samples, (2) spatially-resolved low-energy diffraction which would allow confirmation of the crystalline quality and domain orientation of MoS_2 samples, and, (3) spatially-resolved spectroscopy, which would allow electronic structure mapping of MoS_2 samples. Moreover, we have developed a preparation procedure for samples that yield, a surface-probe ready, ultra-clean, and can be transferred on an arbitrary substrate.

In this thesis, to fully understand the physics in MoS_2 such as direct-to-indirect band gap transition, hole mobility, strain, or large spin-orbit splitting, we investigate our sample using micro-probe angle-resolved photoemission (μ-ARPES), which is a powerful tool to directly measure the electronic structure. We find that the valence bands of monolayer MoS_2, particularly the low-binding-energy bands, are distinctly different from those of bulk MoS_2 in that the valence band maximum (VBM) of a monolayer is located at $\bar{K}$ of the first Brillouin zone (BZ), rather than at $\bar{\Gamma}$, as is the case in bilayer and thicker MoS_2 crystals. This result serves as a direct evidence, if complemented with the photoluminescence studies of conduction bands, which shows the direct-to-indirect transition from mono- to milti-layer MoS_2. We also confirmed this same effect in WSe_2 in our later studies. Also, by carefully studying the uppermost valence band (UVB) of both exfoliated and CVD-grown monolayer MoS_2, we found a compression in energy in comparison with the calculated band, an effect, which were also observed in suspended sample with minimum-to-none substrate interaction. We tentatively attribute it to an intrinsic effect of monolayer MoS_2 owning to lattice relaxation. The degree of compression in CVD-grown MoS_2 is larger than that in exfoliated monolayer MoS_2, likely due to defects, doping, or stress. Furthermore, we find that the uppermost valence band near $\bar{K}$ of

monolayer MoS_2 is less dispersive than that of the bulk, which leads to a striking increase in the hole effective-mass and, hence, the reduced carrier mobility of the monolayer compared to bulk MoS_2.

Beyond monolayer MoS_2, we have studied the evolution of bandgap as a function of interlayer twist angles in a bilayer MoS_2 system. Our μ-ARPES measurements over the whole surface-Brillouin zone reveal the $\overline{\Gamma}$ state is, indeed, the highest lying occupied state for all twist angles, affirming the indirect bandgap designation for bilayer MoS_2, irrespective of twist angle. We directly quantify the energy separation between the high symmetry points $\overline{\Gamma}$ and $\overline{K}$ of the highest occupied states; this energy separation is predicted to be directly proportional to the interlayer separation, which is a function of the twist angle. We also confirm that this trend is a result of the energy shifting of the top-most occupied state at $\overline{\Gamma}$, which is predicted by DFT calculations. Finally, we also report on the variation of the hole effective mass at $\overline{\Gamma}$ and $\overline{K}$ with respect to twist angle and compare it with theory. Our study provides a direct measurement and serves as an example for how the interlayer coupling can affect the band structure and electron transitions, which is crucial in designing TMDs devices.

To the end of this thesis, I briefly sum up our angle-resolve two-photon photoemission (2PPE) studies on self-assembly molecules, organic molecules, and graphene on highly-crystalline metal systems, and our investigation of their interfacial charge transfer/trapping, image potential states, and coverage-dependent dipole moments, as well as their work functions by using a tunable ultra-fast femtosecond laser.

Table of Contents

List of Figures

that the reflectivity of the background Si substrate was raised by doping, indicating a lowered work function. Potassium nucleation islands (marked by the yellow arrows) form on the surface upon potassium deposition. The density of these islands increases with potassium deposition. (c), (f) LEEM images taken after potassium was removed from the surface via annealing at 160 ^{o}C for 1.5 hour and then at 350 ^{o}C for 15 min. This annealing reduces the density of the potassium islands and returns the work function to its original level prior to potassium deposition. (g) A sketch illustrating how the CVD MoS_2 adhered on a PDS layer was transferred onto a pre-patterned Si chip. (h) LEEM images with examples of polycrystalline MoS_2 aggregates of different orientations obtained under different growth conditions. In this particular case, differently oriented domains of MoS_2 islands intersected during CVD growth, and exhibited fracturing along their faceted tilt grain boundary after sample transfer. The electron energies used in LEEM are (a) 0.9 eV (b) 1.9 eV (c) 1 eV (d) 0.54 eV (e) 2.1eV (f) 1 eV and (h) 0.58 eV. 79

Figure 3.4 Comparison of 1ML MoS_2 using μ-LEED (a)-(c) CVD MoS_2 on SiO_2, (d)-(f) CVD MoS_2 transferred onto native-oxide terminated silicon, (g)-(i) exfoliated and transferred onto native oxide terminated silicon. (a), (d), (g) LEEM images at energy 0.06 eV, 0.46 eV, and 5 eV respectively. (b), (e), (h) corresponding LEED patterns at 40 eV electron energy. (c), (f), (i) LEED at 50 eV. The LEED pattern shows transitions between 3- and 6-fold symmetry at different electron energies. Also, the (00) LEED spot widths for (d) and (g) are comparable. (j) Intensity-normalized line profile of the (00) LEED spot of CVD and exfoliated MoS_2 on Si; horizontal axis units are in $Å^{-1}$. (k) Comparison between pre-transferred MoS_2 on SiO_2 and post-transferred MoS_2 on Si for two different energies.

Acknowledgements

In countless moments in our life, if we were lucky enough to achieve something of memorable value, or to sputter a spark of brilliance in our works, it is actually not possible without the accumulative effort of the people around us. Naturally, we tend to credit our success to our own intellectual capability, hard work, and dedication. Yet, this is just part of the story. What really brings me here today, is the people around me that give me the kindness that I never asked for but received without any condition. For me, as I venture through in my long journey of pursuing knowledge and self-exploration, while searching for a few stars in the universe of Science on my way, I always feel I am deeply loved by numerous people that offer me assistance, guidance, and their kindness for no return. I am blessed. I am privileged. I am grateful.

Looking back in my life as a graduate student in Columbia University, I have owed an enormous debt and my gratitude to the people who have helped me, or influenced me during my time at the states. Without their help and support, I could not have been able to complete the degree, and to complete myself. Foremost, I would like to thank my advisor, Prof. Richard Osgood, Jr., who has been a constant source of encouragement, guidance and support. He has provided a research environment that has enabled me to grow and develop as a scientist, without losing a creative engineering state of mind. The most important of all, is that he casts his magic to inspire me and he set up an example by his actions. Every day as I can remember, he shows up early, on his schedule, working hard, and trying his best to help people. I also appreciate those immediate and benign corrections he made to my phrasing and grammars during our group meetings or when I was preparing for big

talks. Oh, and the "secret handshake" technique that he cannot emphasize more, which is always the elixir when I collaborate with others. Not to mention how we have been doing "monkey-around" and "horse-around" works together, writing papers together, and fighting hard to be awarded as "a proud member in a concentration camp built by Chairmen Mao." Last, his understanding and support to Taiwan, as a country, and to Taiwanese people, means a lot to me.

I am very gratitude to all the professors that I have met along the way. Each of them shows me the true nature of being a professor in such a distinguished school with great history. To name a few: Prof. Philip Kim showed me that humbleness is a strength; Prof. Tony Heinz showed me a different way of looking at physics; Prof. James Hone showed me his swiftness and ambition, and we had a good time in collaboration. Prof. Abhay Pasupathy showed me his love and dedication for science. Prof. Irving Herman showed me his sharp sense in physics and in humor. There are other excellent professors that inspired me in their own way: Prof. James Yardley, Prof. Cory Dean, Prof. Robert Laibowitz, Prof. John Kymissis, Prof. George Flynn, Prof. Louis Brus, Prof. Keren Bergman, Prof. Amiya Sen, and Prof. Paul Diamond in Columbia; Prof. Dirk Englund, Prof. Alberto Morgante, Prof. Marko Kralj, and Prof. Dr. Thomas Fauster. Although I did not have the privilege to directly collaborate with you, I do learn and inspired by your examples.

In Osgood group, what can I say! The people here are the corner stones for what I have achieved today, and they are my friends for a life time. I owed a lot to my long term collaborators: Sung-Young Hong, Wencan Jin, Nader Zaki, and Jerry Dadap. Sung-Young is the dream lab partner – dedicate, hardworking, and is a true gentleman. It was really because of his encourage and persistence that I can endure all the setbacks and stress when

I struggled to fix the instruments to get experiments going. Wencan is the guy that really leads me into the Pantheon of ARPES, and we have done a lot together, amazing. To me, Nader is an intellect with no swelling ego, always ready to engage in critical thinking. He is really the propelling engine behind most of my papers. Big thanks. Jerry is my mentor in Osgood's group. Especially when I just joined the group, still working on my master degree, not knowing too much about how to do research, and felt like an outsider, Jerry was the Deus ex machina that appeared and helped me through it. I am very grateful to him.

Furthermore, in Osgood group, I would like to thank Stan (Hsu-Cheng Huang), my fellow Taiwanese friend, for sharing with me his warmest friendship, his love in his research, and his well-thought advices. How lucky is it to have him here with me. I am indebted to the Z man (Zhisheng Li) for his generous deed that helped me in many ways, his uplifting words when I was down, and his inputs in my works. I also want to thank Kevin Knox, my senior in surface physics research, who explained everything he knew to me, again and again, with great patience and detail, which was such a big help to a me. I also want to give credit to Denis Potapenko for helping me building my UHV apparatus, giving me a lot of precious advices about UHV system, and for whom is such an honest and kind person. Also there's the little "Richie", Richard Grote, who is a true scientist with crazy ideas, good humor, and a mind as a rocker. I really enjoy our small talks. This list can just go on-and-on with no ending. Therefore I would like to give my biggest gratitude to people that has helped me in many means: Xiaoping Liu, Manolis Antonoyiannakis, Alex Meng, Jeffrey Driscoll, Brian Souhan, Ophir Gaathon, Nicholas Biekert, Nick Choi,

Ida Delač, David Nobis, Eugene Cho, Yang Lou, Ilkyu Lee, Yi lin, Jacob Rothenberg, Peter Bullen, Shuai Chang, and Nathan Abrams.

Right outside the Osgood kingdom, there are a tons of people I am indebted with: my collaborators Nick Petron, Arend van der Zande, Daniel Chenet, Ghidewon Arefe, Datong Zhang, Johnathan Liou, Carlos Arguello, Ethan Rosenthal, and Erick Andrade. They are the role model of graduate student: always helping, coordinating, and working hard. There are some other very important collaborators that works in synchrotrons: my sincere thanks to Jurek Sadowski, Abdullah Al-Mahboob, Peter Sutter, Andrea Locatelli, Tevfik Mentes, Alessandro Sala, Alexey Barinov, Pavel Dudin, and many.

There are many other people that have helped me but did not appear in my papers. They are my friends, and my source of happiness in Columbia: Yumeng You, Xiaoxiao Zhang, Alexey Chernikov, Dezheng Sun, Omer Yaffe, Archana Raja, Yilei Li, and Ozgur (Burak) Asla from Heinz group, they are the goodfellas, my source of inspiration and laughers; there are Alex (Xu) Cui, Xia Zhang, Yufeng Hao, Mufeng Hu (my ex-roommate!), Sunwoo Lee (my karaoke partner, one night in Beijing), Fan Zhang, Liuyan Zhao, Christopher Gutierrez, Amir Zabet, Jiayang Hu, that have helped me in my experiment, shared with me their knowledge, and so on so forth.

I want to thank my friends, my fellows, and my relatives. I wish all the best to them and will always keep their kindness in my heart. It is sad that I don't usually enjoy the privilege to meet them frequently.

Last, I would like to express my deepest thanks to my family – my mom, my dad, my brother, my loved ones, and my hometown, Taiwan. When I went to the states, far far away from her for almost 6 years, a lot happened. With this opportunity to get away, I

finally realized how much I love this land and her people. Taiwan is my only country, my family, and my root. I wish all my family members, friends, and all the good people living in this beautiful island can live long and prosper. A year ago (2014), I was deeply moved by the 318 "Sunflower" student movement. We as people, speak, act, and fight in many ways, by many means, and going restlessly against the injustice in the law, the bureaucracy and the lack of transparency of our government in policy making, the abuse of power, to protect our democracy. This is a new generation of Taiwanese people. I am so proud to see them rise. I feel there is hope in our nation's future. Thank you all.

For myself, I want to leave this quote for my future self:

"*Do one thing that scares you every day. Stay hungry, stay foolish.*"

To my family, my loved ones, esp. to my dear Mom and Dad

Chapter 1

Introduction

"There's plenty of room at the bottom." - Richard P. Feynman

1.1 Two Dimensional Surface Systems

Two-dimensional (2D) materials [1] have historically been one of the most extensively studied classes of materials due to the wealth of unusual physical phenomena that occur when charge and heat transport is confined to a plane. Many materials have novel properties dominated by their two-dimensional structural units as stacks of strongly bonded layers with weak interlayer attraction, allowing exfoliation into individual, atomically thin layers. For example, the layered metal dichalcogenides (LMDCs), copper oxides, and iron pnictides exhibit correlated electronic phenomena such as charge density waves (CDW) and high-temperature superconductivity [1][2][3]. The most-discussed 2D material is graphene, the monolayer counterpart of graphite. The discovery [4][5] of single-layer graphene in 2004 by Novoselov and Geim has shown that it is not only possible to exfoliate stable, single-atom or single-polyhedral-thick 2D materials from van der Waals solids, but that these materials can exhibit unique and fascinating physical properties. For instance, the electronic band structure of graphene has a linear dispersion near the K point, and

charge carriers can be described as massless Dirac fermions, providing researchers with an abundance of new physics. Most importantly, graphene is also an extremely thin electrical and thermal conductor with very high carrier mobility.

In addition, there exists an entire periodic table of crystalline solid-state materials each having different electronic, mechanical, and transport properties. It is also possible to create single-atom or few-atom single layer from a polyhedral structure. Thus, after the "rise" of graphene, transition metal dichalcogenides (TMDCs) began to receive much attention. TMDCs are layered materials with strong in-plane bonding and weak out-of-plane van der Waals interaction, and, most importantly, they are semiconductors with a large bandgap. Although TMDCs have been studied for decades, recent advances in nanoscale materials characterization and device fabrication have opened up new opportunities for two-dimensional layers of thin TMDCs in nanoelectronics and optoelectronics. It was shown decades ago by *Frindt et al.* that the layered metal dichalcogenides could be mechanically and chemically exfoliated into few and single layers [6][7]. This early works focused on attempts to obtain and characterize these thin layers [6]-[10]. It was not until the past decade that these 2D system researches had finally dedicated their effort on synthesizing, transferring, detecting, characterizing, and manipulating the properties of mono- to multi-layer van der Waals materials. Also, the (re)invention of some novel synthetic methods including topo-tactic, solution-based, solvothermal, and ultra-high vacuum (UHV), or 10^{-10} torr (760 torr = 1 atm, atmospheric pressure) surface epitaxial approaches have help unleashed the potential to create new van der Waals solids and single-layer-thick materials. These established methods have enabled the field of 2D materials beyond graphene to mature very quickly.

In this dissertation, I will present a comprehensive study of surface structure, morphology, and electronic structure of mono- and multi-layer MoS_2 and WSe_2. I will focus on the evolution of their band structure as a function of thickness and interlayer twist angles, and also on their interaction with the underlying substrate. I will discuss the origin of these physical phenomena – the out-of-plane quantum confinement and interlayer coupling, and how they change the band dispersion, the hole effective mass, and the bandgap. In addition, in chapter 8, I will briefly discuss the interfacial electronic structure of organic/metal interfaces, which is a sub-monolayer to monolayer, surface sensitive, single-crystal metal substrate 2D system.

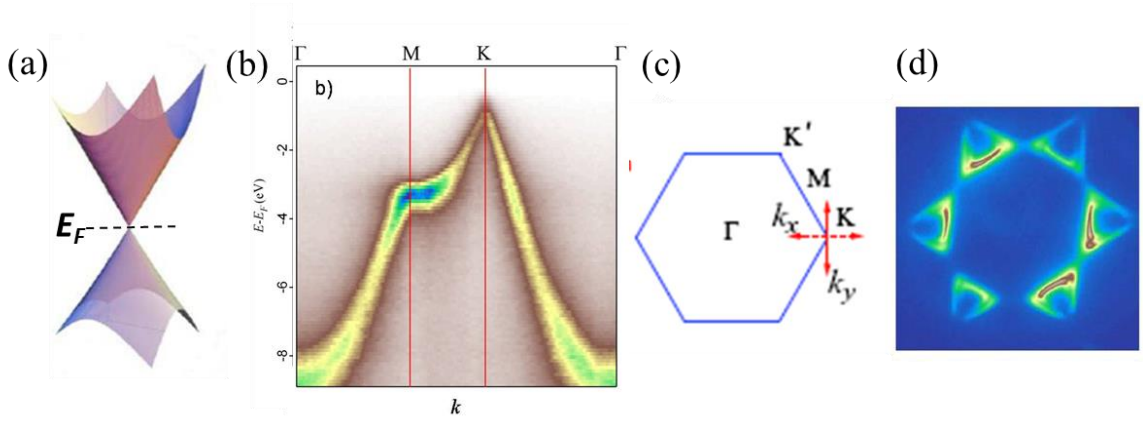

Figure 1.1 Graphene band structure near Diract point: (a) A cartoon made from theoretical calculation; (b) direct band measurement. (c) Graphene high-symmetry points in momentum space. (d) Direct band mapping of the graphene Fermi surface. Each triangular cone lies on one of the high-symmetry directions.

1.2 Graphene – One-Atomic-Thin Layered Material

As we have briefly mentioned in the introduction, graphene, a thin sheet of sp2-bonded carbon atoms, is the first well-known two dimensional nanomaterial to exist in truly one atomic layer thin and stable form that can be prepared using the so-called scotch-tape method by Novoselov and Geim in 2004 [5]. It has become a hot topic for the past decade mainly due to its extraordinary electronic, optical, mechanical, and transport properties and promising applications. It has a very special electronic structure as it has a linear band dispersion near K point (Diract point, Figure 1.1) which enables extremely high mobility ~ 2.5×10^5 cm^2 V^{-1} s^{-1} at room temperature [11] (Fermi velocity equals ~1% of the speed of light) and flat absorption band in visible light. Monolayer graphene is semi-metallic and its carriers are massless Dirac fermions whose dynamics are described by the Dirac equation [12]. The maximum current density that monolayer graphene can bear is several million times larger than that in copper [12]. In terms of its mechanical properties, monolayer graphene has a Young's modulus of 0.5 – 1.0 TPa and a high intrinsic strength of ~130 GPa [14]. Furthermore, monolayer graphene has a high thermal conductivity of ~3000 W mK^{-1} [15][16], extremely high resistance to gas permeation [17], a high transmittance of ~97.7% [18], etc. These outstanding properties and promising applications have stimulated research in graphene and graphene-based materials. Also, graphene has been proposed for a host of applications ranging from electronic devices, photonic devices, advanced composites, paint, coatings, energy storage, sensors, metrology, biology, etc.

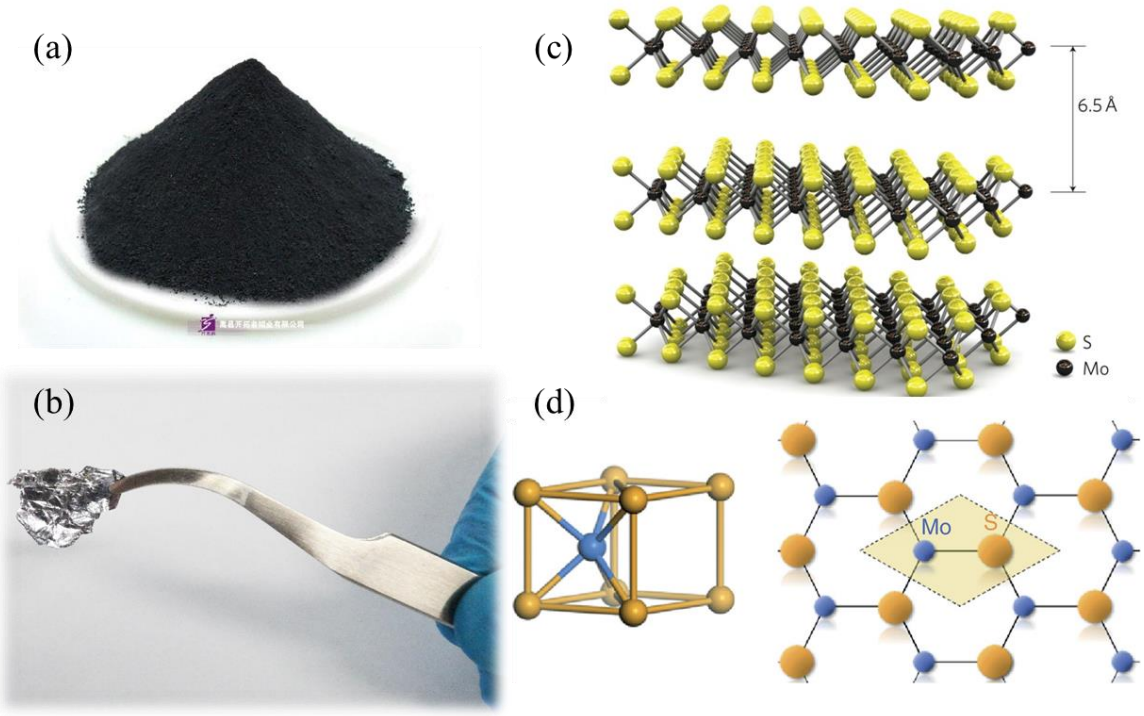

Figure 1.2 MoS_2, a widely used powder as industrial lubricant, as is shown in (a). (b), MoS_2 in high purity form ready for exfoliation. (c) Its layered atomic structure and (d) unit cell and Brilloiun zone. Pictures adapted from Ref. [31][34][35][36], respectively.

1.3 Beyond Graphene – Transition Metal Dichalcogenides

In addition to graphene, there still lies a large family of 2D inorganic layered nanomaterials that also have great importance and interesting physics. One important quest in 2D material research is to search for the "new graphene" that overcomes the intrinsic limit of graphene – lack of bandgap. Although researchers have tried several different methods to tackle the issue, for example, by applying a large electrical field or by artificial strain, they can merely create a bandgap up to 300meV in the bilayer graphene case [19]. Among all the 2D layered material, transition

metal dichalcogenides (TMDs, or TMDCs), such as MoS_2, TiS_2, TaS_2, WS_2, $MoSe_2$, WSe_2, etc., have received most of the attention as a strong candidate for the "new graphene" in recent years, because of their semiconducting or even superconducting properties. In addition, they are abundant and accessible in their nature form.

TMDC monolayers are atomically thin semiconductors of the type MX_2, with M a transition metal atom (Mo, W, Sn, Zr, Hf, Ta, Nb, etc.) and X a chalcogenide atom (S, Se, and Te), as shown in Figure 1.3 (c). One layer of M atoms is sandwiched between two layers of X atoms. A layer of TMDC is less than 10 Å , for example, monolayer MoS_2 is ~6.5 Å thick. Featuring 2D morphology and ultrathin thickness, these TMDC sheets present some unusual physical, chemical or electronic properties compared to their bulk counterparts and therefore hold great promise for a variety of applications [20]-[26]. One of the most important features is that all of the monolayer MoS_2, WSe_2, $MoSe_2$, WS_2 are direct bandgap materials, and they will transform into indirect bandgap in their bilayer or multilayer form. This unique feature has been experimentally observed using a direct band mapping probe, as presented in this thesis. It can be utilized as ultra-thin transistors and optical emitters/detectors [27][28][29]. Also, the TMDC monolayer crystal structure has no inversion center. This lack of inversion symmetry allows researchers to access a new degree of freedom of charge carriers, namely the k-valley index, and to open up a new field of physics: valleytronics [30]-[33]. Moreover, the strong spin-orbit coupling in TMDC monolayers leads to a spin-orbit splitting of hundreds meV in the valence band and a few meV in the conduction band. This special property gives rise to studies on controlling the electron spin by tuning the excitation laser photon energy.

1.4 Sub-Monolayer 2D system

Beside our interests in layered materials and the physics regarding interlayer interactions and interactions with substrate, a fundamental question arises: what happened at the interface? To answer this question, let start with a fundamental model system: solids with crystallinity. In solids, their interfaces are defined as a few atomic or molecular layers forming at a boundary between two solid materials. In the simplest interface: solid-vacuum interface, the electronic wave function from the solid is very different from the Bloch waves in the bulk materials, due to the sudden termination of the crystal periodicity that breaks solid's symmetry at the interface. The long-range-interaction related wave-functions that extend outside bulk will be decaying quickly toward the vacuum; while some localized, surface states related wave-functions will remain at the surface but they will propagate along the interface. In this sense, in the vicinity of a solid-solid interface, it is more complicated as it involves another solid and its localized interactions.

Thus, in my dissertation, I will briefly discuss the molecule-metal interface, as well as graphene-metal interface, for which has many different and strong interfacial interactions that lead to energy level alignment, work function modification, broadening of molecular states, and appearance of new states. The electronic properties of the molecule/metal interface has many potential technological applications. One example is the heterogeneous catalytic reaction, which involves all of the molecular/metal interactions such as adsorption, diffusion, desorption, and dissociation between the metal substrate and the reactant molecules. Another example is the widely-used organic devices built by one or a few organic materials sandwiched between two electrodes. Its performance is dominated by charge transfer processes across the interfaces and

through the bulk. Thus, the scattering and trapping of charges at the interface can boost or lower its performance, especially in 2D like devices. Thus, the operating voltage in organic light-emitting diode and conversion efficiency in organic solar cell is extremely sensitive to the molecules or solution and other physical properties of at the interface. Thus, understanding the interfacial electronic structure and charge dynamics is the key to designing organic semiconductor devices, its substrates, and condition control of fabrication processes.

In this thesis, I will also explain the powerful apparatus we used to study the interfaces: two-photon photoemission (2PPE) in an UHV system. UHV technology enables the preparation of clean surface and the precise control of adsorbate thickness. The method of 2PPE is very sensitive to sample surface and is efficient in determining unoccupied states above Fermi level. In addition, we uses a femtosecond laser combined with pump-probe technique to study interfacial ultrafast dynamical processes of the states.

1.5 References

[1] Wilson, J. A., and A. D. Yoffe. "The transition metal dichalcogenides discussion and interpretation of the observed optical, electrical and structural properties." *Advances in Physics* 18, no. 73 (1969): 193-335.

[2] Bednorz, J. G. "Possible High T_c Superconductivity in the Ba-La-Cu-O System." Zeit. Phys. B., 64, 189-193 (1986)." *English translation*.

[3] Kamihara, Yoichi, Takumi Watanabe, Masahiro Hirano, and Hideo Hosono. "Iron-Based Layered Superconductor La [O1-x F x] FeAs (x= 0.05-0.12) with T_c= 26 K." *Journal of the American Chemical Society* 130, no. 11 (2008): 3296-3297.

[4] May, John W. "Platinum surface LEED rings." *Surface Science* 17, no. 1 (1969): 267-270.

[5] Novoselov, Kostya S., Andre K. Geim, S. V. Morozov, D. Jiang, Y_ Zhang, S. V. Dubonos, I. V. Grigorieva, and A. A. Firsov. "Electric field effect in atomically thin carbon films." *Science* 306, no. 5696 (2004): 666-669.

[6] Frindt, R. F. "Single crystals of MoS_2 several molecular layers thick." *Journal of Applied Physics* 37, no. 4 (1966): 1928-1929.

[7] Joensen, Per, R. F. Frindt, and S. Roy Morrison. "Single-layer MoS_2."*Materials research bulletin* 21, no. 4 (1986): 457-461.

[8] Frindt, R. F. "Superconductivity in Ultrathin $NbSe_2$ Layers." *Physical Review Letters* 28, no. 5 (1972): 299.

[9] Divigalpitiya, W. M. R., R. F. Frindt, and S. Roy Morrison. "Inclusion systems of organic molecules in restacked single-layer molybdenum disulfide." *Science* 246, no. 4928 (1989): 369-371.

[10] Yang, D., S. Jiménez Sandoval, W. M. R. Divigalpitiya, J. C. Irwin, and R. F. Frindt. "Structure of single-molecular-layer MoS_2." *Physical Review B* 43, no. 14 (1991): 12053.

[11] Mayorov, Alexander S., Roman V. Gorbachev, Sergey V. Morozov, Liam Britnell, Rashid Jalil, Leonid A. Ponomarenko, Peter Blake et al. "Micrometer-scale ballistic transport in encapsulated graphene at room temperature. " *Nano letters* 11, no. 6 (2011): 2396-2399.

[12] Novoselov, K. S. A., Andre K. Geim, SVb Morozov, Da Jiang, MIc Katsnelson, IVa Grigorieva, SVb Dubonos, and AAb Firsov. "Two-dimensional gas of massless Dirac fermions in graphene." *Nature* 438, no. 7065 (2005): 197-200.

[13] Moser, Joel, Amelia Barreiro, and Adrian Bachtold. "Current-induced cleaning of graphene." *Applied Physics Letters* 91, no. 16 (2007): 163513.

[14] Lee, Changgu, Xiaoding Wei, Jeffrey W. Kysar, and James Hone. "Measurement of the elastic properties and intrinsic strength of monolayer graphene." *Science* 321, no. 5887 (2008): 385-388.

[15] Balandin, Alexander A. "Thermal properties of graphene and nanostructured carbon materials." *Nature Materials* 10, no. 8 (2011): 569-581.

[16] Balandin, Alexander A., Suchismita Ghosh, Wenzhong Bao, Irene Calizo, Desalegne Teweldebrhan, Feng Miao, and Chun Ning Lau. "Superior thermal conductivity of single-layer graphene." *Nano Letters* 8, no. 3 (2008): 902-907.

[17] Bunch, J. Scott, Scott S. Verbridge, Jonathan S. Alden, Arend M. van der Zande, Jeevak M. Parpia, Harold G. Craighead, and Paul L. McEuen. "Impermeable atomic membranes from graphene sheets." *Nano Letters* 8, no. 8 (2008): 2458-2462.

[18] Nair, R. R., P. Blake, A. N. Grigorenko, K. S. Novoselov, T. J. Booth, T. Stauber, N. M. R. Peres, and A. K. Geim. "Fine structure constant defines visual transparency of graphene." *Science* 320, no. 5881 (2008): 1308-1308.

[19] Mak, Kin Fai, Chun Hung Lui, Jie Shan, and Tony F. Heinz. "Observation of an electric-field-induced band gap in bilayer graphene by infrared spectroscopy." *Physical Review Letters* 102, no. 25 (2009): 256405.

[20] Chhowalla, Manish, Hyeon Suk Shin, Goki Eda, Lain-Jong Li, Kian Ping Loh, and Hua Zhang. "The chemistry of two-dimensional layered transition metal dichalcogenide nanosheets." *Nature Chemistry* 5, no. 4 (2013): 263-275.

[21] Huang, Xiao, Zhiyuan Zeng, and Hua Zhang. "Metal dichalcogenide nanosheets: preparation, properties and applications." *Chemical Society Reviews* 42, no. 5 (2013): 1934-1946.

[22] Wang, Qing Hua, Kourosh Kalantar-Zadeh, Andras Kis, Jonathan N. Coleman, and Michael S. Strano. "Electronics and optoelectronics of two-dimensional transition metal dichalcogenides." *Nature Nanotechnology* 7, no. 11 (2012): 699-712.

[23] Xu, Mingsheng, Tao Liang, Minmin Shi, and Hongzheng Chen. "Graphene-like two-dimensional materials." *Chemical Reviews* 113, no. 5 (2013): 3766-3798.

[24] Nicolosi, Valeria, Manish Chhowalla, Mercouri G. Kanatzidis, Michael S. Strano, and Jonathan N. Coleman. "Liquid exfoliation of layered materials." *Science* 340, no. 6139 (2013): 1226419.

[25] Sun, Yongfu, Shan Gao, and Yi Xie. "Atomically-thick two-dimensional crystals: electronic structure regulation and energy device construction." *Chemical Society Reviews* 43, no. 2 (2014): 530-546.

[26] Li, Hai, Jumiati Wu, Zongyou Yin, and Hua Zhang. "Preparation and applications of mechanically exfoliated single-layer and multilayer MoS_2 and WSe_2 nanosheets." *Accounts of Chemical Research* 47, no. 4 (2014): 1067-1075.

[27] Mak, Kin Fai, Changgu Lee, James Hone, Jie Shan, and Tony F. Heinz. "Atomically thin MoS_2: a new direct-gap semiconductor." *Physical Review Letters* 105, no. 13 (2010): 136805.

[28] Splendiani, Andrea, Liang Sun, Yuanbo Zhang, Tianshu Li, Jonghwan Kim, Chi-Yung Chim, Giulia Galli, and Feng Wang. "Emerging photoluminescence in monolayer MoS_2." *Nano Letters* 10, no. 4 (2010): 1271-1275.

[29] Ross, Jason S., Philip Klement, Aaron M. Jones, Nirmal J. Ghimire, Jiaqiang Yan, D. G. Mandrus, Takashi Taniguchi et al. "Electrically tunable excitonic light-emitting diodes based on monolayer WSe2 pn junctions." Nature Nanotechnology 9, no. 4 (2014): 268-272.

[30] Rycerz, A., J. Tworzydło, and C. W. J. Beenakker. "Valley filter and valley valve in graphene." *Nature Physics* 3, no. 3 (2007): 172-175.

[31] Cao, Ting, Gang Wang, Wenpeng Han, Huiqi Ye, Chuanrui Zhu, Junren Shi, Qian Niu et al. "Valley-selective circular dichroism of monolayer molybdenum disulphide." *Nature Communications* 3 (2012): 887.

[32] Mak, Kin Fai, Keliang He, Jie Shan, and Tony F. Heinz. "Control of valley polarization in monolayer MoS_2 by optical helicity." *Nature Nanotechnology* 7, no. 8 (2012): 494-498.

[33] Zeng, Hualing, Junfeng Dai, Wang Yao, Di Xiao, and Xiaodong Cui. "Valley polarization in MoS_2 monolayers by optical pumping." *Nature Nanotechnology* 7, no. 8 (2012): 490-493.

[34] Picture was adapted from Alibaba.com, item "Molybdenum disulfide MoS_2 additive lubricant", provided by Tianjin Okeyou International Trade Co., Ltd.

[35] Picture was adapted from Graphene-supermarket.com, item "Molybdenum Disulfide (MoS_2) Crystals", provided by Graphene Supermarket.

[36] Radisavljevic, Branimir, Aleksandra Radenovic, Jacopo Brivio, V. Giacometti, and A. Kis. "Single-layer MoS2 transistors." *Nature Nanotechnology* 6, no. 3 (2011): 147-150.

Chapter 2

Experimental Techniques

"The true method of knowledge is experiment." - William Blake

This chapter covers a wide range of specialized experimental techniques that were employed in the investigations described in this dissertation. The chapter starts with introducing the state-of-art beamlines in synchrotron radiation facilities in Brookhaven National Laboratory (BNL) and Elettra Sincrotrone Trieste. It then specifies the key equipment we used on these beamlines. Our chapter reviews the basic principles underlying these experimental techniques and provides details about the specific experimental setups and our adaption used to acquire data. The sample preparation procedures are also provided to show how challenging it is to prepare various 2D systems as mentioned in Chapter 1.

2.1 Synchrotron Radiation, Beamlines, and SPELEEM system

Figure 2.1 An overview of the NSLS I. Our U5UA beamline was located in this facility, and it has been transferred to the new synchrotron NSLS II.

2.1.1 SPELEEM System and U5UA Beamline at BNL

Most of our MoS_2 and WSe_2 experiments, as well as several "avant-garde" experiments on ReS_2, black phophorene, and perovskites, were performed using the so-called SPELEEM system at beamline U5UA of the National Synchrotron Light Source at Brookhaven National Laboratory[1] in Long Island, New York. SPELEEM stands for spectroscopic photoemission and low-energy electron microscope measurements; it is by far the most versatile multi-technique microscope that includes low-energy electron microscopy (LEEM), photoemission electron microscopy (PEEM), micro-probe low-energy electron diffraction (μ-LEED), micro-probe angle-resolved photoemission (μ-ARPES), Ultraviolet photoelectron spectroscopy (UPS), and in some

cases with energy-filtered X-ray photoemission electron microscopy (XPEEM) capability; this system has been proved to be a powerful tool for studying 2D systems.

The SPELEEM microscope images surfaces, interfaces and ultra-thin films using a range of complementary analytical characterization methods [2][3]. When operated as a LEEM, the microscope probes the specimen using elastically backscattered electrons. This instrument allows direct, real-space imaging of the sample morphology with a 2-100μm field of view (FOV), and with lateral resolution below 10nm; its effective resolution is limited by electron scattering from grain boundaries, edges, or domain walls. As described above, LEEM is highly sensitive to the surface crystalline structure and, due to the favorable backscattering cross-sections of most materials at low energies, allows image acquisition to be obtained at video frame rates.

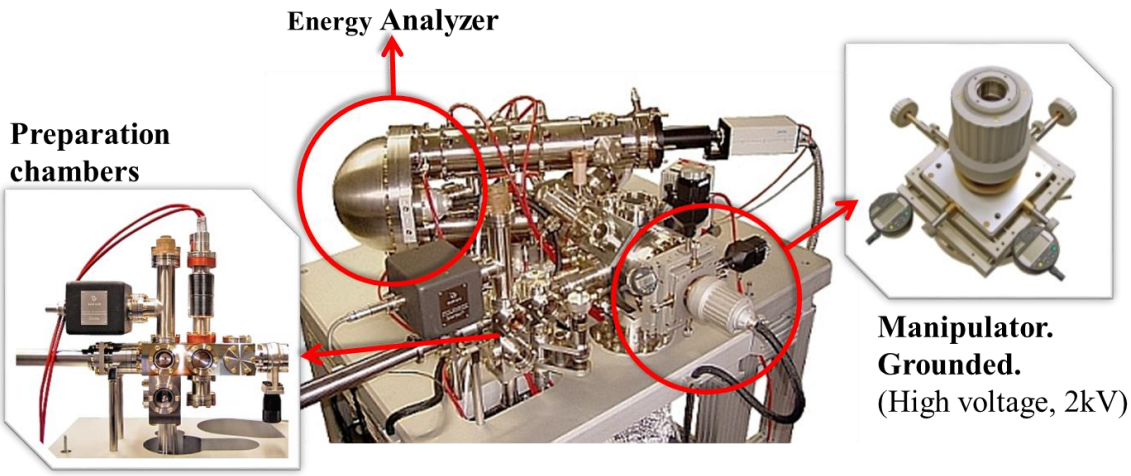

Figure 2.2 The layout of the customized ELMITEC SPELEEM III system that was used at the U5UA beamline.

Along with real-space imaging, the SPELEEM microscope is capable of micro-probe diffraction imaging, i.e. laterally restricted low-energy electron diffraction (μ-LEED) and angle-

resolved photoemission electron spectroscopy (μ-ARPES) measurement when probing with electrons and photons, respectively. In diffraction operation, the microscope images and magnifies the back focal plane of the objective lens. In the ARPES mode, the full angular emission pattern can be imaged on the detector up to a parallel momentum of ~ 2 $Å^{-1}$; at larger parallel momentum the transmission of the microscope decreases. All diffraction measurements are restricted to areas of ~ 2 μm in diameter, which are selected by inserting a field-limiting-aperture into the first image plane along the imaging-optics column of the instrument. Notice that in different applications, one can choose from a range of sizes of the selected-area aperture.

Thus, the SPELEEM enables measurements on samples that are homogeneous over areas of a few square microns. For LEEM and ARPES measurements, the energy resolution is 200 meV and the momentum resolution of the microscope when operated in diffraction mode is ~ 0.018 $Å^{-1}$. This value for the momentum resolution was obtained from calibration on a standard gold target. An alternative method to obtain the momentum resolution is by carefully calibrating the distance between 0^{th} order and 1^{st} order LEED spots in terms of pixel. A more detailed introduction to these surface probes in SPELEEM will be covered in the following sections.

2.1.2 Nanospectroscopy Beamline at ELETTRA

The Nanospectroscopy beamline at ELETTRA[5][6][7][8] also uses a similar SPELEEM system adapted from a customized ELMITEC LEEM V that has higher energy resolution (up to 40meV for ARPES and LEED) and is capable of doing XPEEM (in XPEEM/XPS it's ~106meV and depends on apertures and gratings.) Also, its incident light/electron beam projects onto the sample at an angle of ~16 degree, which differs from the normal-incident SPELEEM in BNL. This

makes the ARPES data exhibit different selection rules and parallel momentum that, in some cases, grants access to bands that were forbidden in the SPELEEM in BNL. The Nanospectroscopy performs the most demanding x-ray spectroscopies in a laterally-resolved manner, giving access to the chemical state, electronic structure and magnetic order of surfaces, interfaces and thin films. Along with spectroscopic imaging, with resolution of tens of nanometers, one can study magnetic domains, electronic and chemical structure of surfaces and interfaces, core levels, and growth dynamics of nanostructured composite surfaces.

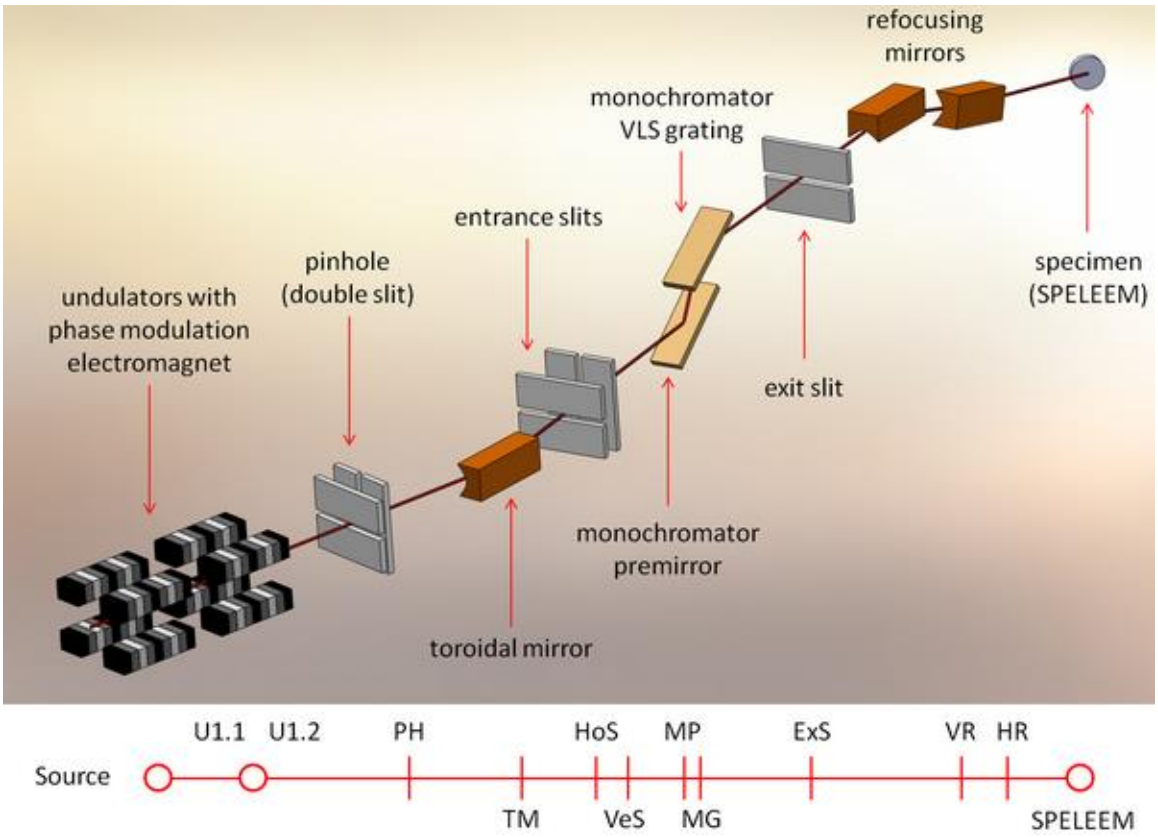

Figure 2.3 Layout of the Nanospectroscopy. It demonstrates how the high photon flux of selected energy being calibrated and focused, and then arrives at the target specimen.

For the layout of the beamline, the light source is at the middle-point between the two undulator sections U1.1 and U1.2 with phase modulator electromagnet (see Figure 2.3). Sitting at 10 meter away from the light source, the pinhole (PH) regulates the angular acceptance of the incident beam and filters out unwanted radiation from the undulator. The toroidal mirror (TM) de-magnifies the source by a factor of 8 and 5.3 in the horizontal and the vertical plane, respectively. The entrance slits are located at the horizontal and vertical foci of the toroidal mirror. After passing through both slits, the light is then dispersed by the monochromator and undergoes a vertical demagnification. After the exit-slit (ExS), a retractable plane mirror allows users to switch between the two branches of the beamline, the light goes into the refocusing mirrors that are two bendable mirrors arranged in a Kirkpatrick-Baez geometry. Finally, the light goes through the selected aperture and hits the specimen.

A schematic diagram of the SPELEEM microscope is given in the Figure 2.4. It has (1) main chamber; (2) preparation chamber with load lock; (3) image column; (4) illumination column; (5) beam separator; (6) connection to the beamline. There are valves between the main chamber and the beamline, between the main chamber and the preparation chamber, between the preparation chamber and the load lock, and between the main chamber and the beam separator.

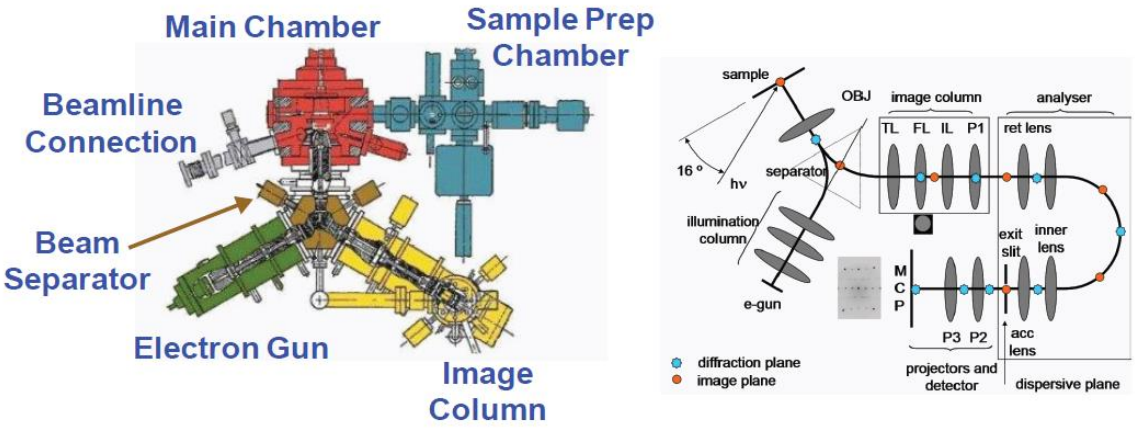

Figure 2.4 (Left) Schematic of SPELEEM microscope. (Right) Details of imaging column and electron analyzer.

One of the important features of the Nanospectroscopy is that it can perform X-ray photoemission electron microscopy (XPEEM) and X-ray photoemission spectroscopy (XPS). In XPEEM mode, the specimen is imaged using the beamline high energy X-ray photons, provided by an undulator source. The lateral resolution in XPEEM approaches a few tens of nm [4], and the horizontal resolution is only limited by the selected aperture. Owing to its high spatial resolution and strong interaction with the atom core level, XPEEM is sensitive to the local chemical and electronic structures, and is ideal for mapping surface composition, coverage, and detecting contamination. Laterally resolved versions of synchrotron-based X-ray absorption (XAS) and photoemission spectroscopy (XPS) are possible (see Figure 2.5). The principles of photoemission will be covered in Section 2.4.

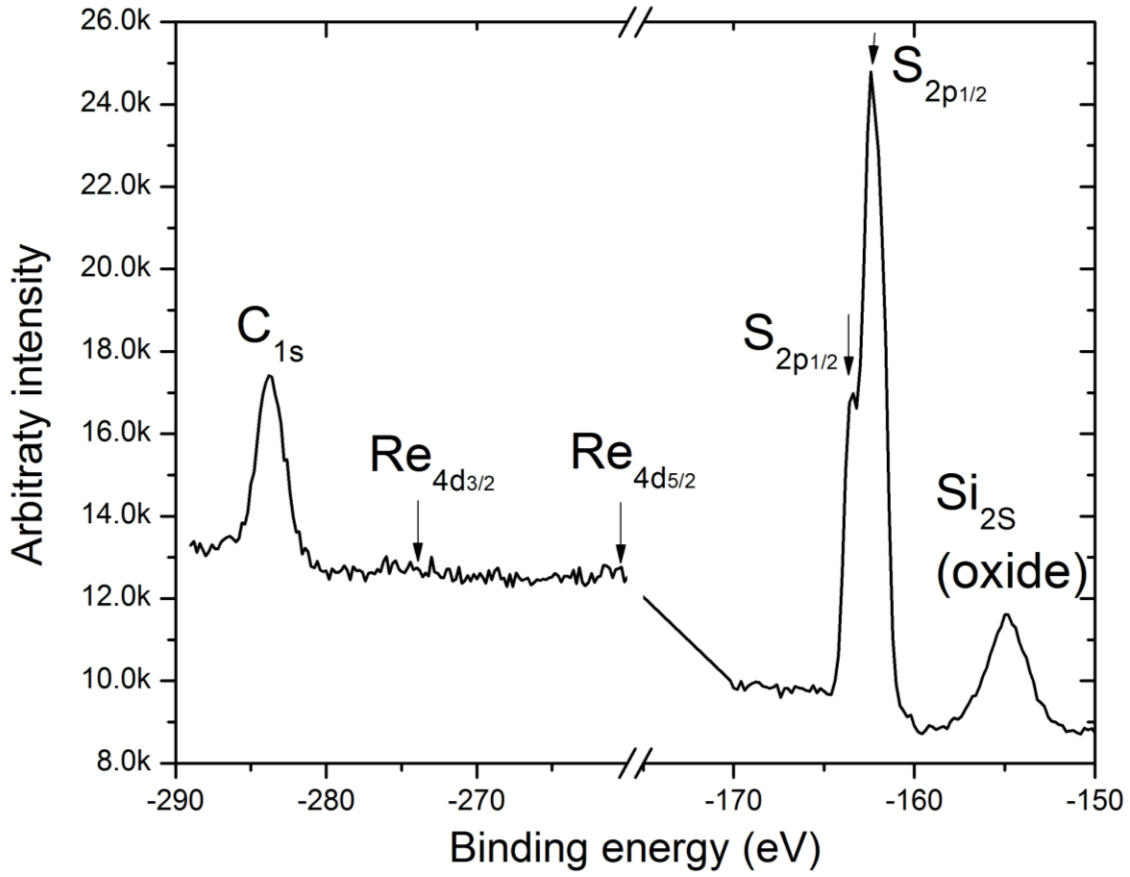

Figure 2.5 An example of an XPS spectrum on a few-layer ReS_2 sample probed using the Nanospectroscopy in Elettra. Instead of scanning through different binding energy, by locking the energy at a specific atom's core level peak, one can image the coverage of that atom in an area of interest in XPEEM mode.

2.1.3 Spectromicroscopy Beamline at ELETTRA

Besides working on the SPELEEM systems, we also used the Spectromicroscopy beamline at ELETTRA [9], which is a state-of-art traditional ARPES system equipped with a micron-sized probe. This measurement is made possible by the combination of the large photon flux of synchrotron radiation sources, the ultraviolet lights or X-rays with high spatial resolution - below

1 micron - afforded by modern synchrotron radiation optical systems, and the micrometer-sized aperture. Per our experimental settings, the Spectromicroscopy beamline can operate at high energy resolution (33meV) and high momentum resolution (2.7mÅ $^{-1}$), as well as a low-temperature capability of ~ 40K. In addition, although the Spectromicroscopy is not equipped with LEEM, it has a photoemission mapping instrument to help locate the sample. Thus, it is also an excellent tool for high-resolution investigation of the band structure of 2D materials like graphene and MoS_2. Furthermore, with a carefully designed sample holder, we can add contacts on the sample to provide electrode gating. Currently, the system can add up to three contacts and one to "ground" the sample. This feature is extremely useful for controlling sample biasing and for potential field-effect transistor device operation.

The beamline works as follows: A low-photon-energy beam (below 100 eV) is focused into a sub-micrometer spot and electrons arising from the photoemission process are collected and analyzed in terms of their angular and energy distributions (ARPES). As a respect of the beam focusing the photoelectron spectrum is acquired as a function of its spatial origin on a sample surface coordinate system. In terms of mechanical design, the final focusing is obtained by multilayer-coated optics of two exchangeable Schwarzschild objectives (SO) and an internal movable hemispherical electron energy analyzer that can perform polar and azimuthal angular scans in ultra-high vacuum, as shown in Figure 2.6. The use of multilayers, on the X-ray mirrors required for high reflectivity at a certain wavelength, restricts the photon-energy range available after the monochromator (20-200 eV) to specific narrow lines. Currently the beamline is equipped with two Schwarzschild objectives designed for 27 and 74 eV of photon energy. As for the ARPES, it is performed by means of internal movable electron-energy analyzer mounted on two-axes

goniometer setup. Moreover, the sample is capable of moving in xyzr directions on a scanning stage and can be operated in temperature range of 40-470K.

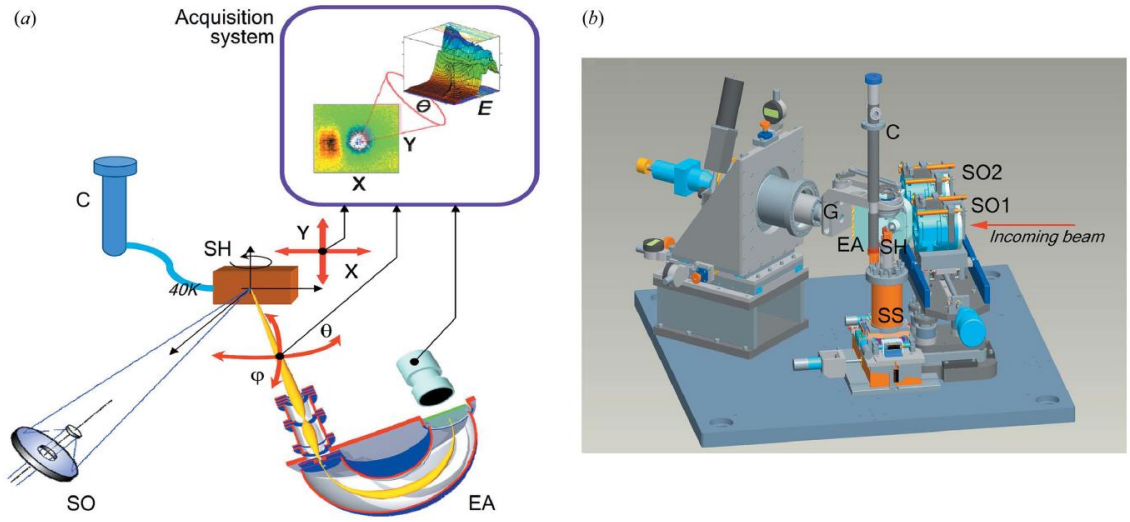

Figure 2.6 Principal scheme (a) and three-dimensional design (b) of the instruments inside the experimental chamber. The incoming beam is focused by one of the two Schwarzschild objectives and the sample can be scanned across the beam to obtain the photoemission intensity distribution maps within selected angle and energy windows. The main components are Schwarzschild objectives (SO1 and SO2), electron analyzer (EA), goniometer (G), sample holder (SH), scanning stage (SS) and cryostat (C).

Thus far, we have used this beamline to study suspended bilayer graphene, the "gating effect" on graphene and MoS_2, and the electronic band structure of suspended and support MoS_2 systems. We will discuss some of the results in the later chapters.

2.2 Low Energy Electron Microscopy

2.2.1 Review of LEEM

Low energy electron microscopy (LEEM) is a UHV surface imaging technique developed by Ernst Bauer and Wolfgang Telieps in 1985. In contrast to scanning microscopy techniques such as scanning electron microscopy (SEM) or scanning tunneling microscopy (STM), which require an electron beam or probe to be focused on a small spot and scanned across the sample surface, LEEM is a true real-time imaging technique, i.e., all imaging pixels are acquired simultaneously from the illuminated area on the surface at a frame rate of 10 frames per second. This enables dynamic processes such as chemical reaction and surface doping to be studied in real time.

The design of an LEEM instrument differs from conventional electron microscopies in four main ways: 1. The sample is illuminated on the same side of the imaging optics, i.e. through the objective lens, because samples are not transparent to low-energy electrons. 2. In order to separate the incident and elastically scattered low energy electrons, researchers use magnetic "electron prism" beam-separators which focus electrons both in and out of the plane of the beam-path to avoid distortions in the image and diffraction patterns. 3. An electrostatic immersion objective lens brings the sample close to that of the gun, slowing the high-energy electrons to a desired energy only just before interacting with the sample surface. 4. The instrument must be able to work under UHV condition. In addition, LEEM operates at electron energies on the order of 1 - 100 eV, which works near the maximum of electron penetration depth. Thus, the technique is highly surface sensitive and allows the probing depth of the electron beam to be tuned by varying the electron energies [10].

2.2.2 Experimental Setup of LEEM

The basic setup of the LEEM instrument in the SPELEEM system is shown in Figure 2.4. High energy electrons (15-20 keV) are emitted from an electron gun and pass through a series of condenser lenses which focus and position the beam. The electrons are then sent through a magnetic beam-separator (used to separate the incoming from the outgoing beams) and an objective lens before impinging on the sample. The sample is held at a very high voltage (15-20 kV) while the electron gun and objective are grounded such that the incoming electrons are decelerated to "low" energies before interacting with the surface. Backscattered electrons are then reaccelerated to high energies as they move away from the surface before passing back through the objective lens. The beam-separator steers the backscattered electrons into the imaging column, after which they are detected by an imaging plate or screen.

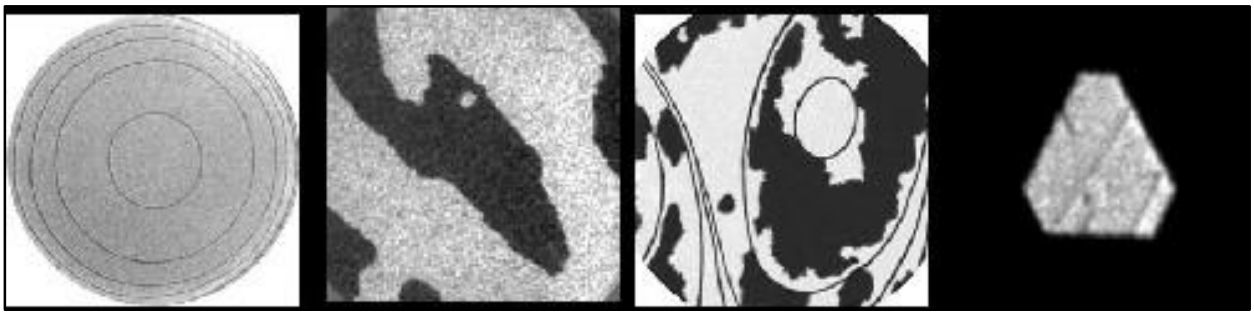

Figure 2.7 Atomic steps, magnetic domains, 2D thin films and 3D islands are just a few examples of objects seen with LEEM. Figure adapted from Ref. [11].

2.2.3 Contrast Mechanisms and Operational Modes of LEEM

The image formation in LEEM is a revisit of multiple contrast mechanisms, which depend on both the electron energy used and the specifics of the sample being probed. At typical LEEM energies (1-100 eV), the cross section for elastic backscattering from the surface atoms depends both on the electron energy and on the chemical species of the scattering atom. Assuming that each electron undergoes only one scattering event, and the incident beam is described as a plane wave with the wavelength defined as:

$$\lambda = \frac{h}{\sqrt{2mE}}$$

where m and E are incident electron mass and energy, respectively. If the wavelength is in the commonly used unit of $Å^{-1}$, then the equation can be put in the form:

$$\lambda\ (in\ Å^{-1}) = \sqrt{\frac{150}{E(in\ eV)}}$$

In particular, the backscattering cross-section is a non-monotonic function of nuclear charge, which allows one to image light adsorbats which may be present on substrates composed of heavier atoms. Additionally, the reflection coefficient for a crystalline solid varies strong with electron energy due to the band structure of the material; incident electrons with energies corresponding to band gaps in the material will be reflected with high probability, while those with energies that can be matched onto electronic states in the crystal will penetrate into the material. This phenomenon is identical to that encountered in an analysis of low-energy electron diffraction. Thus, a natural contrast mechanism for LEEM is based on local differences in the diffractions conditions, which occur if the periodicity of the sample varies as a function of location along the

surface due to strain fields, dislocations, or local variations in surface structure or crystal orientation. This type of contrast is normally called "bright-field imaging", also known as phase or interference contrast imaging, which makes use of the wave nature of the electron to generate vertical diffraction contrast, making steps on the surface visible. Examples of the bright-field LEEM images working in different modes are shown in Figure 2.7.

If the sample contains regions with different crystal orientations, it can still be useful to image non-specularly diffracted beams, a method which is called "dark-field contrast." In dark field imaging (also termed diffraction-contrast imaging), one chooses a desired diffraction spot and uses a contrast aperture to pass only those electrons that contribute to that particular spot. In the image planes after the contrast aperture, it is then possible to observe where the electrons originate from the sample surface, in real space. This technique allows us to study on which areas of a specimen a structure with a certain lattice vector (periodicity) exists. A comparison between bright- and dark- field LEEM is shown in Figure 2.8 (left).

In scenarios where the sample surface is not clean or has low conductivity, causing extensive charging on the surface, the surface of a sample is probed to check its morphology; in this case, mirror electron microscopy (MEM) mode of the LEEM system will be useful. In MEM mode, electrons are slowed in the retarding field of the condenser lens to the limit of the instrument and thus, only allowed to interact with the near-surface region of the sample. While understanding the origin of the exact contrast variations is complicated; the essence is that the height variations of the sample surface change the properties of the retarding field, therefore influencing the reflected (specular) beam. No diffraction pattern (LEED) is formed, because there is no electron

back-scattering; thus, the reflected intensity is very high; The LEEM is then ideal to check the sample surface geometry.

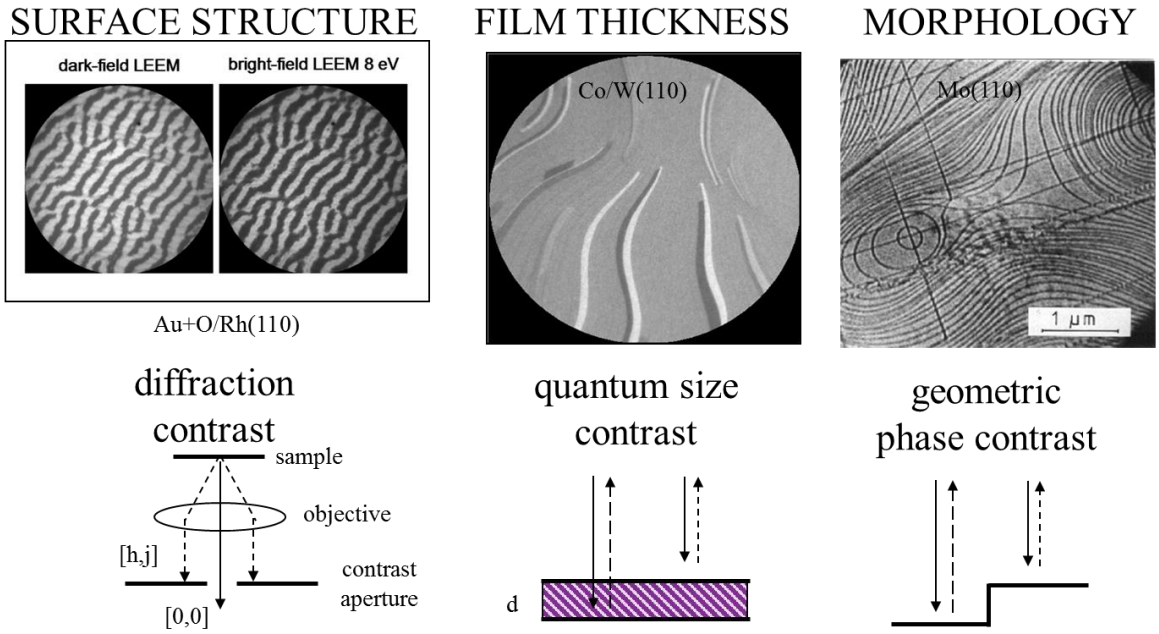

Figure 2.8 LEEM - contrast mechanisms. (Left) Diffraction contrast: dark-field and bright field. Interference contrast: (Middle) geometric phase contrast, (Right) quantum size contrast. Figure adapted from Ref. [10].

Another contrast mechanism is interference contrast due to surface steps or thin films, called "geometric phase contrast" and "quantum size contrast," respectively. Both mechanisms result from the interference caused by the difference in optical path-length for electrons reflected from the terraces bordering a step or from the top and bottom of a thin film. The quantum size effect is analogous to the effect produced by a Fabry-Perot interferometer and is very useful for thin-film growth studies by LEEM [10]. These LEEM contrast mechanisms are illustrated in Figure 2.8.

There are other closely related techniques in a SPELEEM system such as PEEM and LEED. We will visit these techniques in the later part of this chapter.

2.2.4 Experimental Setup for LEEM Measurement

The experimental setup of a typical LEEM system [10][11][12] can be divided into eight essential components: electron gun, imaging optics, illumination beam aperture, magnetic beam splitter, electrostatic immersion object lens, contrast aperture, illumination optics, and image plate/detector. A schematic sketch is shown in Figure 2.9. We will briefly introduce each component below.

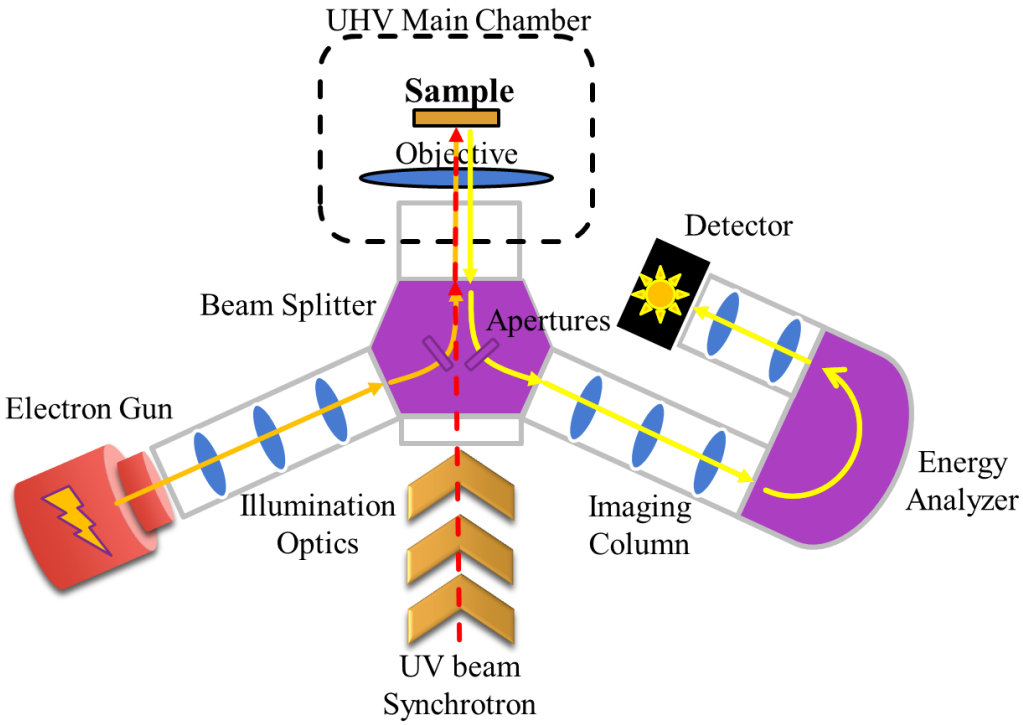

Figure 2.9 Scheme of a typical LEEM system.

The electron gun is used to generate electrons by way of thermionic or field emission from a source tip. In thermionic emission, electrons escape a source tip (usually made of LaB_6) by resistive heating; and with application of an electric field, the work function or the energy for electrons to escape the surface can be effectively lowered. Once the electrons escape, they travel (while accelerating) down to the lens column to the gun potential (set at V = 0). All operation is at UHV conditions such that the electron mean free path is sufficiently long. Also, to generate field emission, one can sharpen the source tip (usually tungsten), making for electrons tunneling from the tip to vacuum level easier.

After leaving the tip, electrons go through several imaging optics to be focused and translated into the illumination beam. In the imaging optics, electromagnetic quadrupole electron lenses are used to improve the electron-beam resolution. However, the ultimate resolution of LEEM is usually determined by that of the objective lens. The electron beam will then pass through an illumination beam aperture, which allows control of the beam projection and to illuminate only the area of interest. The aperture is located in the beam splitter on the illumination side. A magnetic beam splitter is also in the beam splitter chamber; it is used to resolve the illuminating and imaging beam. There has been much development on the technology of electron beam separators; the early separators introduced distortion in either the image or diffraction plane. However, IBM recently developed a hybrid prism array/nested quadratic field design, to focus the electron beams both in and out of the plane of the beam path, allowing for deflection and transfer of the image and diffraction planes without distortion or energy dispersion [12].

The collimated and focused electron-beam is then directed through electrostatic immersion objective lens, which is used to form a real image of the sample by way of a 2/3-magnification virtual image behind the sample. The uniformity of the electrostatic field between the objective lens and specimen are limited by spherical and chromatic aberrations larger than those of any other lenses; uniformity ultimately determines the overall performance of the instrument. The electron reflects back from the sample will go through a contrast aperture, which is located in the center on the projector lens side of the beam splitter. Unlike most of other electron microscopies, where the contrast aperture is introduced into the back focal plan of the objective lens (where the actual diffraction plane lies), the contrast aperture of LEEM is in the middle of the beam splitter. Thus, one can choose the desired spot intensity to imaging using a contrast aperture, including intensities from diffraction (dark field LEEM). Later, the outbound electrons will go through several illumination optics, like imaging optics, to be magnified to form the image or diffraction pattern, and project onto the imaging plate or detector. The choice of detecting screen can be a phosphorescent screen, imaging plate, or a CCD.

2.3 Low Energy Electron Diffraction

2.3.1 Review of LEED

The concept of low energy electron diffraction (LEED) was originated by Louis de Broglie, who introduced wave mechanics and proposed the wavelike nature of all electrons. In his Nobel laureate work, de Broglie postulated that the wavelength of a particle with linear momentum p is given by h/p, where h is Planck's constant. The de Broglie hypothesis was later confirmed experimentally at Bell Labs in 1927 when Clinton Davisson and Lester Germer who directed low-

energy electrons at a high crystalline nickel target and measured the position and intensity of backscattered electrons. They found that when plotted with polar coordinates, the distribution of the backscattered electrons showed diffraction patterns. These observations were consistent with the X-ray diffraction theory developed by Bragg and Laue earlier. Before de Broglie's time, diffraction was believed to be an exclusive nature of waves. Later in the year, Davisson & Germer team and Thompson & Reid team both showed their experimental success in demonstrating electron diffraction. Those experiments revealed the wave property of electrons and opened up an era of electron diffraction study.

Despite its discovery and success in 1927, LEED did not become an important tool for surface analysis until the early 1960s. The main reasons were that monitoring electron directions and detecting intensities of diffracted beams were very difficult due to immature state of vacuum techniques and the lack of rapid detection methods (it used a Faraday cup to detect electrons.) For example, to get a LEED pattern, the sample surface has to be ultra-clean and high crystalline, which were impossible without UHV conditions. In the early 1960s, LEED, LEEM, and many other surface probes experienced a renaissance as UHV became widely accessible and the introduction of a fluorescent screen. Still, this method was not fully optimized until the development of a dynamical electron diffraction theory, which took into account the possibility of electron multiple scattering. With this theory, it is possible to reproduce experimental data with high precision, and to determine surface structures, adsorption sites, bond angles and bond lengths.

The basic principle of a LEED system is using a beam of low-energy electrons to project onto and interact with a specimen, and then collected the diffracted electron spots which depend

on the periodicity of the specimen surface. In a typical LEED measurement, the entire sample surface is illuminated by a parallel beams of electrons, and thus the diffraction pattern will contain information about the entire surface. In some applications like SPELEEM, one can apply an aperture to limit the illuminated area to focus only on an area of interest. The diffraction pattern is formed in the back focal plane of the objective lens, imaged into the object plane of the projective lens (using an intermediate lens), and the final pattern appears on the phosphorescent screen, photographic plate or CCD. A schematic plot is shown in Figure 2.10.

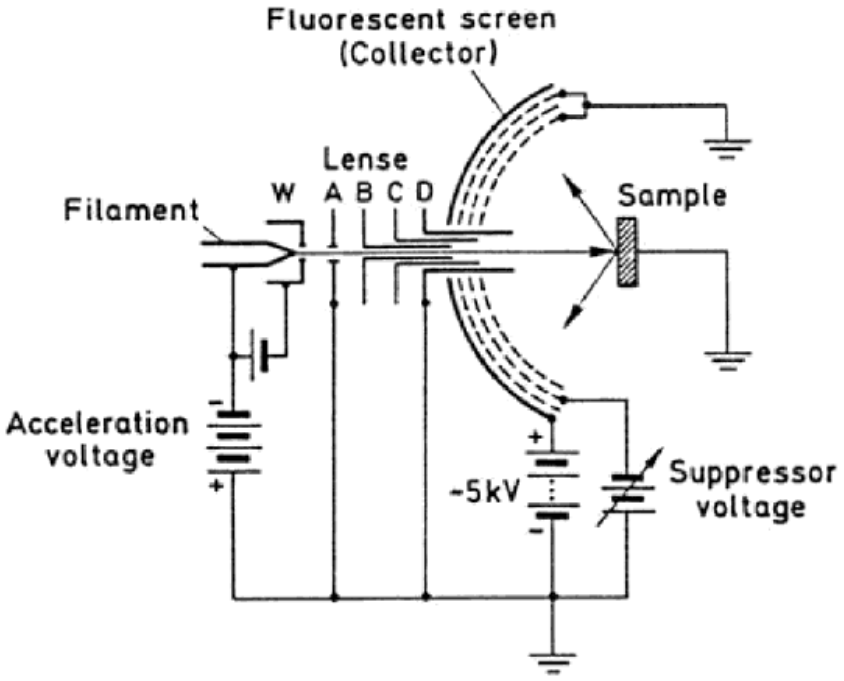

Figure 2.10 Schematic of a three-grid LEED unit. This figure is adapted from Ref. [13]

2.3.2 Experimental Setup for LEED Measurement

In a standard LEED setup, a coherent and parallel electron beam, acting as a plane wave with fixed energy and momentum, is directed at a sample surface mounted in an ultra-high vacuum

chamber. The far-field scattered electron intensity is recorded as a function of scattering angle. Typically, the pattern was detected on a luminescent screen. The electron energy used in LEED ranges from 10 to 500 eV, making the electron wavelengths/penetration depth reaching only the top few layers of the sample (a few Å). Due to the strong interaction between electrons and atoms, the penetration depth of the incident electron beam is typically less than 10 Å. Due to surface sensitivity criteria of LEED, measurements are conducted in UHV chambers. A typical LEED setup is diagrammed in Figure 2.10. Starting from the filament to the left, electrons are generated by a heated cathode filament, and are accelerated and focused by a series of electrostatic lenses: A, B, C and D. The acceleration energy is determined by the potential between the cathode and apertures A and D, while apertures B and C are used to focus the electron beam. The last aperture, D, is grounded as is the sample and the first grid in front of the fluorescent screen; thus, electrons travelling towards the sample as well as the scattered electrons all propagate in a field-free region. The backscattered electrons are detected by the fluorescent screen, which must be kept at a large positive bias (5-7 keV) with respect to the first grid since only high-energy electrons can illuminate the screen. A middle grid is positioned between the first (grounded) grid and the screen and kept at a slight negative bias in order to suppress inelastically scattered electrons. It is worth noting that the spacing of diffracted beams does not increase with kinetic energy as for conventional LEED systems. This is due to the collimation/focus of the imaging column that limit the projected momentum-space, regardless of the incident electron energy. While in the case of a SPELEEM system, the projected momentum space will increase with increasing electron energies.

2.4 Photoemission Spectroscopy

2.4.1 Review of Photoemission

Photoemission spectroscopy (PES) has been established as one of the most important methods to study the electronic structure of molecules, solids and surfaces [13][14]. Today, more than a 100 years after Einstein's explanation of the photoelectric effect, there are many well-established analysis methods based on photoemission. These methods are used in particular for the investigation of solids and surfaces and have contributed substantially to the understanding of the electronic structure of condensed matter. In fact, the present state of knowledge about electronic band structures and Fermi surfaces comes to a large extent from experimental data obtained by PES. With an energy resolution of 1 meV now available, the effects of electron-electron and electron-phonon interaction can be observed and investigated in detail (e.g. band renormalization near the Fermi energy, lifetime width, Kondo resonance and gaps in conventional superconductors). Methods like ESCA (electron spectroscopy for chemical analysis) and photoelectron microscopy are now widespread analytical methods in materials science and chemistry, and gain more and more importance in fields like nanotechnology and biology [15].

Historically, the first experimental attempts to realize photoemission were done by Heinrich Hertz and Wilhelm Hallwachs in 1887 [16][17]. In the earliest experiments, they used monochromatic radiation obtained by passing light from a continuum source through a prism monochromator, and the light was focused onto the surface of a potassium or sodium sample in a vacuum tube. Liberated electrons then traveled on toward a second metal plate within the vacuum, where the current generated was measured as a function of retarding voltage. Thus, the maximum

kinetic energy of the photoelectrons could be determined by adjusting the retarding voltage until the current was completely suppressed. They found that this energy depended on both the frequency of the incident radiation and the metal sample under investigation. The measurement demonstrated that a negative charge, i.e. electron, which was not yet discovered - can be removed from a solid when its surface is irradiated by ultraviolet light, whereas no discharge was observed for positive charge. At that time, nobody was able to explain these observations.

Finally, in 1905, in one of his four famous publications, Albert Einstein introduced the concept of the photon and deduced the relation between the photon energy $\hbar\omega$ and the maximum kinetic energy KE_{MAX} of the emitted electrons, that is his the fundamental photoelectric equation:

$$eU = KE_{MAX} = \hbar\omega - \phi$$

where *U* is the retarding potential, ω the frequency of light, and ϕ a characteristic constant of the sample surface known as the work function today. Thus, the most energetic electrons are those closest to the Fermi level that absorb all the energy of an incoming photon, $\hbar\omega$, and lose the minimum energy ϕ required to escape the metal.

Today, photoemission experiments for spectroscopic purposes are performed surprising similarly to those of 100 years ago. The basic PES scheme is shown in Figure 2.11. Monochromatic photons with energy hν and polarization (A is the vector potential of the electromagnetic field) are produced by a light source, e.g. an Al-Kα x-ray anode for XPS or a helium discharge lamp for UPS, and irridate the sample surface under an angle Ψ with respect to the surface normal. The kinetic energy E_{kin} of the photoelectrons can be collected and filtered by energy in electrostatic

analyzers, which has a retarded field to select only the electrons with desired energies as a function of the emission angles (θ, ψ), polarizations, and in some cases, it is capable of resolving electron spin orientation **σ**. In the end, a detector (usually a microchannel plate (MCP) or charge-coupled device (CCD)) captures the electrons of selection. Note that the whole setup has to be in UHV condition to eliminate spacious photoelectron scattering.

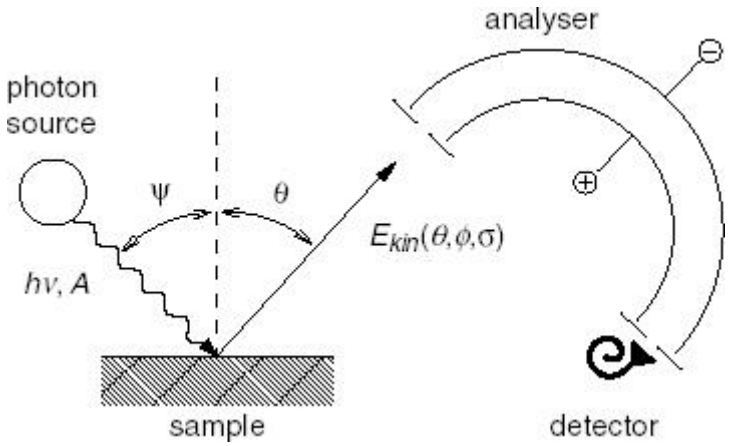

Figure 2.11 Principle of a modern photoemission spectrometer. This figure is adapted from Ref. [18].

The fundamental principle of the photoemission process, i.e. the three-step model, is shown in Figure 2.14 (left). This simplified picture shows the advantage of photoemission, which shows directly the properties of the electronic eigenstates of the investigated system via photoelectrons. There are several ways of photoemission designed to utilize this advantage: ultraviolet photoemission (UPS), mainly for the (angle-resolved) investigation of valence band states (ARUPS), and X-ray photoemission spectroscopy (XPS), providing the investigation of core-level states at higher binding energies. The differences here only lie mainly in the light source and modifications to the detector. Although the line width is usually small enough for many

applications, i.e. a few meV for the discharge lamp and slightly below 1 eV for X-ray anodes, an additional monochromator can prove extremely useful to improve energy resolution and to suppress background and satellites noises. Also, in Figure 2.14 (right) shows a schematic view of the photoemission process in the single-particle picture. Electrons with an initial state energy E_i can be excited above the vacuum level E_v by photons with energy $h\nu > E_i + \phi$. The photoelectron distribution I (E_{kin}) can be measured by the analyzer and is – to the first order - an image of the occupied density of electronic states N (E_i) of the sample. Thus, simply by plotting the total number of photoelectrons as a function of final state kinetic energy, the band structure of the solid can be drawn. Note that the kinetic energies of the final state are referenced to the vacuum level E_V, while binding energies in solids are generally referenced to the Fermi level, E_F, as both a positive value. Thus, given the work function of the material ($\phi = E_V - E_F$), the binding energy of the initial states can be calculated from its final-state kinetic energy according to:

$$\hbar\omega = E_B + KE_f = E_{final} - E_{initial} = \phi + E_F - E_{initial}$$

Moreover, an important properties of the photoelectron is that its parallel momentum, $k_{||}$, is conserved in the photoemission process. Thus, $k_{||}$ for the initial state can be easily derived from the final-state kinetic energy and the angle of emission, θ, (which corresponds to electron momentum) as:

$$k_{||} = \frac{\sqrt{2m_e KE_f}}{\hbar} sin\theta$$

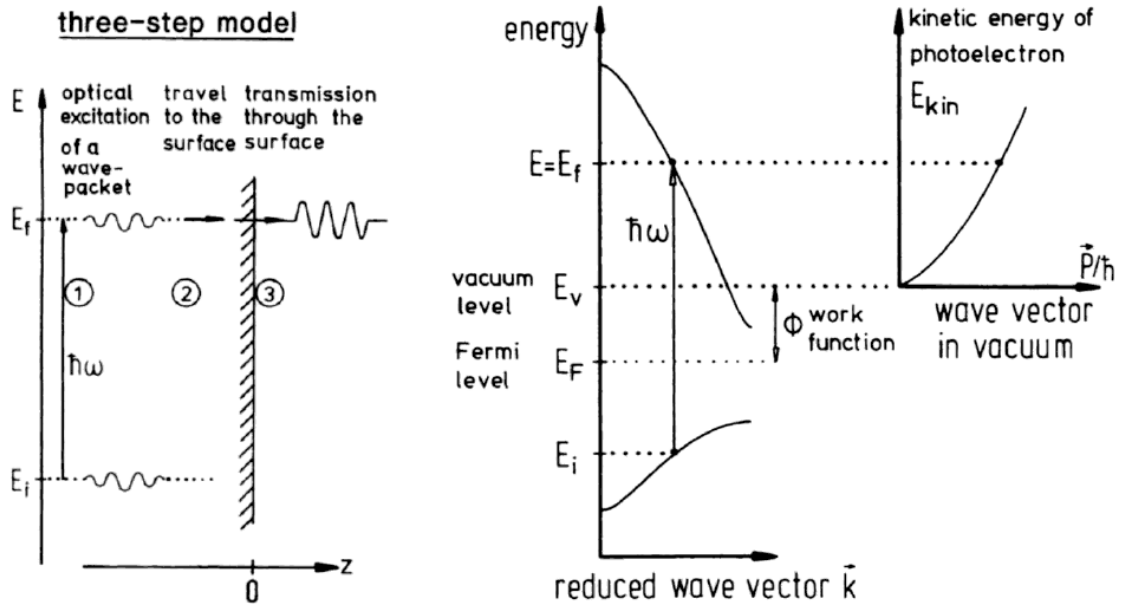

Figure 2.12 (Left) Three-step model of photoemission. (Right) Excitation within the reduced zone scheme. Figure adapted from Ref. [15].

2.4.2 Angle-Resolved Ultraviolet Photoelectron Spectroscopy

Ultraviolet photoelectron spectroscopy (UPS) refers to the measurement of the kinetic energy spectra of photoelectrons emitted by a highly crystalline material surface, which has absorbed ultraviolet photons, in an attempt to determine molecular orbital energies in the occupied states (valence band in most case.) Angle-resolved ultraviolet photoelectron spectroscopy (ARUPS, or simply ARPES when not specifying the light source) also measures valence band structure directly but with much larger angular coverage, which maps the momentum space along certain directions, thus providing a complete picture of the Fermi surface and a three-dimensional mapping of the occupied states. In short, ARUPS/ARPES studies the E(k), energy-momentum relation, of a system. In addition to the band structure, which is a consequence of the one-particle

approximation, the results of the field-theory methods in the many-body problem, the quasiparticle spectral function and the self-energy, are directly observable via ARUPS. ARUPS works in much the same way as neutron diffraction has given information about the dispersion of phonons in solids. In the simplest model of photoemission, the transitions are vertical in a reduced zone scheme; they occur without the participation of other excitations. Figure 2.14 shows the basic photoemission mechanism, and Figure 2.15 shows a typical setup of ARUPS and its excitation scheme in a nutshell.

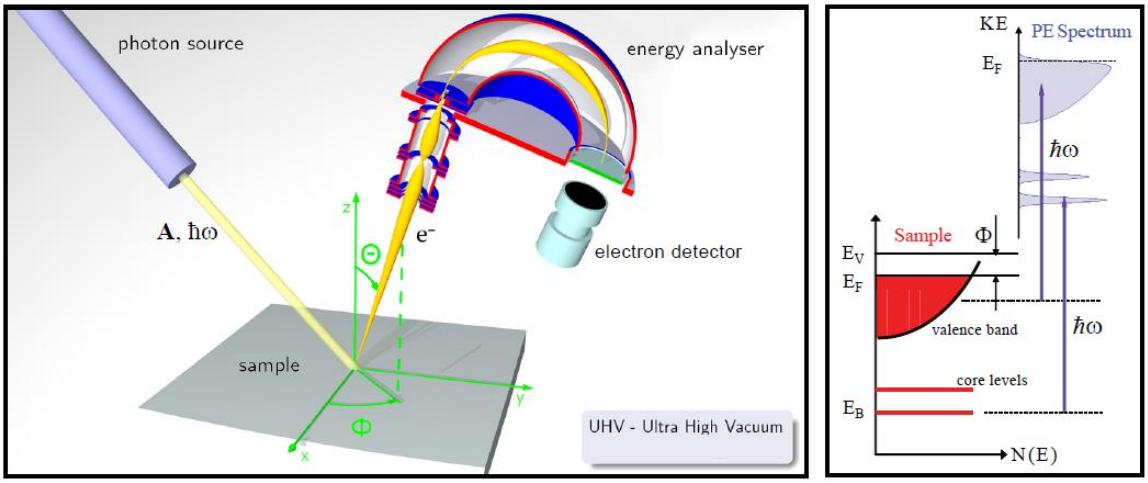

Figure 2.13 (Right) ARUPS setup. The incident light which carries photon energy $\hbar\omega$ and vector potential A arrives at the surface, and photoemission happens. The photoelectrons with preserved out-of-plane momentum will be collected at different emission angles and kinetic energies. Figure adapted from Ref. [19]. (Left) An energy level diagram showing core levels and valence band in a solid sample along with the corresponding angle integrated energy distribution curve for photoelectrons. Note that the grey area under the peaks reflects the electron density of states, and the peak position reflects the energy level of the states.

The three-step model is the most commonly used single electron model to interpret photoemission process. As shown in Figure 2.14, the PE process is broken up into 3 basic steps: the excitation of the photoelectron from its initial state to an excited state within the crystal, travel from the bulk to the surface, and escapes from the surface into the vacuum. For a more complete model include multiple electrons, a complimentary density functional theory (DFT) with many-body effect approximation is required, and is beyond the scope of this review. In the three-step model, the first step considers a direct electron transition within the reduced zone scheme, where the electron momentum is conserved up to a reciprocal lattice vector. Note that the photon used here has energy in the soft-UV range, and its momentum is negligible. The equation governing the initial excitation in terms of density of states is:

$$N = \sum_{i,f} \left| M\left(k_f, k_i\right) \right|^2 \delta\left(E_f - E_i - \hbar\omega\right) \delta\left(K_f - K_i - G\right)$$

The delta functions δ is used to indicate the conservation of energy and momentum. The transition matrix, M, is evaluated between an initial and final state block waves within dipole approximation, where the interacting Hamiltonian of the states is given by:

$$H^{int} = \frac{1}{2mc}(A \cdot P)$$

In the second step, we assume that the photoemission happens in a UHV condition, and the mean free path of the emitted photoelectrons is long enough to travel to the surface without being scattered. In the final step, the electrons with sufficient kinetic energy to overcome the surface work function will be collected as photoelectrons. Note that in this step as the electrons cross the

surface potential barrier, they lose perpendicular momentum and preserve parallel momentum. In particular, knowing the electron intermediate excited state before escaping into the vacuum, combined with the knowledge of photon energy, k|| can be calculated directly owning to the preservation of total momentum. This process is illustrated schematically in Figure 2.14 (Left) and Figure 2.15 (Left). Such information can come from *ab initio* band structure calculations. However, if the photon energy is sufficiently high, i.e. much larger than the work function, the photoemission can excite many states and bulk bands below the Fermi level, with several intermediate excited states. In this case, one simply uses the free-electron dispersion mode:

$$E = \frac{\hbar^2 k^2}{2m}.$$

In a step forward from the 3-step mode, the electron is considered as a single-particle spectral function, which is the imaginary part of the Green's function for one-electron excitations (termed: quasiparticles) as $A(\omega, k) = -\pi^{-1}\, Im\, G(\omega, k)$ [20][21]. In the absence of interactions between the electrons, i.e. without many-body interactions, these one-particle states are well defined, $G_0 = \frac{1}{\omega - \varepsilon - i0}$ and $A(\omega, k) = \delta[\omega - \varepsilon(k)]$, where $\varepsilon(k)$ is the dispersion of "bare" (i.e., non-interacting) electrons. Taking into account the interaction in a normal (gapless) state, the Green's function also has a simple form: $G_0 = \frac{1}{\omega - \varepsilon - \Sigma}$, and $A(\omega, k) = -\frac{1}{\pi}\frac{\Sigma''(\omega)}{\left(\omega - \varepsilon(k) - \Sigma'(\omega)\right)^2 + \Sigma''(\omega)^2}$, where $\Sigma = \Sigma' + i\Sigma''$ is the quasiparticle self-energy, which reflects all the interaction of electrons in the crystal. Thus, the structure of one-electron bands with basic intra-band and inter-band interactions will be reflected in ARPES measurement.

Moreover, assume that ARPES spectrum reflects the probability of exciting an electron in the crystal with a certain energy $\hbar\omega$ and momentum $k_{||}$ (hereafter **k**). Using the same 3-step mode mentioned before, the first step is governed by the density of states (electron spectral function), multiplied by the Fermi distribution (probability to find an electron at specific energy), as $A(\omega, \boldsymbol{k})\, f(\omega)$. The second step involves the probability of photon absorption, or the direct transition to the free level, is dictated by matrix elements $M(\, h\nu,\, n,\, \boldsymbol{k})$. Thus, the structure of an ARPES-spectrum consisting of n bands can be written in terms of energy and momentum parameters (ω, **k**) as:

$$\boldsymbol{ARPES}(\omega, k) \propto \sum nM(h\nu, n, k)A(\omega, k)f(\omega).$$

This equation is written for the two-dimensional case, when the dispersive 2D bands can be seemed as a 2D surface in a 3D energy-momentum band structure, where the Fermi surface is presented as contours at the Fermi level, the $(0, k)$-plane (see Figure 2.14). The experimental factors, such as the resolution and the efficiency of the detector channels are also omitted here.

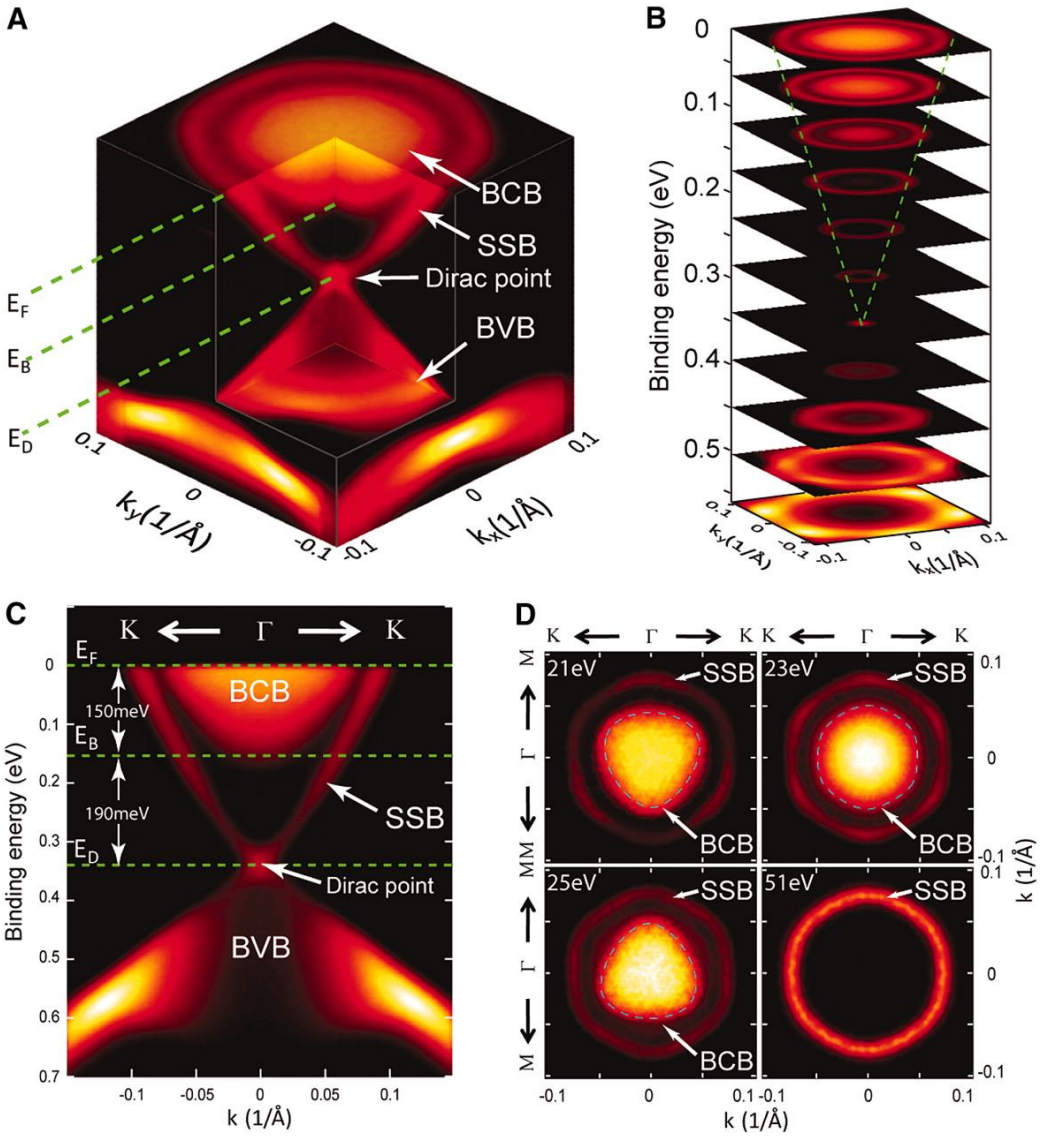

Figure 2.14 An example of the electron band structure of undoped bulk Bi_2Se_3 measured by ARPES, adapted from Ref. [22]. (A) A 3D band structure of the material showing the conduction band (BCB), valence band (BVB), surface-state band (SSB), Dirac point (E_D), Fermi energy (E_F), and the bottom of the BCB (E_B). (B) Constant-energy contours of the band structure. An evolution of the band from higher energy down to the Dirac point is observed (C) Band structure along the high symmetry $\bar{K} - \bar{\Gamma} - \bar{K}$ direction, where Γ is the center of the hexagonal surface Brillouin zone

(BZ), and the K and M points [see (D)] are the vertex and the midpoint of the side of the BZ, respectively. (D) Selected constant energy contours from (B).

2.4.3 Experimental Setup of ARPES and Microprobe ARPES

As in the experimental setup of a UPS system, a typical ARPES setup consists of an electron lens, a hemispherical analyzer, and a multichannel detector (Fig. 2.13 left). In the angular-resolved mode, a spot of focused UV light coming from a monochromator will project on the sample surface (the spot size is of order of hundreds micrometers in diameter) and coincides with the focal point of the electron lens. The electron lens projects the photoelectrons onto the entrance slit of the analyzer. The lens translates the angular information of the received photoelectrons into coordinated real space by forming an angular sweep of electrons along the slit. When the electron beam reaches the analyzer, the electron beam spreads in energy in a plane (2D detecting arrays) or a line (1D arrays) perpendicular onto the slit. As a result, a 2D-spectrum is formed on the 2D-detector (e.g., a microchannel plate), giving information of the electron momentum on k_x and k_y plane as a function of the energy. Further, the k_z momentum can be acquired by mounting the sample on a wedge to change its azimuth angle. The ARPES measurement performs a 2D mapping in each scan and acquires the intensity of photoelectrons as a function of the energy and the emission angle. With special design at the energy analyzer and detector, an ARPES system can also probe electronic states with different life-time, polarization, and electron spin. Figure 2.15 shows an example of a polarimeter installed with a MCP detector in a spin-resolved ARPES system.

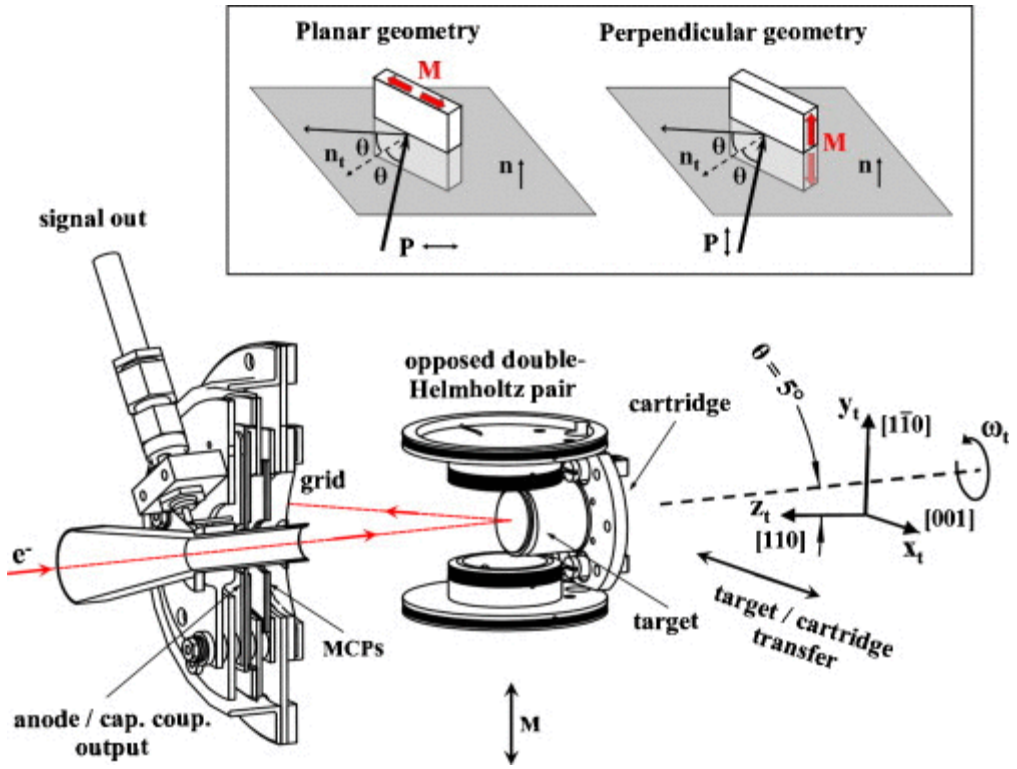

Figure 2.15 Scheme of a low-energy exchange-scattering polarimeter of a spin-ARPES system with scattering and detection components. Figure adapted from Ref. [23]. A MCP with annular tube is shown in the sectioned view to the left. Photoelectrons (red line) that arrive at the polarimeter with selected spin polarization will be scattered toward the detector while the rest of the electrons are discarded. The inset shows two possible scattering geometries to collect electrons with specific spin polarizations.

In most of our work, we use a microprobe ARPES (μ-ARPES) of the SPELEEM system. Similar to other diffraction techniques, the ARPES mode of SPELEEM images the back focal plane of the objective lens. Instead of using low energy electrons (LEED), in ARPES mode, the SPELEEM uses photons of selected energy (via monochromator and gratins) and selects only a micronmeter-size region by inserting an aperture (field limiting or selected area aperture) into the

first image plane along the imaging-optics column of the instrument in the beam separator (Figure 2.9). Also, each time the imaging photons and photoelectrons illuminate an area of interest simultaneously, the electrons are collected by a matrix of detecting units after going through photomultipliers. In terms of taking data, each time the μ-ARPES takes a snapshot of the entire momentum space, for which the size depends on the photon energy used, and each snapshot is taken at a constant energy. By stacking all the slices of the constant energy snapshots (Figure 2.14 (B)), we can construct the entire 3D band structure along all of the high symmetry directions. This is different from typical ARPES, which has limited momentum window. The μ-ARPES has been proven to be extremely useful for studying 2D materials, especially those with momentum space asymmetries.

The μ-ARPES of SPELEEM enables measurements on samples that are homogeneous over an area of about 3 μm^2, with momentum resolution of < 0.1 $Å^{-1}$ and energy resolution < 100meV. The value of the μ-ARPES system is that it can probe samples of size of 10 μm or less, which is often the case of the exfoliated 2D layered materials. Also, μ-ARPES makes probing nearby areas of different crystal orientations possible. The trade-offs of using the μ-ARPES would be its limited energy resolution and its sensitiveness to the sample surface corrugation.

2.4.4 PEEM and XPEEM

Photoemission electron microscopy (PEEM) is a widely-used technique of emission microscopy. PEEM utilizes local variations in electron emission to generate image contrast in area of interest in real time. The electron excitation is usually produced by far-UV light (PEEM) or X-ray (XPEEM) that typically comes from a synchrotron radiation source. When far-UV light or X-

ray is absorbed by matter, electrons are excited from core levels into unoccupied states, leaving empty core states. Secondary electrons are generated scattering of primary electrons. Auger processes or inelastic electron scattering can create a cascade of low-energy electrons inside the sample, and electrons with enough energy will escape the sample surface to vacuum. Thus the corresponding electron energies will feature a wide spectrum of energies between the illumination photon energy and the work function of the surface. This large population of electrons can cause image aberration in the microscope. These indirectly emitted secondary electrons will go through an array of imaging optics and being collected by MCP at a specific, yet tunable, energy. PEEM can be used for surface-sensitive real-time imaging of any flat and conducting surface to probe sample topography contrast, work-function contrast, chemical contrast and magnetic contrast.

The PEEM system essentially consists of an imaging electrostatic lens system and a UV light source for the creation of photoelectrons via photoemission. The photoelectrons emitted from the surface are imaged onto a channel plate for amplification and finally onto a fluorescent screen. The image is acquired using a CCD camera typically. The PEEM system is often equipped with an integrated sample stage for unsurpassed stability and precise sample positioning via remote controlled piezo drives. It also has an *in-situ* variable contrast aperture and the stigmator/deflector makes a PEEM system ideal for laboratory and synchrotron applications. In contrast to a SEM, PEEM does not use a scanned probe beam; instead, it allows a flood beam to uniformly illuminate the sample surface by, far-UV light (PEEM) or X-rays (XPEEM). This way, the high-power beam-induced damage or a strong photo-chemistry reaction on the surface can be avoided. The magnified image of the surface can be observed almost immediately and can be monitored in real-time (it is possible to record at video frame rate if the photon intensity is sufficient) on the fluorescent screen.

In terms of its parallel image acquisition, the basic principle of operation is similar to an optical microscope. However, since electrons are used for imaging, the resolution is no longer limited by the wavelength of a photon beam, but rather to the much smaller electron wavelength. Thus, a strong electrostatic field between the sample and the objective lens accelerates the electrons released to energies of typically 10 to 15 keV. A lateral resolution of up to 20 nm can be achieved. For more details, see Ref. [24].

Due to their similarity in focusing and collecting process, a PEEM system usually can be integrated with LEED and LEEM, for example, in a SPELEEM system. In biology, it is called photoelectron microscopy (PEM), which fits with photoelectron spectroscopy (PES), transmission electron microscopy (TEM), and scanning electron microscopy (SEM).

In our application, we use the PEEM in the SPELEEM system in BNL and Elettra [3]. The electron optical configuration is the same as in LEEM, but the energy slit is inserted in the dispersive plane of the analyzer to act as a band-pass filter to the photoelectron beam. The energy filter is used to select the kinetic energy of photoelectrons, which allows measurement of the binding energies of emission form atom core-levels or accessing the electronic structure of the occupied states, including surface states and resonances. The PEEM probe intensity is proportional to the number of emitters in the top-most layers and thus provides straightforward and quantitative information about the surface chemical composition. If the PEEM from a beamline of a synchrotron radiation is operated at X-ray energy range (400eV-2000eV, by choosing the corresponding gratings and the monochromator), it is called XPEEM and can be used to imaging surface components, residues, and doping coverage dynamically via probing at a specific atom

core level energy. For example, one can use XPEEM to understand molecule deposition on a surface and monitoring its growth rate or coverage.

2.4.5 Two Photon Photoemission

Although ARPES, especially when combined with a SPELEEM system, is extremely powerful, it can only be used to access occupied states. In order to access unoccupied states, inverse photoemission (IPE), using electron capture, is employed to probe the unoccupied valence bands [25][26][27]. One can use two-photon photoemission (2PPE) [28][29][30][31][32], to probe the unoccupied states, or say, intermediate states that located between the Fermi and vacuum level (i.e. in the "forbidden zone" of an ideal band structure of bulk material). In our research scenario, we focus on surface chemisorption, surface dipoles, and interlayer charge transfer. Thus, we use 2PPE that allows us to investigate unoccupied electronic states of molecules or thin-film deposited on highly crystalline metal surface.

In this thesis, we study the unoccupied states and interlayer interaction in self-assembly molecule-metal interfaces and a monolayer semi-metal (graphene)–metal systems using 2PPE. These unoccupied state can be interlayer states, image potential states, or surface relaxation states. 2PPE is sensitive to surface-excited electron structure changes that accompany surface chemical reactions. Our 2PPE system uses a femtosecond-pulse laser that is capable of studying ultrafast relaxation of hot carriers in bulk metals and semiconductors, the spin dynamics of magnetic materials, lifetimes of adsorbate-induced or adsorbate-modified electronic states, and real-time investigations of electron localization in thin molecular films

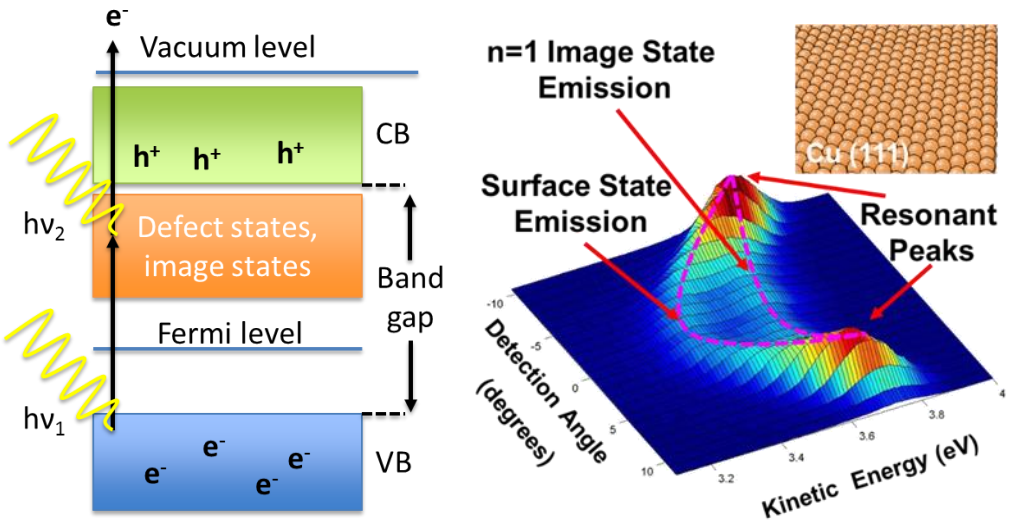

Figure 2.16 (Left) Two-photon photoemission, where one photon is used to pump a previously empty state and a second photon photo-emits an electron from this intermediate state that has a short lifetime. (Right) An example of using 2PPE to probe the surface state and image state of a Cu(111) surface. The band structure is determined by detecting angle (momentum) and photoelectron energy.

The basic scheme of a 2PPE process is sketched in Figure 2.16 (left). The first step is the photoemission of electrons going from one of the occupied bulk state or surface states in the crystal, into a surface Rydberg state. The second step is to excite electrons from the excited surface Rydberg state by absorption of a second photon to gain enough energy to enter vacuum level. Note that the second photoemission can either use the same photon energy (monochromatic) or a different photon energy (bichromatic) than in the first excitation. The kinetic energy and the angular direction of the photo-emitted electrons are measured to obtain information of the bands/surface states. Because of the states having short life-times (~10-100 femto-second), pulsed laser photon sources are used for 2PPE. Pulsed laser sources are also naturally suited to making

time-resolved measurements. If the first pulse has a different energy than the second pulse (bichromatic 2PPE), a time delay can be set between the pump and probe pulses to measure ultrafast dynamics of the surface states.

In 2PPE, the first (pump) laser pulse with photon energy $h\nu_1$ populates the electrons into an unoccupied state |i>, while the second (probe) laser pulse with photon energy $h\nu_2$ photo-emits the electrons above the vacuum level; the $h\nu_1$ is intentionally kept below material work function such that a direct one-step photoemission will not happen. Also, at the output energy spectrum, there will be first a strong energy peak that correspond to directly excited secondary electrons, from states with energy $h\nu_1$ or electron-phonon interactions. The kinetic energy of the photoelectron: $E_{kinetic} = h\nu_2 - E_b$ provides a straightforward means to determine the binding energy E_b of the unoccupied state with respect to the vacuum level. Since the process is, by definition, a second-order process, high photon fluxes are required in order to acquire a good signal-to-noise ratio. Additionally, low photon energies are needed for the pump pulse since the total energy of the pump must be less than the work function to avoid ejecting electrons directly into the vacuum. Typically the energy of these states is between 0.5 – 5 eV above the Fermi level.

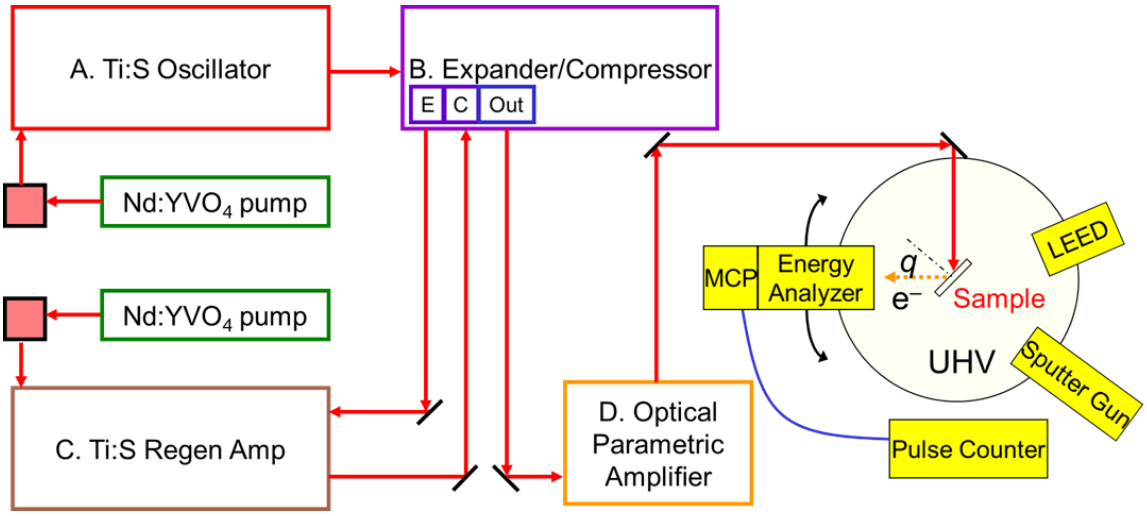

Figure 2.17 Schematic diagram of 2PPE laser setup, optical paths, and UHV chamber setup.

2.4.6 Experimental Setup for 2PPE with Femtosecond Laser System

The 2PPE system used in our experimental setup, as shown in Figure 2.17, is powered by a customized laser system with an ultrafast Ti:Sapphire pulse source (Coherent Rega 9000, 250kHz rep. rate), the pulses of which are amplified in a regenerative amplifier, and then used to drive an optical parametric amplifier (Coherent OPA 9400) to provide a tunable source of visible light. This output is then converted to UV wavelengths by second harmonic-generation in a 1 mm type I BBO crystal, thus producing a train of tunable UV femtosecond (fs) pulses. The UV pulses are again compressed by another prism pair (UV-grade silica) to make it a short-pulsed laser source, before arriving the sample in the UHV chamber. The range of available wavelengths is ~ 340 - 250 nm, which corresponds to a photon energy range of ~ 3.6 – 4.8 eV. The laser has a 250 kHz repetition rate and produces pulses with total energies of the order of 1 nJ; while being focused upon the sample, it generates a maximum fluence of ~10μJ/cm^2. The UV wavelength is determined using a 0.25 m monochromator with a wavelength accuracy of about ~ 1 nm corresponding to ~

20 meV error in the UV photon energy. Most of our measurements were carried using the above settings. For certain 2PPE experiments, the remnant ~400nm laser from our OPA is used as a probe source.

When operating in *bichromatic* mode, the fundamental laser pulse of wavelength ~800nm is used and is divided by a beam splitter into two pulses. The pulse with higher intensity is directed to the OPA, and will be used to generate a UV pulse following the previously-mentioned process, with a selected photon energy. Another pulse with lower intensity with near-infrared (NIR) pulse is compressed by a prism pair (material: SF10), with pulse duration ~50 fs measured by our autocorrelation measurement. Notice that the pulse split from the source is only 2-3% of the total power of the amplifier, such that it does not affect the OPA output. This NIR pulse is then directed to a retro-reflector built from a set of mirrors on a motorized translational stage with minimum step size of 0.1μm for time-delay control. The stage is controlled by a LabVIEW program via a MM2000 GPIB interface. The NIR pulses will then go through an optimization procedure by using a telescope to compress the beam size, and then the pulses will be directed back to the same path by a dichroic mirror. Later, the NIR pulses will be made temporally and spatially overlapping with the previously split-out UV pulses, and this combined beam will be focused at the sample surface to perform bichromatic 2PPE measurements. The overlapping of the UV and NIR pulses was examined by a cross-correlation setup built with another type-I BBO crystal for difference frequency mixing. A neutral density filter is installed to control the intensity of the UV pulses to minimize the spectral bleed-through artifacts when overlapping the UV and the NIR pulses.

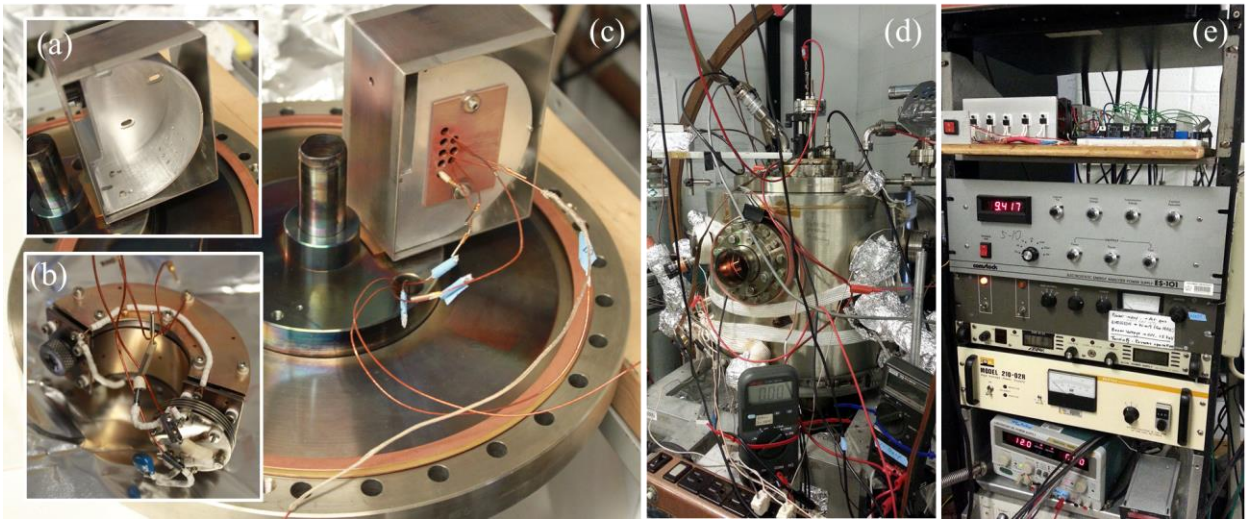

Figure 2.18 (a)-(c) A look inside the 2PPE chamber's top lid, equipped with (a) a detector box, (b) a MCP detector, and (c) a rotational stage. (d) A hosting UHV chamber. The front laser entrance window. (e) Control units: (Top-down) customized high-current supply PCB control unit, electron energy analyzer, ion-gun controller, high-voltage power-supply, and sample DC bias power-supply.

Photoemission-excited photoelectrons are collected using a 160° (36.5-mm radius) spherical-sector energy analyzer (Comstock ES-101) with a microchannel plate (MCP). The energy analyzer has an acceptor cone that yields a momentum resolution of $k_{||} = 0.03 Å^{-1}$ and an energy resolution of ~60 meV (a value greater than the energy resolution limit of the short optical pulse of ~20 meV bandwidth.) A high-voltage power supply (Bertan Associates Inc's model 215) is connected to the MCP. The MCP with electron detector and the sample holder is fixed on independently-rotatable parts of the chamber; these parts are pumped separately via differential stages by roughing and turbo pumps. The incident angle of the laser is fixed at 70° and the angular resolution is achieved by rotating the detector at a fixed rate. To locate the sample orientation and

position, an indicator laser (Uniphase He-Ne laser) was used. The sample is biased at -4eV to reduce the stray electric-field effect and other electron scattering to improve the signal-to-noise ratio. The signal received at the detector/MCP end is further amplified by a pre-amplifier (EG&G Ortec VT120) and then goes to a Comstock ES-101 electron analyzer, which is controlled by the afore-mentioned computer. Figure 2.18 shows some of the apparatus including the MCP and the rotational stage.

2.5 Sample Preparation

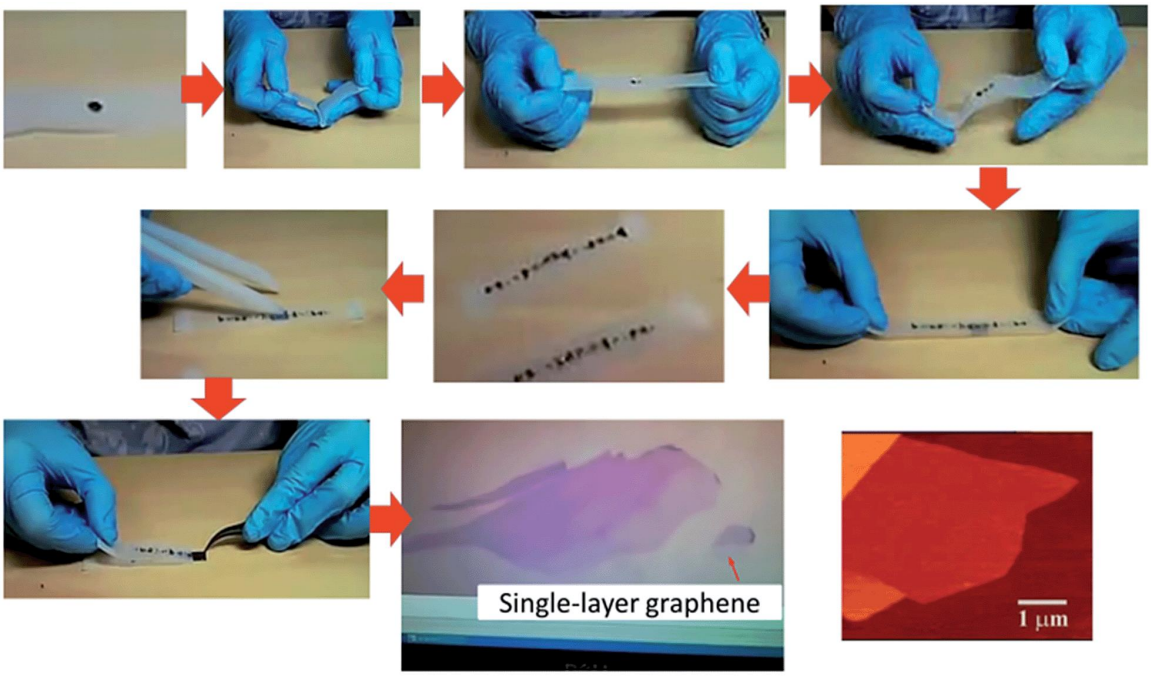

Figure 2.19 An illustrative procedure of the Scotch-tape-based micromechanical cleavage of HOPG. A single layer of graphene is detected on a SiO_2/Si substrate to have high optical contrast. This technique applies to the preparation of other 2D materials such as MoS_2 and WSe_2. This figure is adapted from Ref. [33].

2.5.1 Preparation of 2D Layered Material

Mechanical exfoliation gave birth to the first large-scale graphene flake and yielded the Nobel prize for Physics in 2010 for its founders and important contributors, i.e. Novoselov, Geim, and P. Kim. This idea was conceived by the so-called micromechanical cleavage of HOPG (Highly Ordered Pyrolytic Graphite) in 2004. Since graphite is a layered material with strong intralayer interaction but very weak interlayer bonding, applying a shear force is possible to peel layers of graphite and leave a clean, crystalline surface. Yet, the "game changer" to produce high purity graphene comes into play when the famous "Scotch tape method" was introduced in 2004 by Novoselov and Geim [34], as shown in Figure 2.19. In this micromechanical exfoliation method, graphene is detached from a graphite crystal using a 3M "Magic tape" with limited adhesiveness and residues. One must first lay down clean sample of high purity "kish graphite" (Toshiba Ceramics), and carefully stamp on a section of the tape. After peeling it off the graphite, multiple-layer graphene remains on the tape. By repeated peeling off and stamping on the multiple-layer graphene/ore to increase its coverage on the tape, the graphite will be cleaved into various thin flakes. Later, the tape is attached to the substrate, which is often time a silicon substrate with 285nm SiO_2 providing the best optical contrast to see the thin flakes, due to interference effect [35]. To remove the tape, one either clean the sample to dissolve the residues from the tape, i.e. glue, by acetone, or carefully peel off the sample from the tape, to finish the exfoliation. The flakes generated this way exhibit different size and thickness, and range in size from nanometers to several tens of micrometers. This method has been proven to be simple yet powerful. The as-exfoliated graphene are clean and of very high quality (also depending on the purity of the kish graphite.) However, it is labor intensive and lack of scalability. For our research on 2D material

properties such as graphene, MoS_2, WSe_2, and many others, samples prepared via mechanical exfoliation are ideal for optical and photoemission measurement. However, to really fully exploit its potential for industrial applications, large-area mass production methods are required.

Thus, chemical vapor deposition (CVD), a chemical process used to produce high quality, high-performance, solid materials, has also been introduced to prepare 2D materials. The CVD process is a commonly used technique in the semiconductor industry to produce thin films. In a typical CVD process, the wafer (substrate) is exposed to one or more volatile precursors, which react and/or decompose on the substrate surface to produce the desired thin-film constituents. Frequently, volatile by-products are also produced, which are removed by gas flow through the reaction chamber. Also, CVD is widely used in microfabrication processes to deposit materials in various forms, including: monocrystalline, polycrystalline, amorphous, and epitaxial.

In our experiment, we use CVD-grown MoS_2 and graphene for various applications. To obtain high-quality monolayer MoS_2 flakes, a specific CVD-growth technique [36] was adapted using Si substrates with a 285nm-thick thermal oxide. The substrates were first cleaned by Piranha solution and O_2 plasma etching (5 min). The growth used a solid-source transport approach, with samples mounted upside-down above the Mo-source crucible. MoO_3 and sulfur were used as solid precursors in separate crucibles, with the furnace temperature ramped to 700^{o}C in an N_2-filled environment under laminar flow condition. More detailed temperature ramp/precursor flow steps are described in the supplementary materials in Ref. [36]. Transferred CVD MoS_2 islands were obtained via a PDS-based lift-off process and placed onto a native-SiO_2-on-Si substrate. More

details regarding the transfer process is in the following session. Post transfer cleaning was done in an Ar-N_2 flowing furnace at a temperature of 200 ^oC for five hours.

Note that to examine the quality and thickness of the MoS_2 or graphene flakes, Raman spectroscopy and photoluminescence (PL) were used to determine the layer number of layered 2D materials in each exfoliated flake or CVD single crystal. Separate PL experiments also provided information about the electronic structure and quality. In this thesis, the Raman and PL measurements were accomplished using a Renishaw InVia Raman Microscope with a 532nm laser and an 1800 lines/mm grating. The laser power was 100μW and the collection time was 20 seconds. The layer number of MoS_2, WSe_2, or graphene flakes was determined via Raman phonon modes E_{2g} and A_{1g}, PL, AFM, and optical-contrast analysis all together.

2.5.2 Review on Transfer Techniques

In order to manipulate the as-grown CVD flakes or as-exfoliated thin films, several transfer techniques were introduced in our work. This section will briefly discuss the two major transfer techniques that we used – the wet and the dry transfer using solvents, etchants, and polymers. A wet-transfer technique using PMMA polymer was first introduced in response to the need to use a different substrate, native-oxide Si, other than the typical 285nm SiO_2/Si chip. In this thesis, we started with using exfoliated MoS_2 samples prepared by mechanical exfoliation on a clean 285nm-thick SiO_2/Si substrate. Due to the insulating nature of SiO_2, the exfoliated MoS_2 flakes were grounded via thermally deposited Au/Cr contacts, which were patterned using TEM grids as shadow masks. The metal contacts for the small flake MoS_2 i.e., < 5μm, can provide enough conductivity to convey a high flux of charges generated during electron microscopy or

photoemission process. This approach also depends heavily on sample and contact geometry. However, in ARPES measurements, with MoS_2 flakes of size 10µm+, the metal contacts do not allow good electrical contact with the sample ground. Therefore, an alternative sample preparation method was needed.

Our alternative approach was a wet-transfer process. This method involves exfoliated samples and used the following procedure: first, MoS_2 flakes were exfoliated on a Si chip covered with a sacrificial organic-thin-film transfer layer [23] in order to transfer onto the lithography-patterned-metal Si substrate. The transfer layer here was prepared by spin-coating a layer of 5% Polyvinyl alcohol (PVA) aqueous solution onto a clean Si substrate and with another poly (methyl methacrylate) (PMMA) layer on top. This sample was then annealed at 130^{o}C for two minutes to form an overall 280nm-thick layer. Note that this transfer layer had the same optical sample visibility as the 285nm SiO_2. The thickness of the MoS_2 flakes were exfoliated and then characterized using optical contrast microscopy [38] and Raman spectroscopy [39], the same procedure as preparing them on a typical SiO_2/Si chip. Subsequently, the samples were gently rinsed in distilled water to dissolve the PVA layer, leaving the PMMA layer with MoS_2 flakes suspended on top of the solvent. After removal from the solution, the film samples were left to dry overnight on a metal scoop and were suspended. Later, the film samples were placed carefully on the target substrate (native-oxide Si chip in this case) and were aligned with the help of a long-focus microscope on a transfer stage (a customized 3 axis stage for transport measurement.) Additional annealing at 160^{o}C released the MoS_2 flakes on the desired substrate. Later, samples were rinsed in acetone solution for at least 24 hours to further remove PMMA.

For CVD-prepared sample, we used an etch-assisted transfer process as follows: PMMA layer were spin-coated onto CVD MoS_2 flakes on SiO_2/Si chips at 4000 r.p.m. for 60 s to form 50-nm-thick layers. The chips were floated on 1 M KOH to remove the silicon oxide epi-layer, causing the chips to fall off, and leaving the polymer and MoS_2-coated polymer membrane floating on the liquid surface. The membrane was then transferred to a deionized water, washed several times, and then was scooped onto a TEM grid to left dry. The TEM grids with MoS_2 was baked in UHV condition at 350 °C for 1 hours or then baked in an atmospheric pressure Ar/H2 gas flow for 4 hours to remove PMMA. Before atomic-resolution imaging or any opical/electronic spectroscopy measurement, then sample were baked overnight in an UHV chamber at 350 °C. Note that the CVD sample prepared this way was inevitably suffered certain degree of contamination or surface residues, and thus, the quality was degraded. Also, the wet-transfer process sometimes also induced wrinkles and folding in the MoS_2 flakes.

In an attempt to ease the above mentioned drawbacks of a wet transfer process, a dry transfer technique was developed as follows: first, CVD-grown MoS_2 on SiO_2/Si was attached with a polydimethylsiloxane (PDMS) stamp pressed onto the MoS_2 surface so as to support the flakes and protect the surface. The chip was carefully laid afloat on the 1M KOH solution surface (MoS_2 side facing up) to etch away the SiO_2 epi-layer, causing the chips to fall off, and leaving the PDMS/MoS_2 stack in solution. Later, the stack was rinsed with DI water, left dried for a day, and stamped onto the target substrate. With low heating (30-40 ℃), the PDMS layer was removed mechanically and the MoS_2 in vacuum desiccator for a day. However, note that even though the dry-transfer method provided a cleaner sample surface, the PDMS used in the method still left residue that, in some cases, hampers the measurement.

Therefore, a substitute of the PDMS, cellulose acetate butyrate (CAB) polymer, was introduced in the later stage of our experiments. The transfer process then worked as follows: first, the CAB was spin-coated on the MoS_2 chip. The CAB/MoS_2 stack was then stamped on a native-oxide Si substrate or substrate of one's like. The whole chip was then immersed in acetone to dissolve the CAB layer, rinsed in DI water, and finally dried in vacuum desiccator to complete the transfer. CAB was used because it has generally a strong bond to 2D materials, so it is ideal for picking up flakes. Depending on the type of 2D materials, CAB polymer was used to complete the transfer process. Also, the use of CAB polymer provides a new way to pick and stack a multilayer heterostructures.

2.5.3 Cu(111) and Ir(111) Substrate Preparation

In our molecule/metal or graphene/metal model systems, a high-purity (99.999% purity) single-crystal copper or iridium sample of 1.2-cm diameter disk was used and cut to the desired (111) orientations of the crystal. In our experiment, one disk of our choice was bounded along the pre-engraved side trench by a Ta (Omega, 0.01 inch) wire that connected to two electrodes outside the chamber. The sample was thus connected via the electrodes to a power supply for resistive heating. The sample was then placed into a UHV chamber (base pressure less than 2×10^{-10} Torr) equipped with an ion sputtering gun, a low-energy electron diffraction (LEED) instrument, a quadrupole mass spectrometer (QMS), and a spherical-sector electron-energy analyzer. Also, to measure the temperature, a K-type thermos-couple (Omega. 0.03 inch chromel and alumel hybrid) was placed at the side of the copper or iridium substrate with UHV-compatible glue, and was connected to another pair of electrodes outside the chamber to a thermometer.

The sample was cleaned by several sputtering-annealing clean cycles. A cycle includes Ar+-sputtering at 1.5 keV for 20 min, and subsequent annealing to 500~700 ℃. For iridium, the annealing temperature required is 850-1150 ℃, such that an electron beam heating were prepared using a customized tungsten filament and high voltage source. Each sample-preparation cycle was repeated until sharp LEED spots are observed. For a freshly installed sample, 8-10 times of the cleaning cycle were advised. Otherwise, to remove molecules or CVD graphene thin-film to reset the sample surface, 2-3 times of the cycle should be suffice.

2.6 References

[1] Flege, J. I., E. Vescovo, G. Nintzel, L. H. Lewis, S. Hulbert, and P. Sutter. "A new soft X-ray photoemission microscopy beamline at the National Synchrotron Light Source." *Nuclear Instruments and Methods in Physics Research Section B: Beam Interactions with Materials and Atoms* 261, no. 1 (2007): 855-858.

[2] Schmidt, Th, S. Heun, J. Slezak, J. Diaz, K. C. Prince, G. Lilienkamp, and E. Bauer. "SPELEEM: combining LEEM and spectroscopic imaging." *Surface Review and Letters* 5, no. 06 (1998): 1287-1296.

[3] A. Locatelli and E. Bauer. "Recent advances in chemical and magnetic imaging of surfaces and interfaces by XPEEM." *Journal of Physics: Condensed Matter*, 20:093002, 2008.

[4] Locatelli, A., L. Aballe, T. O. Mentes, M. Kiskinova, and E. Bauer. "Photoemission electron microscopy with chemical sensitivity: SPELEEM methods and applications." *Surface and interface analysis* 38, no. 12-13 (2006): 1554-1557.

[5] D. Cocco, M. Marsi, M. Kiskinova, K. C. Prince, T. Schmidt, S. Heun, and E. Bauer. "Microfocussing VLS grating-based beamline for advanced microscopy." *Proc. SPIE* 3767, 271 (1999)

[6] Locatelli, A., A. Bianco, D. Cocco, S. Cherifi, S. Heun, M. Marsi, M. Pasqualetto, and E. Bauer. "High lateral resolution spectroscopic imaging of surfaces: The undulator beamline "nanospectroscopy" at Elettra." In *Journal de Physique IV (Proceedings)*, vol. 104, pp. 99-102. EDP sciences, 2003.

[7] Bianco, Anna, Giovanni Sostero, and Daniele Cocco. "Kirkpatrick-Baez elliptical bendable mirrors at the Nanospectroscopy beamline: metrological results and x-ray performance." In *International Symposium on Optical Science and Technology*, pp. 74-85. International Society for Optics and Photonics, 2002.

[8] Moreno, Thierry, Rachid Belkhou, Gilles Cauchon, and Mourad Idir. "New optical setup for the generation of variable spot size on third generation synchrotron beamlines." In *Optics & Photonics 2005*, pp. 59210F-59210F. International Society for Optics and Photonics, 2005.

[9] Dudin, Pavel, Paolo Lacovig, Claudio Fava, Eugenio Nicolini, Anna Bianco, Giuseppe Cautero, and Alexei Barinov. "Angle-resolved photoemission spectroscopy and imaging with a submicrometre probe at the SPECTROMICROSCOPY-3.2 L beamline of Elettra." *Journal of synchrotron radiation* 17, no. 4 (2010): 445-450.

[10] Bauer, E. "Low energy electron microscopy." *Reports on Progress in Physics* 57, no. 9 (1994): 895.

[11] Altman, M. S. "Trends in low energy electron microscopy." *Journal of Physics: Condensed Matter* 22, no. 8 (2010): 084017.

[12] R. M. Tromp and M. C. Reuter (1991). “Low Energy Electron Microscopy.” *MRS Proceedings*, 237, 349 doi:10.1557/PROC-237-349.

[13] Lüth, Hans. *Solid surfaces, interfaces and thin films*. Vol. 4. Berlin: Springer, 2001.

[14] Hüfner, Stefan. *Photoelectron spectroscopy: principles and applications*. Springer Science & Business Media, 2003.

[15] Heinrich Hertz: Ü ber den Einfluss des ultravioletten Lichts auf die electrische Entladung. In: Annalen der Physik, Band 267, 1887, S. 983 – 1000.

[16] Hallwachs W “Ü ber den Einfluß des Lichtes auf electrostatisch geladene Körper Annalen der Physik und Chemie,” 33, 1888, 301-12.

[17] Reinert, Friedrich, and Stefan Hüfner. "Photoemission spectroscopy—from early days to recent applications." *New Journal of Physics* 7, no. 1 (2005): 97.

[18] Saiht. General principle of ARPES with description. Wikipedia: The Free Encyclopedia., 2009.

[19] Abrikosov, Alekseĭ Alekseevich, Lev Petrovich Gorkov, Igor Ekhielevich Dzyaloshinski, and Igor′ Ekhiel′evich Dzi͡aloshinskiĭ. *Methods of quantum field theory in statistical physics*. Courier Corporation, 1975.

[20] Mattuck, Richard D. *A guide to Feynman diagrams in the many-body problem*. Courier Corporation, 2012.

[21] Chen, Y. L., J-H. Chu, J. G. Analytis, Z. K. Liu, Kyushiro Igarashi, H-H. Kuo, X. L. Qi et al. "Massive Dirac fermion on the surface of a magnetically doped topological insulator." *Science* 329, no. 5992 (2010): 659-662.

[22] Jozwiak, C., J. Graf, Gennadi Lebedev, Nord Andresen, A. K. Schmid, A. V. Fedorov, Farid El Gabaly, Weishi Wan, Alessandra Lanzara, and Zahid Hussain. "A high-efficiency spin-resolved photoemission spectrometer combining time-of-flight spectroscopy with exchange-scattering polarimetry." *Review of Scientific Instruments* 81, no. 5 (2010): 053904.

[23] Information cited from the FOCUS IS-PEEM product page of Oxford Instruments Omicron NanoScience.

[24] Dose, Volker. "Momentum-resolved inverse photoemission." *Surface Science Reports* 5, no. 8 (1985): 337-378.

[25] Smith, Neville V. "Inverse photoemission." *Reports on Progress in Physics* 51, no. 9 (1988): 1227.

[26] Himpsel, Franz-Josef. "Inverse photoemission from semiconductors." *Surface Science Reports* 12, no. 1 (1990): 3-48.

[27] Giesen, K., F. Hage, F. J. Himpsel, H. J. Riess, and W. Steinmann. "Two-photon photoemission via image-potential states." *Physical review letters* 55, no. 3 (1985): 300.

[28] Steinmann, W. "Spectroscopy of image-potential states by two-photon photoemission." *Applied Physics A* 49, no. 4 (1989): 365-377.

[29] *Laser spectroscopy and photochemistry on metal surfaces*. Vol. 5. Singapore: World Scientific, 1995.

[30] Osgood, Richard M., and Xiaoyi Wang. "Image states on single-crystal metal surface." *Solid State Physics* 51 (1997): 1-80.

[31] Th. Fauster and W. Steinmann. "In Electromagnetic Waves: Recent Developments in Research," Vol. 2: Photonic Probes of Surfaces, ed. P. Halevi, Elsevier, Amsterdam (1995), and references cited therein

[32] Yi, Min, and Zhigang Shen. "A review on mechanical exfoliation for the scalable production of graphene." *Journal of Materials Chemistry* A (2015).

[33] Novoselov, Kostya S., Andre K. Geim, S. V. Morozov, D. Jiang, Y_ Zhang, S. V. Dubonos, I. V. Grigorieva, and A. A. Firsov. "Electric field effect in atomically thin carbon films." *Science* 306, no. 5696 (2004): 666-669.

[34] Casiraghi, C., Achim Hartschuh, E. Lidorikis, Huihong Qian, Hayk Harutyunyan, Tobias Gokus, K. S. Novoselov, and A. C. Ferrari. "Rayleigh imaging of graphene and graphene layers." *Nano letters* 7, no. 9 (2007): 2711-2717.

[35] van der Zande, Arend M., Pinshane Y. Huang, Daniel A. Chenet, Timothy C. Berkelbach, YuMeng You, Gwan-Hyoung Lee, Tony F. Heinz, David R. Reichman, David A. Muller, and James C. Hone. "Grains and grain boundaries in highly crystalline monolayer molybdenum disulphide." *Nature materials* 12, no. 6 (2013): 554-561.

[36] Dean, C. R., A. F. Young, I. Meric, C. Lee, L. Wang, S. Sorgenfrei, K. Watanabe et al. "Boron nitride substrates for high-quality graphene electronics." *Nature nanotechnology* 5, no. 10 (2010): 722-726.

[37] Benameur, M. M., B. Radisavljevic, J. S. Heron, S. Sahoo, H. Berger, and A. Kis. "Visibility of dichalcogenide nanolayers." *Nanotechnology* 22, no. 12 (2011): 125706.

[38] Lee, Yi-Hsien, Xin-Quan Zhang, Wenjing Zhang, Mu-Tung Chang, Cheng-Te Lin, Kai-Di Chang, Ya-Chu Yu et al. "Synthesis of Large-Area MoS2 Atomic Layers with Chemical Vapor Deposition." *Advanced Materials* 24, no. 17 (2012): 2320-2325.

Chapter 3

Substrate-Dependent Long-Range Surface Structure of Single-Layer and Multilayer MoS_2 – A Low-Energy Electron Microscopy and Microprobe Diffraction Study

"The beginning is the most important part of the work."- Plato, *The Republic*

This chapter tells how our journey toward understanding MoS_2 and other TMDCs began. First, the long-range surface structure of the dichalcogenide MoS_2 was probed with nanometer-length spatial resolution using LEEM and μ-LEED. The quality of two differently prepared types of MoS_2, single-layer and multilayer exfoliated crystals, as well as single-layer CVD-grown crystals, was examined. The effects induced by a supporting interface were examined by utilizing two different substrates, SiO_2 and native-oxide-covered Si. In addition, the role of impurities was also studied by way of *in situ* deposition of the alkali-metal potassium. Microprobe measurements revealed that, unlike exfoliated MoS_2, CVD-grown MoS_2 may, in some instances, exhibit large-scale grain-boundary alterations due to the presence of surface strain during growth. However, real-space probing by LEEM in conjunction with k-space probing by μ-LEED shows that the quality of CVD-grown MoS_2 can be comparable to that of exfoliated MoS_2. In short, the work presented in this chapter laid foundation for all of the later works to succeed.

3.1 Introduction

Single-layer MoS_2 is a metal dichalcogenide two-dimensional crystal, that has emerged as a representative of a new class of materials with distinctive physical [1], electronic [2][3][4][5][6] and optical [8][9][10][11][12] properties. Due to its semiconducting [7][8] nature and large intrinsic optical direct bandgap of 1.8 eV [7], monolayer (ML) MoS_2 is ideal for potential applications in nano-optoelectronics and energy harvesting. Recent studies in controlling dynamic valley-spin polarization in ML MoS_2 films [9][10][11] also suggest initial exploration of spintronic applications. Finally, various forms of MoS_2 such as nanotubes [13], nanoparticles [14] and monolayer films [15][16] have been explored. However, while extensive research has been performed on preparation of carbon-based materials, including monolayer graphene, studies on the crystal growth of monolayer MoS_2 are relatively sparse. Among the existing studies, it has been demonstrated that polycrystalline monolayer MoS_2 can be grown via solid-source chemical vapor deposition (CVD) [16][18][19][20][21][22], allowing its use in thin-film micro-device applications. Recently, the Hone Group and their collaborators have shown that it is possible to grow high-quality, ML-thick-crystals of MoS_2 with typical sizes of a few hundreds of micrometers, which have optical and transport properties comparable to those of exfoliated MoS_2 [21]. In short, these developments suggest single-layer MoS_2, including now CVD-grown material, as an ideal candidate for building atomically thin-layered electronic [23][24][25], optical [7][26], and photovoltaic [27]devices.

Despite the promise of this relatively available two-dimensional (2D) material, its characterization has been generally limited to optical and transport probes. Furthermore, the almost

exclusive use of a thick oxide as the supporting substrate has been important in order to allow optical microscopic characterization of the 2D material. Hence, to the best of our knowledge, this has prohibited studies of this material on other surfaces, and it has precluded the discovery of potentially rich interface interactions that may exist between a 2D dichalcogenide, such as MoS_2, and its supporting substrate. In order to study monolayer MoS_2 on other substrates other than thick oxides, it would be ideal for an investigative technique to possess the following three imaging modalities: (1) real-space microscopy which would allow locating of MoS_2 samples, (2) spatially-resolved diffraction which would allow confirmation of crystalline quality and domain orientation of MoS_2 samples, and, (3) spatially-resolved spectroscopy, which would allow electronic structure mapping of MoS_2 samples. In this work, we use electron microprobes in an ultrahigh vacuum (UHV) environment to achieve the first two desired imaging modalities on MoS_2 and discuss new insights into MoS_2 materials that are afforded by this technique.

Specifically, this study has characterized and probed mono- and multi-layer exfoliated MoS_2 and monolayer CVD-grown MoS_2 using a high-resolution direct imaging instrument: *viz.* a spectroscopic photoemission and low-energy electron microscope (SPE-LEEM) [27][28], which is capable of carrying out structural and spectroscopic analysis of the sample at the nanometer scale [29][30][31]. Our studies provide information about the surface corrugation and crystalline structure of the ultrathin films under investigation. Our measurements were carried out on two different substrates: thermally-oxidized 285nm thick SiO_2/Si wafers and a Si wafer with a thin native SiO_2 film. Our results complement earlier optical studies, done using Raman and photoluminescence (PL) measurements [7][8][16]-[21]. Furthermore, in order to tune the Fermi level and/or work function of MoS2 via surface doping [32][33], we have used atomic potassium

dosing. Note that this doping is done *in situ*, thus allowing the surface morphology and structure to be examined by LEEM and microprobe low-energy electron diffraction (μ-LEED) in the presence or absence of doping. A comparative analysis of the results obtained from MoS_2 samples fabricated with different methods and on different substrates provides understanding of the properties and qualities of CVD-grown MoS_2, and sheds light on potential applications of monolayer CVD MoS_2 for improved electronic and optical devices, and on two-dimensional conjoined materials, such as heterojunctions with graphene [25][33][34] and other 2D materials.

3.2 Experimental Methods

The samples examined here were either mechanically exfoliated or prepared by CVD growth on a high-quality SiO_2/Si substrate, as first described in Ref. [21], and they were examined on the growth substrate or transferred onto Si substrates, with thermally grown or native-oxide overlayers, using sacrificial polymer layers [36]. The samples were then annealed at 350 ^oC under a laminar flow of N_2/Ar to complete the transfer procedure. Prior to SPE-LEEM experiments, the samples were degassed at 350 ^oC for several hours under UHV conditions. In certain experiments, the samples were surface-doped with different levels of potassium while in the LEEM chamber (see below).

3.3 Experiment Results: A. Calibration Experiments on Exfoliated MoS_2

3.3.1 LEEM on SiO_2-Supported Exfoliated MoS_2

LEEM measurements were first carried out on mechanically exfoliated MoS_2 flakes prepared *ex situ* on a silicon wafer with a 285-nm-thick SiO_2 overlayer. Since LEEM imposes a relatively large incident electron flux of $5x10^8$ sec^{-1} μm^{-2} onto samples with areas of 20 - 50 μm^2, preventing or reducing charging of the sample was necessary to perform LEEM measurements. The low mobility of ML dichalcogenide systems, especially MoS_2 [37][38], makes this charging issue even more severe. Thus developing a strategy for eliminating charging was a major experimental necessity. Our initial approach was to bring MoS_2 islands into contact with a uniform-potential metallic plane by employing Au grids, which were in electrical contact with the local instrument "ground". This approach was realized by using transmission electron microscopy (TEM) grids as shadow masks to create thermally evaporated Au/Cr/Al, 40/5/10 nm-thick, metal contacts on MoS_2 islands, as shown in Figure 3.1 (a) and (b). Note that in Figure 3.1 (b) the profile of the MoS_2 sample buried under the contacts can be clearly seen via reflectivity differences between the contacts and the MoS_2 in this LEEM image. Despite this "grounding" grid, local charging of the sample effectively prevented LEEM under continuous electron beam illumination. The very low mobility of MoS_2 (<10 cm^2/V-s) [37] prevents compensation of the charge that accumulates in the thick SiO_2 when it is irradiated with electrons in LEEM. In other words, the flux of incoming charges is much larger than the out-going flux which is conducted to ground by metal contacts. Charging was present over a wide range of grid spacings (5 - 30μm) and contact thickness (5 - 100nm). For the example of the MoS_2 sample in Figure 3.1 (b), which consists of

1ML and 2ML regions, the boundaries between the two regions, as well as the edges of the MoS_2 sample in contact with the metal, became blurry after extended (> 5min) exposure to the LEEM electron beam. In an attempt to inhibit charging, potassium deposition was tried; however, this proved ineffective. Note however that in the case of μ-LEED measurements, the incident electron energy was much higher (20 - 100eV) than in the case of LEEM. This higher energy range led to a reduction in surface charging due, in part, to a higher secondary electron yield which helped to balance the incident electron flux. Thus, in this case, it was found that a Au grid was then sufficient to satisfactorily reduce any charge-induced distortion of the LEED pattern.

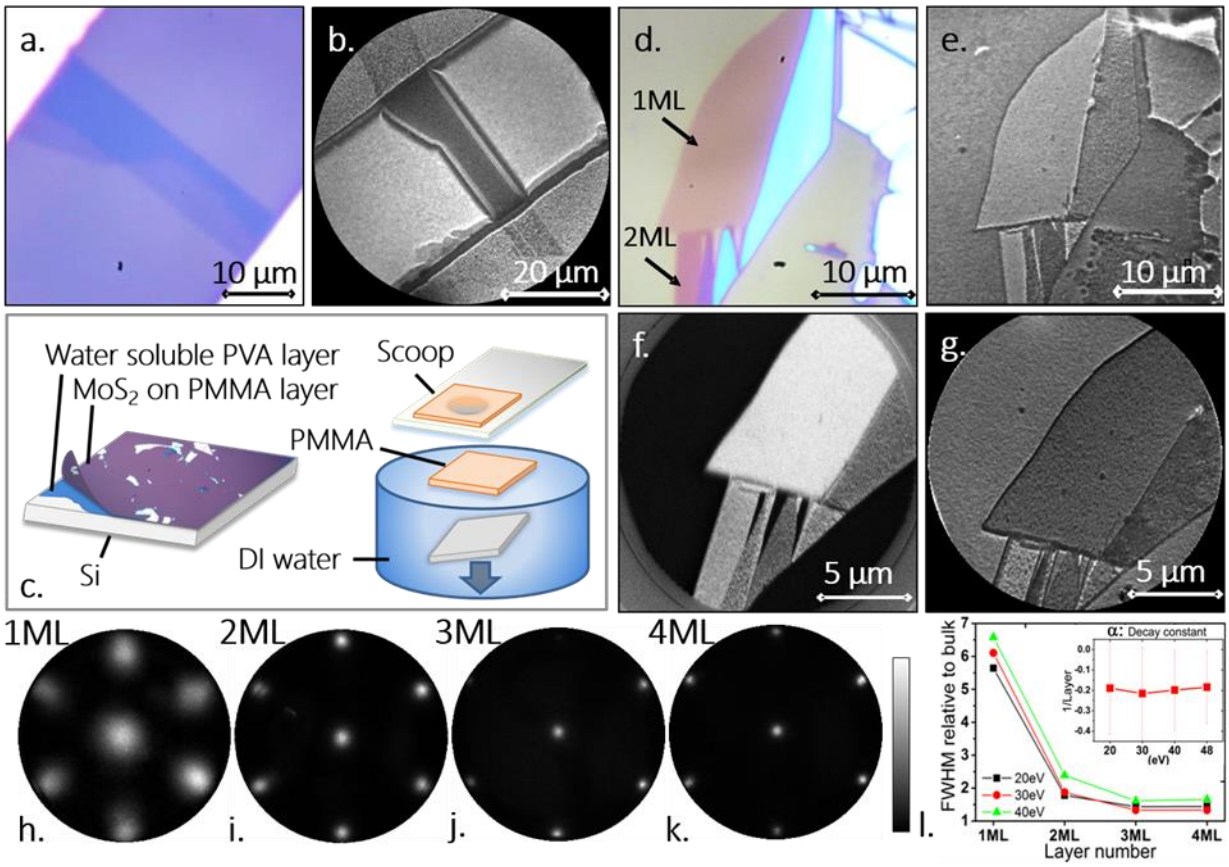

Figure 3.1 Exfoliated MoS_2 on SiO_2 and Si (a) Optical microscope image of an exfoliated 1 - 2ML MoS_2 flake on SiO_2, with both its top and bottom side contacted. The bright areas correspond to Au/Cr/Al contacts. (b) LEEM image of the same sample. At an electron energy of 0.9eV, the MoS_2 beneath the metal contacts can be clearly seen. (c) Illustration of the transfer process of exfoliated MoS_2. The PMMA film with exfoliated *in situ* and bonded *per se* MoS_2 thin flakes is "scooped up" and stamped on a substrate of interest. (d) Optical microscope image of an exfoliated mixed layer flake on SiO_2, before transfer; and (e) after transfer to Si and probed by MEM imaging (0.08eV). (f) LEEM image (5eV) after removal of background signal; (g) MEM image (0.08eV) after K doping. (h)-(k) μ-LEED patterns at 48eV electron energy on exfoliated MoS_2 1 - 4ML post transfer to Si. For samples with thicknesses >1ML, the LEED signal quality is akin to that of a bulk crystal. Also, the LEED (00) spot width decreases with increasing layer number. (l) Full width at half maximum (FWHM) of the (00) LEED spot for 1 - 4ML MoS_2 flakes relative to that of bulk, measured at 20, 30, and 40eV. The inset shows the extracted decay rate of the FWHM with increasing layer number as a function of electron energy.

By using a short-duration (3 - 5min) LEEM electron exposure before the full onset of charging, measurements of a metal-grid-covered MoS_2 surface were possible. These measurements showed a relatively defect-free surface structure, as compared to the speckled appearance of graphene on SiO_2 [39]. In Figure 3.1 (b), the LEEM measurement shows that the image distortion happens mostly on the borders of MoS_2, with SiO_2 and with Au, as a result of charge accumulation. This gives an idea of charge-transfer dynamics in insulator/dichalcogenide and metal/dichalcogenide systems, and the opens the possibility of studying it more extensively using a derivative of this technique.

3.3.2 LEEM on Si-Supported Exfoliated MoS_2

In order to improve the quality of our LEEM measurements, an alternate approach was used, namely transfer of the sample to a Si substrate covered only by a native-oxide layer. A similar approach has been reported previously for imaging ML-thick organic materials of low mobility, i.e., using a conductive substrate so as to provide a large-area channel for charge dissipation [40] in an effort to balance the huge incoming flux of charge from LEEM. The transfer process is illustrated in Figure 3.1 (c). While use of this native-oxide-covered substrate entailed a more complex sample preparation procedure, tunneling through this thin oxide from the MoS_2 sample was found to be effective in preventing charging. However, the thin-native oxide, typically of ~10 Å thickness was too thin to allow sufficient optical contrast for easy optical examination of the MoS_2 thin films. Thus a Si sample with a standard 300nm-thickness-oxide overlayer was used for exfoliation and initial sample handling followed by transfer of the MoS_2 to a separate native-oxide-covered Si substrate for LEEM imaging of the sample. Figures 1d and 1e show examples of optical and LEEM images of a MoS_2 flake before (Figure 3.1 (d)) and after (Figure 3.1 (e)) transfer. It is clear from the sharp image resolution that this approach prevented significant charging of the MoS_2 flake. In addition, LEEM imaging was relatively uniform across the surface, except near the flake edges. In our LEEM imaging, the electron energies were chosen to obtain good contrast between laterally adjacent MoS_2 samples of different thicknesses. Note that removal of electronic-detector-screen artifacts and background signal, by background subtraction of a scaled background image, also improved the image contrast, as shown in Figure 3.1 (f). Finally, as in the SiO_2-substrate-supported case, LEEM measurements of MoS_2 were performed after deposition of potassium; see Figure 3.1 (g). The figure clearly shows that the quality of LEEM images and layer contrast were

improved by the presence of potassium, and as expected, an overall lowering of the work function also occurred. Note that the changes in local work function can be calibrated and measured by mirror electron microscopy (MEM) [41][42][43] via changes in the electron reflectivity [44].

Thus our results show that a doped Si substrate, even in the presence of a native oxide, can ground typical MoS_2 samples such that long-time-scale low-energy electron microscopy can be used for high-resolution imaging of MoS_2. In addition, our results show that potassium deposition enables enhancement of the imaging of surface structure down to ~0.5 μm size. This appears to be due to preferential nucleation of potassium at defect sites, as supported below in our measurements of potassium-dosed CVD grown MoS_2. More generally, this procedure serves as a useful method to enhance the imaging and diagnostic capability of LEEM.

3.3.3 Potassium Deposition

On both exfoliated and CVD-grown samples, we deposited potassium *in situ* in the UHV chamber of the LEEM/MEM/PEEM system using a commercial (SAES Getters) alkali-metal dispenser as a source. The temporal variation of the potassium surface concentration could be monitored using MEM imaging, or the so-called "LEEM Mirror mode",[41][42][42] in which reflected electrons from the surface were collected at a frame rate of 10 s^{-1}. In MEM, when the imaging electrons have energies lower than the mirror potential value, they are reflected back before reaching the sample surface, resulting in high intensity in the corresponding MEM image. At energies corresponding to a mirror potential, the electrons just reach the sample surface, and the reflected or backscattered intensity is the lowest. Changes in the apparent mirror potential (changes in the imaging electron energy corresponding to mirror imaging conditions) in the MEM images

directly correspond to the shift in the effective surface potential. Such potential shift towards lower value is regarded as corresponding to lowering of the work function of the surface.

3.3.4 LEED on Si-Supported Exfoliated MoS_2

The crystal quality and orientation of our 2D materials were probed in reciprocal space using μ-LEED. Initial experimentation showed that an atomically flat, single-domain crystal flake with an area of > 10 × 10 μm^2 was needed to obtain a sharp LEED pattern. Using samples that conformed to these criteria, LEED measurements were performed on "stand-alone" 1-4ML islands, along with a thin bulk MoS_2 flake, shown in Figure 3.1 (h)-(k). Note that for a MoS_2 sample with a layer thickness greater than 1ML, the LEED pattern was almost as sharp as that from bulk MoS_2. The mean free path for 48eV electrons, used in Figure 3.1, is ~5.17 Å [45][46], which is comparable to the thickness of 1ML MoS_2; this suggests that LEED spot broadening observed for 1ML MoS_2 (Figure 3.1 (h)) is, in part, due to scattering from the substrate. With increasing MoS_2 thickness, this scattering contribution would be expected to decrease, as is indeed shown in Figure 3.1 (i)-(k). Our observations of the width of the specular (00) LEED spot support this assertion, and show that background scattering from the substrate is diminished for > 2ML MoS_2. Spot-width broadening may also be due to subtracted-induced roughness, in which the corrugation of the MoS_2 conforms to the corrugation of the underlying substrate, as is the case in monolayer graphene [39]. However, monolayer MoS_2 is much thicker (three atomic layers) than graphene (one atomic layer), and is expected to be much more rigid; the elastic bending modulus of MoS2 is calculated to be 9.61 eV, which is much larger than that of graphene, i.e. 1.4 eV [47]. Thus we expect the effect of substrate-induced roughness to be less in ML MoS_2 compared to

graphene, though we cannot completely rule it out. While beyond the scope of the discussions here, we note that an electron-energy-dependent LEED spot-width analysis, which takes into account the different contributions from Mo and S atoms, could provide important information regarding corrugation in monolayer and multi-layerMoS_2 [39][48].

To summarize, our surface-sensitive reciprocal-space measurements reveal single-crystal MoS_2 after transfer, which complements and verifies the above real-space LEEM measurements. Analysis of the width of the (00) spot reveals a monotonic decrease with thickness, which is attributed to a decrease in the scattering of low-energy electrons by the underlying SiO_2/Si substrate.

3.4 Experimental Results: B. Experiments on CVD-Grown MoS_2

The procedures required for successful LEEM imaging of exfoliated MoS_2, discussed above, allowed us to carry out LEEM measurements on CVD MoS_2 islands grown on SiO_2 substrates. The growth of CVD MoS_2 on SiO_2 has recently been shown to result in the growth of 2D islands with a well-defined set of shapes. One particularly distinctive and prevalent geometry is a ML-thick triangle, with two different types of edge termination [21]; another frequently observed shape is that of a ML hexagram (Figure 3.2 (a)-(c)). The triangular-shaped MoS_2 islands are single-domain crystals [21], and exhibit only a slight deformation at the center and at the edge. The six-point star-shaped islands, on the other hand, exhibit centrosymmetric, cyclic, mirror-twin boundaries, based on dark-field (DF) TEM measurements [21].

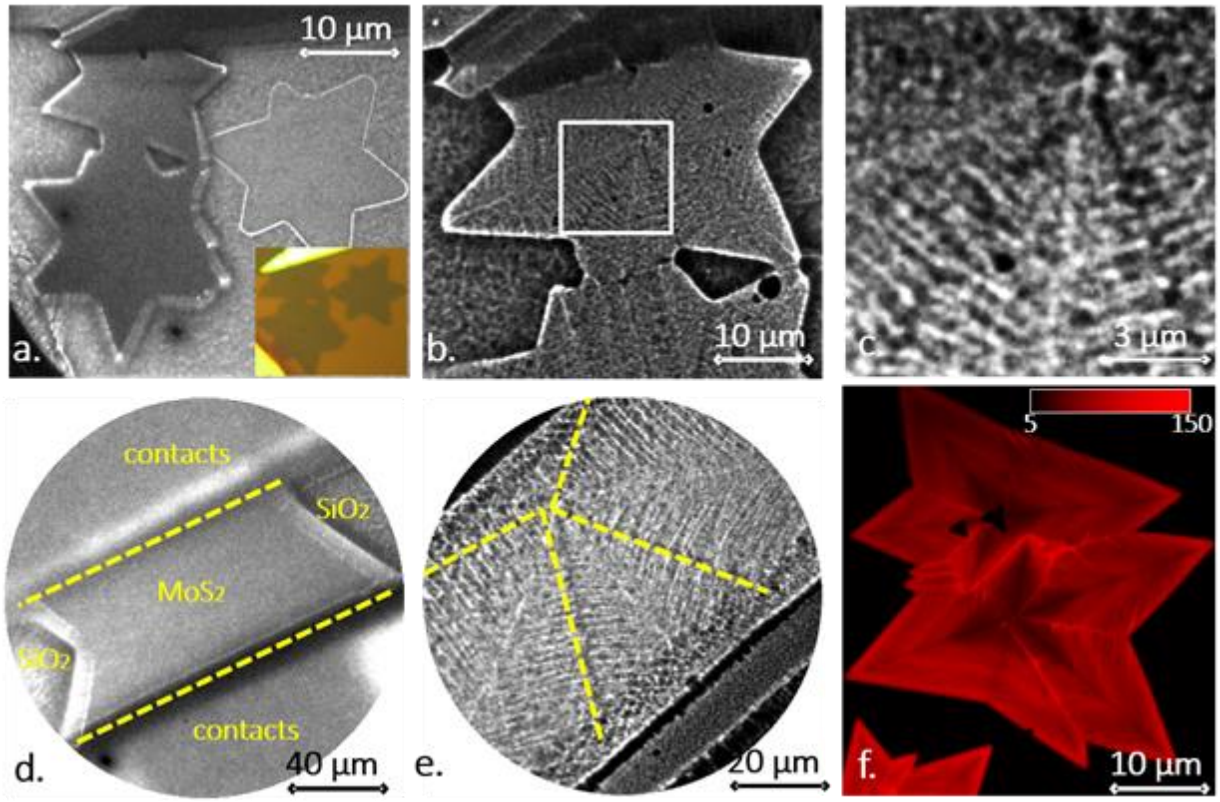

Figure 3.2 CVD MoS_2 on SiO_2 (a), (d) LEEM image of CVD multi-domain MoS_2 stars on SiO_2. In (a), two stars to the left were grounded by Au/Cr/Al contacts, as shown in the optical microscopy inset. As can be seen, however, the persistent onset of charging quickly leads to blurring of the LEEM images. The star to the right which are not connected to the contacts, i.e. is not grounded, and shows weak contrast difference (except for its perimeter) compared to the SiO_2 background. (b), (e) LEEM images after potassium deposition. Potassium deposition enhances the conductivity of the gold-contacted MoS_2 and lowers its work-function. It also enhances the contrast of the MoS_2 islands and their sulfur-terminated grain boundaries, revealing a vein-like structure that extends out to the grain boundaries. The yellow dashed lines indicate the grain boundaries that separate crystalline domains. (c) zoomed-in LEEM image of the selected area in (b). (f) Photoluminescence

mapping of an asymmetric multi-domain CVD MoS_2 island of comparable size to that of the star in (d) (no potassium doping). This image shows that the vein-like structure is not due to potassium doping but is rather a unique feature of CVD MoS_2 grow on SiO_2. The electron energies used in LEEM are (a)-(c) 0.84 eV and (d)-(e) 0.06 eV.

3.4.1 LEEM on SiO_2 Supported CVD MoS_2

Our growth process did not use any form of seeded or nucleated growth. Instead, the best growth condition was obtained with fully cleaned SiO_2 substrates. The average MoS_2-island size ranged from 1 to 100μm, and was predominantly monolayer MoS_2. Most islands were uniformly 1ML in thickness, except for a few islands that exhibited a bilayer or multilayer hexagon patch located in their center region. When present, this patch was no larger than about one-tenth of the island's dimension. MEM images of CVD MoS_2 on SiO_2 are shown in Figure 3.2 (a) and 3.2 (d). In Figure 3.2 (d), a large MoS_2 star (~50 μm from side to side) is in contact with a 10-μm-wide Au grid, with a line spacing of 22.5 μm. As was the case in our experiments on exfoliated MoS_2 on SiO_2, charging effects persisted even in the presence of a metal grid, with LEEM images becoming blurred, especially near island and contact edges during extended electron exposure.

Potassium deposition, though ineffective in eliminating charging, was found to enhance the imaging of surface corrugation. Potassium was deposited until the change in the work function of MoS_2 had saturated with respect to that of the insulating SiO_2 background as monitored dynamically by MEM. Figure 2b shows a LEEM image of a star-shaped island after potassium deposition. The dark dots as marked out in Figure 3.2 (b) on the MoS_2 island are due to residue originating from the CVD process and can be removed via annealing as was confirmed by LEEM.

One of the most interesting aspects of this figure is that it reveals fine leaf-vein like topography patterns; a more detailed image of this pattern is shown in Figure 3.2 (c) and (e). To confirm that the leaf-like structure was intrinsic to the MoS_2 instead of being derived from potassium nucleation or intercalation, the amount of potassium deposited was varied; it was then found that the pattern persisted. However, after annealing the sample for two hours at 300 ^oC to remove potassium, the pattern was no longer visible. By increasing the doping level, the contrast between peaks and valleys of the leaf-like topography pattern increased, although the underlying pattern remained unchanged. This result shows clearly that the deposited potassium enhanced the contrast of our LEEM measurements for the SiO_2-supported samples. To further confirm this intrinsic vein-like micro-structure in CVD MoS_2, we performed PL mapping on a MoS_2 flake of the same origin but without any doping. The result is shown in Figure 3.2 (f). The spatial variations of the PL intensity are consistent with the micro-structure observed by LEEM on potassium doped samples. One plausible explanation for this phenomenon is that the leaf-like pattern is formed from surface strain built up during the CVD process. Surface strain is known [21][22][40] to create pentagon- and heptagon-shaped MoS_2 microstructures that are derived from hexagon MoS_2 by sulfur-site substitutions at one of the sharing Mo sites; this microstructure, with alternating 5- or 7-fold MoS_2 rings, corresponds to the recently reported Mo-oriented dislocation found in Ref. [22]. Moreover, surface strain can also create an 8-4-4 type of fold of MoS_2 rings as reported in Ref. [21].

Thus in summary, our LEEM observations show by direct imaging that the star-shaped crystals are multi-domain crystals, with crystal grain boundaries, that can be resolved through potassium doping. Though we did not perform DF-LEEM measurements here, we note that corresponding DF-TEM results can be found in Ref. [22]. This potassium dosing also reveals vein-

like surface structures, which are attributed to growth-induced strain. This observation reconciles photoluminescence measurements, which show similar nanostructures, albeit with lower resolution.

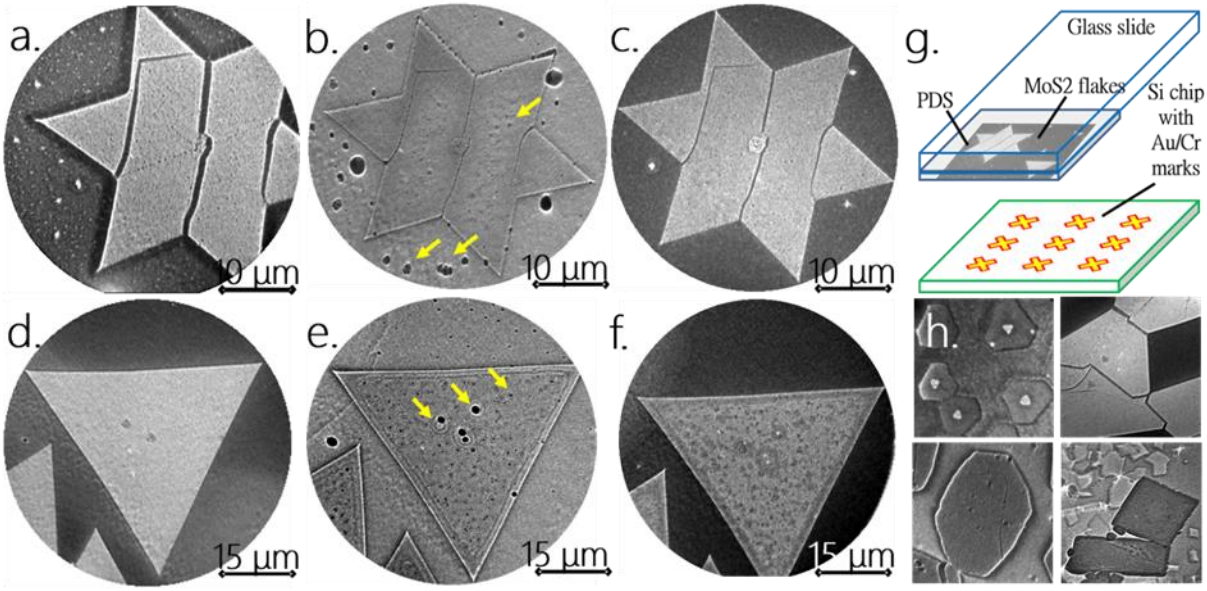

Figure 3.3 CVD MoS_2 on Si (a), (d) LEEM images of selected islands with star and triangular shapes, respectively. Sharp edges indicate they are Mo-terminated [22]. In (a), the dark lines are the cracks along the domain boundaries after the transfer process. (b), (e) LEEM images showing the islands after the first potassium doping cycle (see text); note that the reflectivity of the background Si substrate was raised by doping, indicating a lowered work function. Potassium nucleation islands (marked by the yellow arrows) form on the surface upon potassium deposition. The density of these islands increases with potassium deposition. (c), (f) LEEM images taken after potassium was removed from the surface via annealing at 160 ^{o}C for 1.5 hour and then at 350 ^{o}C for 15 min. This annealing reduces the density of the potassium islands and returns the work function to its original level prior to potassium deposition. (g) A sketch illustrating how the CVD

MoS_2 adhered on a PDS layer was transferred onto a pre-patterned Si chip. (h) LEEM images with examples of polycrystalline MoS_2 aggregates of different orientations obtained under different growth conditions. In this particular case, differently oriented domains of MoS_2 islands intersected during CVD growth, and exhibited fracturing along their faceted tilt grain boundary after sample transfer. The electron energies used in LEEM are (a) 0.9 eV (b) 1.9 eV (c) 1 eV (d) 0.54 eV (e) 2.1eV (f) 1 eV and (h) 0.58 eV.

3.4.2 LEEM on Si-Supported CVD MoS_2

As mentioned above, optimal electron-probe measurements required transfer of CVD-grown MoS_2 islands from the SiO_2/Si substrate to a native-oxide covered Si substrate. Details of the transfer process for CVD MoS_2 can be found in the Supplemental Materials [36]; after transfer, MoS_2/Si samples were annealed at 350 ^oC for 12 hours under UHV prior to measurements. Figure 3 shows LEEM measurements of the transferred MoS_2 islands; these measurements examined the structure and quality of the transferred CVD MoS_2 crystals. In Figure 3.3 (a) and (d), LEEM images of transferred MoS_2 stars and triangles show that the transfer process was successful in preserving the structures originally grown prior to the transfer step. Fractures or cracks, however, were observed along the domain boundaries of star-shaped and other multi-domain MoS_2 islands, as shown in Figure 3.3 (a) and (h). Given that these cracks are not seen in the pre-transferred CVD samples, it is assumed that that the force exerted during the stamping step of the transfer process led to the fracturing. In contrast, triangle-shaped islands did not display any fracturing, which may be explained by their single-domain nature, as confirmed by previously reported TEM measurements performed using MoS_2 on TEM support grids [21]. Besides the multi-domain nature

of some of the grown crystals, μ-LEED measurements of exfoliated and CVD-grown MoS_2 were found to show comparable crystallinity, indicating they are of similar quality. The μ-LEED measurements are discussed in detail below.

Given the value of using potassium deposition to enhance topographic features in SiO_2 supported CVD MoS_2, this same approach was used to investigate the possible presence of fine topographic features in Si supported CVD MoS_2 crystals. As in the exfoliated case, potassium dosing led to a 1.75 eV reduction of the MoS_2 work function. Unlike the case of SiO_2 supported CVD MoS_2 (see Figure 3.2), however, LEEM measurements on transferred MoS_2 stars revealed a smooth and vein-free topography, as verified under different doses of potassium. As shown in Figure 3.3 (d)-(f), LEEM measurements taken after doping with a dose equivalent to that used in Figure 3.2 (b) and (e), revealed no fine vein structure. The absence of the vein structure is attributed to a release of growth-induced crystal strain during sample transfer. On the other hand, it was observed that potassium deposition did in some cases lead to submicron nucleation on both MoS_2 islands and the Si substrate, at sites of surface structural impurities. At room temperature and under UHV conditions, it has been shown that adsorbed potassium does not intercalate with bulk MoS_2 [50], unlike the case of Cs on bulk MoS_2 [51], and that adsorbed potassium can be removed from the surface by annealing, which occurs at a temperature-dependent desorbing rate [50]. It was also found that adsorbed potassium forms 2D islands on bulk MoS_2 at low coverage and that coverage can be calibrated using changes in the work function. [50] In the present case of ML MoS_2, these potassium features nucleated preferentially around defects and/or impurities at low coverage; furthermore, we observed that the density of these nucleation increased with potassium dose.

Having investigated the effects of potassium deposition, as described above, we investigated the ability to desorb it by subjecting the sample to different annealing treatments. While annealing at 100-120 ^{o}C for 70 minutes did not produce a significant change, subsequent annealing of the sample at 150 ^{o}C for 30 minutes decreased the density of potassium nucleation, as shown in Figure 3.3 (c) and 3f. In addition, LEEM measurements of a star-shaped MoS_2 island after annealing revealed a clean crystal with well-defined edges, while in the case of a triangle-shaped MoS_2 island additional annealing at 350 ^{o}C for 12 hours was used to obtain a cleaner triangle-shaped MoS_2 island, with little to no evidence of potassium. Thus, potassium deposition appears to be a non-destructive and reversible technique for enhancing the study of monolayer MoS_2 using electron probe based instruments.

To summarize our observations in this section, LEEM measurements enable examination of the 0.5 µm-scale structure of transferred CVD grown MoS_2. In addition, these measurements revealed occasional fracturing of multi-domain crystals, which was observed to occur along grain boundaries. In contrast to as-grown, CVD MoS_2 supported by thick SiO_2/Si, transferred CVD MoS_2 does not exhibit a vein-like surface structure, which suggests that growth-induced strain is released upon transfer. As in the above cases, potassium deposition is a useful diagnostic technique in enhancing contrast, because it preferentially nucleates at impurity and defect sites, and as shown in this section, is also non-destructive and reversible.

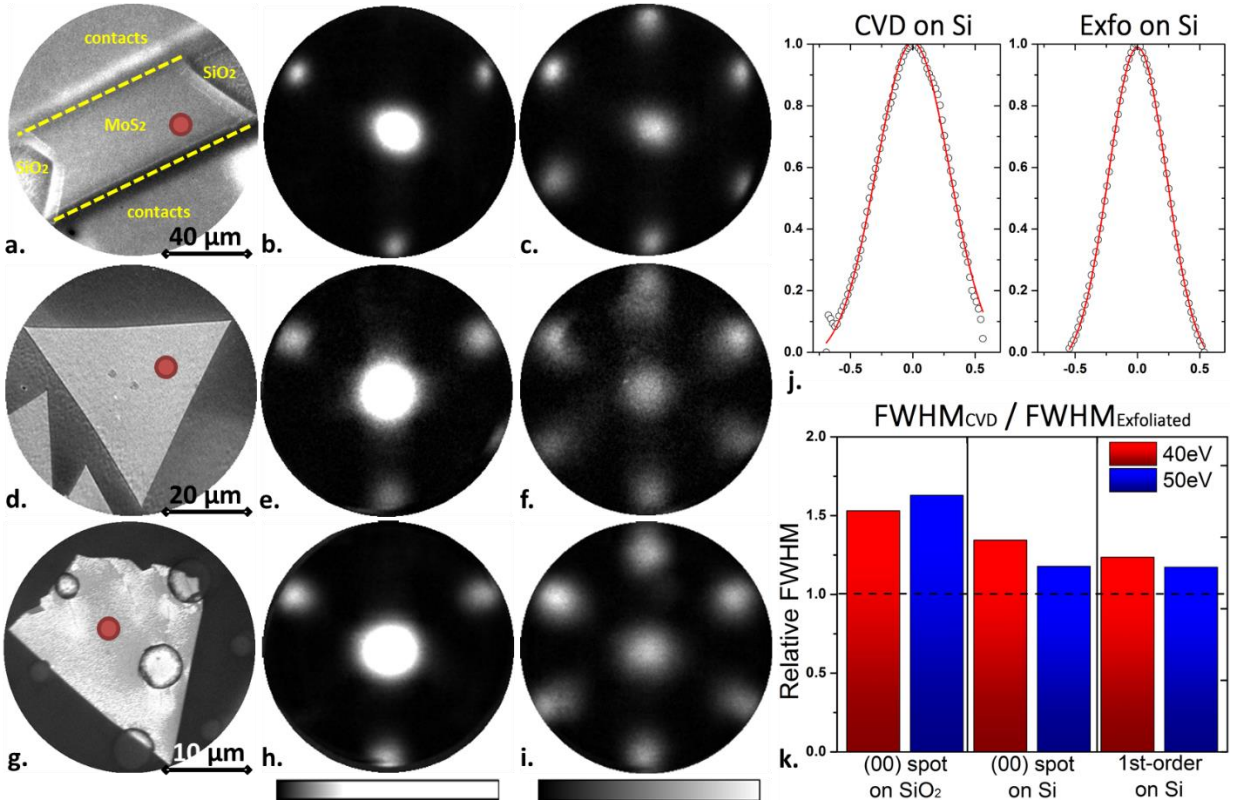

Figure 3.4 Comparison of 1ML MoS_2 using μ-LEED (a)-(c) CVD MoS_2 on SiO_2, (d)-(f) CVD MoS_2 transferred onto native-oxide terminated silicon, (g)-(i) exfoliated and transferred onto native oxide terminated silicon. (a), (d), (g) LEEM images at energy 0.06 eV, 0.46 eV, and 5 eV respectively. (b), (e), (h) corresponding LEED patterns at 40 eV electron energy. (c), (f), (i) LEED at 50 eV. The LEED pattern shows transitions between 3- and 6-fold symmetry at different electron energies. Also, the (00) LEED spot widths for (d) and (g) are comparable. (j) Intensity-normalized line profile of the (00) LEED spot of CVD and exfoliated MoS_2 on Si; horizontal axis units are in $Å^{-1}$. (k) Comparison between pre-transferred MoS_2 on SiO_2 and post-transferred MoS_2 on Si for two different energies. The relative FWHM values are derived from the (00) and the first order spots of the CVD MoS_2 divided by that of exfoliated MoS_2 on the same substrate.

3.4.3 LEED on CVD MoS_2

The crystalline structure of CVD MoS_2 was investigated using μ-LEED measurements on our two types of substrates, as shown in Figure 3.4. As μ-LEED is sensitive to crystal deformation on length scales from ~20 nm to interatomic distances, it complements real-space images by providing additional information about surface deformation at very short length scales, i.e. ~10 nm or less. Figure 3.4 (a)-(c) show measurements on one domain of an electrically contacted multi-domain star-shaped CVD-grown crystal. LEED measurements alternated between three-fold and six-fold symmetric patterns with increasing electron energies [49]. The alternation between three- and six-fold diffraction symmetry corresponds to the LEED beam probing more than the top atomic layer. A complete explanation, however, would require application of LEED multi-scattering theory over the electron probing depth, which is beyond the scope of the discussion here.

As shown in Figure 3.4 (d)-(f), LEED patterns taken from transferred CVD MoS_2 are identical to those from non-transferred CVD MoS_2 on SiO_2, except for a broadening of the spot widths. In the case of exfoliated MoS_2, a similar broadening is present after transfer to a Si substrate. In order to determine if this broadening is intrinsic to MoS_2 rather than extrinsic in nature, we undertook the following analysis. First, we analyzed the widths of the first order diffraction spots since these spots are derived solely from MoS_2 and thus minimize any possible spot-width broadening originating from the underlying substrate, which would appear in the (00) spot. Second, we analyzed the spot widths not only for the case of a transferred exfoliated substrate-supported MoS_2, but also for a transferred exfoliated *suspended* MoS_2. In this case, the MoS_2 is supported above a well, etched [39] in the Si, as shown in Figure 3.4 (g). We find similar spot widths for the supported and the suspended case, which leads us to attribute the spot width broadening post-transfer to primarily intrinsic factors. Although the exact origin of this spot

broadening is unknown at this time, given that it is apparently intrinsic to transferred MoS_2, per the above observations, it appears to be rooted in the transfer process.

Figure 3.4 (g)-(i) show the exfoliated, transferred-to-Si, 1ML, single-crystal MoS_2, which served as a reference for comparison with transferred-to-Si, CVD MoS_2. The LEED spot width is comparable for both the transferred exfoliated and the transferred CVD MoS_2, indicating that the sample quality of CVD MoS_2 islands, including surface quality and crystallinity, is comparable to exfoliated crystals. To better support this statement, a comparison of the full-width at half-maximum (FWHM) of the LEED (00) spot and first-order diffraction spots, as determined by Gaussian fitting after intensity normalization and detector background-signal removal, was performed. An example of this fitting is shown in Figure 3.4 (f), and a comparison of the FWHM of CVD and exfoliated MoS_2 at two different electron energies is shown in Figure 3.4 (k). Before transfer, the CVD grown MoS_2 has a larger FWHM relative to the pre-transferred exfoliated MoS_2, which corresponds to a rougher surface and is presumably due to the strain-induced wrinkles as shown in Figure 3.2. Upon transfer to a Si substrate, however, the strain-induced vein-like wrinkles are no longer present, as noted above, and hence, result in a comparable FWHM between transferred CVD and transferred exfoliated MoS_2. This supports our real-space LEEM measurements in which CVD grown MoS_2 appeared quite similar in quality to exfoliated MoS_2. Thus, our μ-LEED measurements confirmed the structural integrity of as-grown CVD and transferred CVD MoS_2, and enabled the determination of the crystal domain orientations. More importantly, these μ-LEED measurements show that CVD-grown MoS_2 is of comparable quality to exfoliated MoS_2.

3.5 Conclusion

In this work, the surface morphology and structural quality of ultrathin MoS_2 flakes originating from mechanical exfoliation and CVD growth were examined and compared using LEEM and μ-LEED. A major experimental issue for our measurements was sample charging and surface corrugation. The charging was eliminated by transferring MoS_2 crystals to a native-oxide covered Si wafer, a procedure which was compatible with our LEEM and LEED measurements. In addition, surface doping techniques by an alkali metal were crucial for these MoS_2 studies. These electron-probe measurements enabled detailed surface structural characterization and added complementary insight to those obtained earlier from Raman and PL measurements.[7][8] In particular, *real-space* probing by LEEM in conjunction with *k-space* probing by μ-LEED show that CVD-grown MoS_2 single crystals have comparable crystal quality to that of exfoliated MoS_2. In addition, our results have also shown that as-grown CVD MoS_2 sample islands have a fine vein-like or rippled structure, as revealed via potassium deposition; this leaf-like morphology is lost after sample transfer to a silicon substrate. We attribute this structure to strain fields formed during CVD growth. Our observations reported here are an important step toward a broader understanding of MoS_2 surface morphology on different substrates and establishing strategies for MoS_2 synthesis.

3.6 References

[1] Novoselov, K. S. "Nobel lecture: Graphene: Materials in the flatland." *Reviews of Modern Physics* 83, no. 3 (2011): 837.

[2] Mak, Kin Fai, Keliang He, Changgu Lee, Gwan Hyoung Lee, James Hone, Tony F. Heinz, and Jie Shan. "Tightly bound trions in monolayer MoS_2." *Nature materials* 12, no. 3 (2013): 207-211.

[3] Ross, Jason S., Sanfeng Wu, Hongyi Yu, Nirmal J. Ghimire, Aaron M. Jones, Grant Aivazian, Jiaqiang Yan et al. "Electrical control of neutral and charged excitons in a monolayer semiconductor." *Nature communications* 4 (2013): 1474.

[4] Cheiwchanchamnangij, Tawinan, and Walter RL Lambrecht. "Quasiparticle band structure calculation of monolayer, bilayer, and bulk MoS_2." *Physical Review B* 85, no. 20 (2012): 205302.

[5] Ramasubramaniam, Ashwin. "Large excitonic effects in monolayers of molybdenum and tungsten dichalcogenides." *Physical Review B* 86, no. 11 (2012): 115409.

[6] Jin, Wencan, Po-Chun Yeh, Nader Zaki, Datong Zhang, Jerzy T. Sadowski, Abdullah Al-Mahboob, Arend M. van Der Zande et al. "Direct measurement of the thickness-dependent electronic band structure of MoS_2 using angle-resolved photoemission spectroscopy." *Physical review letters* 111, no. 10 (2013): 106801.

[7] Mak, Kin Fai, Changgu Lee, James Hone, Jie Shan, and Tony F. Heinz. "Atomically thin MoS_2: a new direct-gap semiconductor." *Physical Review Letters* 105, no. 13 (2010): 136805.

[8] Splendiani, Andrea, Liang Sun, Yuanbo Zhang, Tianshu Li, Jonghwan Kim, Chi-Yung Chim, Giulia Galli, and Feng Wang. "Emerging photoluminescence in monolayer MoS_2." *Nano letters* 10, no. 4 (2010): 1271-1275.

[9] Mak, Kin Fai, Keliang He, Jie Shan, and Tony F. Heinz. "Control of valley polarization in monolayer MoS_2 by optical helicity." *Nature nanotechnology* 7, no. 8 (2012): 494-498.

[10] Zeng, Hualing, Junfeng Dai, Wang Yao, Di Xiao, and Xiaodong Cui. "Valley polarization in MoS_2 monolayers by optical pumping." *Nature nanotechnology*7, no. 8 (2012): 490-493.

[11] Cao, Ting, Gang Wang, Wenpeng Han, Huiqi Ye, Chuanrui Zhu, Junren Shi, Qian Niu et al. "Valley-selective circular dichroism of monolayer molybdenum disulphide." *Nature communications* 3 (2012): 887.

[12] Li, Yilei, Yi Rao, Kin Fai Mak, Yumeng You, Shuyuan Wang, Cory R. Dean, and Tony F. Heinz. "Probing symmetry properties of few-layer MoS2 and h-BN by optical second-harmonic generation." *Nano letters* 13, no. 7 (2013): 3329-3333.

[13] Brontvein, Olga, Daniel G. Stroppa, Ronit Popovitz-Biro, Ana Albu-Yaron, Moshe Levy, Daniel Feuerman, Lothar Houben, Reshef Tenne, and Jeffrey M. Gordon. "New high-

temperature Pb-catalyzed synthesis of inorganic nanotubes." *Journal of the American Chemical Society* 134, no. 39 (2012): 16379-16386.

[14] Li, Yanguang, Hailiang Wang, Liming Xie, Yongye Liang, Guosong Hong, and Hongjie Dai. "MoS_2 nanoparticles grown on graphene: an advanced catalyst for the hydrogen evolution reaction." *Journal of the American Chemical Society*133, no. 19 (2011): 7296-7299.

[15] Eda, Goki, Hisato Yamaguchi, Damien Voiry, Takeshi Fujita, Mingwei Chen, and Manish Chhowalla. "Photoluminescence from chemically exfoliated MoS_2."*Nano letters* 11, no. 12 (2011): 5111-5116.

[16] Botello-Méndez, Andrés Rafael, F. Lopez-Urias, M. Terrones, and H. Terrones. "Metallic and ferromagnetic edges in molybdenum disulfide nanoribbons." *Nanotechnology* 20, no. 32 (2009): 325703.

[17] Lee, Yi-Hsien, Xin-Quan Zhang, Wenjing Zhang, Mu-Tung Chang, Cheng-Te Lin, Kai-Di Chang, Ya-Chu Yu et al. "Synthesis of Large-Area MoS_2 Atomic Layers with Chemical Vapor Deposition." *Advanced Materials* 24, no. 17 (2012): 2320-2325.

[18] Zhan, Yongjie, Zheng Liu, Sina Najmaei, Pulickel M. Ajayan, and Jun Lou. "Large-Area Vapor-Phase Growth and Characterization of MoS_2 Atomic Layers on a SiO_2 Substrate." *Small* 8, no. 7 (2012): 966-971.

[19] Liu, Keng-Ku, Wenjing Zhang, Yi-Hsien Lee, Yu-Chuan Lin, Mu-Tung Chang, Ching-Yuan Su, Chia-Seng Chang et al. "Growth of large-area and highly crystalline MoS_2 thin layers on insulating substrates." *Nano letters* 12, no. 3 (2012): 1538-1544.

[20] Shi, Yumeng, Wu Zhou, Ang-Yu Lu, Wenjing Fang, Yi-Hsien Lee, Allen Long Hsu, Soo Min Kim et al. "Van der Waals epitaxy of MoS_2 layers using graphene as growth templates." *Nano letters* 12, no. 6 (2012): 2784-2791.

[21] van der Zande, Arend M., Pinshane Y. Huang, Daniel A. Chenet, Timothy C. Berkelbach, YuMeng You, Gwan-Hyoung Lee, Tony F. Heinz, David R. Reichman, David A. Muller, and James C. Hone. "Grains and grain boundaries in highly crystalline monolayer molybdenum disulphide." *Nature materials* 12, no. 6 (2013): 554-561.

[22] Najmaei, Sina, Zheng Liu, Wu Zhou, Xiaolong Zou, Gang Shi, Sidong Lei, Boris I. Yakobson, Juan-Carlos Idrobo, Pulickel M. Ajayan, and Jun Lou. "Vapour phase growth and grain boundary structure of molybdenum disulphide atomic layers." *Nature materials* 12, no. 8 (2013): 754-759.

[23] Radisavljevic, Branimir, Aleksandra Radenovic, Jacopo Brivio, V. Giacometti, and A. Kis. "Single-layer MoS_2 transistors." *Nature nanotechnology* 6, no. 3 (2011): 147-150.

[24] Dean, C. R., A. F. Young, I. Meric, C. Lee, L. Wang, S. Sorgenfrei, K. Watanabe et al. "Boron nitride substrates for high-quality graphene electronics."*Nature nanotechnology* 5, no. 10 (2010): 722-726.

[25] Britnell, L., R. V. Gorbachev, R. Jalil, B. D. Belle, F. Schedin, A. Mishchenko, T. Georgiou et al. "Field-effect tunneling transistor based on vertical graphene heterostructures." *Science* 335, no. 6071 (2012): 947-950.

[26] Yin, Zongyou, Hai Li, Hong Li, Lin Jiang, Yumeng Shi, Yinghui Sun, Gang Lu, Qing Zhang, Xiaodong Chen, and Hua Zhang. "Single-layer MoS_2 phototransistors." *ACS nano* 6, no. 1 (2011): 74-80.

[27] Fontana, Marcio, Tristan Deppe, Anthony K. Boyd, Mohamed Rinzan, Amy Y. Liu, Makarand Paranjape, and Paola Barbara. "Electron-hole transport and photovoltaic effect in gated MoS_2 Schottky junctions." *Scientific reports* 3 (2013).

[28] Schmidt, Th, S. Heun, J. Slezak, J. Diaz, K. C. Prince, G. Lilienkamp, and E. Bauer. "SPELEEM: combining LEEM and spectroscopic imaging." *Surface Review and Letters* 5, no. 06 (1998): 1287-1296.

[29] Bauer, E. "Low energy electron microscopy." *Reports on Progress in Physics*57, no. 9 (1994): 895.

[30] Flege, J. I., E. Vescovo, G. Nintzel, L. H. Lewis, S. Hulbert, and P. Sutter. "A new soft X-ray photoemission microscopy beamline at the National Synchrotron Light Source." *Nuclear Instruments and Methods in Physics Research Section B: Beam Interactions with Materials and Atoms* 261, no. 1 (2007): 855-858.

[31] Sutter, Peter, and Eli Sutter. "Microscopy of graphene growth, processing, and properties." *Advanced Functional Materials* 23, no. 20 (2013): 2617-2634.

[32] Ohta, Taisuke, Aaron Bostwick, Thomas Seyller, Karsten Horn, and Eli Rotenberg. "Controlling the electronic structure of bilayer graphene." *Science*313, no. 5789 (2006): 951-954.

[33] Chen, J-H., C. Jang, S. Adam, M. S. Fuhrer, E. D. Williams, and Masa Ishigami. "Charged-impurity scattering in graphene." *Nature Physics* 4, no. 5 (2008): 377-381.

[34] Choi, Min Sup, Gwan-Hyoung Lee, Young-Jun Yu, Dae-Yeong Lee, Seung Hwan Lee, Philip Kim, James Hone, and Won Jong Yoo. "Controlled charge trapping by molybdenum disulphide and graphene in ultrathin heterostructured memory devices." *Nature communications* 4 (2013): 1624.

[35] Britnell, Líam, R. M. Ribeiro, A. Eckmann, R. Jalil, B. D. Belle, A. Mishchenko, Y-J. Kim et al. "Strong light-matter interactions in heterostructures of atomically thin films." *Science* 340, no. 6138 (2013): 1311-1314.

[36] See chapter 2.5, sample preparation session, for wet transfer process via PMMA/PVA layer for exfoliated MoS_2 and dry transfer process via PDS for CVD MoS_2.

[37] Novoselov, K. S., D. Jiang, F. Schedin, T. J. Booth, V. V. Khotkevich, S. V. Morozov, and A. K. Geim. "Two-dimensional atomic crystals." *Proceedings of the National Academy of Sciences of the United States of America* 102, no. 30 (2005): 10451-10453.

[38] Ayari, Anthony, Enrique Cobas, Ololade Ogundadegbe, and Michael S. Fuhrer. "Realization and electrical characterization of ultrathin crystals of layered transition-metal dichalcogenides." *Journal of applied physics* 101, no. 1 (2007): 014507-014507.

[39] Locatelli, Andrea, Kevin R. Knox, Dean Cvetko, Tevfik Onur Mentes, Miguel Angel Nino, Shancai Wang, Mehmet B. Yilmaz, Philip Kim, Richard M. Osgood Jr, and Alberto Morgante. "Corrugation in exfoliated graphene: an electron microscopy and diffraction study." *ACS nano* 4, no. 8 (2010): 4879-4889.

[40] Sadowski, Jerzy T. "Pentacene growth on 3-aminopropyltrimethoxysilane modified silicon dioxide." *Optical Materials* 34, no. 10 (2012): 1635-1638.

[41] Godehardt, Reinhold. "Mirror electron microscopy." *Advances in Imaging and Electron Physics* 94 (1995): 81-150.

[42] Griffith, O. Hayes, Karen K. Hedberg, Denis Desloge, and Gertrude F. Rempfer. "Low-energy electron microscopy (LEEM) and mirror electron microscopy (MEM) of biological specimens: Preliminary results with a novel beam separating system." *Journal of microscopy* 168, no. 3 (1992): 249-258.

[43] Luk'yanov, A. E., G. V. Spivak, and R. S. Gvozdover. "Mirror electron microscopy." *Soviet Physics Uspekhi* 16, no. 4 (1974): 529.

[44] See chapter 3.3.3, potassium deposition session, for MEM imaging mode in LEEM and surface potential monitoring.

[45] Seah, M. P., and W. A. Dench. "Quantitative electron spectroscopy of surfaces: a standard data base for electron inelastic mean free paths in solids." *Surface and interface analysis* 1, no. 1 (1979): 2-11.

[46] By using the mean free path formula for compounds in ref. [45] and the thickness of MoS_2 = 0.72nm from ref. [16], the mean free path for ML MoS_2 is ~ 5.17456Å .

[47] Jiang, Jin-Wu, Zenan Qi, Harold S. Park, and Timon Rabczuk. "Elastic bending modulus of single-layer molybdenum disulfide (MoS_2): finite thickness effect."*Nanotechnology* 24, no. 43 (2013): 435705.

[48] Feenstra, R. M., N. Srivastava, Qin Gao, M. Widom, Bogdan Diaconescu, Taisuke Ohta, G. L. Kellogg, J. T. Robinson, and I. V. Vlassiouk. "Low-energy electron reflectivity from graphene." *Physical Review B* 87, no. 4 (2013): 041406.

[49] Jona, F., J. A. Strozier Jr, and W. S. Yang. "Low-energy electron diffraction for surface structure analysis." *Reports on Progress in Physics* 45, no. 5 (1982): 527.

[50] Papageorgopoulos, C., M. Kamaratos, S. Kennou, and D. Vlachos. "Coadsorption of K and O 2 on MoS_2 (0001)." *Surface science* 277, no. 3 (1992): 273-281.

[51] Kennou, S., S. Ladas, and C. Papageorgopoulos. "The behavior of Cs on MoS_2." *Surface Science* 152 (1985): 1213-1221.

[52] Benameur, M. M., B. Radisavljevic, J. S. Heron, S. Sahoo, H. Berger, and A. Kis. "Visibility of dichalcogenide nanolayers." *Nanotechnology* 22, no. 12 (2011): 125706.

[53] Van Hove, M. A., S. Y. Tong, and M. H. Elconin. "Surface structure refinements of 2H-MoS_2, 2H-$NbSe_2$ and W(100)p(2×1)-O via new reliability factors for surface crystallography." *Surface Science* 64, no. 1 (1977): 85-95.

Chapter 4

Direct Measurement of the Thickness-Dependent Electronic Band Structure of MoS_2 Using ARPES

In this chapter, we report on the evolution of the thickness-dependent electronic band structure of the two-dimensional layered-dichalcogenide molybdenum disulfide (MoS_2). Micrometer-scale angle-resolved photoemission spectroscopy of mechanically exfoliated and chemical-vapor-deposition-grown crystals provides direct evidence for the shifting of the valence band maximum from the $\bar{\Gamma}$ point to the $\bar{K}$ point, for the case of MoS_2 having more than one layer, to the case of single-layer MoS_2, as predicted by density functional theory. This evolution of the electronic structure from bulk to few-layers to monolayer MoS_2 had earlier been predicted to arise from quantum confinement. Furthermore, one of the consequences of this progression in the electronic structure is the dramatic increase in the hole effective-mass, in going from bulk to monolayer MoS_2 at its Brillouin zone center, which is known as the cause for the decreased carrier mobility of the monolayer form compared to that of bulk MoS_2.

4.1 Introduction

Molybdenum disulfide (MoS_2) is a layered transition-metal dichalcogenide [1] that can be fabricated as an atomically thin two-dimensional (2D) crystal [2]. The fabrication relies on the fact that S-Mo-S slabs in bulk MoS_2 have a layered 2H crystal structure, and are weakly bonded by van der Waals (vdW) interactions [3]. After cleaving, monolayer MoS_2 consists of a single layer of Mo atoms sandwiched between two layers of S atoms in a trigonal prismatic structure [4][5]. Our interest in monolayer MoS_2 stems from the following: (i) There is transition from an indirect to a direct bandgap in going from multi-layer to monolayer crystal due to the missing interlayer interaction in monolayer form [6], and (ii) the strong spin-orbit-coupling induced split valence bands (~160 meV [7][8]) due to broken inversion symmetry, which makes MoS_2 interesting for spin-physics exploration. Properties (i) and (ii) lead to potential applications in nanoelectronic devices [9] and spintronics applications, respectively. In addition, both properties have been predicted with density functional theory (DFT) calculations [7][10] and indirectly demonstrated using photoluminescence [11][12] and Raman spectroscopy [13]. The electronic structure of bulk MoS_2 has been comprehensively studied by both theory and experiments [14-16]. Despite the myriad of experiments on single- and few-layer MoS_2, as well as their distinctive and potential applications, direct experimental determination of the electronic structure of these single-to-few-layer MoS_2 crystals has, thus far, been lacking.

In this work, we directly measure the electronic band structure of exfoliated monolayer, bilayer, and trilayer MoS_2, and compare them to bulk MoS_2 bands and the corresponding theoretically predicted bands, using micrometer-scale angle-resolved photoemission spectroscopy

(micro-ARPES). The band structure of chemical vapor deposition (CVD)-grown monolayer MoS_2 crystals are also measured and compared to the exfoliated monolayer. The main features of the MoS_2 band structure originate from Mo 4*d* states and are in good agreement with results of theoretical calculations. Our findings show the following: First, the valence bands of monolayer MoS_2, particularly the low-binding-energy bands, are distinctly different from those of bulk MoS_2 in that the valence band maximum (VBM) of a monolayer is located at $\overline{K}$ of the first Brillouin zone (BZ), see Fig. 1(e), rather than at $\overline{\Gamma}$, as is the case in bilayer and thicker MoS_2 crystals. Second, the uppermost valence band of both exfoliated and CVD-grown monolayer MoS_2 is compressed in energy in comparison with the calculated band, an effect, which we tentatively attribute to interactions with the substrate. The degree of compression in CVD-grown MoS_2 is larger than that in exfoliated monolayer MoS_2, likely due to defects, doping, or stress. Third, the uppermost valence band near $\overline{K}$ of monolayer MoS_2 is less dispersive than that of the bulk, which leads to a striking increase in the hole effective-mass and, hence, the reduced carrier mobility of the monolayer compared to bulk MoS_2.

4.2 Experimental Methods

4.2.1 Sample Preparation

Large ultrathin MoS_2 flakes (~10×15 μm^2) were fabricated on Si wafers from commercial single-crystal MoS_2 bulk samples (SPI Supplies, USA) using mechanical exfoliation [2], with poly(methyl-methacrylate) (PMMA) and polyvinyl alcohol (PVA) overlayers. Monolayer, bilayer, and trilayer MoS_2 were first identified by optical contrast as shown in Figure 4.1 (a)-(c) and independently confirmed by Raman and photoluminescence spectra [6][17]. The selected MoS_2

flakes were subsequently transferred, using a PMMA membrane as the transfer medium [18], onto a moderately doped silicon substrate, covered with a full native-oxide layer. Bulk MoS_2 flakes were also transferred onto the substrate in this process. Besides exfoliation-derived MoS_2, high-quality crystals of monolayer MoS_2, as grown by CVD with grain sizes up to 120 μm [19], were also transferred onto the same substrate. Gold grid marks written on the substrate were used to locate the target MoS_2 flakes. A sketch of the sample configuration is shown in Figure 4.1 (d). The native-oxide-covered Si substrates proved effective at preventing charging that is present with a thicker SiO_2 substrate, as reported by Han *et al.* [20]. In this case, residual photoionization charge apparently tunnels through the native-oxide layer making photoemission electron microscopy (PEEM) and μ-ARPES measurements possible.

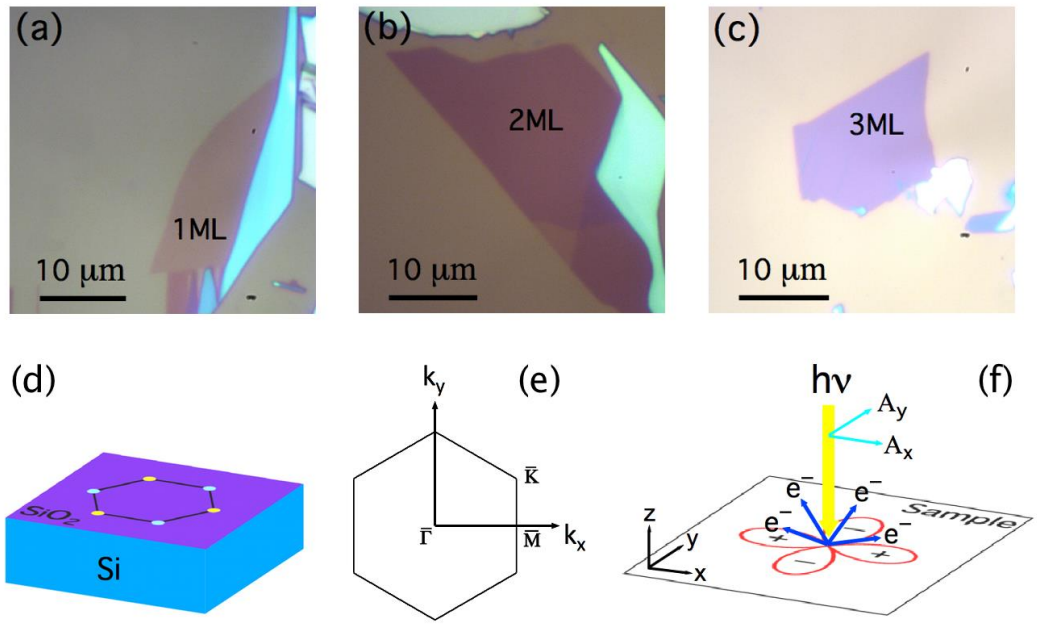

Figure 4.1 (a)-(c) Optical microscope images of the exfoliated MoS_2 samples. The background is from the Si/SiO_2 substrate with PMMA overlayer and the areas with different contrast are from MoS_2 flakes of different thickness. The areas that are labeled as "1ML", "2ML", and "3ML"

correspond to monolayer, bilayer, and trilayer, respectively. (d) Sketch of sample configuration. Monolayer MoS_2 (honeycomb lattice) was transferred onto silicon chip (blue) with native oxide (purple). (e) First Brillouin zone of monolayer MoS_2. (f) Schematic representation of the photoemission process and configuration. Normal incident light excites electrons from $d_{x^2-y^2}$ orbital of the sample.

4.2.2 Instrumentation

Our measurements were performed on the Spectroscopic Photoemission and Low Energy Electron Microscope (SPELEEM) system at the National Synchrotron Light Source (NSLS) beamline U5UA [21][22]. Prior to the measurements, the sample was annealed for 6 hours at 350℃ under ultrahigh vacuum (UHV) to degas and remove contaminants and residual PMMA before transfer into the SPELEEM chamber. In one instance involving CVD MoS_2, potassium was deposited on the sample surface *in-situ* using a commercial alkali metal dispenser (SEAS Getters) to eliminate surface charging, while monitoring the associated change in the work function using LEEM [23]. The deposition was stopped when the workfunction shift had saturated. Subsequently, the potassium was removed from the surface prior to measurements by annealing at 100℃ for 1hr. Low energy electron microscopy (LEEM) was used to locate the macroscopic MoS_2 flakes of interest. Each selected MoS_2 flake was characterized with PEEM (spatial resolution < 50 nm) and micro-spot low energy electron diffraction (micro-LEED) to investigate surface morphology and crystalline structure, respectively. μ-ARPES data were collected using synchrotron ultraviolet radiation ($h\nu$ = 42 eV) within a 2-5 μm diameter spot, following a procedure described in details in Refs. [22][24]. A depiction of the ARPES process and configuration is shown in Figure 4.1 (f).

Linear-polarized light is incident at an angle normal to the sample surface. The inelastic mean free path of the emitted electrons at ~40 eV is estimated to be ~5 Å [25], which is comparable to the thickness of monolayer MoS_2 (~6.5Å) [6][13]. Therefore, the photoelectron signal from the substrate is much weaker than that from MoS_2. Electronic band structure measurements were carried out at room temperature *in-situ* with an energy resolution of ~200 meV. In particular, the energy-filtered photoelectron angular distributions in reciprocal space were measured using the electron optics and detector system of the SPELEEM instrument. The raw data contained photoelectron *k*-space measurements for kinetic energies ranging from 30 eV to 40 eV at an energy step of 0.1 eV. Projections along high-symmetry directions including $\overline{K}-\overline{\Gamma}-\overline{K}$ and $\overline{M}-\overline{\Gamma}-\overline{M}$ in the Brillouin zone were used to generate band dispersion plots.

4.3 Experimental Results

4.3.1 Photoionization Cross-Section, Orbitals, and Fermi Cutoff

The measured valence bands of MoS_2 are derived from hybridization of the Mo 4*d* and S 3*p* orbitals [4][14]. As shown in Figure 4.2 (a), the calculated atomic photoionization cross section of the Mo 4*d* and S 3*p* subshell as a function of photon energy [26] demonstrates that our incident photon energy of 42 eV is near the Cooper minimum of the S 3*p* orbital. Therefore, the dominant features probed here are derived from Mo 4*d* orbital contributions. Moreover, in our normal incidence ARPES configuration, the vector potential associated with the incident light can be expressed as:

$$\mathbf{A} = (A_x, A_y, 0)$$

where A_x and A_y are the in-plane components. The photoemission state-transition matrix element is given by:

$$M_{if} = \langle f|\mathbf{A}\cdot\mathbf{r}|i\rangle$$

where $\mathbf{r}$ is the position operator, and $|i\rangle$ and $|f\rangle$ denote the initial and final states, respectively [27]. In such a geometry, the z-axis contribution of M_{if} vanishes since $A_z = 0$, and therefore, the spectral intensity of in-plane states including $d_{x^2-y^2}$ and d_{xy} orbitals are stronger than that of the out-of-plane states such as d_{z^2}, d_{xz}, and d_{yz} orbitals, which is in agreement with our experimental results.

As seen in Figure 4.2 (b), angle-integrated photoemission spectra of exfoliated monolayer MoS_2 were acquired along high-symmetry directions and over the full BZ. These spectra, which were rescaled relative to the intensity at 5 eV binding energy, show a cut-off feature approximately 1.75 eV above the VBM. The constant energy planes around the cut-off do not show any coherent structure in momentum space, from which we rule out this feature being derived from a non-amorphous region of the substrate. Instead we ascribe this feature to the Fermi cut-off and fit it with a Fermi-Dirac distribution. The value of Fermi level (E_F) was also independently confirmed by measuring the photoemission spectrum of the gold grid marks on the substrate and by assuming a lack of a Schottky barrier at the Au/substrate interface. Since the bandgap of monolayer MoS_2 is ~1.9 eV, obtained both by calculations and experiments [11][28], this measurement also indicates that our sample is heavily electron-doped, possibly by impurities acquired during the transfer process. The strong peaks at binding energies of ~2 eV and ~4 eV, i.e. the main states probed here,

can be assigned to Mo 4*d* states, based on a partial-density-of-states decomposition calculation [28].

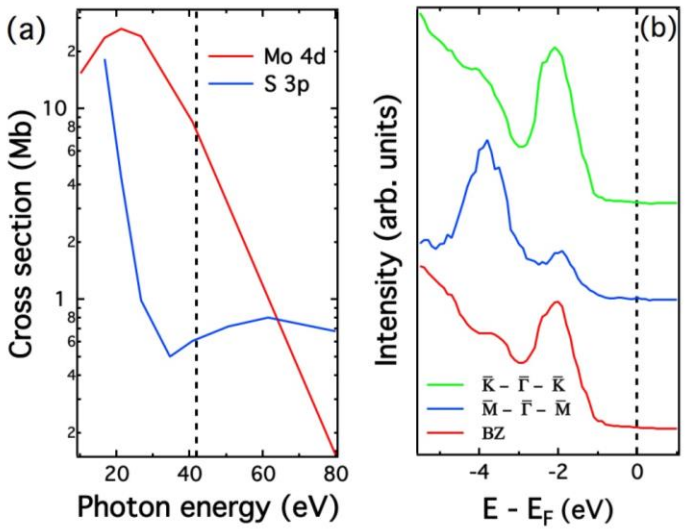

Figure 4.2 (a) Atomic photoionization cross section for Mo 4d and S 3p subshells as a function of photon energy. The dashed line marks incident photon energy of 42 eV. (b) Angle-integrated photoemission spectra of exfoliated monolayer MoS_2 extracted from high-symmetry directions ($\bar{K}-\bar{\Gamma}-\bar{K}$ and $\bar{M}-\bar{\Gamma}-\bar{M}$) of the BZ and over the whole BZ.

4.3.2 ARPES Band Mapping

Figure 4.3 provides the measured band dispersions of exfoliated monolayer MoS_2 along the $\bar{M}-\bar{\Gamma}-\bar{K}$ high-symmetry directions of the BZ. As shown in Figure 4.3 (a), the measured electronic band structure is generally in good agreement with DFT band calculations with spin-orbit interaction taken into account [7]. In the spectra the most distinct features include the VBM at $\bar{\Gamma}$ and $\bar{M}$ originating from Mo d_{z^2} orbitals, the VBM at $\bar{K}$ induced by Mo $d_{x^2-y^2}$ and d_{xy} orbitals, and a saddle point at binding energy ~4 eV, as derived from Mo $d_{x^2-y^2}$ and d_{xy} orbitals

[15][29]. These features are further displayed in the corresponding energy distribution curves (EDCs) (see Figure 4.3 (b)) and momentum distribution curves (MDCs) (see Figure 4.3 (c)). According to the above matrix-element analysis, the VBM at $\bar{\Gamma}$ has a weak intensity as expected. Other bands, which arise from S 3*p* orbitals and Mo d_{xz}, d_{yz} orbitals [15][29] are too weak to be seen due either to their small cross sections or vanishing matrix elements. Although our energy resolution does not allow us to resolve the theoretically predicted spin-orbit splitting near $\overline{K}$, it is apparent that the VBM of the top-most band is located at $\overline{K}$ instead of $\overline{\Gamma}$. A detailed analysis is shown in Figure 4.4 (a). The data in Figure 4.3, thus, provide an evidence for the indirect-to-direct bandgap transition in going from few-layer to monolayer MoS_2.

Figure 4.3 (d)-(f) show the evolution of band structure with monolayer thickness by displaying the μ-ARPES band maps of bilayer, trilayer, and bulk MoS_2, respectively. The spacing between VBM and E_F is ~1.5 eV, which indicates that our few-layer and bulk MoS_2 samples are also heavily electron-doped. A remarkable feature of these few-layer and bulk MoS_2 samples is that the VBM at $\bar{K}$ are all lower than that at $\bar{\Gamma}$. This striking difference between monolayer and few-layer and bulk MoS_2 shows clearly that the band structure changes with thickness. This change has been previously ascribed to quantum confinement. Note that in samples with thickness >1ML, vdW interactions allow coupling of the layers and thickness-dependent changes in confinement. Moreover, the VBM at $\bar{\Gamma}$ vanishes due to weak spectral intensity, which has also been reported in bulk MoS_2 experiments by Mahatha *et al.* [16]. Since this state is also derived from the Mo d_{z^2} orbital in few-layer and bulk MoS_2 [29], the weak spectral intensity has been explained as due to

the small in-plane lattice parameter of bulk MoS_2 [7], which allows for greater shielding by the S 3*p* orbitals [3], which otherwise provide the dominant contribution to the transition strength.

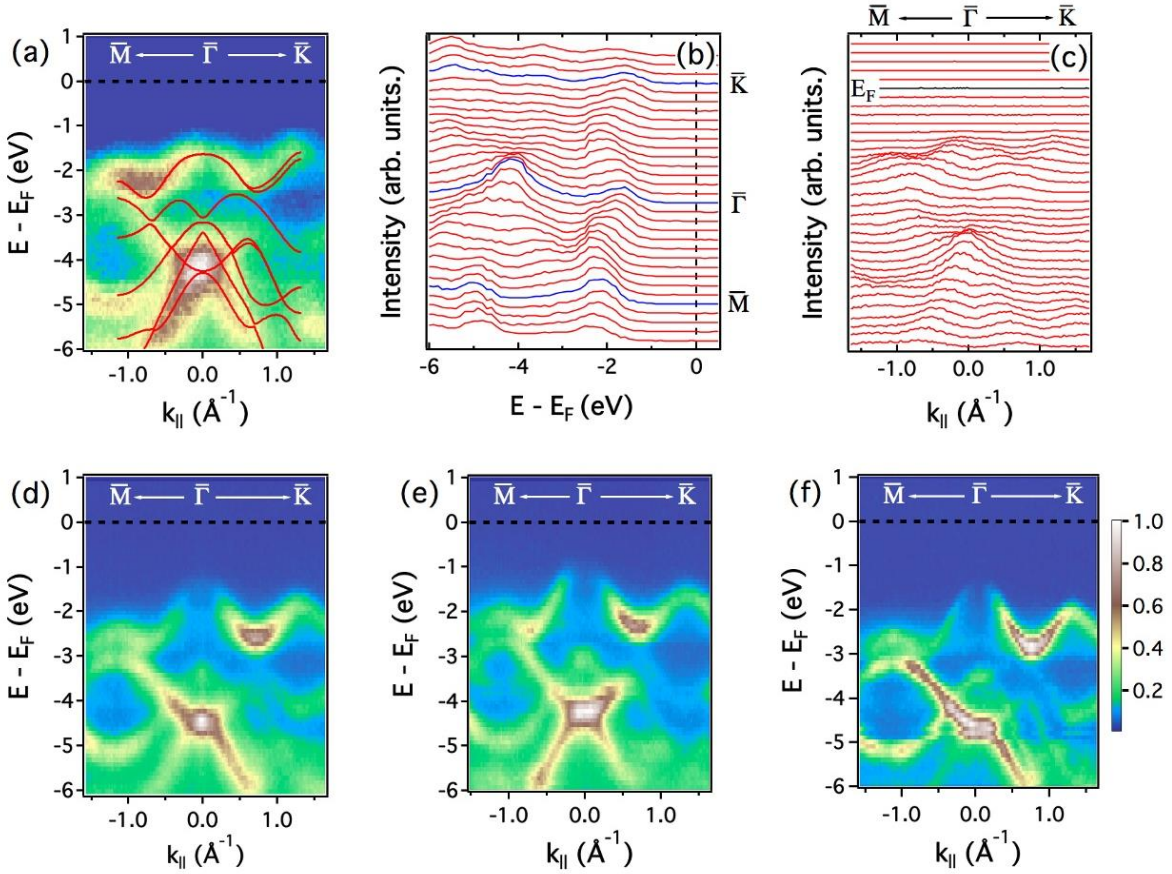

Figure 4.3 (a) ARPES band map of exfoliated monolayer MoS_2 along the $\bar{M}$– $\bar{\Gamma}$– $\bar{K}$ high symmetry lines. DFT band calculations with inclusion of spin-orbit interaction adapted from Ref. 7 (red curves) are overlaid onto it for comparison. (b)-(c) Corresponding EDCs and MDCs, respectively. (d)-(f) ARPES band maps of exfoliated bilayer, trilayer, and bulk MoS_2, respectively.

4.3.3 Second Derivative Band Analysis

To fully investigate the thickness dependence of the low-energy dispersive states, we extract the ARPES features of the uppermost valence band (UVB) along the $\bar{M}-\bar{\Gamma}-\bar{K}$ high-symmetry line by 2D-curvature analysis [30], shown in Figure 4.4 (a)-(d). The UVB of exfoliated 1-3 ML and bulk MoS_2 closely match the corresponding calculated bands. These results provide direct experimental evidence for the trend, in which the VBM at $\bar{\Gamma}$ shift upwards in energy relative to that of $\bar{K}$ as the number of layers increases. The thickness dependence of the energy difference between the VBM of $\bar{K}$ and $\bar{\Gamma}$ is further displayed in Figure 4.4 (e) and compared with theory. This evolution in band structure has been attributed to change in quantum confinement as the number of layers increases. To be specific, the VBM at $\bar{K}$, which is derived from the localized in-plane Mo $d_{x^2-y^2}$ and d_{xy} orbitals, is unlikely to be affected by the quantum confinement modifications along in z direction. By comparison, however, the VBM at $\bar{\Gamma}$, which originates from the rather delocalized out-of-plane Mo d_{z^2} orbitals and S p_z orbitals, is lowered in energy when interlayer interaction decreases in the decreasing number of layers. In addition, one important result is that we reproducibly measure a compression of the UVB in monolayer MoS_2, while the rest of the measured valence bands are identical to the computed bands. Here we define compression as $(UVB_{max}-UVB_{min})_{experiment}/(UVB_{max}-UVB_{min})_{theory}$, where UVB_{min} and UVB_{max} are the minimum and maximum values of the UVB within the $\bar{M}-\bar{\Gamma}-\bar{K}$ directions. The measured compression of the monolayer UVB is ~80%. We tentatively attribute this compression to the interaction with the substrate, as confirmed by calculations for MoS_2 on model Si substrate (see below). A second and separate striking effect is that the VBM of monolayer MoS_2 at $\bar{\Gamma}$ is relatively flat compared to its

bulk counterpart, indicating a substantially larger effective mass of holes in the monolayer. A simple parabolic fit allows us to estimate the experimental hole effective mass at $\bar{\Gamma}$ of $(2.4 \pm 0.3)m_0$ (m_0 is the electron mass) in exfoliated MoS_2, which is in approximate agreement with a theoretical prediction ($\sim 2.8\, m_0$) [31]. The same fit to the bulk band gives a value of $(0.67 \pm 0.1)m_0$, which is very close to the theoretically predicted value of $\sim 0.62\, m_0$ [31]. From bulk to monolayer MoS_2, the hole effective mass at $\bar{K}$ only slightly increases. The overall hole effective mass of monolayer MoS_2 is thus remarkably larger than that of bulk. This result evidently explains the relatively poor carrier mobility (less than $10\ \mathrm{cm}^2/\mathrm{V}\cdot\mathrm{s}$) [2][32] of monolayer MoS_2 compared to that of bulk (in the 50-200 $\mathrm{cm}^2/\mathrm{V}\cdot\mathrm{s}$ range at room temperature) [33].

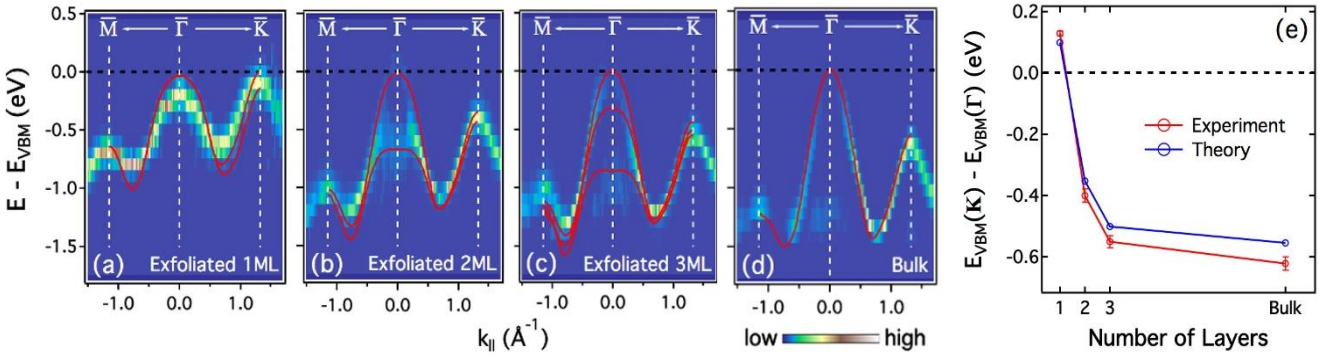

Figure 4.4 (a)-(d) 2D curvature intensity plot of the low energy valence band of exfoliated monolayer, bilayer, trilayer, and bulk MoS_2, respectively. Red curves are the corresponding DFT calculated bands. (e) Thickness dependence of the energy difference between VBM at $\bar{K}$ and $\bar{\Gamma}$. The theoretical and experimental results are plotted together for comparison.

4.3.4 ARPES Study on CVD Monolayer MoS_2

In addition to the experiments on exfoliated MoS_2, we have also carried out electronic structure measurements on CVD-grown monolayer MoS_2. Prior to ARPES measurements, high-resolution PEEM was employed to examine the quality of CVD MoS_2 islands. Figure 4.5 (a) shows a PEEM image of a well-defined triangular CVD MoS_2 island with a grain size of ~50 μm. The uniform contrast in PEEM confirms that the island used for our ARPES measurements is composed of a high-quality monolayer MoS_2 crystal—except for a very small region of bilayer or few-layer MoS_2 at the center of the triangle [19]. The surface is clean and smooth without visible impurities or potassium ions; the sharp and straight edges indicate that the island consists of a single-crystalline MoS_2 grain with Mo zigzag termination [19]. Figure 4.5 (b) shows the band structure of CVD monolayer MoS_2 along high-symmetry directions of the BZ. The dispersion generally matches that of the DFT calculations, with the same distinct band features as in the exfoliated case. An unexpected difference between CVD and exfoliated monolayer MoS_2 is that the energy band compression for the CVD MoS_2 is even more pronounced, as shown in the 2D curvature intensity plot of the UVB (see Figure 4.5 (c)). The measured compression of the UVB for CVD MoS_2 is ~50%. Note that μ-ARPES measurements were also performed on a CVD-grown monolayer MoS_2 crystal without potassium deposition and yielded a similar amount of band compression. Furthermore, interaction with substrate, defects, doping, or stress, which are relatively more important in CVD films, may also play a role in the more pronounced compression in the CVD case.

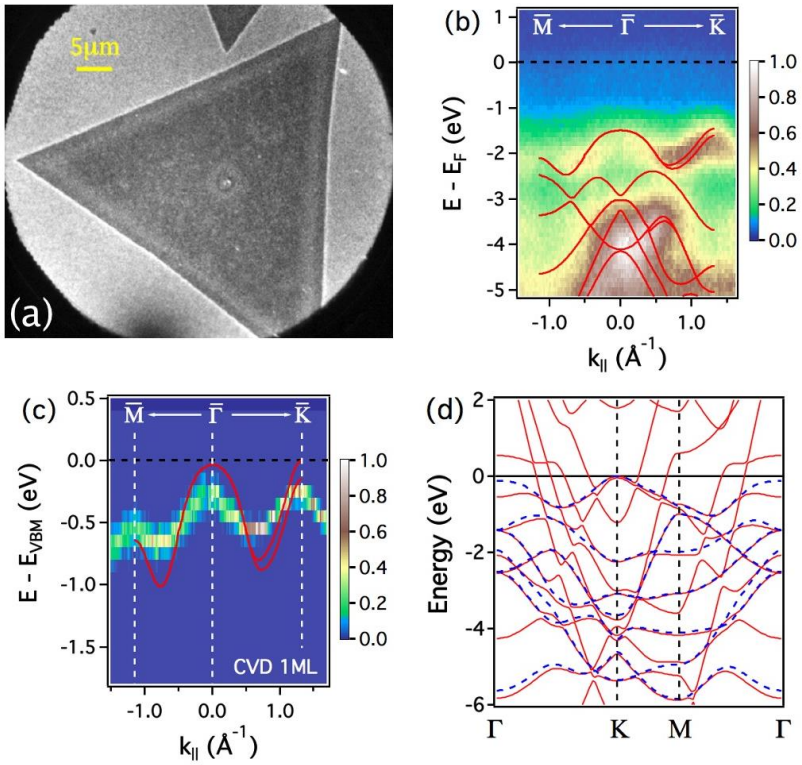

Figure 4.5 (a) PEEM image of a well-defined triangle CVD monolayer MoS_2 island with a small bilayer or multilayer region at its center. (b)An ARPES band map along $\bar{M}-\bar{\Gamma}-\bar{K}$ direction, respectively. DFT band calculations with inclusion of spin-orbit interaction adapted from Ref. 8 (red curves) are overlaid onto ARPES band maps for comparison. (c) 2D curvature intensity plot of the uppermost valence band of CVD monolayer MoS_2. VBM of the calculated band (red curve) is set to be the reference line of energy (black dashed line). The experimental band is shifted in energy to best match the theory. (d) Calculated band structures (red curves) for monolayer MoS_2 on top of *pseudo*-Si. Calculated bands of free-standing monolayer MoS_2 (blue dashed curves) are superimposed onto the hybridized bands for comparison.

4.4 Simulation Using DFT

In an attempt to explain the compression of the UVB observed for both exfoliated and CVD monolayer MoS_2, we tested several possible assumptions by conducting preliminary first-principles calculations using the ABINIT code [34][35]. The generalized gradient approximation (GGA) was applied to describe the exchange-correlation potential. One possible explanation is the presence of a relaxation of the atomic positions in the monolayer MoS_2 due to the missing interlayer interactions. In this case, we performed structural calculations of monolayer MoS_2 by relaxing the atomic positions: in-plane only (*a* lattice-spacing), out-of-plane only (*c* lattice-spacing), and both in-plane and out-of-plane (*a* and *c* lattice-spacings were scaled equally). Our results indicate that the band structure is very sensitive to relaxation as previously reported by others [10]. A 10% expansion of both *a* and *c* lattice spacing can indeed compress the band width of the UVB, but it also significantly changes the calculated higher binding energy bands and, in fact, calculated bands results do not match our experimental observations. Therefore, relaxation is unlikely to be the primary reason for the discrepancy between experiment and theory. Another explanation is that interactions with the substrate could modify the electronic structure of monolayer MoS_2. To check for this possibility, we simulated the interaction with substrate by putting monolayer MoS_2 on top of three layers of a *pseudo*-Si(111) plane. To simplify the model, we assumed that the lattice parameters and crystal structure of Si(111) are the same as those of MoS_2, thus avoiding the complications of lattice mismatch; a more accurate theoretical model is beyond the scope of the discussion here. Our calculations shown in Figure 4.5 (d) indicate that when the spacing between the lower S layer of MoS_2 and the top of the Si layer is set to be 3 Å,

which is comparable to the interlayer distance of bilayer MoS_2 [10], the UVB at $\bar{\Gamma}$ is compressed by ~50% while the valence bands at higher binding energy remain nearly unaffected. These results suggest that dielectric interactions with the substrate are likely the main reason for the observed UVB compression in monolayer MoS_2. If indeed this is the case, this opens up one possible route to modifying band dispersion, and with it the hole effective mass and mobility in MoS_2 by way of substrate engineering.

4.5 Conclusion

In conclusion, we have used μ-ARPES measurements to probe the valence bands of monolayer MoS_2 derived from the Mo 4*d* orbitals. The results match the DFT predictions generally well and show a striking difference when compared with few-layer and bulk MoS_2. The observed increase in the VBM at $\bar{K}$ in monolayer MoS_2 provides a direct measurement of the indirect-to-direct band gap transition in going from few-layer to monolayer MoS_2. The concomitant decrease in the dispersion of the VBM at $\bar{\Gamma}$ leads to a substantially larger hole effective-mass, which explains the low hole mobility of monolayer MoS_2 compared to bulk MoS_2.

4.6 References

[1] Wilson, J. A., and A. D. Yoffe. "The transition metal dichalcogenides discussion and interpretation of the observed optical, electrical and structural properties."*Advances in Physics* 18, no. 73 (1969): 193-335.

[2] Novoselov, K. S., D. Jiang, F. Schedin, T. J. Booth, V. V. Khotkevich, S. V. Morozov, and A. K. Geim. "Two-dimensional atomic crystals." *Proceedings of the National Academy of Sciences of the United States of America* 102, no. 30 (2005): 10451-10453.

[3] Böker, Th, R. Severin, A. Müller, C. Janowitz, R. Manzke, D. Voß, P. Krüger, A. Mazur, and J. Pollmann. "Band structure of MoS_2, $MoSe_2$, and α-$MoTe_2$: angle-resolved photoelectron spectroscopy and ab initio calculations." *Physical Review B* 64, no. 23 (2001): 235305.

[4] Mattheiss, L. F. "Band structures of transition-metal-dichalcogenide layer compounds." *Physical Review B* 8, no. 8 (1973): 3719.

[5] Bromley, R. A., R. B. Murray, and A. D. Yoffe. "The band structures of some transition metal dichalcogenides. III. Group VIA: trigonal prism materials."*Journal of Physics C: Solid State Physics* 5, no. 7 (1972): 759.

[6] Splendiani, Andrea, Liang Sun, Yuanbo Zhang, Tianshu Li, Jonghwan Kim, Chi-Yung Chim, Giulia Galli, and Feng Wang. "Emerging photoluminescence in monolayer MoS_2." *Nano letters* 10, no. 4 (2010): 1271-1275.

[7] Zhu, Z. Y., Y. C. Cheng, and Udo Schwingenschlögl. "Giant spin-orbit-induced spin splitting in two-dimensional transition-metal dichalcogenide semiconductors." *Physical Review B* 84, no. 15 (2011): 153402.

[8] Xiao, Di, Gui-Bin Liu, Wanxiang Feng, Xiaodong Xu, and Wang Yao. "Coupled spin and valley physics in monolayers of MoS_2 and other group-VI dichalcogenides." *Physical Review Letters* 108, no. 19 (2012): 196802.

[9] Radisavljevic, Branimir, Aleksandra Radenovic, Jacopo Brivio, V. Giacometti, and A. Kis. "Single-layer MoS_2 transistors." *Nature nanotechnology* 6, no. 3 (2011): 147-150.

[10] Yun, Won Seok, S. W. Han, Soon Cheol Hong, In Gee Kim, and J. D. Lee. "Thickness and strain effects on electronic structures of transition metal dichalcogenides: 2H-MX_2 semiconductors (M= Mo, W; X= S, Se, Te)."*Physical Review B* 85, no. 3 (2012): 033305.

[11] Mak, Kin Fai, Changgu Lee, James Hone, Jie Shan, and Tony F. Heinz. "Atomically thin MoS_2: a new direct-gap semiconductor." *Physical Review Letters* 105, no. 13 (2010): 136805.

[12] Mak, Kin Fai, Keliang He, Jie Shan, and Tony F. Heinz. "Control of valley polarization in monolayer MoS_2 by optical helicity." *Nature nanotechnology* 7, no. 8 (2012): 494-498.

[13] Lee, Changgu, Hugen Yan, Louis E. Brus, Tony F. Heinz, James Hone, and Sunmin Ryu. "Anomalous lattice vibrations of single-and few-layer MoS_2." *ACS nano* 4, no. 5 (2010): 2695-2700.

[14] Coehoorn, R., C. Haas, J. Dijkstra, C. J. F. Flipse, R. A. De Groot, and A. Wold. "Electronic structure of $MoSe_2$, MoS_2, and WSe_2. I. Band-structure calculations and photoelectron spectroscopy." *Physical Review B* 35, no. 12 (1987): 6195.

[15] Han, Sang Wook, Gi-Beom Cha, Emmanouil Frantzeskakis, Ivy Razado-Colambo, José Avila, Young S. Park, Daehyun Kim et al. "Band-gap expansion in the surface-localized electronic structure of MoS_2 (0002)." *Physical Review B* 86, no. 11 (2012): 115105.

[16] Mahatha, S. K., and Krishnakumar SR Menon. "Inhomogeneous band bending on MoS_2 (0001) arising from surface steps and dislocations." *Journal of Physics: Condensed Matter* 24, no. 30 (2012): 305502.

[17] Li, Hong, Qing Zhang, Chin Chong Ray Yap, Beng Kang Tay, Teo Hang Tong Edwin, Aurelien Olivier, and Dominique Baillargeat. "From bulk to monolayer MoS_2: evolution of Raman scattering." *Advanced Functional Materials* 22, no. 7 (2012): 1385-1390.

[18] Reina, Alfonso, Xiaoting Jia, John Ho, Daniel Nezich, Hyungbin Son, Vladimir Bulovic, Mildred S. Dresselhaus, and Jing Kong. "Large area, few-layer graphene films on arbitrary substrates by chemical vapor deposition." *Nano letters* 9, no. 1 (2008): 30-35.

[19] van der Zande, Arend M., Pinshane Y. Huang, Daniel A. Chenet, Timothy C. Berkelbach, YuMeng You, Gwan-Hyoung Lee, Tony F. Heinz, David R. Reichman, David A. Muller, and James C. Hone. "Grains and grain boundaries in highly crystalline monolayer molybdenum disulphide." *Nature materials* 12, no. 6 (2013): 554-561.

[20] Han, S. W., Hyuksang Kwon, Seong Keun Kim, Sunmin Ryu, Won Seok Yun, D. H. Kim, J. H. Hwang et al. "Band-gap transition induced by interlayer van der Waals interaction in MoS_2." *Physical Review B* 84, no. 4 (2011): 045409.

[21] Flege, J. I., E. Vescovo, G. Nintzel, L. H. Lewis, S. Hulbert, and P. Sutter. "A new soft X-ray photoemission microscopy beamline at the National Synchrotron Light Source." *Nuclear Instruments and Methods in Physics Research Section B: Beam Interactions with Materials and Atoms* 261, no. 1 (2007): 855-858.

[22] Sutter, P., M. S. Hybertsen, J. T. Sadowski, and E. Sutter. "Electronic structure of few-layer epitaxial graphene on Ru (0001)." *Nano letters* 9, no. 7 (2009): 2654-2660.

[23] Babout, M., C. Guittard, M. Guivarch, R. Pantel, and M. Bujor. "Mirror electron microscopy applied to the continuous local measurement of work-function variations." *Journal of Physics D: Applied Physics* 13, no. 7 (1980): 1161.

[24] Sutter, Peter, and Eli Sutter. "Microscopy of graphene growth, processing, and properties." *Advanced Functional Materials* 23, no. 20 (2013): 2617-2634.

[25] Lince, Jeffrey R., Thomas B. Stewart, Malina M. Hills, Paul D. Fleischauer, Jory A. Yarmoff, and Amina Taleb-Ibrahimi. "Chemical effects of Ne+ bombardment on the MoS_2 (0001) surface studied by high-resolution photoelectron spectroscopy." *Surface Science* 210, no. 3 (1989): 387-405.

[26] Yeh, J. J., and I. Lindau. "Atomic subshell photoionization cross sections and asymmetry parameters: $1 \leq Z \leq 103$." *Atomic data and nuclear data tables* 32, no. 1 (1985): 1-155.

[27] Wang, X-P., P. Richard, Y-B. Huang, H. Miao, L. Cevey, N. Xu, Y-J. Sun et al. "Orbital characters determined from Fermi surface intensity patterns using angle-resolved photoemission spectroscopy." *Physical Review B* 85, no. 21 (2012): 214518.

[28] Kuc, Agnieszka, Nourdine Zibouche, and Thomas Heine. "Influence of quantum confinement on the electronic structure of the transition metal sulfide TS_2."*Physical Review B* 83, no. 24 (2011): 245213.

[29] Castellanos-Gomez, Andres, Rafael Roldán, Emmanuele Cappelluti, Michele Buscema, Francisco Guinea, Herre SJ van der Zant, and Gary A. Steele. "Local strain engineering in atomically thin MoS_2." *Nano letters* 13, no. 11 (2013): 5361-5366.

[30] Zhang, Peng, P. Richard, T. Qian, Y-M. Xu, X. Dai, and H. Ding. "A precise method for visualizing dispersive features in image plots." *Review of Scientific Instruments* 82, no. 4 (2011): 043712.

[31] Peelaers, Hartwin, and Chris G. Van de Walle. "Effects of strain on band structure and effective masses in MoS 2." *Physical Review B* 86, no. 24 (2012): 241401.

[32] Ayari, Anthony, Enrique Cobas, Ololade Ogundadegbe, and Michael S. Fuhrer. "Realization and electrical characterization of ultrathin crystals of layered transition-metal dichalcogenides." *Journal of applied physics* 101, no. 1 (2007): 014507-014507.

[33] Fivaz, R_, and E. Mooser. "Mobility of charge carriers in semiconducting layer structures." *Physical Review* 163, no. 3 (1967): 743.

[34] Gonze, Xavier. "A brief introduction to the ABINIT software package." *Zeitschrift für Kristallographie* 220, no. 5/6/2005 (2005): 558-562.

[35] Gonze, Xavier, B. Amadon, P-M. Anglade, J-M. Beuken, F. Bottin, P. Boulanger, F. Bruneval et al. "ABINIT: First-principles approach to material and nanosystem properties." *Computer Physics Communications* 180, no. 12 (2009): 2582-2615.

Chapter 5

Layer-dependent electronic structure of an atomically heavy 2D dichalcogenide – A WSe_2 Study Using SPELEEM

In this chapter, we describe angle-resolved photoemission spectroscopic measurements of the evolution of the thickness-dependent electronic band structure of the heavy-atom two-dimensional layered, dichalcogenide, tungsten-diselenide (WSe_2). Our data, taken on mechanically exfoliated WSe_2 single-crystals, provide direct evidence for shifting of the valence-band maximum from $\bar{\Gamma}$ (multilayer WSe_2), to $\bar{K}$, (single-layer WSe_2). Further, our measurements also set a lower bound on the energy of the direct band-gap and provide direct measurement of the hole effective mass.

5.1 Introduction

Single layers of two-dimensional metal dichalcogenides (TMDCs) such as MoS_2, have emerged as a new class of non-centrosymmetric direct-bandgap materials with potential photonic and spintronic applications [7][8]. Among the TMDC family, tungsten-based dichalcogenides, such as WSe_2, exhibit high in-plane carrier mobility and allow electrostatic modulation of the conductance [42][43], characteristics, which make them promising for device applications. For example, bulk WSe_2 possesses an indirect bandgap of 1.2 eV [40][44] and has been used as the channel of a field-effect transistor (FET) with an intrinsic hole mobility of up to 500 $cm^2/(V\text{-}s)$ [45]. By comparison, WSe_2, in its monolayer form (ML), should have a direct band gap, as predicted by theory [46][47][48][49][50][51], and a promising intrinsic hole mobility of 250 $cm^2/(V\text{-}s)$, as recently demonstrated in the performance of top-gated FETs [43]. In addition, ML WSe_2 has been demonstrated to be the first TMDC material possessing ambipolar, i.e., both p-type and n-type conducting behavior [43][51], thus making it possible to design additional electronic functionality, such as p-n junctions or complementary logic circuits.

Despite these intriguing characteristics, measurements of ML WSe_2 have generally been limited to probing of optical and transport properties [43][44][45]. In this work, we report thickness-dependent measurements of the surface and electronic structure of exfoliated WSe_2, using low-energy electron microscopy (LEEM), diffraction (LEED), and micrometer-scale angle-resolved photoemission spectroscopy (μ-ARPES) of samples supported on a native-oxide terminated silicon substrate. Our experimental results provide direct evidence for a predicted valence-band maximum (VBM) symmetry-point change,

which leads to an indirect-to-direct bandgap transition. Because TMDCs have a large carrier effective mass and reduced screening in two dimensions, electron–hole interactions are much stronger than in conventional semiconductors [52][53][54]. Our results allow us to obtain a direct measurement of the hole effective mass. Finally, our measurements allow us to directly infer a lower bound on the energy of the direct band gap.

5.2 Experimental Methods

Our measurements were performed using the spectroscopic photoemission and low-energy electron microscope (SPELEEM) system at the National Synchrotron Light Source (NSLS) beamline U5UA [39][56]. The spectrometer energy resolution of this instrument was set to 100 meV at 33 eV incident photon energy with a beam spot size of 1 μm in diameter. The momentum resolution is ~0.02 $Å^{-1}$. Exfoliated WSe_2 samples were transferred to a native-oxide covered Si substrate; prior to measurements, these samples were annealed at 350 ^oC for ~12 hours under UHV conditions. The layer number of the sample is determined by Raman and photoluminescence spectroscopy [57][58].

5.2.1 Sample Preparation and Characterization

The samples examined here were first mechanically exfoliated with sacrificial PMMA/PVA thin films on Si. The films have a thickness of 280 ± 5 nm which provides the same optical contrast as on a 280nm-thick SiO_2-coated Si substrate. The layer number of the sample was determined by Raman and photoluminescence spectroscopy using the method described in Ref. [18][19] and in its supplementary material section. The samples were excited using a commercial Renishaw InVia Raman Microscope with a 532nm laser

and an 1800 lines/mm grating. The spectra were normalized to Raman A_{1g} peak for Raman shift study. For photoluminescence study, the samples were examined for wavelengths from 500-1000nm, which correspond to 2.48 – 1.24 eV in photon energy. A non-contacting atomic force microscope was used to help determine the sample thickness. Later, the samples were wet-transferred onto a native-oxide Si substrate to eliminate the charging effect [16][25][47]. An example of the optical and LEEM images of the samples before and after transfer is shown in Figure 5.1 (c). After the transfer, the samples were then rinsed in acetone for 24 hours to complete the transfer procedure. Prior to any measurements, the samples were degassed and annealed to 350 ^{o}C for several hours under UHV conditions. Also, careful examination using LEEM to investigate unwanted surface residues was essential for our ARPES measurements.

Sample quality and crystal orientation were examined using both LEEM and μ-LEED (Figure 5.1). Diffraction patterns (at a primary electron energy of 48 eV) of exfoliated WSe_2 flakes of 1 - 3 ML and bulk are shown in Figure 5.2 (a)-(d), respectively, and clearly display the six-fold crystal symmetry. At an electron energy of 48eV, the mean free path of the low-energy electrons is ~5.2 Å [59] which is comparable to the thickness of a single covalently bound Se-W-Se unit of monolayer WSe_2 (~7 Å) [43][60]. With increasing WSe_2 thickness, the LEED spots become sharper due, in part, to decreased scattering from the substrate [61]. This assertion is supported by the monotonically decreasing full-width-at-half- maximum (FWHM) of the (00) diffraction spot, plotted for different electron energies in Figure 5.2 (e) [61].

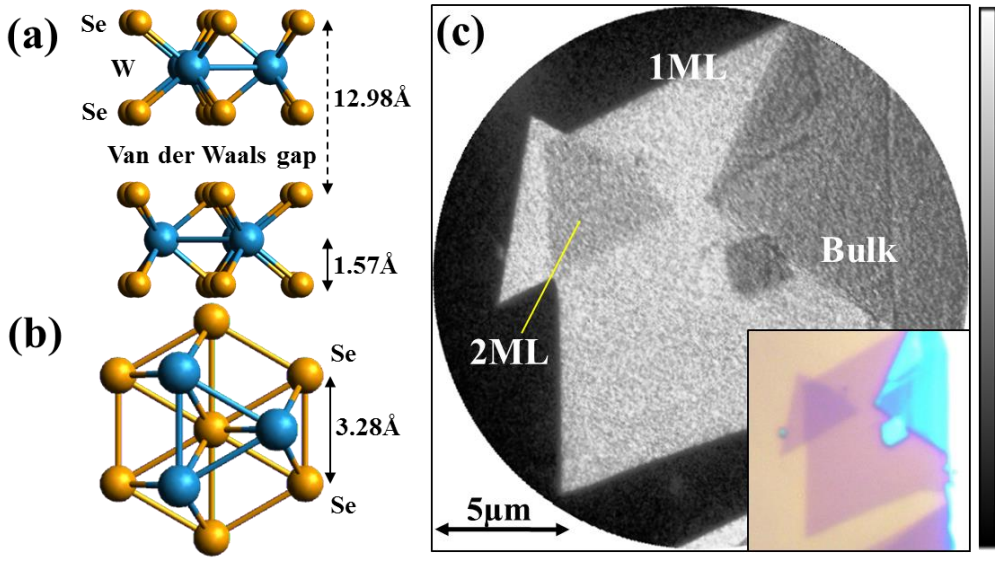

Figure 5.1 (a) Side view and (b) top view of the trigonal prismatic coordination of the atoms in 2H-WSe_2. (c) LEEM image of 1ML WSe_2 after transfer (detector artifacts and background signal have been removed.) The inset is the corresponding optical microscope image of the same sample. LEEM images were taken at an electron energy of 1.8 eV.

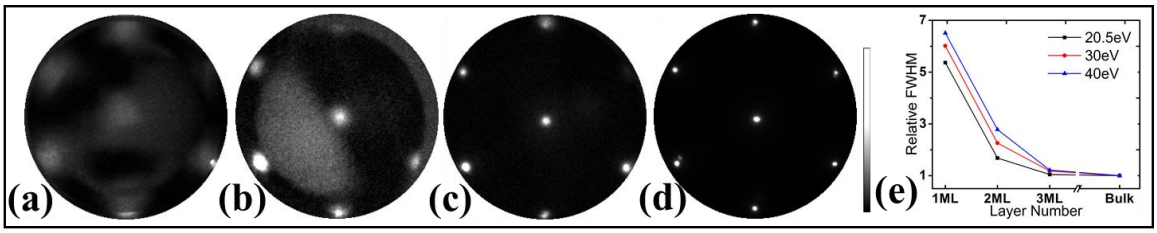

Figure 5.2 (a)-(d) Micro-LEED patterns at 48eV electron energy on exfoliated WSe_2 1 ML (a), 2 ML (b), 3 ML (c), and bulk (d) after transfer to Si. The halo around 1ML (00) spot came from edge deflection of electrons due to a limited sample size. (e) Measured FWHM of the (00) LEED spot for 1-3ML WSe_2 flakes relative to that of bulk, measured at 20.5, 30, and 40 eV electron energy. The FWHM decreases with increasing number of layers, since electrons elastically backscattered from the Si substrate are progressively decreased.

5.3 Experimental Results

5.3.1 Photoionization Cross-Section, Orbitals, and Fermi Cutoff

The electronic structure of the top-lying valence bands of WSe_2 is derived from the W 5d and Se 4p orbitals [62][63], each of which possesses a strongly varying photon-energy-dependent photoionization cross-section [64], as displayed in Figure 5.3 (b). Prior work [64] has shown that the cross-section of the W 5d subshell is an order of magnitude larger than that of Se 4p at the photon energy of 33 eV used in our experiments (indicated by the vertical line in Figure 5.3 (b).) Thus the primary contributions to our μ-ARPES measurements, shown in Figure 5.4, are from the W 5d orbitals. Angle-integrated photoemission spectra of 1ML WSe_2 along high symmetry directions and over the full Brillouin Zone (BZ) are shown in Figure 5.3 (c). These spectra show a clear energy cut-off at about 1.8 ± 0.1 eV above the VBM, which we identify as the position of the Fermi level EF. The bandgap of ML WSe_2 has previously been reported to be in the range of 1.4 to 2.3 eV [58][65][66]. Based on our identification of the Fermi energy, the minimum bandgap value of WSe_2 must be greater than at least 1.8 eV; this result also suggests that our exfoliated ML WSe_2 is heavily electron-doped, i.e. the Fermi level falls near the conduction band minimum.[67][68] The energy differences between the Fermi level (E_F) and the VBM for 2ML, 3ML, and bulk, are approximately 1.5 eV, 1.5 eV, and 1.1 eV, respectively. Taking into account the previously reported bandgap energies of these materials, we find that these energy differences are consistent with our samples being heavily electron-doped, regardless of thickness. This result suggests that our electron-doping is more likely to be intrinsic to the layered material and not due to charge transfer from the substrate.

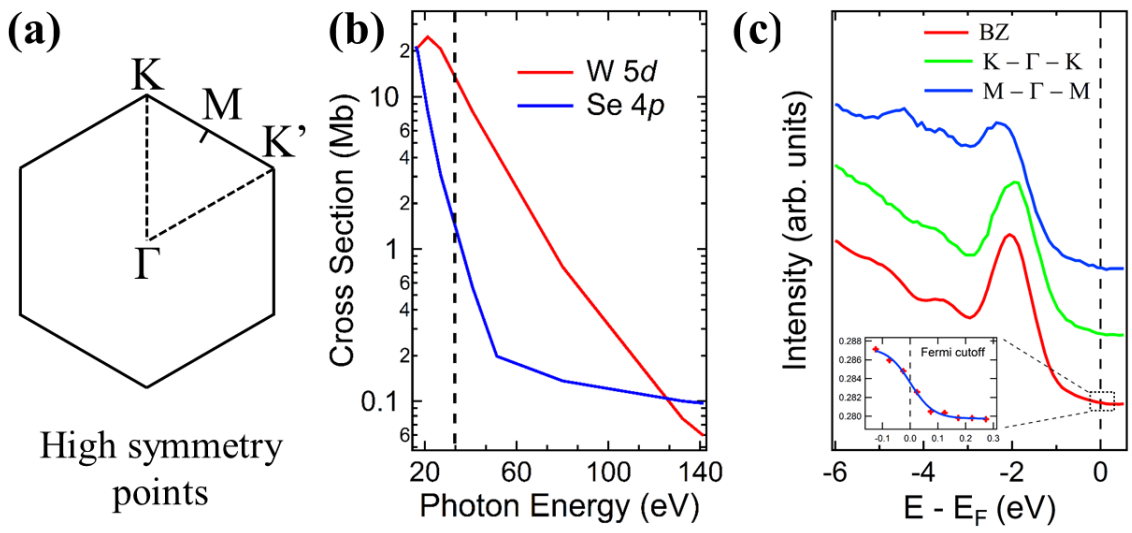

Figure 5.3 (a) Brillouin zone and high-symmetry points of WSe_2. (b) Atomic photoionization cross-section for W 5d and Se 4p subshells as a function of ARPES photon energy [64]. At 33 eV, the cross-section between W 5d and Se 4p has an order-of-magnitude difference. Therefore, the dominant features in our ARPES measurement are the contribution of W 5d subshell. Note that the Cooper minimum of the Se orbital is ~50 eV. (c) Angle-integrated photoemission spectra of monolayer WSe_2 extracted from high symmetry directions $\bar{K}$-$\bar{\Gamma}$-$\bar{K}$ and $\bar{M}$-$\bar{\Gamma}$-$\bar{M}$, and over the full BZ, referenced with respect to the Fermi level.

5.3.2 ARPES Band Mapping

Our μ-ARPES measurements of 1 - 3ML and bulk WSe_2 along the high symmetry directions $\bar{M}$-$\bar{\Gamma}$-$\bar{K}$, given in Figure 5.4, clearly show a transition in the occupied electronic structure with change in layer thickness. Superimposed on the measured data are the corresponding DFT-LDA band calculations, computed using ABINIT without spin-orbit interaction [69][70]. In the spectra, the distinctive features include the VBM at $\bar{\Gamma}$, derived

from the W d_{z^2} and Se p_z orbitals, the VBM at $\bar{K}$, derived from the W $d_{x^2-y^2}/d_{xy}$ and Se p_x/p_y orbitals, and the valley between $\bar{\Gamma}$ and $\bar{K}$, derived from a crossover to the W $d_{x^2-y^2}/d_{xy}$ orbitals from the W d_{z^2} and Se p_z orbitals [50][71][72], as shown and labeled in Figure 5.4 (a). Bands of higher binding energies and along other high-symmetry directions have been previously calculated and discussed in the literature [50][62][63][71][72][73]. These features are further displayed in the corresponding energy distribution curves (EDCs) [see Figure 5.4 (b)] and momentum distribution curves (MDCs) [see Figure 5.4 (c)]. Note that several of the WSe_2 bands are not detected in our ARPES measurements due to matrix-element selection rules as well as the above-mentioned difference in the photoionization cross-section between W- and Se-derived states. In our experiments, the incident photon flux was directed normal to the sample surface so that its polarization is in the plane of the WSe_2 crystal, thus suppressing excitation of states with out-of-plane character. This result explains why the W- and Se-derived states with a z or out-of-plane component, i.e., d_{z^2} or p_z orbital, in the uppermost valence band (UVB) near $\bar{\Gamma}$ have a consistently relatively weaker, but non-zero, intensity for 1 - 3ML and bulk WSe_2.

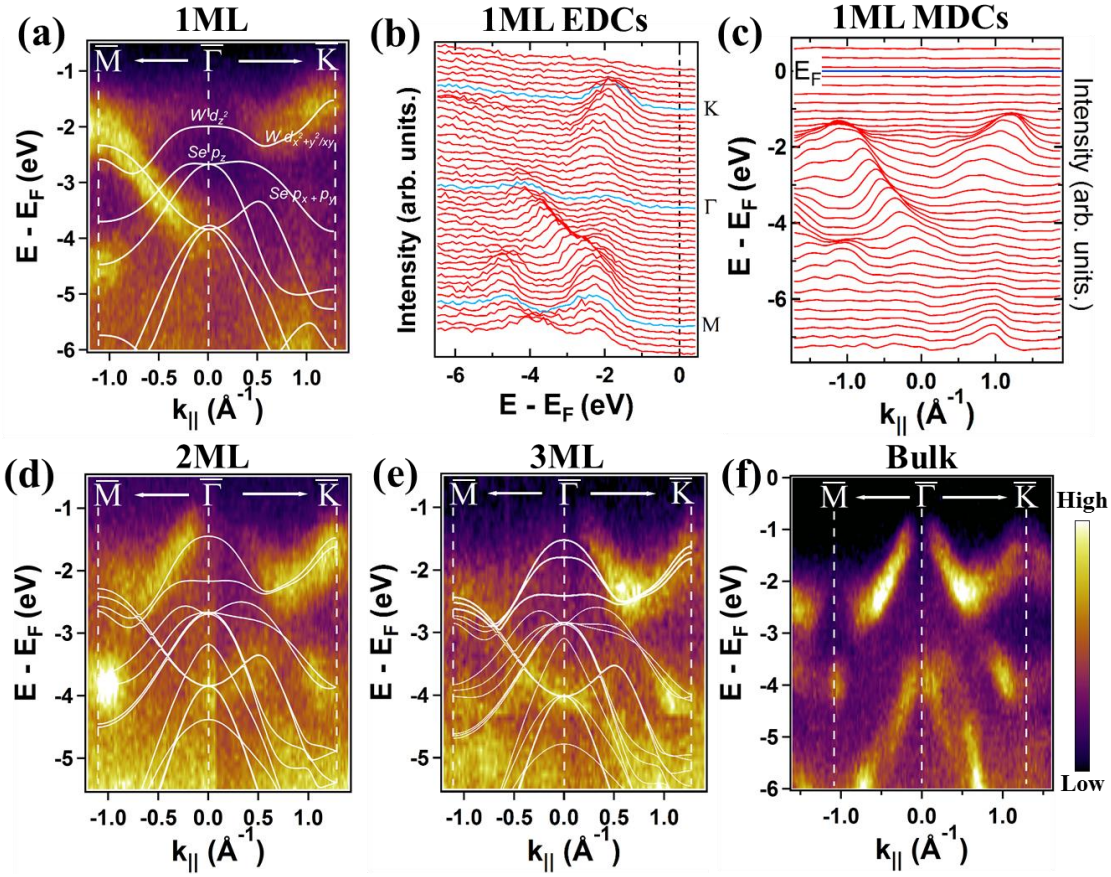

Figure 5.4 μ-ARPES band mapping of exfoliated WSe_2 for (a) 1ML (d) 2ML (c) 3ML and (f) bulk along the high-symmetry path $\bar{M}$-$\bar{\Gamma}$-$\bar{K}$ in the Brillouin zone. E=0 denotes the Fermi level. The overlaid white lines are our DFT-calculated band structures. The calculations do not include the effect of spin-orbit coupling. (b), (c) Corresponding EDCs and MDCs of 1ML WSe_2, respectively.

5.3.3 Second Derivative Band Analysis

An important feature of our measurements is the change in the energy of the upper-most valence band (UVB) at $\bar{\Gamma}$ and $\bar{K}$ for 1ML WSe_2 compared to that of few-layer WSe_2. Our μ-ARPES spectra show that the valence band maximum is at $\bar{K}$ for 1ML WSe_2 and

shifts to $\bar{\Gamma}$ for multilayer WSe_2. Previous reports [74][75][76][77][78] using traditional ARPES and inverse photoemission instruments have confirmed that the location of the VBM in bulk WSe_2 to be at $\bar{\Gamma}$; note that for bulk WSe_2, ARPES measurements over a large enough photon energy range are required in order to take into account the k_z dependence of the observed states. To fully quantify the VBM transition as a function of thickness, we used curvature analysis [79], or the second-derivative method, to help delineate the electronic band structure, as shown in Figure 5.5. Figure 5.5 (a)-(d) give the bands for the 1 - 3ML and bulk WSe_2 samples, derived from the data in Figure 5.4 using this method, and with the zero energy referenced to the VBM. The UVB of exfoliated WSe_2 closely matches the corresponding calculated bands (white curves), except for the monolayer case where the measured energy difference between $\bar{\Gamma}$ and $\bar{K}$ is less than that predicted by theory, and where the dispersion at $\bar{\Gamma}$ is greater than that in the calculated bands. The experimentally measured and theoretically predicted [50] energy differences between $\bar{\Gamma}$ and $\bar{K}$ for monolayer and multilayer WSe_2 are plotted in Figure 5.5 (e). The measured energy differences are: 0.21 eV, -0.14 eV, and -0.25 eV for 1 - 3ML; the value for bulk WSe_2 has been reported previously to be -0.3 eV [75][77]. The error bars denote the standard deviation of the fittings from all six high symmetry equivalent directions, and they are well under the detector error of ± 0.10 eV. Thus, these results provide direct experimental evidence for a thickness-dependent shift in the relative energy of the VBM at $\bar{\Gamma}$ and at $\bar{K}$ and, hence, strong support for a shift from an indirect to a direct bandgap in going from 2 to 1 ML WSe_2.

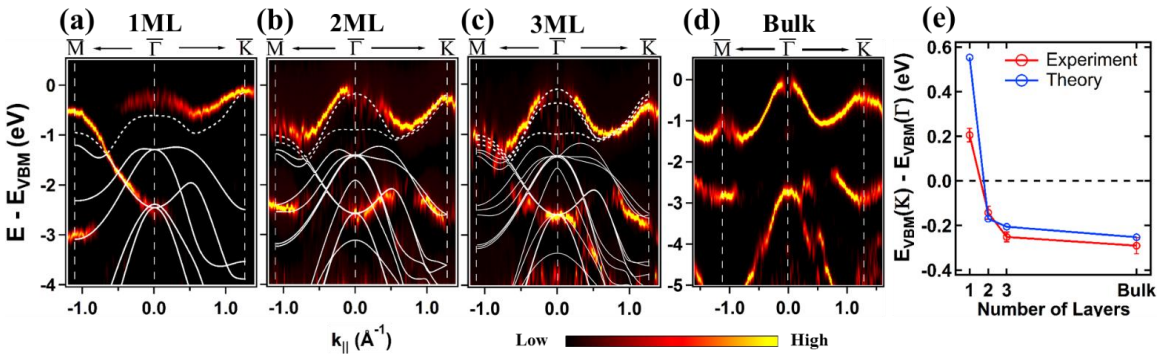

Figure 5.5 (a)-(d) Second derivative plots of the low-energy valence bands along high symmetry points of exfoliated 1 - 3ML and bulk WSe_2, respectively, generated from the μ-ARPES band maps of Figure 5.4. The white lines are the corresponding DFT-calculated bands as in Figure 5.4. The dashed-white lines refer to the top valence bands, which illustrate the layer-number dependence of the electronic structure near the VBM. Here the energy scale is set to zero at the VBM. (e) Layer-number-dependent VBM transition of the energy difference between $\bar{K}$ and $\bar{\Gamma}$ points. The error bars denote the standard deviation of the fittings from all six high symmetry equivalent directions, and they are well under the detector error of ± 0.10 eV. The theoretical and experimental results are plotted for comparison.

5.3.4 Effective Mass

An analysis of the curvature of the bands from the μ-ARPES measurements also allows us to deduce the effective mass of monolayer and bilayer WSe_2. For monolayer WSe_2, we determined an experimentally derived hole effective mass of 1.4 ± 0.6 m_0 [80] (where m_0 is the electron mass) at $\bar{K}$, which is ~3x larger than theoretical predictions, and a hole effective mass of 3.5 ± 1.8 m_0 [80] at $\bar{\Gamma}$. The later quantity is approximately half as

large as theoretical predictions (7.1 ± 0.2 m_0) [46][47][48][49][81]. For the case of bilayer WSe_2, however, we determined an experimentally derived hole effective mass of 0.4 ± 0.1 m_0 at $\bar{K}$, which agrees well with theoretical predictions [46][48]. The origin of the discrepancy between experiment and DFT calculations for the case of a monolayer is uncertain at this time. Our finite energy resolution does contribute to the measurement error. However, it is also apparent that there is an overall difference in band dispersion between our relatively simple theory calculation and experiment. This reasoning indicates that the above discrepancy is more complicated than simple instrumentation limits. Note that our DFT-derived effective-mass value of 0.44 m_0 for monolayer WSe_2 at $\bar{K}$ is in reasonable agreement with previous theoretical reports [46][47][48][49]. Also since $m_{eff} \propto \left|\frac{\partial^2 E}{\partial^2 k}\right|^{-1}$, slight measurement errors are accentuated by the flat-like dispersion curve in the vicinity of $\bar{\Gamma}$. "Renormalization" in bands of other 2D dichalcogenides have also been reported [82][83], though the reason for this remains in question. Other possible explanations beyond that of an intrinsic nature of WSe_2 include effects of substrate interaction, such as strain, dielectric screening, etc.

Note that the lattice constant of WSe_2 can have a variation of up to 1% between DFT calculations [7][8][9][10][11] and bulk experiments. This contributes insignificantly to the variation of the effective mass, as the effective mass is approximately inversely proportional to a^2. Therefore, we are able to compare the hole effective mass across different literature values. In our analysis, we use the experimentally measured bulk lattice constant, i.e. 3.28 Å.

5.3.5 Spin-Orbit Coupling

In comparison to monolayer MoS_2, monolayer WSe_2 is expected to have an even larger spin-orbit splitting in the vicinity of $\overline{K}$, with a theoretically predicted value of ~0.46 eV v.s. ~0.16 eV of MoS_2 [50][84]. The expected splitting of the valence band along the $\overline{\Gamma}$ - $\overline{K}$ direction of monolayer WSe_2 is due to the strong spin-orbit coupling originating from the high mass of the constituent elements and the lack of inversion symmetry [50][84][85][86]. The theoretically predicted value (~0.46 eV) is larger than our experiment energy resolution and thus, should have been resolved directly in our measurements. However, despite the presence of an increasing linewidth of the UVB in the direction of $\overline{\Gamma}$-$\overline{K}$, which may be attributed to spin-orbit-splitting of the bands, we do not see two clear peaks in the vicinity of $\overline{K}$. We conjecture sample roughness, induced in the transfer process, is broadening the linewidth [87] of the spin-orbit split bands, leading to a broad unresolved band in our ARPES measurements. We have shown in previous works [61][83], using an analysis of LEED spot widths, that the transfer process introduces corrugation in monolayer MoS_2. Thus, resolving the spin-orbit-splitting in monolayer dichalcogenides is demanding in terms of a flat transfer procedure.

5.4 Conclusion

In conclusion, we have probed the surface structure and occupied electronic bands of 1 – 3 layer exfoliated WSe_2 crystals prepared by transfer to a native-oxide-terminated Si substrate. LEEM and μ-LEED provided real-space and reciprocal-space structural measurements of WSe_2, revealing clearly resolved thickness-dependent contrast and diffraction spot widths, respectively. Our μ-ARPES measurements have probed the

occupied valence-band structure and confirmed the transition of the valence band maximum from $\bar{\Gamma}$ to $\bar{K}$ as the thickness is reduced from few-layer to 1ML WSe_2; this observation provides support for an indirect-to-direct bandgap transition. For monolayer WSe_2, we have found a lower bound of 1.8 eV for the bandgap and measured a hole effective mass of 1.4 m_0 at $\bar{K}$ and 3.5 m_0 at $\bar{\Gamma}$. We expect that these results will provide insight to the understanding of the optical and electronic properties of monolayer and multilayer WSe_2 that is important for novel devices made from this transition-metal-dichalcogenide material.

5.5 References

[1] Mak, Kin Fai, Changgu Lee, James Hone, Jie Shan, and Tony F. Heinz. "Atomically thin MoS_2: a new direct-gap semiconductor." *Physical Review Letters* 105, no. 13 (2010): 136805.

[2] Splendiani, Andrea, Liang Sun, Yuanbo Zhang, Tianshu Li, Jonghwan Kim, Chi-Yung Chim, Giulia Galli, and Feng Wang. "Emerging photoluminescence in monolayer MoS_2." *Nano letters* 10, no. 4 (2010): 1271-1275.

[3] Braga, Daniele, Ignacio Gutiérrez Lezama, Helmuth Berger, and Alberto F. Morpurgo. "Quantitative determination of the band gap of WS_2 with ambipolar ionic liquid-gated transistors." *Nano letters* 12, no. 10 (2012): 5218-5223.

[4] Fang, Hui, Steven Chuang, Ting Chia Chang, Kuniharu Takei, Toshitake Takahashi, and Ali Javey. "High-performance single layered WSe_2 p-FETs with chemically doped contacts." *Nano letters* 12, no. 7 (2012): 3788-3792.

[5] Yousefi, G. H. "Optical properties of mixed transition metal dichalcogenide crystals." *Materials Letters* 9, no. 1 (1989): 38-40.

[6] Podzorov, V., M. E. Gershenson, Ch Kloc, R. Zeis, and E. Bucher. "High-mobility field-effect transistors based on transition metal dichalcogenides. "*Applied Physics Letters* 84, no. 17 (2004): 3301-3303.

[7] Kumar, A., and P. K. Ahluwalia. "Electronic structure of transition metal dichalcogenides monolayers 1H-MX_2 (M= Mo, W; X= S, Se, Te) from ab-initio theory: new direct band gap semiconductors." *The European Physical Journal B-Condensed Matter and Complex Systems* 85, no. 6 (2012): 1-7.

[8] Ramasubramaniam, Ashwin. "Large excitonic effects in monolayers of molybdenum and tungsten dichalcogenides." *Physical Review B* 86, no. 11 (2012): 115409.

[9] Yun, Won Seok, S. W. Han, Soon Cheol Hong, In Gee Kim, and J. D. Lee. "Thickness and strain effects on electronic structures of transition metal dichalcogenides: 2H-MX_2 semiconductors (M= Mo, W; X= S, Se, Te)."*Physical Review B* 85, no. 3 (2012): 033305.

[10] Shi, Hongliang, Hui Pan, Yong-Wei Zhang, and Boris I. Yakobson. "Quasiparticle band structures and optical properties of strained monolayer MoS_2 and WS_2." *Physical Review B* 87, no. 15 (2013): 155304.

[11] Zhu, Z. Y., Y. C. Cheng, and Udo Schwingenschlögl. "Giant spin-orbit-induced spin splitting in two-dimensional transition-metal dichalcogenide semiconductors." *Physical Review B* 84, no. 15 (2011): 153402.

[12] Liu, Wei, Jiahao Kang, Deblina Sarkar, Yasin Khatami, Debdeep Jena, and Kaustav Banerjee. "Role of metal contacts in designing high-performance monolayer n-type WSe_2 field effect transistors." *Nano letters* 13, no. 5 (2013): 1983-1990.

[13] Jones, Aaron M., Hongyi Yu, Nirmal J. Ghimire, Sanfeng Wu, Grant Aivazian, Jason S. Ross, Bo Zhao et al. "Optical generation of excitonic valley coherence in monolayer WSe_2." *Nature nanotechnology* 8, no. 9 (2013): 634-638.

[14] Mak, Kin Fai, Keliang He, Changgu Lee, Gwan Hyoung Lee, James Hone, Tony F. Heinz, and Jie Shan. "Tightly bound trions in monolayer MoS_2." *Nature materials* 12, no. 3 (2013): 207-211.

[15] Ross, Jason S., Sanfeng Wu, Hongyi Yu, Nirmal J. Ghimire, Aaron M. Jones, Grant Aivazian, Jiaqiang Yan et al. "Electrical control of neutral and charged excitons in a monolayer semiconductor." *Nature communications* 4 (2013): 1474.

[16] Sadowski, Jerzy T. "Pentacene growth on 3-aminopropyltrimethoxysilane modified silicon dioxide." *Optical Materials* 34, no. 10 (2012): 1635-1638.

[17] Sutter, P., M. S. Hybertsen, J. T. Sadowski, and E. Sutter. "Electronic structure of few-layer epitaxial graphene on Ru (0001)." *Nano letters* 9, no. 7 (2009): 2654-2660.

[18] Zeng, Hualing, Gui-Bin Liu, Junfeng Dai, Yajun Yan, Bairen Zhu, Ruicong He, Lu Xie et al. "Optical signature of symmetry variations and spin-valley coupling in atomically thin tungsten dichalcogenides." *Scientific reports* 3 (2013).

[19] Zhao, Weijie, Zohreh Ghorannevis, Leiqiang Chu, Minglin Toh, Christian Kloc, Ping-Heng Tan, and Goki Eda. "Evolution of electronic structure in atomically thin sheets of WS_2 and WSe_2." *Acs Nano* 7, no. 1 (2012): 791-797.

[20] Seah, M. P., and W. A. Dench. "Quantitative electron spectroscopy of surfaces: a standard data base for electron inelastic mean free paths in solids." *Surface and interface analysis* 1, no. 1 (1979): 2-11.

[21] Kalikhman, V. L., and Ya S. Umanskiĭ. "Transition-metal chalcogenides with layer structures and features of the filling of their brillouin zones." *Physics-Uspekhi* 15, no. 6 (1973): 728-741.

[22] Yeh, Po-Chun, Wencan Jin, Nader Zaki, Datong Zhang, Jerzy T. Sadowski, Abdullah Al-Mahboob, Arend M. van der Zande et al. "Probing substrate-dependent long-range surface structure of single-layer and multilayer MoS_2 by low-energy electron microscopy and microprobe diffraction." *Physical Review B*89, no. 15 (2014): 155408.

[23] Mattheiss, L. F. "Band structures of transition-metal-dichalcogenide layer compounds." *Physical Review B* 8, no. 8 (1973): 3719.

[24] Coehoorn, R., C. Haas, J. Dijkstra, C. J. F. Flipse, R. A. De Groot, and A. Wold. "Electronic structure of $MoSe_2$, MoS_2, and WSe_2. I. Band-structure calculations and photoelectron spectroscopy." *Physical Review B* 35, no. 12 (1987): 6195.

[25] Yeh, J. J., and I. Lindau. "Atomic subshell photoionization cross sections and asymmetry parameters: $1 \leq Z \leq 103$." *Atomic data and nuclear data tables* 32, no. 1 (1985): 1-155.

[26] Deshpande, M. P., G. K. Solanki, and M. K. Agarwal. "Optical band gap in tungsten diselenide single crystals intercalated by indium." *Materials Letters* 43, no. 1 (2000): 66-72.

[27] Wilson, J. A., and A. D. Yoffe. "The transition metal dichalcogenides discussion and interpretation of the observed optical, electrical and structural properties." *Advances in Physics* 18, no. 73 (1969): 193-335.

[28] Späh, R., U. Elrod, M. Lux-Steiner, E. Bucher, and S. Wagner. "pn junctions in tungsten diselenide." *Applied Physics Letters* 43, no. 1 (1983): 79-81.

[29] Upadhyayula, L. C., J. J. Loferski, A. Wold, W. Giriat, and R. Kershaw. "Semiconducting Properties of Single Crystals of n-and p-Type Tungsten Diselenide (WSe_2)." *Journal of Applied Physics* 39, no. 10 (1968): 4736-4740.

[30] Gonze, Xavier. "A brief introduction to the ABINIT software package." *Zeitschrift für Kristallographie* 220, no. 5/6/2005 (2005): 558-562.

[31] Gonze, Xavier, B. Amadon, P-M. Anglade, J-M. Beuken, F. Bottin, P. Boulanger, F. Bruneval et al. "ABINIT: First-principles approach to material and nanosystem properties." *Computer Physics Communications* 180, no. 12 (2009): 2582-2615.

[32] Liu, Gui-Bin, Wen-Yu Shan, Yugui Yao, Wang Yao, and Di Xiao. "Three-band tight-binding model for monolayers of group-VIB transition metal dichalcogenides." *Physical Review B* 88, no. 8 (2013): 085433.

[33] Cappelluti, E., Rafael Roldán, J. A. Silva-Guillén, Pablo Ordejón, and F. Guinea. "Tight-binding model and direct-gap/indirect-gap transition in single-layer and multilayer MoS_2" *Physical Review B* 88, no. 7 (2013): 075409.

[34] Klein, A., S. Tiefenbacher, V. Eyert, C. Pettenkofer, and W. Jaegermann. "Electronic band structure of single-crystal and single-layer WS 2: Influence of interlayer van der Waals interactions." *Physical Review B* 64, no. 20 (2001): 205416.

[35] Straub, Th, K. Fauth, Th Finteis, M. Hengsberger, R. Claessen, P. Steiner, S. Hüfner, and P. Blaha. "Valence-band maximum in the layered semiconductor WSe_2: Application of constant-energy contour mapping by photoemission."*Physical Review B* 53, no. 24 (1996): R16152.

[36] Finteis, Th, M. Hengsberger, Th Straub, K. Fauth, R. Claessen, P. Auer, P. Steiner et al. "Occupied and unoccupied electronic band structure of WSe_2."*Physical Review B* 55, no. 16 (1997): 10400.

[37] Finteis, Th, M. Hengsberger, Th Straub, K. Fauth, R. Claessen, P. Auer, P. Steiner et al. "Erratum: Occupied and unoccupied electronic band structure of WSe_2 [Phys. Rev. B 55, 10 400 (1997)]." *Physical Review B* 59, no. 3 (1999): 2461.

[38] Traving, M., M. Boehme, L. Kipp, M. Skibowski, F. Starrost, E. E. Krasovskii, A. Perlov, and W. Schattke. "Electronic structure of WSe_2: A combined photoemission and inverse photoemission study." *Physical Review B* 55, no. 16 (1997): 10392.

[39] Yu, S-W., T. Lischke, R. David, Norbert Müller, Ulrich Heinzmann, C. Pettenkofer, A. Klein et al. "Spin resolved photoemission spectroscopy on WSe_2." *Journal of electron spectroscopy and related phenomena* 101 (1999): 449-454.

[40] Zhang, Peng, P. Richard, T. Qian, Y-M. Xu, X. Dai, and H. Ding. "A precise method for visualizing dispersive features in image plots." *Review of Scientific Instruments* 82, no. 4 (2011): 043712.

[41] The estimated error here is a combination of the standard error in parabolic fitting and the standard deviation of the effective mass along different high symmetry directions.

[42] Based on our DFT-LDA calculation.

[43] Zhang, Yi, Tay-Rong Chang, Bo Zhou, Yong-Tao Cui, Hao Yan, Zhongkai Liu, Felix Schmitt et al. "Direct observation of the transition from indirect to direct bandgap in atomically thin epitaxial $MoSe_2$." *Nature nanotechnology* 9, no. 2 (2014): 111-115.

[44] Jin, Wencan, Po-Chun Yeh, Nader Zaki, Datong Zhang, Jerzy T. Sadowski, Abdullah Al-Mahboob, Arend M. van Der Zande et al. "Direct measurement of the thickness-dependent electronic band structure of MoS_2 using angle-resolved photoemission spectroscopy." *Physical review letters* 111, no. 10 (2013): 106801.

[45] Kośmider, K., J. W. González, and J. Fernández-Rossier. "Large spin splitting in the conduction band of transition metal dichalcogenide monolayers." *Physical Review B* 88, no. 24 (2013): 245436.

[46] Xiao, Di, Ming-Che Chang, and Qian Niu. "Berry phase effects on electronic properties." *Reviews of modern physics* 82, no. 3 (2010): 1959.

[47] Xiao, Di, Gui-Bin Liu, Wanxiang Feng, Xiaodong Xu, and Wang Yao. "Coupled spin and valley physics in monolayers of MoS_2 and other group-VI dichalcogenides." *Physical Review Letters* 108, no. 19 (2012): 196802.

[48] Knox, Kevin R., Andrea Locatelli, Mehmet B. Yilmaz, Dean Cvetko, Tevfik Onur Menteş, Miguel Ángel Niño, Philip Kim, Alberto Morgante, and Richard M. Osgood Jr. "Making angle-resolved photoemission measurements on corrugated monolayer crystals: Suspended exfoliated single-crystal graphene. "*Physical Review B* 84, no. 11 (2011): 115401.

[49] Flege, J. I., E. Vescovo, G. Nintzel, L. H. Lewis, S. Hulbert, and P. Sutter. "A new soft X-ray photoemission microscopy beamline at the National Synchrotron Light Source." *Nuclear Instruments and Methods in Physics Research Section B: Beam Interactions with Materials and Atoms* 261, no. 1 (2007): 855-858.

[50] See the Supplemental Material section of the paper: http://link.aps.org/supplemental/10.1103/PhysRevLett.111.106801 for more details about sample preparation, ARPES configuration, and matrix-element analysis.

[51] Sutter, Peter, and Eli Sutter. "Microscopy of graphene growth, processing, and properties." *Advanced Functional Materials* 23, no. 20 (2013): 2617-2634.

Chapter 6

Substrate Interactions with Suspended and Supported Monolayer MoS_2 – An ARPES Study

In this chapter, we report the direct measurement of the electronic structure of exfoliated monolayer molybdenum disulfide (MoS_2) using micrometer-scale angle-resolved photoemission spectroscopy. Measurement of both suspended and supported monolayer MoS_2 elucidate the effects of interaction with a substrate. A suggested relaxation of the in-plane lattice constant is found for both suspended and supported monolayer MoS_2 crystals. For suspended MoS_2, a careful investigation of the measured uppermost valence band gives an effective mass at $\bar{\Gamma}$ and $\bar{K}$ of 2.00 m_0 and 0.43 m_0, respectively. We also measure an increase in the band linewidth from the midpoint of $\bar{\Gamma} - \bar{K}$ to the vicinity of $\bar{K}$ and briefly discuss its possible origin.

6.1 Introduction

Two-dimensional (2D) crystals of monolayer transition metal dichalcogenides (TMD) are of increasing interest both for their unusual physics and for their potential use in novel nanoelectronic devices [1][2]. In particular, their substantial intrinsic bandgap of 1.3-1.9 eV [3], which is thickness dependent, makes them a promising alternative to the most well studied 2D material, graphene, which lacks an intrinsic bandgap. Several fabrication techniques, including micromechanical exfoliation, chemical vapor deposition, and molecular beam epitaxy have been used to produce atomically thin TMD sheets on a variety of substrates. However, the substrate and any adsorbates may affect the electronic structure of TMD crystals and films via a modification of their dielectric environment or by the introduction of short- or long-range disorder. The latter is caused by chemical bonding or surface roughness. Particularly, in their monolayer form, interactions with a supporting substrate or adsorbed impurities are also known to influence the electronic structure [4] and significantly affect the electrical performance of van der Waals materials [5][6]. In addition, it has been shown that the substrate dielectric constant plays an important role in determining the excitonic binding energy as well as quasiparticle lifetime in 2D layered materials [7][8]. Such phenomena thus make understanding of the effects of the substrate on 2D materials of pressing importance for both fundamental studies and potential applications in devices.

In order to minimize the effect of substrate interactions on atomically thin crystals, one of two different ameliorating procedures is typically utilized. One approach is to decouple the sample from the substrate by intercalating alkali metals such as Li and K, and,

in the process, induce electron doping of the sample [9]. Another approach reduces interaction by placing samples over patterned cavities or trenches etched into a supporting substrate [10][11]. Samples prepared using either of these approaches have shown that suspended MoS_2 samples exhibit altered electronic properties from those of MoS_2 supported directly on the substrate, including a photoluminescence blueshift in the optical gap in freestanding monolayer MoS_2 [12] and a 2- to 10-fold improvement in the carrier mobility in suspended MoS_2 [13].

In this chapter, we study the properties and key parameters of suspended monolayer MoS_2 by measuring its electronic structure using micrometer-scale angle-resolved photoemission spectroscopy (μ-ARPES). For comparison, measurements on substrate-supported monolayer MoS_2 were also carried out to provide a baseline case, in which a substrate was present. In addition, the results were independently cross examined using a spectroscopic photoemission-low energy electron microscope (SPELEEM) system. First, our measurements suggest that there is a change in the lattice constant of monolayer MoS_2 *vs.* that in its bulk crystal form. In particular by determining the absolute size of the surface Brillouin zone (SBZ) of monolayer MoS_2, we find a ~3.6% decrease in the SBZ, indicative of a ~3.6% expansion of the in-plane lattice parameter (denoted as **a** in Figure 6.1(d)), compared to bulk MoS_2. Second, our results provide insight into the effect of the substrate on the monolayer MoS_2 electronic structure. Due to interactions with the substrate in supported monolayer MoS_2, band structure distortion is observed in comparison to the suspended case. Third, by fitting our measured band dispersions, we extract the effective mass at $\bar{\Gamma}$ and $\bar{K}$ in both suspended and supported monolayer MoS_2.

6.2 Experimental Methods

Our experiments were performed at two synchrotron beamlines. The first was the Spectromicroscopy Beamline at the Elettra Synchrotron light source [14], which provided scanning photoemission microscopy (SPEM) and micro-ARPES measurements of suspended and supported monolayer MoS_2. The spectrometer energy resolution of this instrument was set to 100 meV at a 27 eV incident photon energy and with a beam spot size of 1 μm in diameter. ARPES band structure measurements were also obtained on a SPELEEM system at the National Synchrotron Light Source (NSLS) beam line U5UA [15][16]. The SPELEEM instrument also allowed imaging by photoemission electron microscopy (PEEM). For both measurements, the samples were annealed in ultra-high vacuum for 2 hours at ~350 ℃ prior to the acquisition of photoemission spectra.

Our crystal samples were exfoliated monolayer MoS_2 flakes, which were examined and calibrated using Raman spectroscopy. To obtain areas of suspended MoS_2, coexisting with supported regions of the flakes, substrates patterned by lithography and etching were used. As schematically shown in Figure 6.1(a), a grid pattern of cylindrical cavities with diameters of 2 or 5 μm, and depths of 1 μm were etched into a Si wafer covered with a native oxide; monolayer MoS_2 flakes were then exfoliated and transferred onto the patterned substrate using the same procedure as described in Ref.[17]. SPEM was used to characterize the sample before investigating the band structure *in-situ* with μ-ARPES. Figure 6.1(b) & (c) show an optical image of an exfoliated monolayer MoS_2 flake before transfer onto the patterned substrate, and the corresponding SPEM image of the partially suspended flake after transfer to the patterned substrate, respectively. Contrast between the

suspended MoS_2, supported MoS_2, and the bare substrate is obtained by acquiring locally excited photoelectrons in a kinetic energy window of 18-22 eV, imaged by scanning the sample. Figures 6.1(e) & (f) show an optical image of a MoS_2 flake before transfer, and the corresponding PEEM image of the same flake after transfer to the patterned substrate. Both SPEM and PEEM measurements show clear contrast between suspended and supported MoS_2; thus allowing accurate selection of regions of interest for μ-ARPES measurements in the two different sample regions.

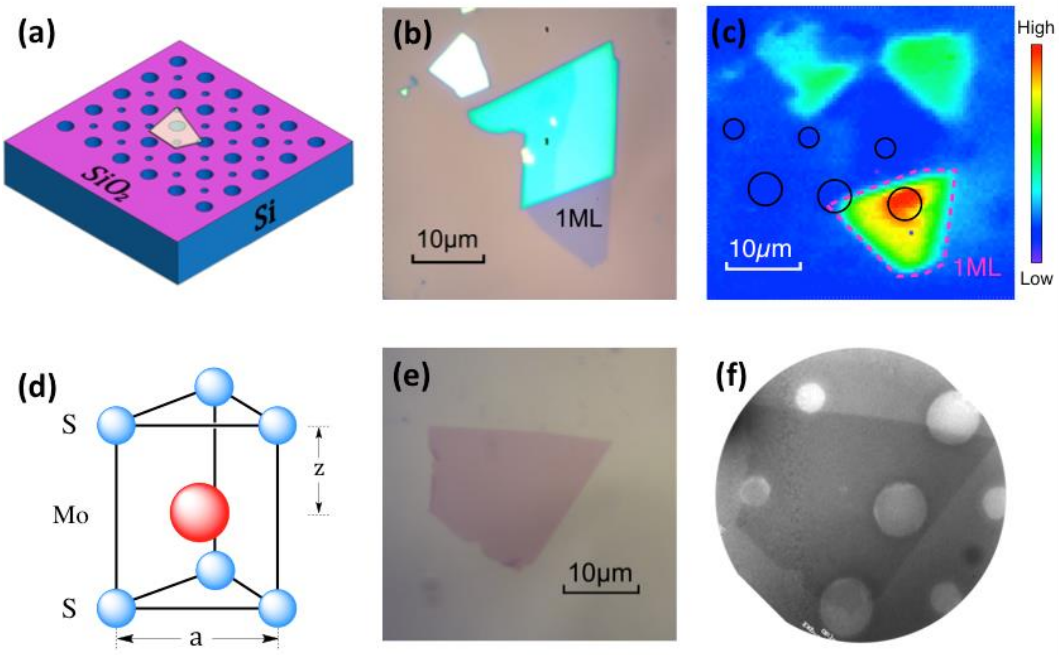

Figure 6.1 (a) Sketch of the sample configuration. Monolayer MoS_2 flakes were transferred onto patterned silicon chips (blue) with native oxide (purple). (d) Atomic structure of monolayer MoS_2. The in-plane lattice constant is denoted as **a**, and the interplane distance between Mo and S atomic planes in the same 'monolayer' sheet is denoted as **z**. (b) & (e) Optical microscope images of the exfoliated monolayer MoS_2 samples. (c) Scanning photoemission microscopy map corresponding to the sample shown in panel (b), acquired

with a photon energy of 27 eV by collecting photoelectrons with an energy window of 18-22 eV. The area of monolayer MoS_2 flake is enclosed by a dashed pink frame, and the suspended regions are marked with black circles. (f) PEEM image of sample shown in panel (e).

6.3 Experimental Results

6.3.1 ARPES Band Mapping

Figures 6.2(a)-(b) show the μ-ARPES band maps of suspended monolayer MoS_2 along the $\bar{\Gamma}$-$\bar{M}$ and $\bar{\Gamma}$-$\bar{K}$ high-symmetry lines of the SBZ, respectively. To better visualize the ARPES features, we perform 2D-curvature processing [18], which is similar to the widely used 1D second-derivative method. The 2D-curvature intensity plot is shown in Figure 6.2(c). For the μ-ARPES measurements performed at Elettra, the off-normal photon angle-of-incidence uses different selection rules than that of the normal photon angle-of-incidence configuration of the SPELEEM system at U5UA; this difference enabled us to observe the previously invisible S 3*p*-derived bands [19]. By measuring beyond the first SBZ, we determined the positions of $\bar{K}$ and $\bar{M}$, and found that $\overline{\Gamma K}$ = 1.28 ± 0.04 $Å^{-1}$, and $\overline{\Gamma M}$ = 1.11 ± 0.04 $Å^{-1}$, values which are 3.58 ± 3.01% smaller than those of the bulk SBZ ($\overline{\Gamma K}$ = 1.3256 $Å^{-1}$, $\overline{\Gamma M}$ = 1.1479 $Å^{-1}$); see Figure 6.3. While this result is limited by the large error, our measurement suggests the presence of a ~3.6% lateral lattice expansion in monolayer MoS_2 compared to bulk, yielding a lattice constant of 3.28 ± 0.10 Å. In X-ray diffraction and Raman-scattering studies of single layer MoS_2 prepared by exfoliation of Li-intercalated MoS_2 powder immersed in water, Yang *et al.* also reported that the in-plane

lattice constant expands to 3.27 ± 0.015 Å, about 3.5% larger than the accepted bulk value (3.16 Å) [20]. The authors attributed this lattice expansion to a change in the Mo coordination from trigonal prismatic for the case of dry MoS_2 to bulk octahedral for the water immersed MoS_2. On a different but related note, there have also been several reports of a blue-shift in the in-plane E^1_{2g} phonon mode of monolayer MoS_2 [21], which has been attributed to reduced interlayer interaction [22]. Our observation of a larger in-plane lattice constant for monolayer Mos_2 would be expected to produce a redshift in the in-plane E^1_{2g} phonon mode. It thus appears that the reduced interlayer interaction has more of an effect on this phonon mode than our experimentally suggested in-plane lattice constant expansion. We should also note that in our previous SPELEEM measurements, we calibrated the momentum space by assuming that the lattice spacing is unaffected when a MoS_2 crystal is thinned down to a monolayer, i.e., we assumed the same in-plane lattice parameter as for bulk MoS_2 [19].

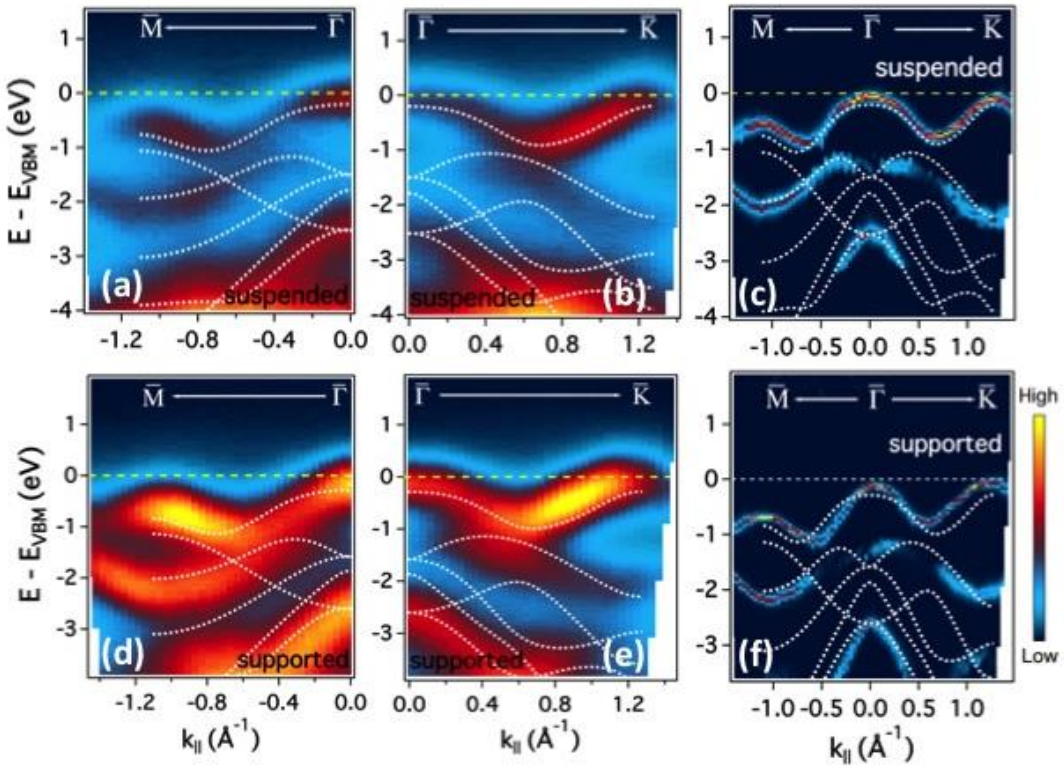

Figure 6.2 (a)-(b) Micro-ARPES band maps of suspended MoS_2 along $\bar{\Gamma} - \bar{M}$ and $\bar{\Gamma} - \bar{K}$, respectively. (c) 2D-curvature intensity plot of the suspended MoS_2 bands along $\bar{M} - \bar{\Gamma} - \bar{K}$ high symmetry line. (d)-(e) ARPES band maps of supported MoS_2 along $\bar{\Gamma} - \bar{M}$ and $\bar{\Gamma} - \bar{K}$, respectively. (f) 2D-curvature intensity plot of the supported MoS_2 bands along $\bar{M} - \bar{\Gamma} - \bar{K}$ high symmetry line. DFT-calculated bands using the relaxed lattice parameters are overlaid onto all the band maps for comparison.

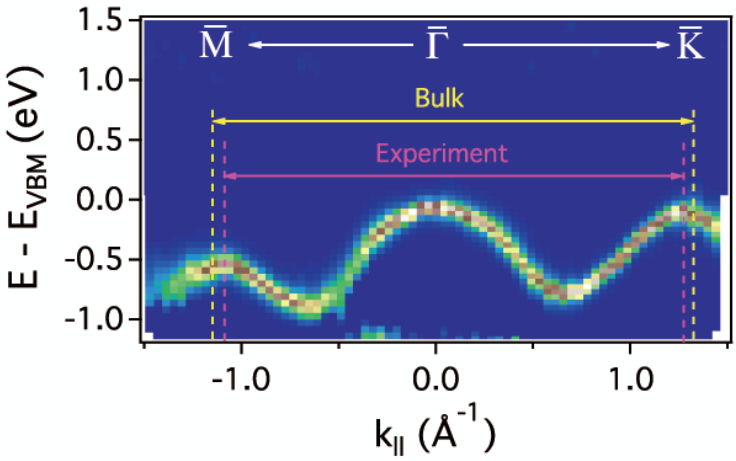

Figure 6.3 2D curvature plot of the uppermost valence band (UVB) of suspended monolayer MoS_2 along high symmetric direction. Pink dashed lines mark the local maximum of the UVB extracted from ARPES measurement and the yellow dashed lines denote the positions of $\bar{M}$ and $\bar{K}$ using the lattice constant of bulk MoS_2.

6.3.2 DFT Calculation

There are a plethora of density functional theory (DFT) calculations on the band structure of monolayer MoS_2. In addition, there have been several studies of the relaxation of the in-plane lattice constant by way of structural optimization calculations [23-25]. While a thorough theoretical understanding of the full lattice relaxation of MoS_2 is beyond the scope of this experimental study, we have performed DFT calculations using a range of different out-of-plane lattice constants with the primary purpose of seeking better agreement with our measured electronics structure. In particular, we used the ABINIT code [26, 27], with a generalized gradient approximation (GGA) functional [28]; note that Van der Waals interactions are not pertinent for calculation of our experimentally realized suspended monolayer MoS_2 crystal. These calculations investigated the corresponding

modification of the intraplane distance (denoted as **z** in Figure 6.1(b)) between the Mo and S atomic planes while utilizing the experimentally determined in-plane lattice constant stated above. Our result shows that when **z** is allowed to increase by ~2% compared to its bulk value (z = 1.586Å) [29], the calculated bands agree surprisingly closely with the experimental measurements, even though our calculation does not capture many of the detailed physics of our crystal, such as spin-orbit coupling. Note that our suggested increase in **z** is in contrast to a low-energy-electron-diffraction study of the top layer of single-crystal bulk MoS_2, which reported a ~5% decrease of **z** within the topmost layer [30]. We again note that our deduction of an expansion of the out-of-plane lattice constant is driven simply by a desire to seek better agreement of the DFT-derived bands with measurements and is not a definitive finding.

6.3.3 Discussion

The intrinsic nature of the experimentally suggested increase in the in-plane monolayer lattice constant is supported by our μ-ARPES measurements of supported monolayer MoS_2, from which an approximately identical relaxed lattice constant, within our error, is extracted (a = 3.30 ± 0.10 Å , see supplementary materials). Figures 6.2(d)-(e) show the ARPES band maps of supported monolayer MoS_2 along the $\bar{\Gamma}$-$\bar{M}$and $\bar{\Gamma}$-$\bar{K}$ high-symmetry lines of the SBZ, respectively. Figure 6.2(f) is the corresponding 2D-curvature intensity plot [18]. Our calculated bands (using the relaxed lattice parameters) are overlaid onto Figure 6.2(a)-(f) for comparison. Note that Figure 6.2(a)-(b) & (d)-(e) are all normalized to the highest intensity of their respective band maps.

Note that, as shown in Figure 6.2 (e) & (f), the valence band maximum at $\bar{K}$ is still higher than that at $\bar{\Gamma}$, which means that the relaxation of the lattice constant for monolayer MoS_2 does not alter the location of the valence band maximum in the BZ. This result indicates that the key conclusion in our previous work [19], i.e., the valence band maximum shift from $\bar{\Gamma}$ to $\bar{K}$, when MoS_2 is thinned down to 1ML, remains intact.

In our previous study, we had also tentatively attributed a "compression" in the measured dispersion of the UVB, relative to the DFT derived UVB, to surface interaction. The present work, which measures both supported and suspended monolayer MoS_2, suggests, on the other hand, that the compression is predominately due to lattice relaxation. While surface interactions are present, we deduce them to be relatively weak, due to the fact that electronic structure of the substrate-supported monolayer MoS_2 does not differ significantly from that of the suspended case.

TABLE I: Effective mass extracted from DFT calculation (Ref. [18], [23]-[26]) and ARPES measurements.

	Package/functional	$\bar{\Gamma}$	$\bar{K}$
S.W. Yun et al	FLAPW/GGA	3.524	0.637
Andor Kormányos et al	VASP/HSE06	2.24	0.53
H. Peelaers et al	VASP/HSE06	2.8	0.44
T. Cheiwchanchamnangij et al	Quasiparticle GW/LDA	3.108	0.428
Experiment on suspended MoS_2	N/A	2.00	0.43
Experiment on supported MoS_2	N/A	1.85	0.48
This work (without spin-orbit interaction)	ABINIT/ GGA	2.65	0.52

6.3.4 Effective Mass

Figure 6.4(a) shows the UVB of suspended monolayer MoS_2 and Figure 6.4(b)-(c) along with the corresponding energy distribution curves (EDCs). Our measurements of suspended MoS_2 that are free from substrate interaction, and the access to precise absolute parallel momentum values afforded by the spectromicroscopy instrumentation, enable us to fully investigate the effective mass (m_{eff}) of intrinsic MoS_2. Note that effective mass is a particularly important parameter in transport measurements since it plays a crucial role in determining the sample mobility. Despite many theoretical predictions of the effective mass of monolayer MoS_2, there remains a glaring lack of agreement. Further transport measurements of the effective mass have thus far been lacking. Table I summarizes several predicted values of the effective mass reported by different theoretical groups using different DFT techniques/functionals (Ref. [7], [25], [33]-[35].) The simplest approach to fitting the data uses a parabolic fitting over a range of ± 0.08 Å^{-1}; we extract the effective mass at $\bar{\Gamma}$ and $\bar{K}$ to be $(2.00 \pm 0.35)m_0$ and $(0.43 \pm 0.02)m_0$, respectively. The value at $\bar{K}$ agrees most closely with the value reported by Kormányos *et al.*, while the value at $\bar{\Gamma}$ is very close to the value reported by Cheiwchanchamnangij *et al*.

In the substrate-supported case, we extract values of the hole effective mass that are not too different from that of intrinsic, i.e., suspended MoS_2. We find values of m_{eff} at $\bar{\Gamma}$ and $\bar{K}$ of $(1.85 \pm 0.22)m_0$ and $(0.48 \pm 0.02)m_0$, respectively. We note that the effective mass value stated here is somewhat lower than that quoted in our previous work [19]. We attribute that difference to the improved energy resolution and better signal to noise

available using the SPEM; also, the inverse relation between dispersion and effective mass accentuates small differences in the relatively flat dispersion around $\bar{\Gamma}$.

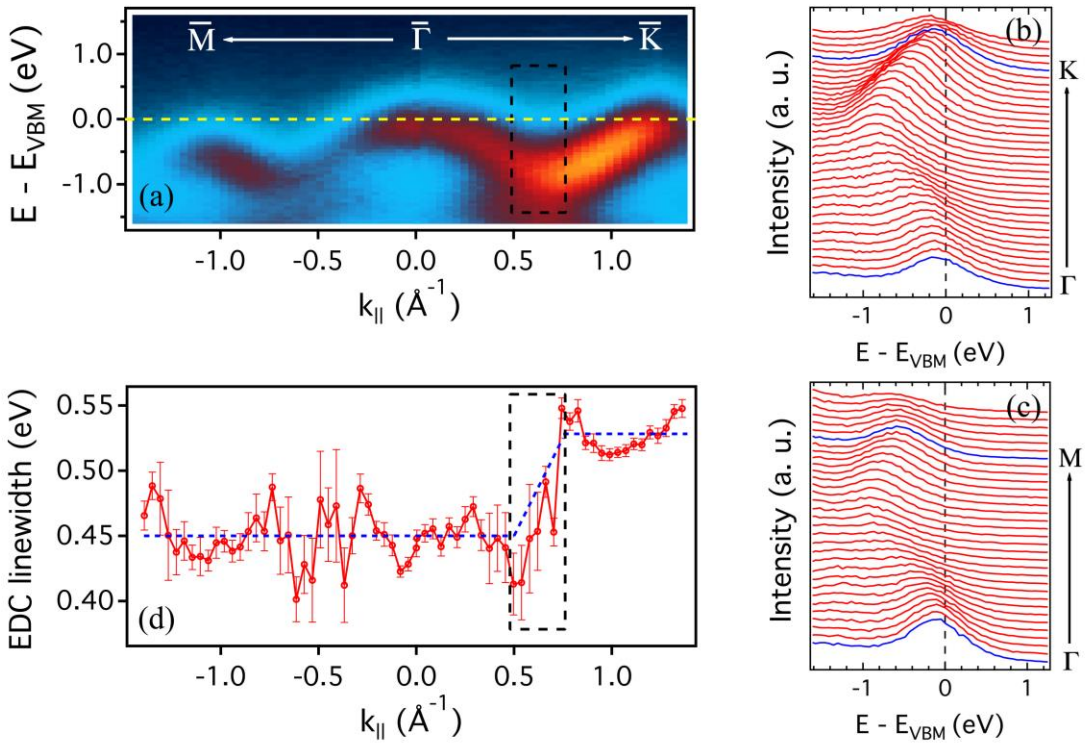

Figure 6.4 (a) UVB of suspended monolayer MoS_2. (b)-(c) EDCs of the UVB along the $\bar{\Gamma}$-$\bar{K}$ and $\bar{\Gamma}$-$\bar{M}$ direction, respectively. (d) Gaussian linewidth *vs* momentum plot. The blue dashed lines are the guide to the eyes to trace the evolution of the linewidth with momentum. The black dashed boxes in (a) & (d) enclose the transition region where the linewidth increases.

6.3.5 Spin-Orbit Coupling

At $\overline{\mathrm{K}}$ in crystal momentum space, the UVB of monolayer MoS_2 is derived primarily from the Mo $d_{x^2-y^2}$/ d_{xy} orbitals. Due to broken inversion symmetry and strong spin-orbit coupling, a spin-splitting of 148 meV at $\overline{\mathrm{K}}$ has been predicted by theory [23]. This splitting in the upper valence band has been of recent interest for exploration of the coupling of spin and valley degree of freedom in MoS_2 [36]. Since we were not able to directly resolve this spin-orbit splitting in our ARPES measurements, we did examine carefully the variation of the linewidth of the upper-most valence band with change in crystal momentum, and observe the following. We performed single Gaussian peak fitting (with a linear background) to the EDCs of the upper-most valence band to extract the FWHM of the Gaussian peak. The linewidth vs momentum plot is shown in Figure 6.4 (d). Using the blue dashed line as a guide to the eye, we find that the EDC linewidth remains constant with a small variation (450 ± 19 meV) from $\bar{M}$ to the midpoint (defined as $\bar{A}$) of $\overline{\Gamma K}$. Note that the relatively bigger error bars in the vicinity of $k_{\parallel}$ = -0.5Å $^{-1}$ is due to the vanishing spectrum intensity. In the vicinity of the midpoint of $\overline{\Gamma K}$, which is enclosed by a black dashed box in Figure 6.4(a) & (d), the linewidth gradually increases. In the vicinity of $\bar{K}$, the linewidth (528 ± 13 meV) is found to be larger than that at $\bar{M}$ and $\bar{\Gamma}$.

Regarding the origin of this increased linewidth, we make the following observation. There are two possible explanations for this sharp linewidth increase in the vicinity of $\bar{A}$ to $\bar{K}$: 1) a decrease in the quasi-particle lifetime or 2) a splitting of the spin degenerate band into two bands due to spin-orbit coupling. We favor the latter explanation due to-the location being consistent with theoretical calculations of the splitting in MoS_2.

However it is clear that a definitive conclusion of this linewidth increase awaits higher resolution studies.

6.4 Conclusion

In conclusion, we have performed ARPES measurements on the valence bands of suspended and supported monolayer MoS_2. Our ARPES measurements of suspended MoS_2 reveal good qualitative and quantitative agreement with theory and elucidate the effects of a native-oxide covered Si substrate on the band structure of monolayer MoS_2. We find a suggested expansion of the in-plane lattice constant and deduce an expansion of the intra-plane lattice constant, which may be indicative of an atomic structure that is sensitive to stacking. Fitting of the measured valence band dispersion provides an experimentally derived value for the effective mass of both suspended and substrate-supported monolayer MoS_2. We also measure an increase in the linewidth over the band region from the midpoint of $\bar{\Gamma} - \bar{K}$ to the vicinity of $\bar{K}$.

6.5 References

[1] Radisavljevic, Branimir, Aleksandra Radenovic, Jacopo Brivio, V. Giacometti, and A. Kis. "Single-layer MoS_2 transistors." *Nature nanotechnology* 6, no. 3 (2011): 147-150.

[2] Lembke, Dominik, and Andras Kis. "Breakdown of high-performance monolayer MoS2 transistors." *ACS nano* 6, no. 11 (2012): 10070-10075.

[3] Mak, Kin Fai, Changgu Lee, James Hone, Jie Shan, and Tony F. Heinz. "Atomically thin MoS_2: a new direct-gap semiconductor." *Physical Review Letters* 105, no. 13 (2010): 136805.

[4] Zhou, S. Y., G-H. Gweon, A. V. Fedorov, P. N. First, W. A. De Heer, D-H. Lee, F. Guinea, AH Castro Neto, and A. Lanzara. "Substrate-induced bandgap opening in epitaxial graphene." *Nature materials* 6, no. 10 (2007): 770-775.

[5] Chen, Jian-Hao, Chaun Jang, Shudong Xiao, Masa Ishigami, and Michael S. Fuhrer. "Intrinsic and extrinsic performance limits of graphene devices on SiO_2." *Nature nanotechnology* 3, no. 4 (2008): 206-209.

[6] Dean, C. R., A. F. Young, I. Meric, C. Lee, L. Wang, S. Sorgenfrei, K. Watanabe et al. "Boron nitride substrates for high-quality graphene electronics."*Nature nanotechnology* 5, no. 10 (2010): 722-726.

[7] Cheiwchanchamnangij, Tawinan, and Walter RL Lambrecht. "Quasiparticle band structure calculation of monolayer, bilayer, and bulk MoS_2." *Physical Review B* 85, no. 20 (2012): 205302.

[8] Molina-Sanchez, Alejandro, and Ludger Wirtz. "Phonons in single-layer and few-layer MoS_2 and WS_2." *Physical Review B* 84, no. 15 (2011): 155413.

[9] Eda, Goki, Hisato Yamaguchi, Damien Voiry, Takeshi Fujita, Mingwei Chen, and Manish Chhowalla. "Photoluminescence from chemically exfoliated MoS_2." *Nano letters* 11, no. 12 (2011): 5111-5116.

[10] Locatelli, Andrea, Kevin R. Knox, Dean Cvetko, Tevfik Onur Mentes, Miguel Angel Nino, Shancai Wang, Mehmet B. Yilmaz, Philip Kim, Richard M. Osgood Jr, and Alberto Morgante. "Corrugation in exfoliated graphene: an electron microscopy and diffraction study." *ACS nano* 4, no. 8 (2010): 4879-4889.

[11] Knox, Kevin R., Andrea Locatelli, Mehmet B. Yilmaz, Dean Cvetko, Tevfik Onur Menteş, Miguel Ángel Niño, Philip Kim, Alberto Morgante, and Richard M. Osgood Jr. "Making angle-resolved photoemission measurements on corrugated monolayer crystals: Suspended exfoliated single-crystal graphene."*Physical Review B* 84, no. 11 (2011): 115401.

[12] Ochedowski, Oliver, Kolyo Marinov, Nils Scheuschner, Artur Poloczek, Benedict Kleine Bussmann, Janina Maultzsch, and Marika Schleberger. "Effect of contaminations and surface preparation on the work function of single layer MoS_2." *Beilstein journal of nanotechnology* 5, no. 1 (2014): 291-297.

[13] Jin, Taiyu, Jinyeong Kang, Eok Su Kim, Sunhee Lee, and Changgu Lee. "Suspended single-layer MoS_2 devices." *Journal of Applied Physics* 114, no. 16 (2013): 164509.

[14] Dudin, Pavel, Paolo Lacovig, Claudio Fava, Eugenio Nicolini, Anna Bianco, Giuseppe Cautero, and Alexei Barinov. "Angle-resolved photoemission spectroscopy and imaging with a submicrometre probe at the SPECTROMICROSCOPY-3.2 L beamline of Elettra." *Journal of synchrotron radiation* 17, no. 4 (2010): 445-450.

[15] Flege, J. I., E. Vescovo, G. Nintzel, L. H. Lewis, S. Hulbert, and P. Sutter. "A new soft X-ray photoemission microscopy beamline at the National Synchrotron Light Source." *Nuclear Instruments and Methods in Physics Research Section B: Beam Interactions with Materials and Atoms* 261, no. 1 (2007): 855-858.

[16] Sutter, P., M. S. Hybertsen, J. T. Sadowski, and E. Sutter. "Electronic structure of few-layer epitaxial graphene on Ru (0001)." *Nano letters* 9, no. 7 (2009): 2654-2660.

[17] Yeh, Po-Chun, Wencan Jin, Nader Zaki, Datong Zhang, Jerzy T. Sadowski, Abdullah Al-Mahboob, Arend M. van der Zande et al. "Probing substrate-dependent long-range surface structure of single-layer and multilayer MoS_2 by low-energy electron microscopy and microprobe diffraction." *Physical Review B*89, no. 15 (2014): 155408.

[18] Zhang, Peng, P. Richard, T. Qian, Y-M. Xu, X. Dai, and H. Ding. "A precise method for visualizing dispersive features in image plots." *Review of Scientific Instruments* 82, no. 4 (2011): 043712.

[19] Jin, Wencan, Po-Chun Yeh, Nader Zaki, Datong Zhang, Jerzy T. Sadowski, Abdullah Al-Mahboob, Arend M. van Der Zande et al. "Direct measurement of the thickness-dependent electronic band structure of MoS_2 using angle-resolved photoemission spectroscopy." *Physical review letters* 111, no. 10 (2013): 106801.

[20] Yang, D., S. Jiménez Sandoval, W. M. R. Divigalpitiya, J. C. Irwin, and R. F. Frindt. "Structure of single-molecular-layer MoS_2." *Physical Review B* 43, no. 14 (1991): 12053.

[21] Lee, Changgu, Hugen Yan, Louis E. Brus, Tony F. Heinz, James Hone, and Sunmin Ryu. "Anomalous lattice vibrations of single-and few-layer MoS_2." *ACS nano* 4, no. 5 (2010): 2695-2700.

[22] Luo, Xin, Yanyuan Zhao, Jun Zhang, Qihua Xiong, and Su Ying Quek. "Anomalous frequency trends in MoS_2 thin films attributed to surface effects." *Physical Review B* 88, no. 7 (2013): 075320.

[23] Zhu, Z. Y., Y. C. Cheng, and Udo Schwingenschlögl. "Giant spin-orbit-induced spin splitting in two-dimensional transition-metal dichalcogenide semiconductors." *Physical Review B* 84, no. 15 (2011): 153402.

[24] Ramasubramaniam, Ashwin. "Large excitonic effects in monolayers of molybdenum and tungsten dichalcogenides." *Physical Review B* 86, no. 11 (2012): 115409.

[25] Yun, Won Seok, S. W. Han, Soon Cheol Hong, In Gee Kim, and J. D. Lee. "Thickness and strain effects on electronic structures of transition metal dichalcogenides: 2H-MX_2 semiconductors (M= Mo, W; X= S, Se, Te)."*Physical Review B* 85, no. 3 (2012): 033305.

[26] Gonze, Xavier. "A brief introduction to the ABINIT software package." *Zeitschrift für Kristallographie* 220, no. 5/6/2005 (2005): 558-562.

[27] Gonze, Xavier, B. Amadon, P-M. Anglade, J-M. Beuken, F. Bottin, P. Boulanger, F. Bruneval et al. "ABINIT: First-principles approach to material and nanosystem properties." *Computer Physics Communications* 180, no. 12 (2009): 2582-2615.

[28] Perdew, John P., Kieron Burke, and Matthias Ernzerhof. "Generalized gradient approximation made simple." *Physical review letters* 77, no. 18 (1996): 3865.

[29] Böker, Th, R. Severin, A. Müller, C. Janowitz, R. Manzke, D. Voß, P. Krüger, A. Mazur, and J. Pollmann. "Band structure of MoS_2, $MoSe_2$, and α-$MoTe_2$: angle-resolved photoelectron spectroscopy and ab initio calculations." *Physical Review B* 64, no. 23 (2001): 235305.

[30] Mrstik, B. J., R. Kaplan, T. L. Reinecke, M. Van Hove, and S. Y. Tong. "Surface-structure determination of the layered compounds MoS_2 and $NbSe_2$ by low-energy electron diffraction." *Physical Review B* 15, no. 2 (1977): 897.

[31] Knox, Kevin R., Shancai Wang, Alberto Morgante, Dean Cvetko, Andrea Locatelli, Tevfik Onur Mentes, Miguel Angel Niño, Philip Kim, and R. M. Osgood Jr. "Spectromicroscopy of single and multilayer graphene supported by a weakly interacting substrate." *Physical Review B* 78, no. 20 (2008): 201408.

[32] Ishigami, Masa, J. H. Chen, W. G. Cullen, M. S. Fuhrer, and E. D. Williams. "Atomic structure of graphene on SiO_2." *Nano letters* 7, no. 6 (2007): 1643-1648.

[33] Peelaers, Hartwin, and Chris G. Van de Walle. "Effects of strain on band structure and effective masses in MoS_2." *Physical Review B* 86, no. 24 (2012): 241401.

[34] Kormányos, Andor, Viktor Zólyomi, Neil D. Drummond, Péter Rakyta, Guido Burkard, and Vladimir I. Fal'ko. "Monolayer MoS_2: Trigonal warping, the Γ valley, and spin-orbit coupling effects." *Physical Review B* 88, no. 4 (2013): 045416..

[35] Kormányos, Andor, Viktor Zólyomi, Neil D. Drummond, and Guido Burkard. "Spin-orbit coupling, quantum dots, and qubits in monolayer transition metal dichalcogenides." *Physical Review X* 4, no. 1 (2014): 011034.

[36] Mak, Kin Fai, Keliang He, Jie Shan, and Tony F. Heinz. "Control of valley polarization in monolayer MoS_2 by optical helicity." *Nature nanotechnology* 7, no. 8 (2012): 494-498.

Chapter 7

Direct Measurement of the Tunable Electronic Structure of Bilayer MoS_2 by Interlayer Twisting

In this chapter, we explore beyond the direct bandgap, energy stable A-B stacked monolayer 2H-MoS_2, and began a study of van der Waals bounded, indirect-bandgap bilayer MoS_2. In particular, we investigate this simple stack with an artificial interlayer twist. Thus, using angle-resolved photoemission, we directly measure the interlayer angle-dependent electronic band structure of bilayer MoS_2. Our measurements are performed on a chemical-vapor-deposition sample, with arbitrarily-stacked bilayer MoS_2 flakes. Our measurements provide direct evidence for the evolution of the valence-band at $\bar{\Gamma}$ with interlayer coupling tuned by the interlayer twist angle. Such a twist leads to an energy variation of ~200 meV for an interlayer twist angle of ~39°. Further, our direct measurements of the valence band provide a detailed outlook on the band dispersion that evolves with twist angle, such that we can extract the hole-effective- mass as a function of the interlayer coupling. These results directly confirm theoretical explanations given in recently published photoluminescence reports, and provide insight to the understanding of twisted-bilayer dichalcogenide device physics. This twisted bilayer MoS_2 is also an ideal model system for other bilayer heterostructure studies.

7.1 Introduction

Van der Waals layered materials, especially the transition metal dichalcogenides (TMDs), can be prepared as atomically thin semiconductors[1] with high-quality homo- or hetero-junction interfaces without restriction of lattice matching or interlayer crystallographic alignment. The utilization of layered materials opens up potential applications for bandgap engineering by using strain [2], stacking up of layers [3][4], or building of heterojuntions [5]. For TMDs such as MoS_2, $MoSe_2$, WS_2, and WSe_2, their electrical, optical [1][6], and vibrational properties [7] are also known to be significantly dependent on interlayer coupling. One of the well-known consequences of interlayer coupling in TMDs is the direct-to-indirect bandgap transition from monolayer to multilayer films. The magnitude of the indirect band gap has also been predicted to vary with both the number of layers and the interlayer separation distance,[7] due to interlayer electronic coupling . To date, however, the experimentally-resolved electronic band structure of interlayer interaction in TMDs has only been studied in the case of crystallographically aligned layers, as found in samples exfoliated from bulk materials [1][6][7][8][9]. Recently, photoluminescence (PL) [10][11][12][13] and density functional theory (DFT) [14] studies on arbitrary-aligned bilayer MoS_2 flakes prepared by stacking chemical-vapor-deposition (CVD) monolayer MoS_2 have been reported.

Based on these recent PL results and their corresponding Raman measurements on characteristic phonon modes E_{2g} and A_{1g} for twisted-bilayer MoS_2 [10][11][12][13], one can conclude that (1) the interlayer coupling of bilayer MoS_2 has a local maximum for 60-degree twist angle, (2) the interlayer coupling has a global maximum for 0-degree twist

angle, and (3) the interlayer coupling is at a minimum when the twist angle approaches 30-40 degrees. By way of density functional theory, these reports all attribute their results to a twist-angle-dependent layer separation, which consequently determines the amount of energy splitting of the highest occupied states around $\bar{\Gamma}$. The extent of this energy splitting is reflected as a variation in the photon energy of the photoluminescence measurements. In light of these recent reports, it is important to confirm their findings using a different probe, and to verify their theoretical predictions via direct experimental measurements of the energy-momentum dispersion that is not accessible through photoluminescence studies. Furthermore, given the current intense interest in the field to the fabrication and electronic engineering of heterostructures composed of two-dimensional-monolayer materials, it is important to characterize the electronic structure via a direct band structure probing tool, such as angle resolved photoemission (ARPES).

In this chapter, we directly measure the energy-momentum-dispersion of CVD-grown and transferred twisted bilayer MoS_2 ($TBMoS_2$) for several twist angles ranging from 0° to 60° using micrometer-scale angle-resolved photoemission spectroscopy (μ-ARPES). Utilizing bright-field (BF) low-energy electron microscopy (LEEM) we locate twisted bilayer regions of interest and determine their relative twist angle and region boundaries by way of micrometer-scale low-energy electron diffraction (μ-LEED) and dark-field (DF) LEEM imaging. Our μ-ARPES measurements over the whole surface-Brillouin zone reveal the $\bar{\Gamma}$ state is, indeed, the highest lying occupied state for all twist angles, affirming the indirect bandgap designation for bilayer MoS_2, irrespective of twist angle, made by the photoluminescence reports[10][11][12]. We directly quantify the

energy separation between the high symmetry points $\overline{\Gamma}$ and $\overline{K}$ of the highest occupied states; this energy separation is predicted to be directly proportional to the interlayer separation, which is a function of twist angle. We confirm this with our μ-ARPES measurements and we observe the same trend reported by the above mentioned photoluminescence and Raman studies. We also confirm that this trend is a result of the energy shifting of the top-most occupied state at $\overline{\Gamma}$, which was predicted by DFT calculations [10]-[14]. Finally, we also report on the variation of the hole effective mass at $\overline{\Gamma}$ and $\overline{K}$ with respect to twist angle and compare it with theory.

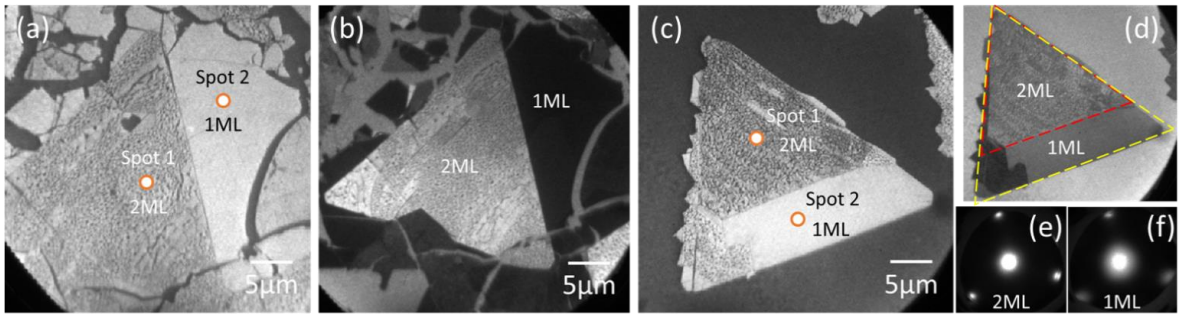

Figure 7.1 Bright field and dark field LEEM images of $TBMoS_2$ of twist angle (a), (b) at 47° and (c), (d) at ~0°, respectively. The CVD-grown MoS_2 exhibits islands and a continent of patches. Both were used in our experiment. The markers in (a) and (c) indicate where the measurement were taken. In (a), the spot 1 sits on the top layer (triangular) and the spot 2 lies on the large flake that extended outside the top layer. The same goes in (c), where the top and bottom flakes are both triangular. Since their twist angle is nearly zero, their (d) DF image shows almost of contrast difference, and their (e), (f) LEED pattern orientation is the same. The electron energies used were (a) 3.5eV (b) 40eV (c) 4.6eV (d) 36.4eV (e), (f) 40eV.

7.2 Experimental Methods

Our measurements were performed using the spectroscopic photoemission and low-energy electron microscope (SPE-LEEM) system at the National Synchrotron Light Source (NSLS) beamline U5UA [15][16]. The spectrometer energy step of this instrument was set to 100 meV at 42 eV incident photon energy with a beam spot size of 1-μm diameter. The momentum resolution is ~0.02 $Å^{-1}$. The $TBMoS_2$ samples were stacked and pre-transferred to a native-oxide covered Si substrate. After transfer, the sample was checked by Scanning Electron Microscopy (SEM) to confirm whether the transfer was successful (Figure 7.1(a)), since few-layer MoS_2 films lack optical contrast on a native-oxide Si substrate. Prior to measurements, these samples were annealed at 350℃ for ~12 hours under UHV conditions to remove contaminants. BF/DF LEEM and PEEM were utilized as they provide rich information on surface morphology and work function information for the post-transferred $TBMoS_2$ (Figure 7.1(b)-(d)).

7.2.1 Sample Preparation

Measuring bilayer MoS_2 of different twist angles is made possible by transferring two sheets of chemical vapor deposition (CVD) grown monolayer MoS_2, one on top of another, on a native-oxide Si substrate [3][17]. The monolayer CVD MoS_2 samples were prepared using the solid precursor growth technique [18] on a 285nm SiO_2 coated Si chip. The growth substrates were pre-cleaned in acetone and isopropanol, followed by 2 hr rinsing in Piranha solution and 2 minutes of O_2 plasma etching. More details on the growth procedure can be found in Ref. [18]. The CVD growth yields monolayer MoS_2 with

different shaped flakes ranging from triangular/polygonal islands to large continuous patches. The thickness of the sample is examined by Raman and photoluminescence spectroscopy [19][20] prior to transfer. Two sheets of ML CVD MoS_2 containing randomly-orientated flakes are transferred on a native-oxide Si substrate; this allows one to create arbitrary bilayer MoS_2 flakes and patches exhibiting different twist angles.

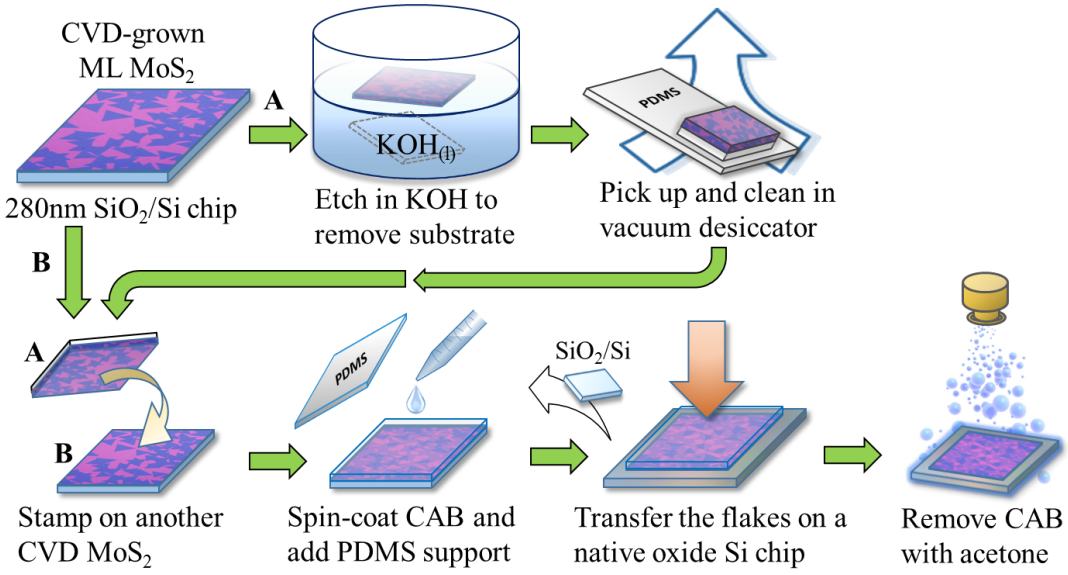

Figure 7.2 The making of $TBMoS_2$ via transferring two monolayer CVD grown MoS_2 sheets on a native-oxide Si substrate. Note that the interface of the two ML MoS_2 remains clean during transfer, only exposed to air for a short time.

Figure 7.2 shows the flowchart of the transfer method. CVD grown MoS_2 on SiO_2/Si (flake A) was carefully laid afloat on a 1M KOH solution, with a PDMS stamp pressed on the MoS_2 surface to support the flakes and to protect the surface cleanness. The KOH etched away the SiO_2 epi-layer, causing the chips to fall off, and leaving the PDMS/MoS_2 stack in solution. Later, the stack was rinsed with DI water, left dried for a

day, and scooped up using a PDMS sample holder. After removing the first PDMS cover from the stack, the MoS_2 was cleaned in a vacuum desiccator, and then was stamped onto another CVD MoS_2 (flake B) on SiO_2/Si. Notice that the interface of the two MoS_2 monolayers are clean and untouched by any solution. Now, the PDMS sample holder used earlier was removed from the MoS_2/MoS_2/substrate stack and a layer of cellulose acetate butyrate (CAB) polymer was spin-coated on top of the stack. Extra CAB polymer was cut out, leaving only a square of CAB covering the MoS_2 flakes. A drop of water was put along the cut to help peel off the SiO_2/Si substrate. Note that the MoS_2 flakes are prone to attach to the CAB film instead of the SiO_2/Si substrate. The CAB/MoS_2/MoS_2 stack was then stamped on a native-oxide Si substrate that has been cleaned and pre-patterned with Au alignment marks. Now, the whole chip was immersed in acetone to dissolve the CAB layer, then rinsed in DI water, and then dried in a vacuum desiccator to complete the transfer.

7.2.2 Sample Identification and Quality Check

Sample quality and crystal orientation of $TBMoS_2$ were examined using both BF- and DF- LEEM and μ-LEED (Figure 7.1).DF-LEEM greatly enhances the contrast between ML MoS_2 flakes of different crystal orientations (Figure 7.1(b) and 7.1(d)), as compared to BF-LEEM (Figure 7.1(a) and 7.1(c)). DF-LEEM also allows us to identify the boundary of the region of interest. Note that in Figure 7.1(d), for the case of the ~0° twist angle, the DF-LEEM image shows the same relative contrast between the top (red line) and bottom (yellow line) layer as in the case of BF-LEEM, as expected for identically oriented layers. The corresponding diffraction patterns (at a primary electron energy of 40 eV) of the top and bottom layer of the 0-degree $TBMoS_2$ are shown in Figure 7.1(e) and 7.1(f),

respectively. At this energy, the LEED patterns clearly show a 3-fold symmetry, and can be used to identify crystal orientation. Note that the LEED pattern of $TBMoS_2$ at this energy corresponds to the orientation of the top-most layer due to the limited electron penetration depth [21].

7.3 Experimental Results

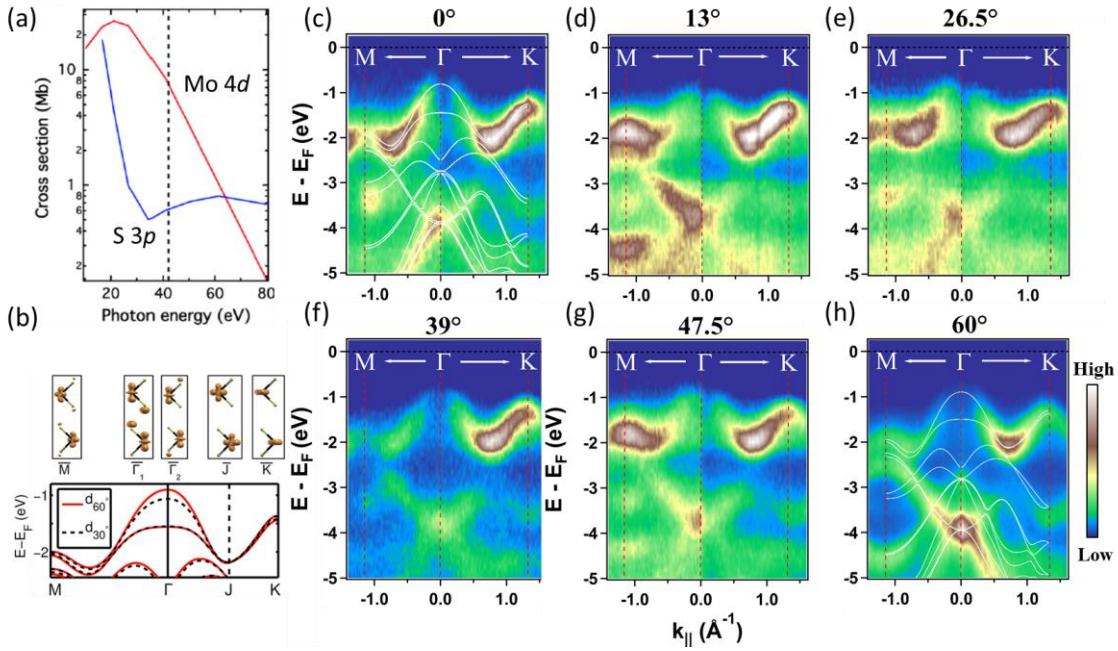

Figure 7.3 (a) Atomic photoionization cross-section for Mo 4d and S 3p subshells as a function of ARPES photon energy. At 42eV, Mo 4d has a higher photoionization cross-section than that of S 3p by an order-of-magnitude difference. Therefore, the dominant features in our ARPES measurement are the contributions of Mo 4d subshell. Note also that the Cooper minimum of the S orbital is ~34eV. (b) DFT-calculated electronic structure of $TBMoS_2$ at 60° (solid lines) and 30° (dashed lines), highlighting the impact of layer separation, in which the interlayer separation is larger for $\theta = 30°$ compared to that of $\theta =$

60° by ~0.3 Å. The band of the top-most valence band at $\bar{\Gamma}$ varies strongly with the interlayer spacing change, while the $\bar{K}$ point at conduction band minimum and valence band remains intact. μ-ARPES measurements of TBMoS$_2$ cut along $\bar{M}$-$\bar{\Gamma}$-$\bar{K}$ at (c) 0° (d) 13° (e) 26.5° (f) 39° (g) 47.5° (h)60°. The overlaying white lines are DFT-calculated bands. ARPES intensity maps were normalized for each direction, $\bar{\Gamma}$-$\bar{K}$ and $\bar{\Gamma}$-$\bar{M}$, independently to achieve better contrast.

7.3.1 ARPES Band Mapping

Our μ-ARPES measurements of twisted bilayer MoS$_2$ along the high symmetry directions $\bar{M}$-$\bar{\Gamma}$-$\bar{K}$, covering twist angles θ = 0° (AA stacking), 13°, 26°, 39°, 47° and 60° (AB stacking, normal bilayer), are shown in Figure 7.3. (The 60° data was taken from an earlier report [3]). The electronic structure of the top-lying valence bands of MoS$_2$ is derived from hybridization of the Mo 4d and S 3p orbitals [22][23] each of which possesses a strongly varying photon-energy-dependent photoionization cross-section [24], as shown in Figure 7.3(a). In our measurement, a photon energy of 42eV was utilized, for which the corresponding photon ionization cross-section of the Mo 4d subshell is an order of magnitude larger than that of S 3p (indicated by the vertical dashed line in Figure 7.3(a)). Thus, the primary contribution to our μ-ARPES measurements, shown in Figure 7.3(c)-(h), are from the Mo 4d orbitals. In our experiments, the incident photon flux was directed normal to the sample surface so that its polarization is in the plane of the MoS$_2$ layers, thus suppressing excitation of states with out-of-plane character. This explains why the Mo- and S-derived states with a z or out-of-plane component, i.e., d_{z^2} or p_z, located in the

uppermost valence band (UVB) near $\bar{\Gamma}$ have a consistently relatively weaker, but non-zero, intensity.

The bandgap of bilayer MoS_2 has previously been reported to be an indirect transition of ~1.6 eV [3][6] between the valence band maximum (VBM) at $\bar{\Gamma}$ and the conduction band minimum (CBM) at $\bar{K}$, as shown in Figure 7.3(b). Based on our measurement of the Fermi energy, the lower bound of the bandgap of $TBMoS_2$ must be greater than 0.9 eV; this result also suggests that our CVD-grown $TBMoS_2$ is slightly electron-doped. As deduced from theoretical calculations [14] and photoluminescence measurements [10][11][12][13], the evolution of the uppermost valence band and the lowermost conduction with twist angle in $TBMoS_2$ changes only the VBM at $\bar{\Gamma}$, while leaving the VBM at $\bar{K}$ and the CBM at $\bar{K}$ almost intact (the direct gap changes by ≤ 20 meV between 30° and 60° of twist angle [10]). This situation is confirmed by DFT calculations for twist angles between 30° and 60°, shown in Figure 7.3(b) and in our ARPES-measured band structure in Figure 7.3(c)-(h), which shows a changing $\bar{\Gamma}$ state and a fixed $\bar{K}$ state for several twist angles and referenced to the Fermi level. To see this $\bar{\Gamma}$ state evolution more clearly, we used the second-derivative filtering method to extract the top-most valence band for each twist angle as shown in Figure 7.4. The bands were referenced with respect to the $\bar{K}$ state maximum for this latter case.

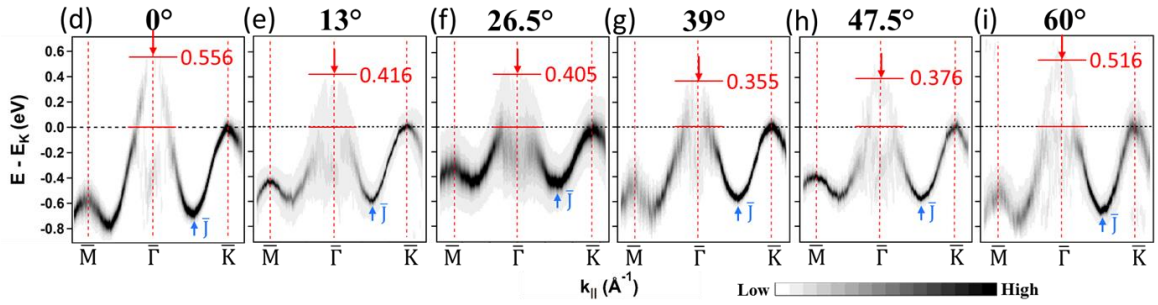

Figure 7.4 (a)-(f): The corresponding second-derivative-filtered top-most valence band of Fig. 2 (c)-(h), respectively. The number overlaid on each bands is an averaged value of the energy difference of $\bar{\Gamma}$ and $\bar{K}$ over all six high symmetry directions $\bar{K}$-$\bar{\Gamma}$-$\bar{K}$.

7.3.2 Twist Angle Dependent Bandgap Transition

In Figure 7.4, it is clear that for TBMoS$_2$ the VBM lies at $\bar{\Gamma}$ instead of $\bar{K}$, contrary to the ML case, in agreement with earlier ARPES [3][25] and photoluminescence [10][11][12][13] reports which correspond to an indirect transition shown in Figure 7.3(b). The VBM at $\bar{\Gamma}$ shifts downward in energy as the twist angle is varied from 0° or 60° to ~40°. This is explained by the weakening of interlayer-coupling that affects only the out-of-plane Mo d_{z^2} and S p_z orbitals, i.e., the states located about $\bar{\Gamma}$. Note that in Figure 7.4, the indicated values, which denote the energy difference between the $\bar{\Gamma}$ and $\bar{K}$ valence band maxima, were derived from the averaged value of all six high-symmetry equivalent directions, $\bar{\Gamma}$-$\bar{K}$, via careful peak fittings. These extracted values are further compared to the PL measurements and theoretical calculations in Figure 7.5(c).

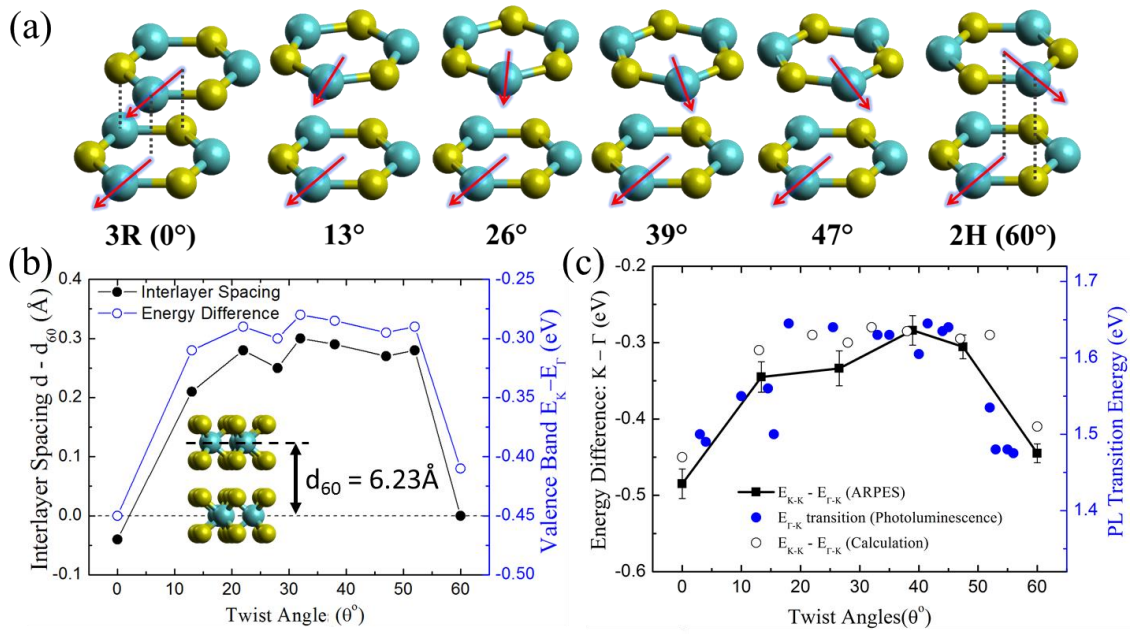

Figure 7.5 (a) Atomic structure of each twist angle measured in this work. The arrows denoted the orientation of each layer. (b) Calculated interlayer spacing and its corresponding energy difference between VBM at $\bar{\Gamma}$ and $\bar{K}$ versus twist angles, derived from DFT. The interlayer spacing is defined as the separation between the Mo-Mo or S-S layers, and is referenced with respect to the 60° (normal bilayer MoS_2). This result is adapted from Arend *et al.* [10]. (c) A comparison of the energy difference from our ARPES results (blue lined-dots), the PL measurement [10] (solid circles), and the calculation [10] (empty circles). Note that the ARPES and PL data are normalized for comparison by aligning at 60°.

The origin of the band gap opening with twist angle is the interlayer coupling that predominately affects valence band states derived from out-of-plane orbitals. The relative orientation of the top and bottom layers of bilayer MoS_2 leads to a change in the interlayer spacing which, intuitively, and as predicted by theoretical calculations, is proportional to

the degree of interlayer coupling (see Figure 7.5(b)). The VBM at $\bar{\Gamma}$, derived from out-of-plane Mo d_{z^2} and S p_z orbitals, is sensitive to the out-of-plane interlayer coupling . Increasing the twist angle of TBMoS_2 from 0° to 30-40°, decreases the interlayer spacing and thus leads to a decrease in the interlayer coupling, resulting in an overall downward shifting in energy up to 200 meV of the $\bar{\Gamma}$ state. Since the $\bar{K}$ state, either occupied or un-occupied, is effectively invariant to the interlayer coupling for the range of interlayer spacings encountered here, the interlayer-twisting-induced bandgap shift is solely determined by the $\bar{\Gamma}$ state. This correlation between twist angle and both the indirect optical excitation and the $\bar{K}$ - $\bar{\Gamma}$ energy difference is shown using previously reported PL measurements and our ARPES measurements, respectively, in Figure 7.5(c). The evolution of the $\bar{K}$ - $\bar{\Gamma}$ energy difference vs twist angle is clearly observed by our ARPES measurements, which shares the same trend with the PL data [10] and theoretical calculations [10]. Note that the ARPES and PL data shown in Figure 7.5(c) are aligned with respect to the 2H (60degree) bilayer MoS_2 and the error bars denote the standard deviation of the fittings from all six high-symmetry equivalent directions, which are well under the detector error of ± 0.10 eV. Thus, this result provides direct experimental evidence for the mechanism controlling the indirect bandgap opening in a bilayer MoS_2 system by interlayer angle twisting.

In addition, note that the interlayer spacing is slightly different between θ = 0° and 60° as shown in Figure 7.5(b), and it reaches a maximum value at θ = 30-40°. This result leads to the asymmetry in energy between θ = 0° and 60°, and a global energy maximum value at θ ≈ 30-40°, respectively, shown in Figure 7.5(c). Notice that in different DFT

calculations provided in Ref.[10]-[14], the twist angle of 0° can have an interlayer spacing that is either equivalent to or slightly different from that of 60° due to different atomic registrations. This can be understand by considering a finite in-plane translational displacement in the AA-stacking configuration which leads to a change in the interlayer spacing. Note, however, that this in-plane displacement or horizontal registration is not directly responsible for energy shifting or bandgap variation [12][14], likewise, twisting the layers but keeping the interlayer separation fixed will not change the interlayer coupling strength, as predicted by DFT [10]. Further discussions can be found in Ref. [10][12][14] and their supplemental materials. We also note that we don't see evidence of coupling due to long range structural order, e.g. Moiré, in our measurements.

7.3.3 Effective Mass

Hole Effective Mass ($Å^{-1}$) vs Twist Angle (θ°)

	0°	*13°*	*26°*	*39°*	*47°*	*60°*
At K	0.91 ± 0.07	1.55 ± 0.06	1.57 ± 0.09	1.30 ± 0.19	1.10 ± 0.10	1.06 ± 0.31
At Γ	0.50 ± 0.03	0.44 ± 0.13	0.48 ± 0.09	0.48 ± 0.07	0.60 ± 0.03	0.56 ± 0.06

Table 1 Hole effective mass in unit of electron mass m_e, extracted from ARPES measured band structure at $\bar{K}$ and $\bar{\Gamma}$ for several twist angles.

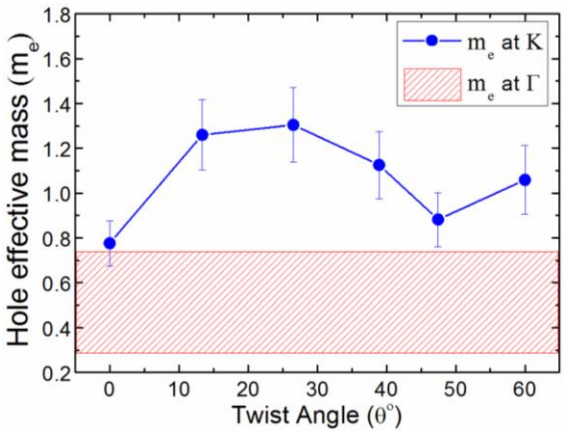

Figure 7.6 Plot of hole effective mass vs twist angles. The hole effective mass at $\bar{\Gamma}$ appears to be angle independent, though the accuracy of resolved band near $\bar{\Gamma}$ is limited by the ARPES selection rule. The hole effective mass at $\bar{K}$ is angle-dependent and has a maximum near 30°.

An analysis of the curvature of the bands from the μ-ARPES measurements also allows us to deduce the effective mass of $TBMoS_2$. Figure 7.6 shows the evolution of the hole effective mass at $\bar{K}$ and at $\bar{\Gamma}$ for each measured twist angle; the corresponding values are also found in Table 1. We find that the hole effective mass at $\bar{\Gamma}$ varies very little with twist angle, and has an average value of $0.51 \pm 0.03 m_0$ (where m_0 is the electron mass), indicated by the red dashed line as a guide to the eye in Figure 7.6. However, the hole effective mass at $\bar{K}$ has a significant variation of up to ~70% between $\theta = 0°$ and 26°. Also, the hole effective mass at $\bar{K}$ is in general larger than that predicted by DFT calculations [11] for twist angles away from 30° (0.91 ± 0.07 vs 0.582 at 0°and 1.06 ± 0.31 vs 0.577 at 60°), but becomes comparable when reaching 30° (0.48 ± 0.09 at 26° vs 0.44 at 30°). The origin of the discrepancy between experiment and DFT calculations is uncertain at this time. Our finite energy resolution and slight asymmetry along each high symmetry

direction does contribute to the measurement error. However, it is also apparent that there is an overall difference in band dispersion between theory and experiment. We note that "renormalization" in bands of other similar 2D dichalcogenides have also been reported [26][27][28][29].

7.4 Conclusion

In conclusion, we have studied the surface structure and occupied electronic bands of CVD-grown and transferred bilayer MoS_2 with arbitrary twist angles ranging from 0° to 60°. Bright field LEEM provided real-space structural measurements of $TBMoS_2$, while dark-field LEEM imaging, combined with μ-LEED, helped us define the interlayer crystal orientations. Our μ-ARPES measurements have probed the occupied valence-band structure of bilayer MoS_2 at twist angles of 0°, 13°, 26°, 39°, 47°, and 60°. We observed an energy shift of up to 200 meV at the VBM at $\bar{\Gamma}$ when the twist angle reaches 40°. Since the VBM and CBM at $\bar{K}$ are predicted to be independent of interlayer twisting, bandgap opening is solely determined by the energy level of the VBM at $\bar{\Gamma}$. This variation at $\bar{\Gamma}$ is due to the evolution of the interlayer coupling strength which in turn is a function of the interlayer spacing. Thus, the $\bar{\Gamma}$ VBM state shifts in energy with twist angle, and thus one can tune the bandgap of bilayer MoS_2. This observation agrees well with theory and PL measurements. We expect that these results will provide physical insight to the understanding of the optical and electronic properties of $TBMoS_2$, and to engineering the bandgap by tuning the interlayer coupling, since the ability to control the interlayer coupling is important to the development of TMD-based devices.

7.5 References

[1] Splendiani, Andrea, Liang Sun, Yuanbo Zhang, Tianshu Li, Jonghwan Kim, Chi-Yung Chim, Giulia Galli, and Feng Wang. "Emerging photoluminescence in monolayer MoS_2." *Nano letters* 10, no. 4 (2010): 1271-1275.

[2] Conley, Hiram J., Bin Wang, Jed I. Ziegler, Richard F. Haglund Jr, Sokrates T. Pantelides, and Kirill I. Bolotin. "Bandgap engineering of strained monolayer and bilayer MoS_2." *Nano letters* 13, no. 8 (2013): 3626-3630.

[3] Jin, Wencan, Po-Chun Yeh, Nader Zaki, Datong Zhang, Jerzy T. Sadowski, Abdullah Al-Mahboob, Arend M. van Der Zande et al. "Direct measurement of the thickness-dependent electronic band structure of MoS_2 using angle-resolved photoemission spectroscopy." *Physical review letters* 111, no. 10 (2013): 106801.

[4] Yeh, Po-Chun, Wencan Jin, Nader Zaki, Datong Zhang, Jonathan T. Liou, Jerzy T. Sadowski, Abdullah Al-Mahboob et al. "Layer-dependent electronic structure of an atomically heavy two-dimensional dichalcogenide." *Physical Review B* 91, no. 4 (2015): 041407.

[5] Kośmider, Krzysztof, and Joaquín Fernández-Rossier. "Electronic properties of the MoS_2-WS_2 heterojunction." *Physical Review B* 87, no. 7 (2013): 075451.

[6] Mak, Kin Fai, Changgu Lee, James Hone, Jie Shan, and Tony F. Heinz. "Atomically thin MoS_2: a new direct-gap semiconductor." *Physical Review Letters* 105, no. 13 (2010): 136805.

[7] Lee, Changgu, Hugen Yan, Louis E. Brus, Tony F. Heinz, James Hone, and Sunmin Ryu. "Anomalous lattice vibrations of single-and few-layer MoS2." *ACS nano* 4, no. 5 (2010): 2695-2700.van der Zande, Arend M., Jens Kunstmann, Alexey Chernikov, Daniel A. Chenet, YuMeng You, XiaoXiao Zhang, Pinshane Y. Huang et al. "Tailoring the electronic structure in bilayer molybdenum disulfide via interlayer twist." *Nano letters* 14, no. 7 (2014): 3869-3875.

[8] Wu, Sanfeng, Jason S. Ross, Gui-Bin Liu, Grant Aivazian, Aaron Jones, Zaiyao Fei, Wenguang Zhu et al. "Electrical tuning of valley magnetic moment through symmetry control in bilayer MoS_2." *Nature Physics* 9, no. 3 (2013): 149-153.

[9] Yuan, Hongtao, Mohammad Saeed Bahramy, Kazuhiro Morimoto, Sanfeng Wu, Kentaro Nomura, Bohm-Jung Yang, Hidekazu Shimotani et al. "Zeeman-type spin splitting controlled by an electric field." *Nature Physics* 9, no. 9 (2013): 563-569.

[10] van der Zande, Arend M., Jens Kunstmann, Alexey Chernikov, Daniel A. Chenet, YuMeng You, XiaoXiao Zhang, Pinshane Y. Huang et al. "Tailoring the electronic structure in bilayer molybdenum disulfide via interlayer twist." *Nano letters* 14, no. 7 (2014): 3869-3875.

[11] Huang, Shengxi, Xi Ling, Liangbo Liang, Jing Kong, Humberto Terrones, Vincent Meunier, and Mildred S. Dresselhaus. "Probing the Interlayer Coupling of Twisted Bilayer MoS_2 Using Photoluminescence Spectroscopy." *Nano letters*14, no. 10 (2014): 5500-5508.

[12] Liu, Kaihui, Liming Zhang, Ting Cao, Chenhao Jin, Diana Qiu, Qin Zhou, Alex Zettl, Peidong Yang, Steve G. Louie, and Feng Wang. "Evolution of interlayer coupling in twisted molybdenum disulfide bilayers." *Nature communications* 5 (2014).

[13] Castellanos-Gomez, Andres, Herre SJ van der Zant, and Gary A. Steele. "Folded MoS_2 layers with reduced interlayer coupling." *Nano Research* 7, no. 4 (2014): 572-578.

[14] Cao, Boxiao, and Tianshu Li. "Interlayer Electronic Coupling in Arbitrarily Stacked MoS_2 Bilayers Controlled by Interlayer S-S Interaction." *The Journal of Physical Chemistry C* (2014).

[15] Sadowski, Jerzy T. "Pentacene growth on 3-aminopropyltrimethoxysilane modified silicon dioxide." *Optical Materials* 34, no. 10 (2012): 1635-1638.

[16] Sutter, P., M. S. Hybertsen, J. T. Sadowski, and E. Sutter. "Electronic structure of few-layer epitaxial graphene on Ru (0001)." *Nano letters* 9, no. 7 (2009): 2654-2660.

[17] Yeh, Po-Chun, Wencan Jin, Nader Zaki, Datong Zhang, Jerzy T. Sadowski, Abdullah Al-Mahboob, Arend M. van der Zande et al. "Probing substrate-dependent long-range surface structure of single-layer and multilayer MoS_2 by low-energy electron microscopy and microprobe diffraction." *Physical Review B*89, no. 15 (2014): 155408.

[18] van der Zande, Arend M., Pinshane Y. Huang, Daniel A. Chenet, Timothy C. Berkelbach, YuMeng You, Gwan-Hyoung Lee, Tony F. Heinz, David R. Reichman, David A. Muller, and James C. Hone. "Grains and grain boundaries in highly crystalline monolayer molybdenum disulphide." *Nature materials* 12, no. 6 (2013): 554-561.

[19] Splendiani, Andrea, Liang Sun, Yuanbo Zhang, Tianshu Li, Jonghwan Kim, Chi-Yung Chim, Giulia Galli, and Feng Wang. "Emerging photoluminescence in monolayer MoS_2." *Nano letters* 10, no. 4 (2010): 1271-1275.

[20] Mak, Kin Fai, Changgu Lee, James Hone, Jie Shan, and Tony F. Heinz. "Atomically thin MoS_2: a new direct-gap semiconductor." *Physical Review Letters* 105, no. 13 (2010): 136805.

[21] Feenstra, R. M., N. Srivastava, Qin Gao, M. Widom, Bogdan Diaconescu, Taisuke Ohta, G. L. Kellogg, J. T. Robinson, and I. V. Vlassiouk. "Low-energy electron reflectivity from graphene." *Physical Review B* 87, no. 4 (2013): 041406.

[22] Mattheiss, L. F. "Band structures of transition-metal-dichalcogenide layer compounds." *Physical Review B* 8, no. 8 (1973): 3719.

[23] Coehoorn, R., C. Haas, J. Dijkstra, C. J. F. Flipse, R. A. De Groot, and A. Wold. "Electronic structure of $MoSe_2$, MoS_2, and WSe_2. I. Band-structure calculations and photoelectron spectroscopy." *Physical Review B* 35, no. 12 (1987): 6195.

[24] Yeh, J. J., and I. Lindau. "Atomic subshell photoionization cross sections and asymmetry parameters: $1 \leq Z \leq 103$." *Atomic data and nuclear data tables* 32, no. 1 (1985): 1-155.

[25] Eknapakul, Tanachat, Philip DC King, M. Asakawa, Pornpana Buaphet, R-H. He, S-K. Mo, Hidenori Takagi et al. "Electronic structure of a quasi-freestanding MoS_2 monolayer." *Nano letters* 14, no. 3 (2014): 1312-1316.

[26] Jin, Wencan, Po-Chun Yeh, Nader Zaki, Datong Zhang, Jonathan T. Liou, Jerzy T. Sadowski, Alexey Barinov et al. "Substrate interactions with suspended and supported monolayer MoS_2: Angle-resolved photoemission spectroscopy." *Physical Review B* 91, no. 12 (2015): 121409.

[27] Zhang, Yi, Tay-Rong Chang, Bo Zhou, Yong-Tao Cui, Hao Yan, Zhongkai Liu, Felix Schmitt et al. "Direct observation of the transition from indirect to direct bandgap in atomically thin epitaxial $MoSe_2$." *Nature nanotechnology* 9, no. 2 (2014): 111-115.

[28] Ugeda, Miguel M., Aaron J. Bradley, Su-Fei Shi, H. Felipe, Yi Zhang, Diana Y. Qiu, Wei Ruan et al. "Giant bandgap renormalization and excitonic effects in a monolayer transition metal dichalcogenide semiconductor." *Nature materials* 13, no. 12 (2014): 1091-1095.

[29] Ugeda, Miguel M., Aaron J. Bradley, Su-Fei Shi, H. Felipe, Yi Zhang, Diana Y. Qiu, Wei Ruan et al. "Giant bandgap renormalization and excitonic effects in a monolayer transition metal dichalcogenide semiconductor." *Nature materials* 13, no. 12 (2014): 1091-1095.

Chapter 8

2PPE Study on Coverage-dependent Interfacial Charge Transfer Barrier, Work Function, and Electronic Structure at 2D Molecule/Metal Interfaces

This chapter briefly discusses our experiments with 2PPE. The experiments incldue works on (1) organic self-assembled monolayers (SAMs) of thiolates and fluorinated thiolates on Cu(111) and their interfacial electronic structure of as a function of molecular coverage; (2) electronic structure of a hexa-*cata*-hexabenzocoronene (HBC) / Cu(111) interface from 0 to 2 monolayers; (3) image states of epitaxial-grown graphene on Ir(111). Our goal is to improve our fundamental understanding of adsorbate-induced interfacial charge barrier and coverage dependent electronic structure of an extreme hetero-layer of a single crystal metal. In addition, these works shed light on the intermediate states and image potential state of 2D surface system. Our publications related to this chapter can be found in Ref. [1][2][3].

8.1 Introduction

Organic-materials-based electronics are of increasing interest because their materials system can be lightweight, thin, flexible and exhibit new functionalities [4]. Despite these advantages major challenges remain in improving their performance; these include increased efficiency, control of electronic and optical properties, and reduction of any spurious reactivity. In most cases understanding interfacial electronic structure is one of the most important factors in solving many of these chemical and electronic issues [4][5]. For example, since organic interfaces are complex and manifold, it is necessary to influence or control electronic structure to make transport through the interface facile. In addition, interfacial charge physics are important for determining barrier heights for carrier transport [4][5][6]. Many of these fundamental science questions can be best addressed using a well characterized model interface. These include the nature of interface polarization, the height and thickness of interfacial energy barriers and level alignment, molecule control and chemical state, substrate sharpness, and local charge density.

8.2 Coverage-Dependent Interfacial Electronic Structure of Thiophenol and p-Fluorothiophenol on Cu(111)

Thiols have been of particular interest to the organic electronics community both as a model molecular type as well as one that is useful for a series of practical applications including nanoscale contacts and controlling thin films morphologies and interfaces [6]. Thiols are an organosulfur compound having a SH head group. In some cases, thiols interact with the surface and other adsorbates, either with or without loss of hydrogen at

the head group, to form a self-assembled monolayer of the intact thiol or as thiolates, respectively, on metal surfaces [7]. These layers can be used to control the electron- or hole-injection barrier of an electrode by changing its work function. The selection of tail group can also be useful for work function tuning [6].

In our study, we focus on one particular type of thiols: aromatic thiols, which can be an organic semiconductor with chemical contact to the substrate. As a result, understanding the interactions of this molecular class with surfaces and their interfacial electronic structure is needed to control charge transfer or transport properties. We use two-photon photoemission (2PPE) to make a comparative examination of thiopheonol and 4-fluorothiophenol (Figure 8.1) adsorbed on a Cu(111) surface as a function of coverage, i.e. 0-0.3ML. The central difference between the two molecules is that in the latter the para-positioned hydrogen is replaced by fluorine. This replacement leads to the dipoles of comparable magnitude, i.e. $|\mu_0|$ = 1.24D for thiophenol and $|\mu_0|$ = 1.11D for 4-fluorothiophenol, but with very different dipole orientation, i.e. $\Delta\theta \sim 83°$, based on a MP2 calculation [8]. In our experiment setup, we use gas dosing within a UHV system to deposit thiol films of controllable thickness on a Cu(111) surface at 300K. Our 2PPE experiments have shown a marked difference in the interfacial dipoles of the two molecules and show how the interaction of the adsorbed molecule with the surface electron leads to a marked shift due confinement of the surface electron [9].

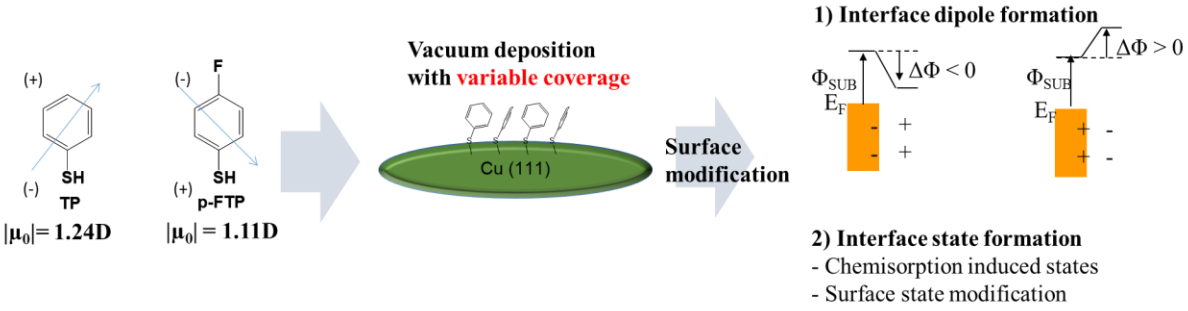

Figure 8.1: Thiophenol (TP) and p-flurothiophoenol (p-FTP) of aromatic thiols group self-assembled on Cu(111) with varable coverage and their interface dipole formation.

In the photoemission data, a series of secondary electron energy cutoff data show the vacuum energy level shift with coverage due to interface dipole formation and changes. A representative set of data, taken at normal incidence and $h\nu$ = 3.76 eV (TP) and 3.88 eV (p-FTP) for a series of doses, is shown in Figure 8.2. Prior to any exposure, measurements were made on the pristine Cu (111) surface, which in each case exhibited a sharp LEED pattern. In Figure 8.2, as seen in Feature A, on the clean surface, an EDC from a clearly resolved Shockley surface state is obtained at the well known [10] binding energy of ~0.4 eV. When the surface was exposed to TP, the signal from the Shockley surface state decreases with each increasing exposure and a new state, labeled B, grows with the coverage. This peak is located at the energy of −0.16 eV below the Fermi level. In addition, as the exposure increases the low-kinetic-energy cutoff decreases in energy; this decrease originates from a decrease in the surface work-function. In addition, another low coverage data were also taken for p-FTP at low coverage and it was found that a similar appearance of a new state as the coverage increased except in this case was located at −0.11 eV.

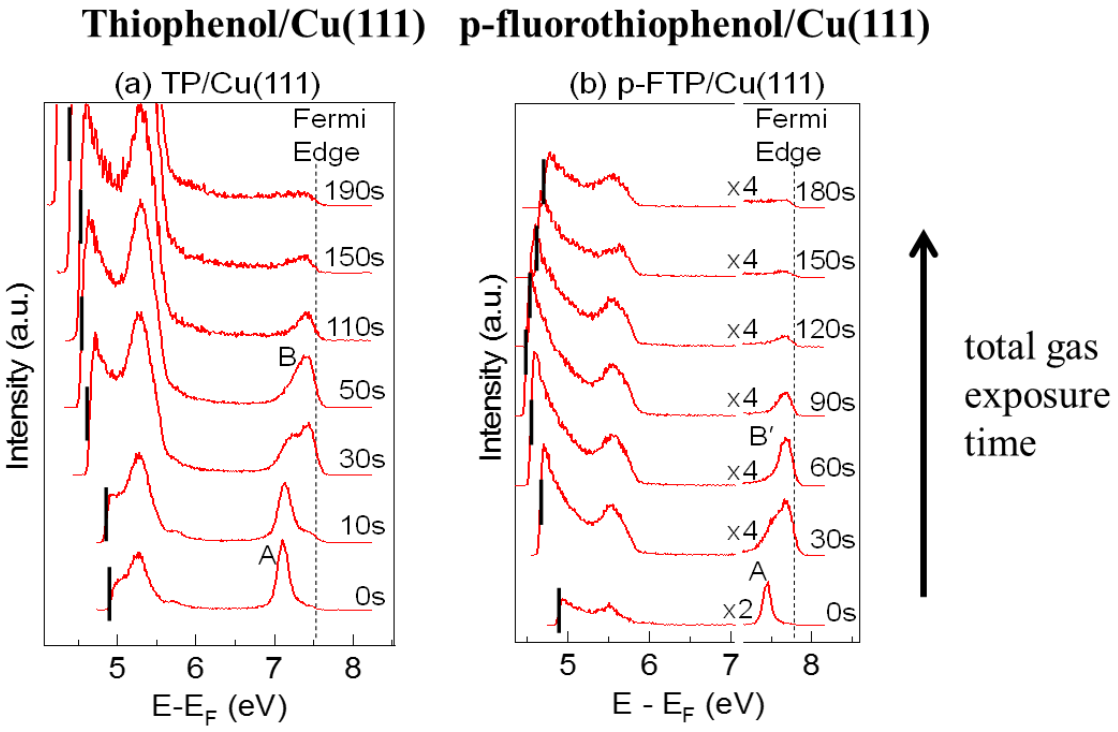

Figure 8.2 2PPE spectra of (Left) TP/Cu(111) and (Right) p-FTP/Cu(111) at low coverage. These series of spectra were collected at different exposure times shown in the right side of each figure. The photon energies used are 3.76 and 3.88 eV for TP and p-FTP, respectively. At the bottom of each panel, the TPPE spectrum of clean Cu(111) is shown. Each thick solid line indicates the low-energy cut-off for each photoemission spectrum. The Fermi edge is also indicated as a dashed line. Features A (surface state), B and B′ (new features) have binding energies of ~ 0.4, 0.16, and 0.14 eV, respectively.

One of our most striking observations is the strong change in low-energy cutoff with coverage that is observed for both TP and p-FTP, as well as the fact that this behavior occurs with opposite polarity for each of the two molecules. This shift in low-energy cutoff can be related to a more fundamental quantity, the change in work-function, by using the fact that in photoemission work-function depends on photon energy and the difference

between low-energy-cut-off and Fermi level, i.e. $\Phi = 2h\nu - (E_F - E_{LC})$, where E_F and E_{LC} are Fermi edge and low-energy cutoff in the 2PPE spectra, respectively. The coverage-dependence of interface dipole (or work-function) is due to the orientation of benzene/fluorobenzne group of molecule. At low density, a lying-down geometry of the deposited molecules is preferred/energy-favorable, but at high density a standing-up geometry is dominating. This result is shown in Figure 8.3.

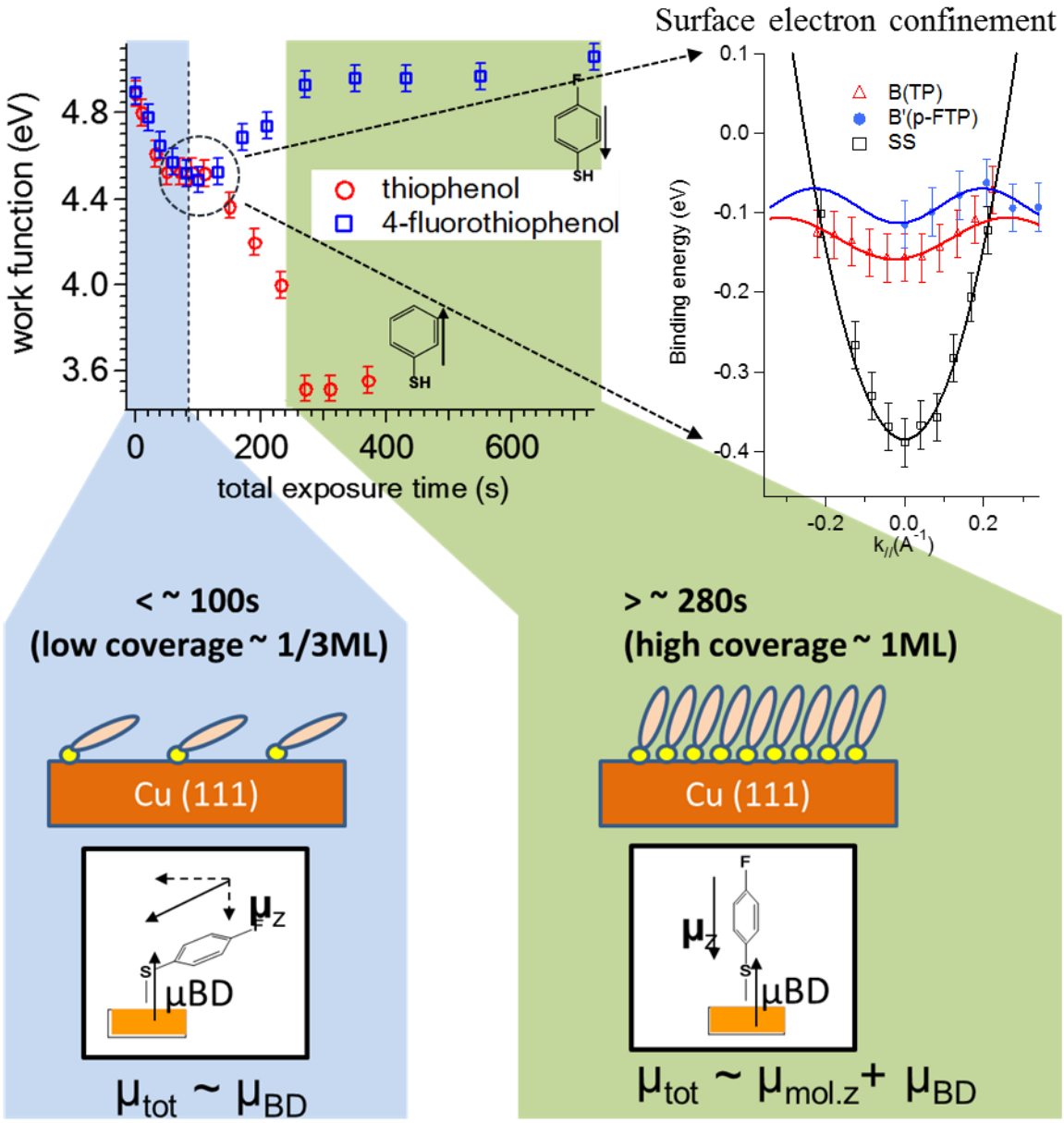

Figure 8.3 Work-function as a function of the total exposure time of TP (red circle) and p-FTP (blue square) on Cu(111). The dashed line indicates the inflection point of both curves, which is at ~100s. The plateau indicates the saturation of the coverage of the adsorbed molecules on the substrate. TP and p-FTP are drawn with the arrow indicating the dipole projected along the 1-4 molecular axis.

To sum up, in this session we studied how a low coverage of benzenethiols on Cu(111) affects electronic structure of the molecule–metal interface. Our first observation is that adsorption alters the surface polarization of the interfacial layer. Our results show that at low coverage the formation of an adsorbate metal bond provides the dominant source of polarization and as the coverage increases the change in adsorbate geometry to an upright geometry further shifts the surface dipole layer and hence the surface polarization. In addition, our results also show the importance of molecule-based surface confinement of the Cu surface electrons in altering their energetic location and dispersion of this surface band.

8.3 Coverage-Dependent Modification of the Surface Electronic Structure of an Organic-Semiconductor-Adsorbate Layer – HBC on Cu(111)

In this work, we use the model system of the organic semiconductor, hexa-*cata*-hexabenzocoronene (HBC), on Cu(111) to develop a fundamental atom-level understanding of the interfacial electronic structure. We use 2PPE in conjunction with UHV surface preparation to probe the interfacial electronic structure of a pristine HBC/Cu(111) interface. It is found that increasing the HBC coverage shifts the vacuum level of the Cu substrate until this shift saturates at a coverage of ~2 ML. Over this same range of coverage, the Shockley and the bare-surface Cu(111) image-potential states are shown to be quenched, while new unoccupied states appear and grow in strength with coverage. The use of momentum- and polarization-resolved photoemission spectra reveals that the new states are modified image states.

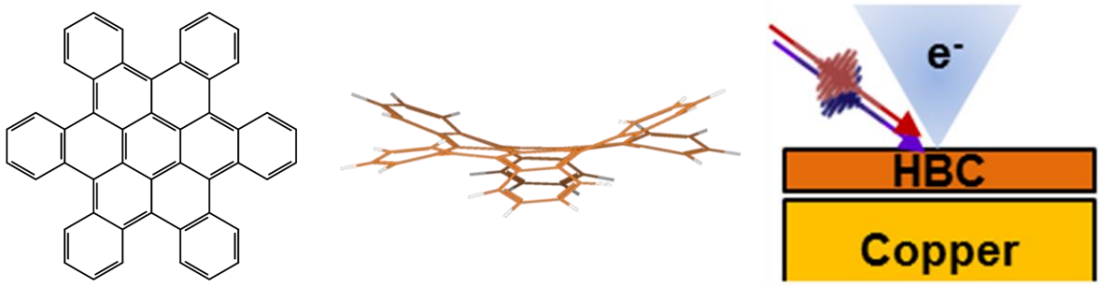

Figure 8.4 Molecular structure of hexa-cata-hexabenzocoronene. The molecule is ~14 Å in width and has a bending angle for the intersecting pentacene-like subunits of ~20˚. (Right) A schematic plot showing our experiment model system set-up.

Our choice of model system is based on recent interest in and synthesis of HBC, a promising organic photovoltaic material, as shown in Figure 8.4. HBC is known to be a non-planar p-type organic semiconductor, which is photoconductive with high-efficiency of charge separation [11]. The material is also chemically air-stable when processed in organic solution. It has also been characterized/tested via the fabrication of HBC solar photovoltaic devices, as described in Ref. [12]. HBC is a robust molecular species; thus differential scanning calorimetry experiments have shown that HBC is thermally stable up to 320˚C.

Figure 8.5 shows our highly-tunable bichromatic photoemission measurement of HBC on Cu(111) at low coverages. These data show clearly an evolution of the electronic structure with coverage. First, at the spectral feature A: when coverage increases to 0.1 ML, this feature rises above the signal-to-noise ratio and then grows with increasing coverage. In fact, a plot of the intensity of this feature normalized to that of the image state (IS) vs coverage, shows clearly that the spectral intensity of this peak vs coverage is anti-correlated to that of the image-state intensity. Note that the n = 1 image state (IS) is found

in the bichromatic 2PPE spectra, while this state is not observed in other monochromatic photoemission spectra. The reason that this state is observed in bichromatic 2PPE is because the energy of the pump photon in bichromatic 2PPE $E_{h\nu,\,pump}$ = 4.72 eV (with $E_{h\nu,\,probe}$ = 1.55 eV) is high enough to access the image state in the first step of the two-photon photoemission scheme, whereas in the monochromatic pumping scheme used here the pump photon energy is $E_{h\nu} < 4$ eV and is energetically unable to access the image-state.

Second, this coverage-dependent measurements also show that the energy of the A state, as measured by its peak location, is independent of the sample work function even for a work-function change (decrease) of ~ 0.3 eV. This absence of a shift with work function change is also seen, for example, in the case of the bare-surface Cu(111) image state, which is denoted by the label IS. In this connection, extensive prior measurements of image states on metal crystals have shown that such states, which are intermediate states for 2PPE, are ”pinned” to the Cu(111) *local* vacuum level. The present results suggest that the A state is an unoccupied state located at ~3.7 eV above the Fermi level (or 1.15 eV below vacuum level at 0.3 ML); thus for our excitation scheme, it is an intermediate state. In order to confirm that this state was an intermediate state, experiments were carried out to measure the photon-energy dependence of monochromatic 2PPE at large detection angles or $k_{\|} > 0.20$ Å $^{-1}$. These experiments (not shown in the figures) showed that the peak of the A state shifted linearly with photon energy, thus positively identifying it as an intermediate state.

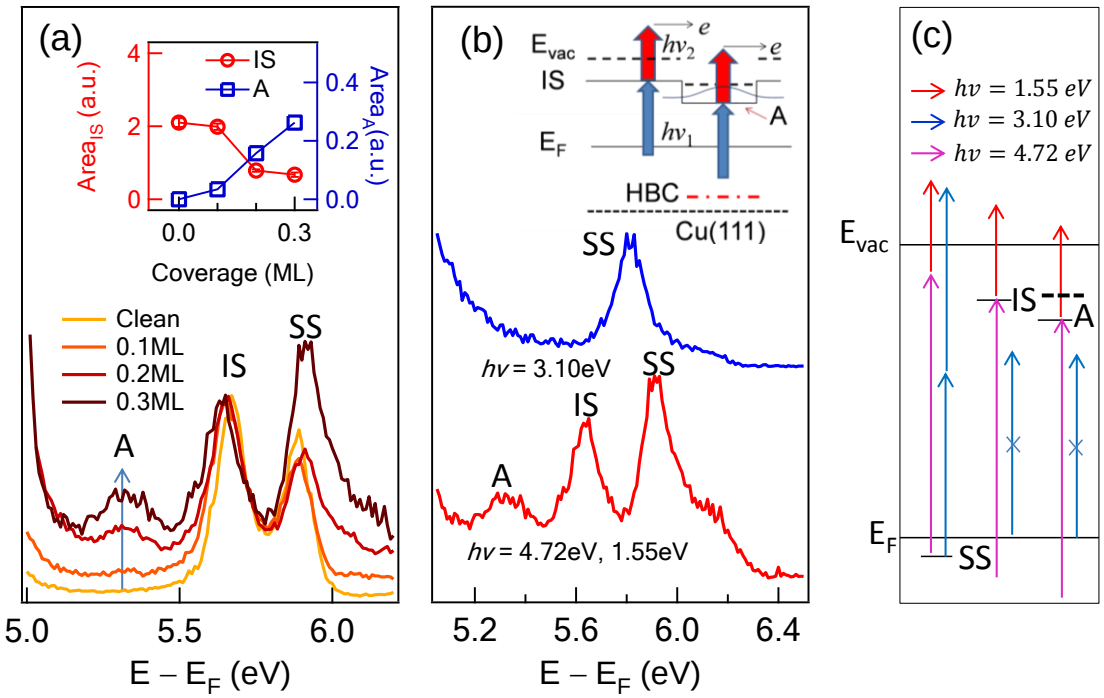

Figure 8.5 (a) Normal incidence bichromatic 2PPE spectra of 0.0 (bare Cu), 0.1, 0.2, and 0.3 ML HBC/Cu(111) with $E_{h\nu,\,pump}$ = 4.72 eV and $E_{h\nu,\,probe}$ = 1.55 eV. The arrow indicates a new state "A", which grows in intensity with coverage. IS and SS are the image state (n =1) and Shockley surface state, respectively. The data is normalized with respect to the intensity of the IS. (Inset) Area of IS (red) and A (blue) as a function of coverage. (b) Normal incidence monochromatic ($E_{h\nu}$ = 3.10 eV) and bichromatic 2PPE spectra of 0.3ML HBC/Cu(111). Intermediate states such as A and IS appear in the bichromatic spectrum only, as is discussed in the text. (Inset) Schematic position-dependent energy diagram of an HBC island on Cu(111). (c) The excitation pathways of resonance states for the monochromatic and bichromatic 2PPE data are shown in (b); the pathways are determined using the known photon energies and the energies of the surface states. The local work function for the A state is indicated by the horizontal dashed line.

In order to examine the extent, to which the states were localized, as well as to assist in their identification, bichromatic *angle-resolved* 2PPE measurements were made in the vicinity of peak A using $E_{h\nu,\,pump}$ = 4.68 eV and $E_{h\nu,\,probe}$ = 1.55 eV for a surface with 0.3 ML coverage; this set of data is shown in Figure 8.6(a) as electron distribution curves at a set of angles and the binding energy vs. parallel momentum. Figure 8.6(b) shows clearly that state A is dispersive. In addition, observe that despite the limit to our energy resolution, the data in Fig. 8.6 have been measured using bichromatic and angle-resolved measurements to separate their dispersion curves for the states shown in Fig. 8.6(c). In Figure 8.6(c), the dispersion curves of the state A are plotted for electron kinetic energy *vs.* parallel momentum. Our data show that the effective mass of state A (m_A*) is 1.1 ± 0.1 m_e. In addition, the image state, IS, appears possibly less dispersive, i.e., m* = 1.5 ± 0.5 m_e, than for typical image states, m* = 1.0 m_e, on clean surfaces. In addition, the data also show that there is no change in the Shockley surface-state dispersion with low HBC coverage. Finally, note that the linearly dispersive bulk copper *sp* state is apparent as a weak spectral feature adjacent to the image state at high $k_{\|}$, in accord with earlier measurements [13].

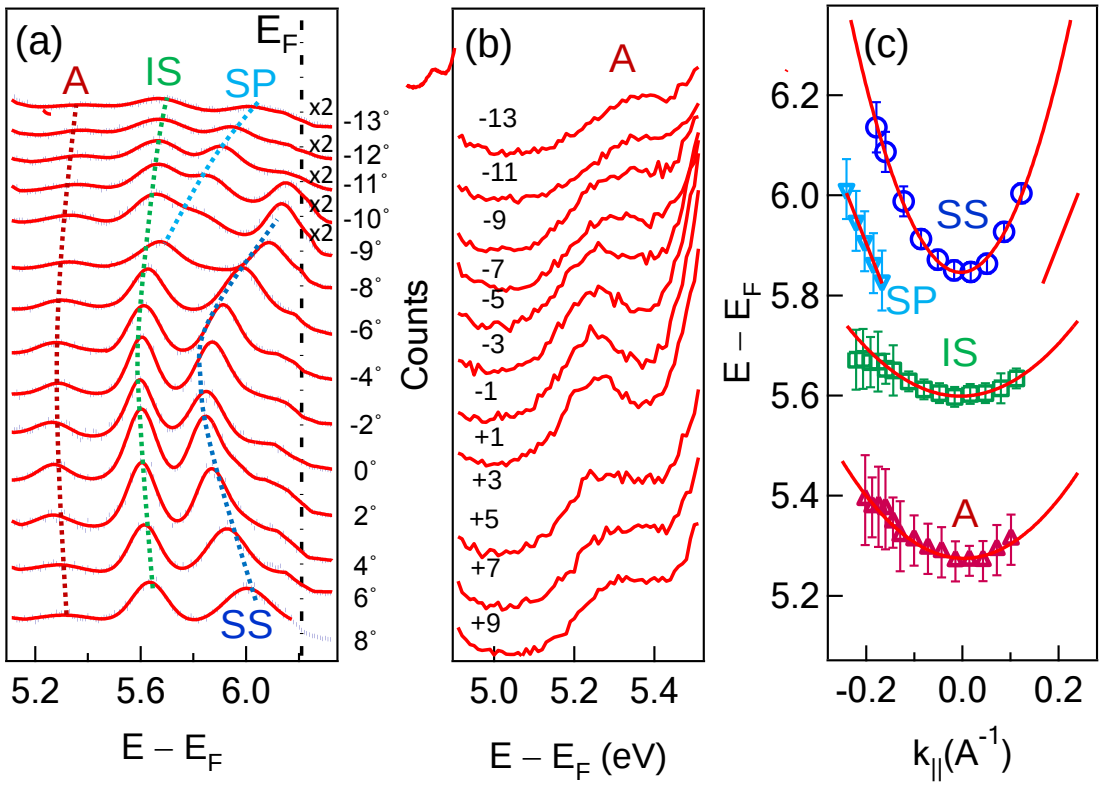

Figure 8.6 (a) Angle-resolved 2PPE spectra of 0.3 ML HBC on Cu(111) in the vicinity of peak A with $E_{h\nu,\,pump}$ = 4.68 eV and $E_{h\nu,\,probe}$ = 1.55 eV. (A: a new state, IS: image state (n = 1), SS: Shockley surface state, SP: bulk Cu intermediate state [13]). (b) Data taken in a selected energy range with $E_{h\nu,\,pump}$ = 4.62 eV and $E_{h\nu,\,probe}$ = 1.55 eV to improve the signal-to-noise ratio. (c) The dispersion curves of the state A, image state, and surface state derived from (a).

To conclude, the surface states of a metal surface, say an electrical contact, are sensitive probes of the adsorption and modification of its surface structure and its electronic properties by an adsorbed organic layer. In our experiment, a promising organic semiconductor for photovoltaic applications, HBC, was deposited on a Cu(111) substrate prepared using a precisely controlled gas-phase doser and in accordance with our

understanding from prior annealing tests. The electronic structure of the newly formed interface was then monitored by angle- and polarization-resolved 2PPE at a sample temperature of 300 K. While the work function of the HBC/Cu system monotonically decreases with an increase in coverage of up to 2ML, the image potential state evolves in a more complex manner. As coverage increases for Θ = 0 - 1ML, the n = 1 state of the bare Cu surface is converted to state A, which has the σ symmetry of a typical image state. At the same time, the Cu *sp* surface state is quenched with coverage. For Θ = 1 - 2 ML, an additional state, B, begins to grow and becomes the most predominant feature among the unoccupied surface states. As for the case of state A, state B is dispersive, with a binding energy comparable to the n =1 image state of Cu. The energetic position of both of these intermediate states is indicative of the image electrons being trapped by the local work function discontinuity at the HBC island edge in each of the coverage regimes. The value of the local work function for each state is compatible with prior observations of work functions of organic species on Cu(111).

8.4 Trapping Surface Electrons on Graphene Layers and Islands on Ir(111) – an Image Potential State Study

In this session, we applied the same surface analysis technique using angle-resolved 2PPE and ARPES to map the bound, unoccupied electronic structure of the weakly coupled graphene/Ir(111) system. The energy, dispersion, and lifetime of the lowest three image-potential states are measured. In addition, the weak interaction between Ir and graphene permits observation of resonant transitions from an unquenched Shockley-type surface state of the Ir substrate to graphene/Ir image-potential states. The image-

potential-state lifetimes are comparable to those of midgap clean metal surfaces. Evidence of localization of the excited electrons on single-atom-layer graphene islands is provided by coverage-dependent measurements.

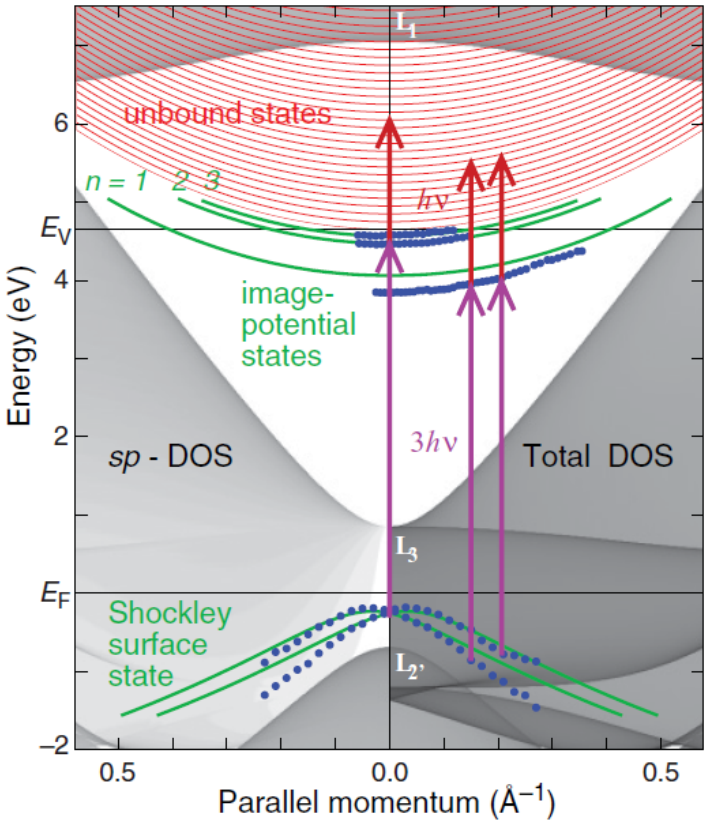

Figure 8.7 Schematic plot of 2PPE transitions (arrows) between surface and image-potential states. The experimental results (dots) are compared to calculations (lines). The projected bulk-band structure of Ir(111) along the $\overline{\Gamma K}$ direction is shaded according to the total and *sp*- density of states (DOS) at the right and left, respectively.

We have observed and measured the properties of image-potential states on a graphene monolayer on Ir(111). A schematic plot is shown in Figure 8.7, and the measurement is shown in Figure 8.8. The binding energy of the n = 1 image-potential state

is 40% larger than expected from the position of the graphene vacuum level relative to the Ir(111) band gap. There is no prominent indication of a second main series of image-potential states as predicted for free-standing graphene [14]. Apparently, the underlying metal substrate breaks the mirror symmetry of the graphene layer and the state of odd symmetry shifts up in energy, as has been calculated for graphene on Ru(0001) [15]. In addition, the image-potential states can be excited efficiently from a downward dispersing Shockley surface state in the sp-band gap of the Ir(111) band structure (Figure 8.8), indicating a sizable overlap of the wave functions of these states located at the substrate interface and graphene surface, respectively.

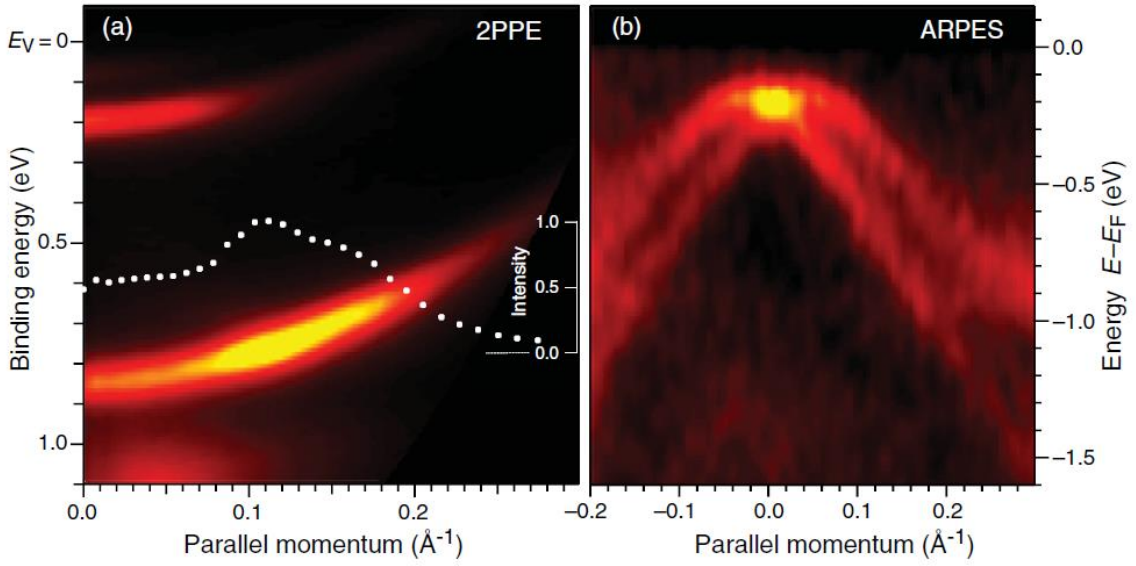

Figure 8.8 (a) Intensity map of the 2PPE signal recorded with photon energy $h\nu$ = 1.59 eV for 1 ML graphene on Ir(111). Points represent the intensity of the lowest n = 1 band. (b) ARPES map showing initial states for $h\nu$ = 55 eV.

Moreover, we measured the average work function Φ was measured via monochromatic 2PPE and the expression $\Phi = 2h\nu - \Delta E$, i.e., where $h\nu$ is the photon energy

and ΔE is the difference between the Fermi level cutoff and the low-energy cutoff. As has been shown in earlier work [16] that the average and local work functions play an important role in interfacial electron localization. Figure 8.9 displays the work function (open symbols) as a function of graphene coverage. The work function decreases approximately linearly from a value 5.79 ± 0.10 to 4.65 ± 0.10 eV from Ir(111) to 1ML graphene. Reported values of the work function for Ir(111) are 5.76 and 5.79 eV [17][18]. The work function of the graphene-covered surface on Ir(111) is between the values for Pt(111) of 4.87 eV and free-standing graphene of 4.48 eV [19], which is consistent with the weak bonding between the Ir(111) and the graphene overlayer and a *p* doping of the graphene [20]. The linear decrease of the work function is known for other systems and is due to the averaging over substrate and overlayer islands [16].

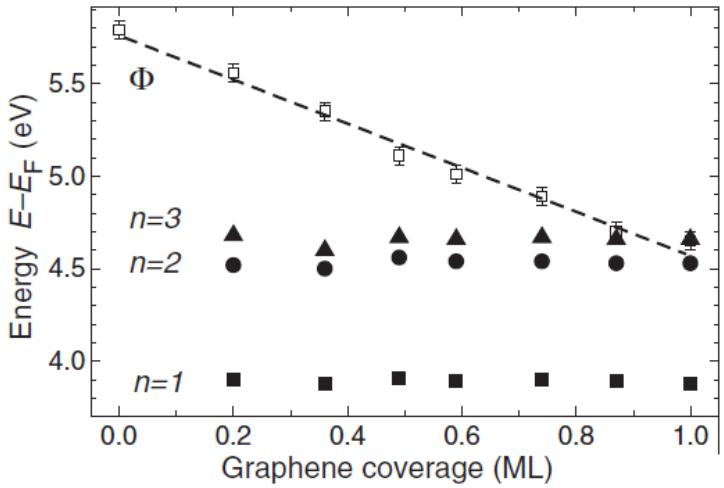

Figure 8.9 Sample work function (open symbols) and image potential states n = 1, 2, and 3 binding energies (solid symbols) as a function of graphene coverage. The dashed line represents a linear fit for the work-function change.

8.4 References

[1] Hong, Sung-Young, Po-Chun Yeh, Jerry I. Dadap, and Richard M. Osgood Jr. "Interfacial dipole formation and surface-electron confinement in low-coverage self-assembled thiol layers: thiophenol and p-fluorothiophenol on Cu (111)."*ACS nano* 6, no. 12 (2012): 10622-10631.

[2] Hong, Sung-Young, Po-Chun Yeh, Ilkyu Lee, Jaeeun Yu, Jerry I. Dadap, Colin Nuckolls, and Richard M. Osgood. "Coverage-Dependent Modification of the Surface Electronic Structure of an Organic-Semiconductor-Adsorbate Layer."*The Journal of Physical Chemistry C* 118, no. 12 (2014): 6214-6225.

[3] Niesner, Daniel, Th Fauster, Jerry I. Dadap, N. Zaki, K. R. Knox, P-C. Yeh, R. Bhandari, R. M. Osgood, M. Petrović, and M. Kralj. "Trapping surface electrons on graphene layers and islands." *Physical Review B* 85, no. 8 (2012): 081402.

[4] Koch, Norbert. "Organic electronic devices and their functional interfaces." *ChemPhysChem* 8, no. 10 (2007): 1438-1455.

[5] Ishii, Hisao, Kiyoshi Sugiyama, Eisuke Ito, and Kazuhiko Seki. "Energy level alignment and interfacial electronic structures at organic/metal and organic/organic interfaces." *Advanced Materials* 11, no. 8 (1999): 605-625.

[6] Heimel, Georg, Lorenz Romaner, Egbert Zojer, and Jean-Luc Bredas. "The interface energetics of self-assembled monolayers on metals." *Accounts of Chemical Researchc* 41, no. 6 (2008): 721-729.

[7] Love, J. Christopher, Lara A. Estroff, Jennah K. Kriebel, Ralph G. Nuzzo, and George M. Whitesides. "Self-assembled monolayers of thiolates on metals as a form of nanotechnology." *Chemical reviews* 105, no. 4 (2005): 1103-1170.

[8] Schmidt, Christian, Alexander Witt, and Gregor Witte. "Tailoring the Cu (100) Work Function by Substituted Benzenethiolate Self-Assembled Monolayers."*The Journal of Physical Chemistry A* 115, no. 25 (2011): 7234-7241.

[9] Hörmandinger, G., and J. B. Pendry. "Interaction of surface states with rows of adsorbed atoms and other one-dimensional scatterers." *Physical Review B* 50, no. 24 (1994): 18607.

[10] Hengsberger, M., F. Baumberger, H. J. Neff, T. Greber, and J. Osterwalder. "Photoemission momentum mapping and wave function analysis of surface and bulk states on flat Cu (111) and stepped Cu (443) surfaces: A two-photon photoemission study." *Physical Review B* 77, no. 8 (2008): 085425.

[11] Cohen, Y. S.; Xiao, S.; Steigerwald, M. L.; Nuckolls, C.; Kagan, C. R., Enforced One-Dimensional Photoconductivity in Core-Cladding Hexabenzocoronenes. *Nano Lett.* **2006,** *6*, 2838-2841.

[12] Tremblay, N. J.; Gorodetsky, A. A.; Cox, M. P.; Schiros, T.; Kim, B.; Steiner, R.; Bullard, Z.; Sattler, A.; So, W.-Y.; Itoh, Y.; Toney, M. F.; Ogasawara, H.; Ramirez, A. P.; Kymissis, I.; Steigerwald, M. L.; Nuckolls, C., Photovoltaic Universal Joints: Ball-and-Socket Interfaces in Molecular Photovoltaic Cells. *ChemPhysChem* **2010,** *11*, 799-803.

[13] Hao, Zhaofeng, J. I. Dadap, K. R. Knox, M. B. Yilmaz, N. Zaki, P. D. Johnson, and R. M. Osgood. "Nonequilibrium Band Mapping of Unoccupied Bulk States below the Vacuum Level by Two-Photon Photoemission." *Physical review letters* 105, no. 1 (2010): 017602.

[14] Silkin, V. M., J. Zhao, F. Guinea, E. V. Chulkov, P. M. Echenique, and H. Petek. "Image potential states in graphene." *Physical Review B* 80, no. 12 (2009): 121408.

[15] Borca, B., S. Barja, M. Garnica, D. Sánchez-Portal, V. M. Silkin, E. V. Chulkov, C. F. Hermanns et al. "Potential energy landscape for hot electrons in periodically nanostructured graphene." *Physical review letters* 105, no. 3 (2010): 036804.

[16] Fischer, R., S. Schuppler, N. Fischer, Th Fauster, and W. Steinmann. "Image states and local work function for Ag/Pd (111)." *Physical review letters* 70, no. 5 (1993): 654.

[17] Strayer, R. W., W. Mackie, and L. W. Swanson. "Work function measurements by the field emission retarding potential method." *Surface Science* 34, no. 2 (1973): 225-248.

[18] Nieuwenhuys, B. E., R. Bouwman, and W. M. H. Sachtler. "The changes in work function of group Ib and VIII metals on xenon adsorption, determined by field electron and photoelectron emission." *Thin Solid Films* 21, no. 1 (1974): 51-58.

[19] Giovannetti, G., P. A. Khomyakov, G. Brocks, V. M. Karpan, J. Van den Brink, and P. J. Kelly. "Doping graphene with metal contacts." *Physical Review Letters*101, no. 2 (2008): 026803.

[20] Pletikosić, Ivo, Marko Kralj, Petar Pervan, Radovan Brako, Johann Coraux, A. T. N'diaye, C. Busse, and Th Michely. "Dirac cones and minigaps for graphene on Ir (111)." *Physical Review Letters* 102, no. 5 (2009): 056808.

Chapter 9

Summary and Outlook

"It is change, continuing change, inevitable change, that is the dominant factor in society today. No sensible decision can be made any longer without taking into account not only the world as it is, but the world as it will be." - Isaac Asimov

9.1 Summary

This fascinating story of 2D materials dates all the way back to the early 20th century, when the existence of two-dimensional (2D) materials was a highly debated topic in the physics community. In fact, Peierls and Landau have stated that, from a statistical physics perspectives, 2D materials are thermodynamically instable at any finite temperature due to thermal lattice fluctuations. It was not until 2004 when Novoselov and Geim successfully isolated the first truly 2D single-layer material – graphene that started an epoch of atomic-scale 2D material research, pushing the physical boundary of material science to its extreme. The existence of graphene did not violate the physics laws that Peierls and Landau warned of, on the contrary, it broadened the physics in low dimensions and lead us into this new 2D "flat land."

The invention of graphene as well as its early success showed that it is possible to create stable, single and few-atom- thick layers of van der Waals materials, with excellent stiffness provided by 2D confinement-induced long range interactions. These van der

Waals materials have a rich spectrum of properties and can potentially be engineered on-demand. They also have shown exciting possibilities in device applications ranging from electronics, photonics, energy harvesting, flexible electronics, transparent electrodes, and sensing. For example, graphene is semi-metallic and has extremely high carrier mobility and high on-and-off ratio for transport devices; hexagonal-boron nitride (h-BN) is insulating and ultra-flat, and has an almost identical lattice constant to graphene that makes it a perfect substrate; "beyond graphene", there are monolayers of transition metal dichalcogenides, e.g. MoS_2 and WSe_2 that are direct bandgap semiconductors with thickness dependent bandgaps. Each of these materials has their unique advantage for device application, and when combined, new physics and a library of novel devices arise.

In this thesis, we focus on the semiconducting transition-metal dichalcogenides (TMDCs), MoS_2 and WSe_2; both of them have a direct bandgap in monolayer form that avoids the Achilles's heel of graphene of being a gapless material. We study the surface morphology and electronic structure of MoS_2 and WSe_2 by using a SPELEEM system that gives us the capability of probing micro-sized surface structure, crystallinity, and band structure all at once.

Our research started with probing the surface morphology and structural quality of ultrathin MoS_2 flakes, prepared by mechanical exfoliation or CVD, using LEEM and μ-LEED. We tackled and solved the issues of sample charging and surface corrugation by transferring MoS_2 crystals to a native-oxide-covered Si wafer. In addition, we developed a surface doping technique using alkali-metal ions to image grain boundaries. We have investigated MoS_2 films on different substrates, of different thickness, as well as using different preparation methods, and under different alkali-metal doping levels, to optimize

our model system for studying electronic structure. We found that *real-space* probing by LEEM in conjunction with *k-space* probing by μ-LEED has shown that CVD-grown MoS_2 single crystals have comparable crystal quality to that of exfoliated MoS_2. Our results have also shown that as-grown CVD MoS_2 sample islands have a fine vein-like or rippled structure, as revealed via potassium deposition; this leaf-like morphology is lost after sample transfer to a silicon substrate. We attribute this structure to strain fields formed during CVD growth. We also developed a procedure to transfer and clean the MoS_2 sample that has been proven very crucial in all of the surface sensitive optical and electrical measurements. These early works are an important step toward a broader understanding of MoS_2 surface morphology on different substrates and establishing strategies for MoS_2 synthesis.

On the basis of the sample preparation procedure we developed, later, we successfully performed μ-ARPES measurements to probe the valence bands of monolayer MoS_2 derived from the Mo 4*d* and S 3*p* orbitals. The result matches the DFT predictions generally well and shows a striking difference when compared with few-layer and bulk MoS_2. The observed increase in the VBM at $\overline{K}$ in monolayer MoS_2 provides a direct measurement of the indirect-to-direct band gap transition in going from few-layer to monolayer MoS_2. The concomitant decrease in the dispersion of the VBM at $\overline{\Gamma}$ leads to a substantially larger hole effective-mass, which explains the low hole mobility of monolayer MoS_2 compared to bulk MoS_2. This direct observation of MoS_2 band structure transition is the first direct proof to the previous theoretical predictions and optical measurements.

Following the MoS_2 measurement, we also probed the surface structure and occupied electronic bands of 1 – 3 layer exfoliated WSe_2 crystals prepared by transfer to

the same ultra-clean and pre-patterned native-oxide Si substrate. Other than having a larger bandgap, WSe_2 is of interest because it also has a strong spin-orbit splitting and can be fabricated into both p- and n- type transistors, making building a bilayer WSe_2 p-n junction device possible. We used LEEM and μ-LEED to probe real-space and reciprocal-space structure of WSe_2. The results reveal clearly-resolved thickness-dependent contrast and diffraction spot widths, respectively. We used μ-ARPES to probe the occupied valence-band structure and have confirmed the transition of the valence band maximum from $\bar{\Gamma}$ to $\bar{K}$ as the thickness is reduced from few-layer to 1ML WSe_2; this observation provides support for an indirect-to-direct bandgap transition. For monolayer WSe_2, we have found a lower bound of 1.8 eV for the bandgap and measured a hole effective mass of 1.4 m_0 at $\bar{K}$ and 3.5 m_0 at $\bar{\Gamma}$. We expect that these results will provide insight to the understanding of the optical and electronic properties of monolayer and multilayer WSe_2.

To go a step further, we studied the MoS_2-substrate interactions. We performed ARPES measurements on suspended and supported monolayer MoS_2 using a different SPELEEM system. Our ARPES measurements of suspended MoS_2 reveal good qualitative and quantitative agreement with theory and elucidate the effects of a native-oxide Si substrate on the band structure of monolayer MoS_2. We found a suggested expansion of the in-plane lattice constant and deduce also an expansion of the intra-plane lattice constant, which may be indicative of an atomic structure that is sensitive to layer stacking. By comparing both supported and suspended monolayer MoS_2, where the in-plane lattice constant expansion is prevail in both cases, we deduce that this expansion is a structural lattice relaxation due to the removal of out-of-plane confinement when thinned down to one layer. We also found that the effective mass of suspended monolayer MoS_2 is less than

the substrate-supported monolayer MoS_2 by ~10%, indicating a mobility boost via suspension.

We now shift our focus to study the interlayer coupling of bilayer MoS_2 and how the electronic structure changes with interlayer twist angles. We prepared CVD-grown large area monolayer MoS_2 flakes, and stacked the two sheet of monolayer MoS_2 with arbitrary twist angles from 0° to 60° via transfer techniques. We then imaged these twist bilayer MoS_2 flakes using both bright-field and dark-field LEEM. The bright-field LEEM imaging provides real-space structural measurements of twisted-bilayer MoS_2 ($TBMoS_2$), while dark-field LEEM imaging, combined with μ-LEED, help us define the interlayer crystal orientations. We also probed the occupied valence-band structure of bilayer MoS_2 at twist angles of 0°, 13°, 26°, 39°, 47°, and 60° using μ-ARPES. We observed an energy shift of up to 200 meV at the VBM at $\bar{\Gamma}$ when the twist angle reaches ~30°. Since the VBM and CBM at $\bar{K}$ are predicted to be independent of interlayer twisting, bandgap opening is solely determined by the energy level of the VBM at $\bar{\Gamma}$. This variation at $\bar{\Gamma}$ is due to the evolution of the interlayer coupling strength which in turn is a function of the interlayer spacing. Thus, the $\bar{\Gamma}$ VBM state shifts in energy with twist angle, and thus one can tune the bandgap of bilayer MoS_2. This observation agrees well with theory and PL measurements. We expect that these results will provide physical insight to the understanding of the optical and electronic properties of $TBMoS_2$, and to engineering the bandgap by tuning the interlayer coupling, since the ability to control the interlayer coupling is important to the development of TMD-based devices.

In the final part of this thesis, we briefly discuss our studies on classical 2D surface systems – high-crystalline metal surfaces, Cu(111) and Ir(111). First, we studied self-

assembly molecules, thiopheonol and 4-fluorothiophenol, adsorbed on a Cu(111) surface to understand their work function, interfacial dipoles, and interfacial states as a function of coverage. We found that the orientation of the molecules and their intrinsic dipole moments played an important role in surface polarization and their self-assembled structures. We also developed the apparatus and procedure to carefully deposit the molecules at well-controlled temperature and dosage. We took a step further to apply these techniques to study another molecule/metal system – HBC, an non-planar organic semiconductor for photovoltaic applications, on Cu(111) surface. We investigated the interfacial electronic structure of HBC on Cu(111) as a function of coverage. Based on our polarization- and momentum-resolved 2PPE, we concluded that the porous structure of HBC film causes a strong localization of image electrons from zero to one monolayer coverage. The local film structure transformed from porous to smooth by increasing the HBC coverage. As a result, a highly dispersive image state on 2ML HBC islands became predominant. Last, we studied epitaxial graphene grown on Cu(111) as a model system using 2PPE and angle-resolved 2PPE, and our data were confirmed by theory and earlier experimental results. Then, we studied as grown CVD-prepared graphene on Ir(111) suface. We confirmed that the surface states excited by the two-photon process in Gr on Cu(111) system were image potential states, and the origin of these image states is due to electrons trapped in the interface of graphene and bulk metal.

9.2 Outlook

Thus far, we have investigated several 2D systems using LEEM, LEED, ARPES, XPS, XPEEM, and 2PPE to understand their surface and electronic structure. However, a complete understanding of the 2D material family and their unique electrical and optical properties is still far from complete. In terms of understanding the electronic structure of TMDs, there remain many interesting and fundamental physical phenomena to explore, for example, the strong spin-orbit coupling in TMDc that induces a large spin-orbit splitting at $\overline{K}$ point, band renormalization, interfacial charge transfer, and bandgap engineering via changing interlayer spacing, strain, or modifying structural configuration. To fully investigate the physics behind these phenomena, we propose to use spin-resolved ARPES embedded with molecular beam epitaxy (MBE) growth capability, and an angle- and spin-resolved 2PPE system with an ultra-fast laser probe. These apparatus are, in part, aceessible in the newly-built National Synchrotron Light Source II in Brookhaven National Laboratory. We plan to start with our model system, MoS_2 and WSe_2, to measure the spin-valley coupling and their Rashba spin-orbit splitting using spin-resolved ARPES system. Also, measurements carried out at low temperature and various doping levels will be performed. These measurements will be extremely valuable in designing, fabricating and optimizing these materials for future device applications.

Other than single-specie TMD materials measured in this thesis, recent research focus in 2D community have been extended to heterostructure and heterojunction of TMDs, i.e. junctions and devices made by stacking two or more layers of different 2D crystals. Since heterostructures of semiconductors and metals form fundamental building blocks of

modern electronic and photonic devices, the basic idea here is to build new 2D material devices by stacking different 2D layers, for which each material possesses their own unique functionality. In these heterostructure model systems, strong covalent bonds provide in-plane stability of 2D crystals, whereas relatively weak, van-der-Waals-like forces are sufficient to keep the stack together due to large contacting area. This property creates an atomically sharp, coherent, and surface passivated interfaces; this interface is ideal for building high mobility transistors, solid state lasers, light emitting devices, and solar cells. For example, hexagonal boron nitride (h-BN) has been used extensively to be a protection layer or an ultra-flat platform for holding graphene and many 2D layered materials, as graphene has been considered a perfect buffering contact that bridges 2D materials and 3D metal contacts, forming an ohmic contact with 2D materials and metals. Our current work (in progress) has focused on graphene-MoS_2 heterostructures, as the next step from our twist bilayer MoS_2 studies. We have studied the hybrid electronic structure of bilayer graphene-MoS_2 system, as a function of interlayer twist angles and stacking sequence. We found that the as-transferred graphene bands do not hybrid with MoS_2 bands, and the afore-mentioned out-of-plane interlayer coupling still affects the top-most-valence bands and is also a function of the twist angles. We also plan to study other heterostructure systems, such as MoS_2-$MoSe_2$ or MoS_2-WS_2, which has highly proximate atomic registrations. The ultimate goal is to minimize or enhance the interlayer coupling in order to modify the band structure by interlayer twisting, or via applying hydrostatic pressure using a diamond anvil cell (DAC), or by replacing one dichalcogenide atoms with another (e.g. $MoS_{2-x}Se_x$, $x < 1$).

Moreover, there still remain many promising candidates in the large 2D material family. Beyond graphene and TMDs, there are many other 2D layered materials with novel

properties for promising applications; for example, we are currently examing mono- and multi-layer rhenium disulphide (ReS_2), black phosphorous (phosphorene for its monolayer film), and several metal-organic perovskites using our established techniques in sample preparation and surface probing. Distorted 1T-ReS_2 has a unique feature that, it remains a direct bandgap material from mono- to multi-layers. This behavior is observed using Raman spectroscopy, which the spectrum of bandgap transition shows no dependence on the number of layers. Even after further modulation on the interlayer distance (coupling) by external hydrostatic pressure, the optical absorption and Raman spectrum remain unchanged in 1T-ReS_2, implying that the interlayer interaction is indeed rather weak (S. Tongay *et al*.) Thus, this makes 1T-ReS_2 multi-layer crystals an ideal platform to probe 2D excitonic and lattice physics, circumventing the challenge of preparing large-area, single-crystal monolayers. It is an ideal model system to study the relation of interlayer coupling and the band structure. We have probed several thin exfoliated 1T-ReS_2 flakes using LEEM, LEED, and ARXPS. A thorough study of its surface and electronic structure using ARPES is needed.

Another hot topic in the 2D community is the afore-mentioned (black) phosphorene. Phosphorene, like MoS_2, is a semiconducting layered material that is flexible and can be mechanically exfoliated from black phosphorous ore. It has been reported to have a comparable hole mobility to that of a bulk MoS_2, and a layer-dependent direct bandgap like the 1T-ReS_2. Because the band gap is a fundamental factor in determining electronic screening and corresponding many-electron interactions in the material, the optical spectra and excitonic effects of few-layer phosphorene shall also be controlled by the number of stacking layers. Therefore, studying few-layer phosphorene provides a chance to observe

how the electronic structure and excitonic properties of a 2D material transition to that of a 3D material. So far, due to the ready reactivity of phosphorene to oxidation, a direct ARPES measurement with *ex situ* prepared phosphorene is not yet successful. One solution is to coat a protection layer on the phosphorene sample, before introducing it to the UHV experiment chamber. Another move is to grow the phosphorene *in situ* in UHV chamber without exposure to air.

Furthermore, we are working on thin-films of perovskites such as lithium niobate ($LiNbO_3$) and butyl ammonium lead iodide. For the case of $LiNbO_3$, it is a material of a long history of industrial and research development and rich applications in laser-frequency doubling, non-linear optics, Pockels cells, optical parametric oscillators, and Q-switching devices for optical systems. Here, we propose to transfer graphene on $LiNbO_3$ thin-film consisting of two different poling to measure its band structure and surface potential. As for butyl ammonium lead iodide (or lead iodide perovskite), an organic-metal perovskite that is also a layered material and can be prepared by mechanical exfoliation, it can be used for making ultra-thin and high performance solar cells or photovoltaic devices. A hybrid lead iodide perovskite and lead sulfide quantum dot heterojunction solar cell has been reported to exhibit high efficiency and open-circuit voltages of 1 V. We propose to study the exfoliated mono- to multi- layer lead iodide perovskite, and with alkali metal surface doping, to understand its electronics structure, the effect of intrinsic defects, and to optimize its performance as a solar cell device. Also, on top of Raman studies, we aim to study the origin of its dynamic disorders using SHG and two-photon luminescence.

Appendix

We summarize some of our experimental work on unconventional samples using important figure.

A. Black phosphorous and phospherene

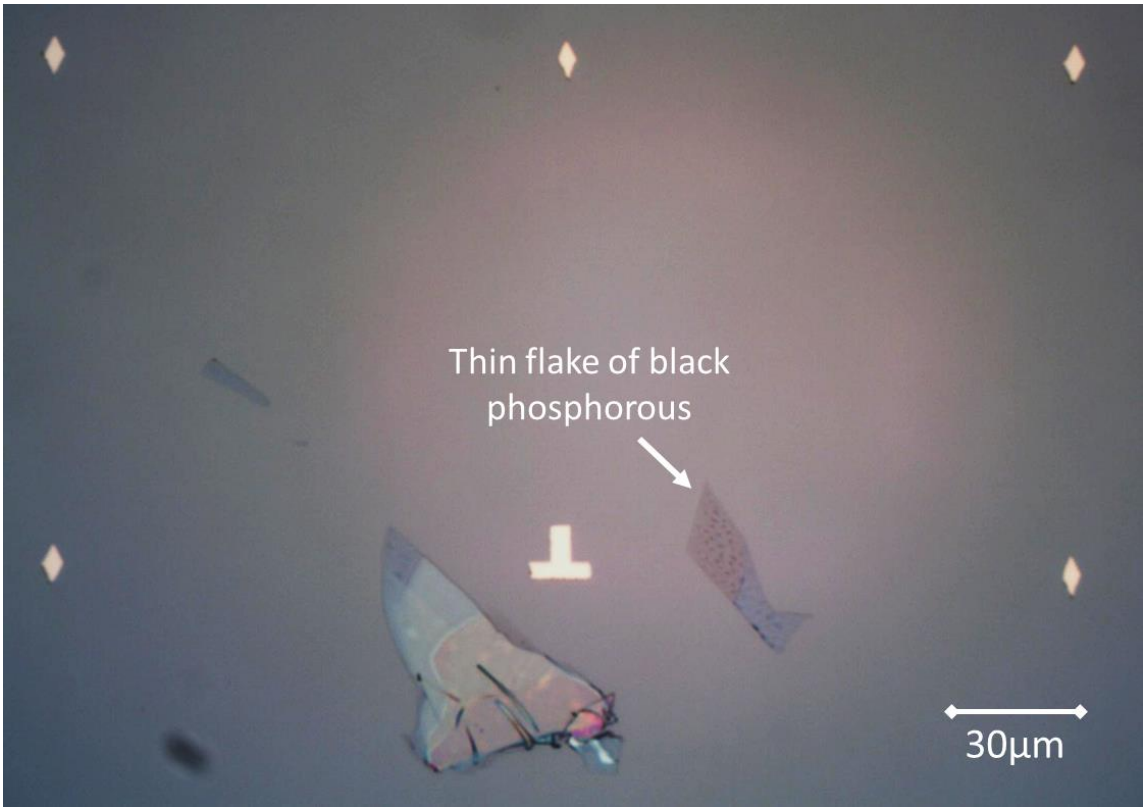

Optical microscope image of black phosphorous (BP) on a native-oxide/silicon sample; water, air, and light induced degradation of BP is reflected by the small blackdots on the sample. It is found that the thinner the BP flake, the faster it degrades.

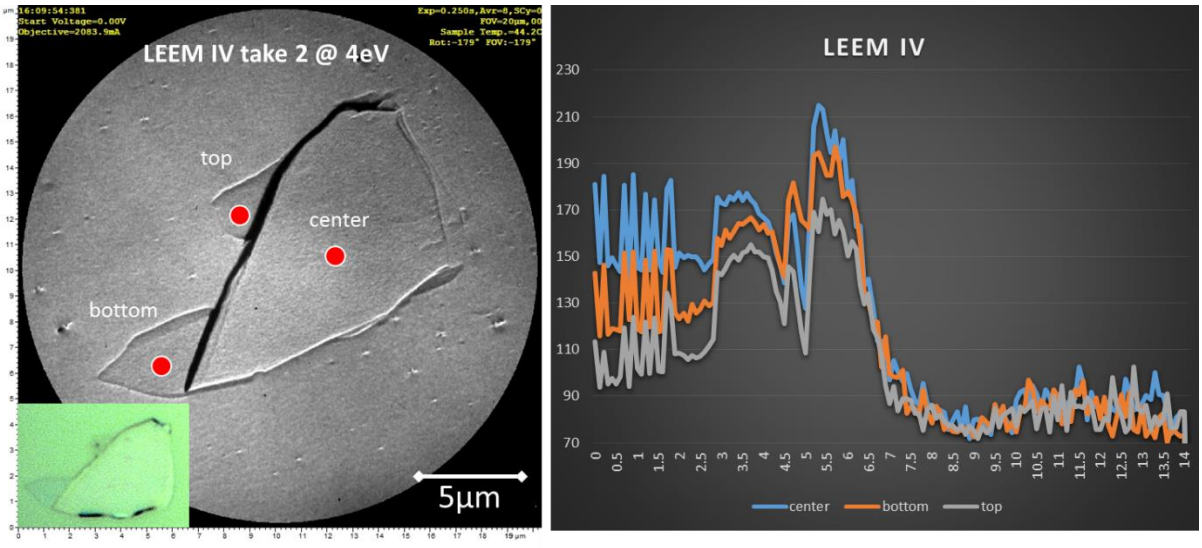

BF-LEEM image of a thin flake of black phosphorous sample prepared by mechanical exfoliation; and LEEM IV measurements on three spots of different thickness. The flake thickness is such that center > bottom >> top. The inset is the corresponding optical microscope image.

B. 1T-ReS_2 thin films

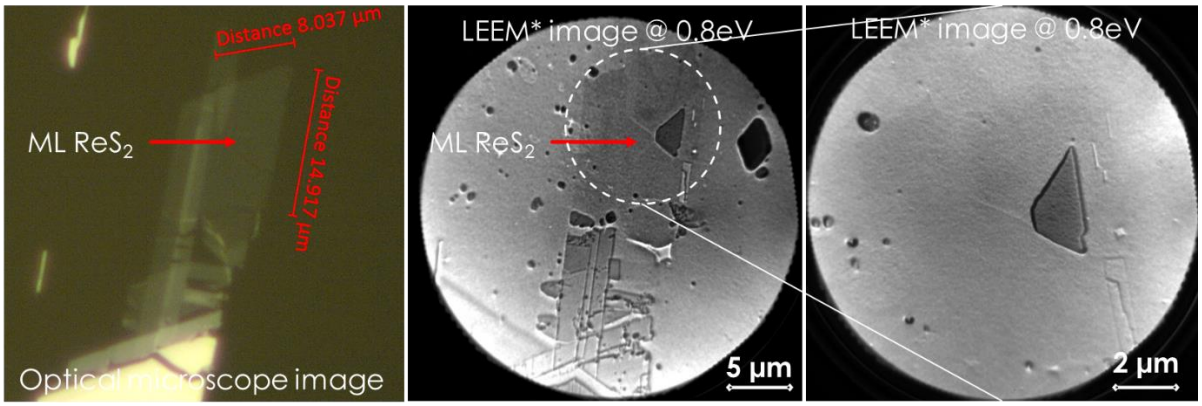

Exfoliated monolayer 1T-ReS_2 on a native-oxide/silicon substrate and its optical corresponding optical-microscope and LEEM images. Its XPS spectrum (below) shows little to no Re signal:

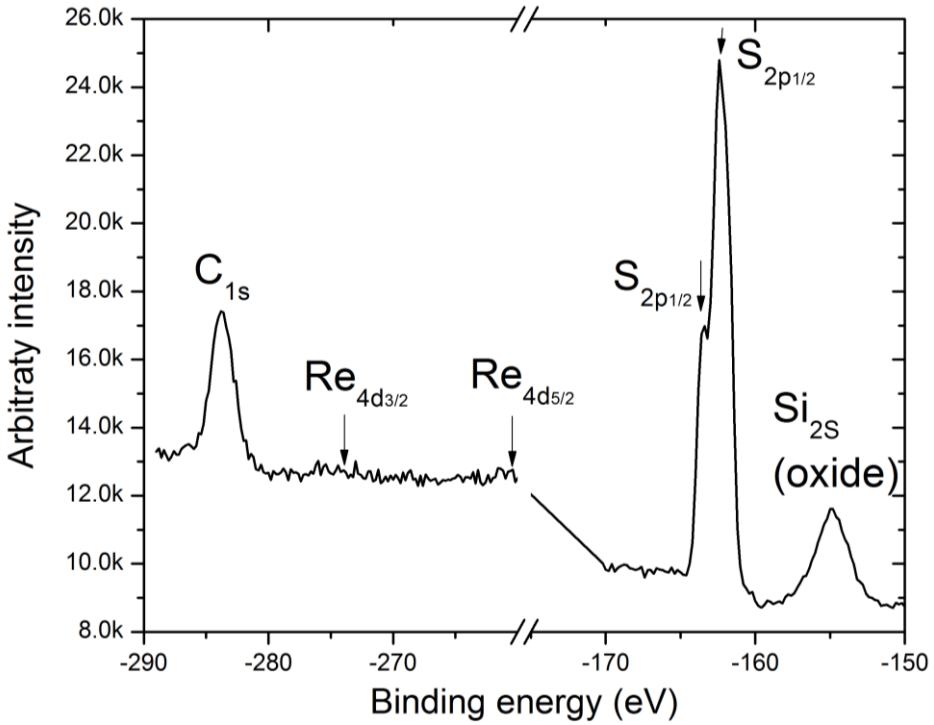

XPS spectrum of the core levels of the ReS_2 flakes, the substrate, and the surface residue on the sample.

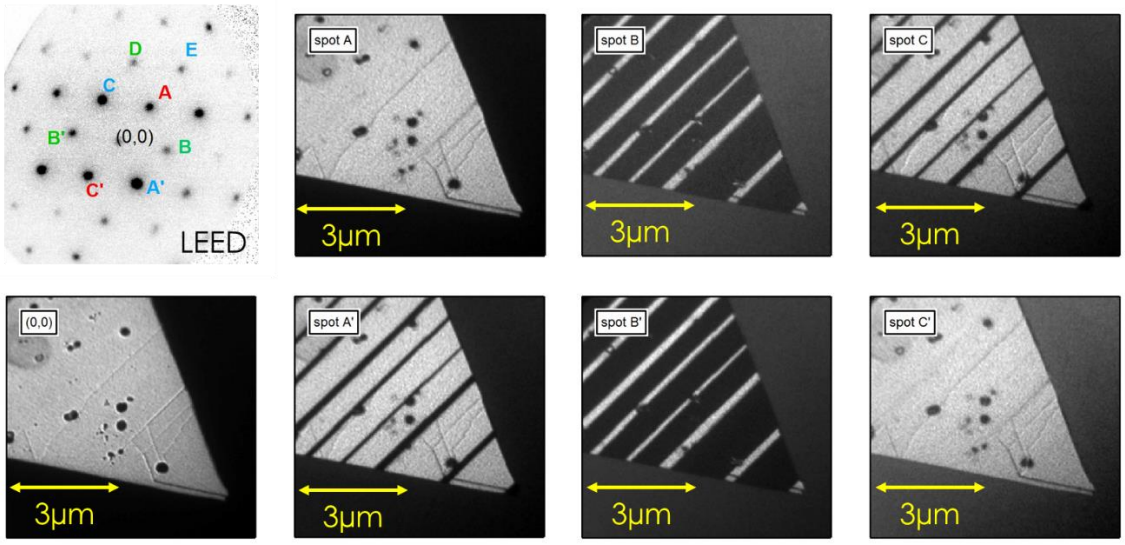

LEED and DF (dark field) - LEEM patterns of a thin bulk 1T-ReS_2. The 1T structure of ReS_2 is very different from the usual 2H structure.

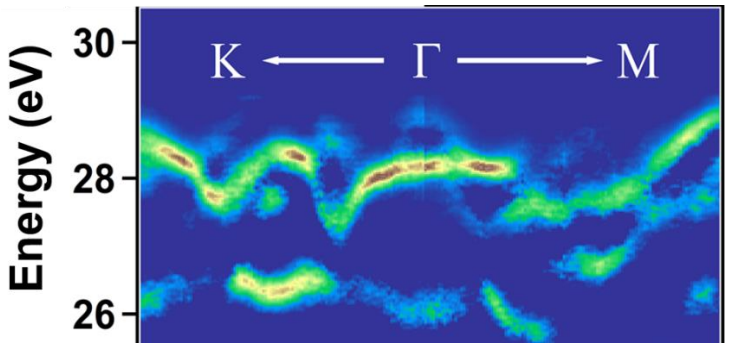

ARPES measurement of thin-bulk 1T-ReS_2 and its band dispersion along the high-symmetry direction K-Γ-M and with curvature filtering.